UNIVERSITAT DE BARCELONA

Study of Cu-ZnO-Ga_2O_3- and Mo_xC-based Catalysts for the Reverse Water Gas Shift Reaction

Xianyun Liu

ADVERTIMENT. La consulta d’aquesta tesi queda condicionada a l’acceptació de les següents condicions d'ús: La difusió d’aquesta tesi per mitjà del servei TDX (**www.tdx.cat**) i a través del Dipòsit Digital de la UB (**diposit.ub.edu**) ha estat autoritzada pels titulars dels drets de propietat intel·lectual únicament per a usos privats emmarcats en activitats d’investigació i docència. No s’autoritza la seva reproducció amb finalitats de lucre ni la seva difusió i posada a disposició des d’un lloc aliè al servei TDX ni al Dipòsit Digital de la UB. No s’autoritza la presentació del seu contingut en una finestra o marc aliè a TDX o al Dipòsit Digital de la UB (framing). Aquesta reserva de drets afecta tant al resum de presentació de la tesi com als seus continguts. En la utilització o cita de parts de la tesi és obligat indicar el nom de la persona autora.

ADVERTENCIA. La consulta de esta tesis queda condicionada a la aceptación de las siguientes condiciones de uso: La difusión de esta tesis por medio del servicio TDR (**www.tdx.cat**) y a través del Repositorio Digital de la UB (**diposit.ub.edu**) ha sido autorizada por los titulares de los derechos de propiedad intelectual únicamente para usos privados enmarcados en actividades de investigación y docencia. No se autoriza su reproducción con finalidades de lucro ni su difusión y puesta a disposición desde un sitio ajeno al servicio TDR o al Repositorio Digital de la UB. No se autoriza la presentación de su contenido en una ventana o marco ajeno a TDR o al Repositorio Digital de la UB (framing). Esta reserva de derechos afecta tanto al resumen de presentación de la tesis como a sus contenidos. En la utilización o cita de partes de la tesis es obligado indicar el nombre de la persona autora.

WARNING. On having consulted this thesis you’re accepting the following use conditions: Spreading this thesis by the TDX (**www.tdx.cat**) service and by the UB Digital Repository (**diposit.ub.edu**) has been authorized by the titular of the intellectual property rights only for private uses placed in investigation and teaching activities. Reproduction with lucrative aims is not authorized nor its spreading and availability from a site foreign to the TDX service or to the UB Digital Repository. Introducing its content in a window or frame foreign to the TDX service or to the UB Digital Repository is not authorized (framing). Those rights affect to the presentation summary of the thesis as well as to its contents. In the using or citation of parts of the thesis it’s obliged to indicate the name of the author.

Facultat de Química

Departament de Química Inorgànica i Orgànica

Secció de Química Inorgànica

Programa de Doctorat en Química Orgànica

Study of Cu-ZnO-Ga_2O_3- and Mo_xC-based Catalysts for the Reverse Water Gas Shift Reaction

Xianyun Liu

Directors:

Dra. Maria Pilar Ramírez de la Piscina Millán
Dr. Narcís Homs Martí

Tutor:

Dra. Maria Pilar Ramírez de la Piscina Millán

April 2018

La Dra. Maria Pilar Ramírez de la Piscina Millán y el Dr. Narcís Homs Martí, Catedráticos de la Universitat de Barcelona, CERTIFICAN:

Que la memoria titulada **“Study of Cu-ZnO-Ga_2O_3- and Mo_xC-based Catalysts for the Reverse Water Gas Shift Reaction”,** presentada por Xianyun Liu para optar al título de Doctor en el programa de Química Orgánica de la Universitat de Barcelona ha sido realizada bajo su dirección en el Grup de Materials Catalítics del Departament de Química Inorgànica i Orgànica, Secció de Química Inorgànica, de la Universitat de Barcelona.

Dra. Maria Pilar Ramírez de la Piscina Millán　　　　Dr. Narcís Homs Martí

Contents

Chapter 1

Introduction

1.1. CO_2 emissions and utilization

For millions of years, CO_2 is playing a key role in the well-known carbon cycle, which operates in Earth; CO_2 is a feedstock, which in combination with water and solar energy, via photosynthesis, contributes to the development of vegetal life. In fact, the Earth's cycle of carbon comprises several additional ways of CO_2 transformation, for example to $CaCO_3$, or in the absence of oxygen to CH_4 by the action of bacteria. Of course, life on Earth liberates CO_2 through different processes such as animal life and human activities!

The CO_2 concentration in the atmosphere plays a significant role in the climate of our planet through the greenhouse effect. Over the last centuries, CO_2 exchange between vegetation, atmosphere and oceans has changed. This is partly because of deforestation and due to the extensive use of fossil fuels. As a result, the CO_2 natural equilibrium has been modified.

The accumulation of CO_2 in the atmosphere has increased significantly, compared to the level before the Industrial Revolution [1,2]. In December 2017, the concentration of CO_2 in the atmosphere was about 407 ppm [3], which was roughly 40% above the level in the mid-1800s [2]. The average surface temperature of the planet has risen about 1.1 °C since 19 th century [4]; the rising of temperature can contribute to the warming of the ocean, the shrinking of the ice cover and the increase of the sea level.

Thus, the mitigation of atmospheric CO_2 becomes more and more crucial. Although CO_2 emissions can be reduced through carbon capture and storage (CCS) by geologic storage process, the use of CO_2 in processes to manufacture valuables and fuels is more desirable. In recent years, many efforts have been devoted to developing efficient techniques for the capture and separation of CO_2 from different effluents, mainly corresponding to combustion, gasification and fermentation processes [5]. Nowadays, it is possible to obtain large amounts of relatively clean CO_2 from post-combustion effluents through, among others, the amine absorption process, the carbonate looping technology and the so-called oxyfuel process [6,7]. Today CO_2 is not only considered a waste, CO_2 can be also conveniently used as raw material for industrial applications. The reuse of CO_2 through its chemical recycling, is a promising route which could contribute to the decrease of globally emitted CO_2 [8,9,10]. Thus, nowadays we can consider CO_2 as a truly key molecule in a sustainable development.

Figure 1.1 illustrates most of the current and potential pathways for CO_2 utilization. In general, CO_2 can be used in two different categories, direct use of CO_2 and conversion of CO_2 to valuable chemicals and fuels [11]. However, some disadvantages are still present for many of these CO_2 uses, such as small-scale utilization and CO_2 emission to the atmosphere after use.

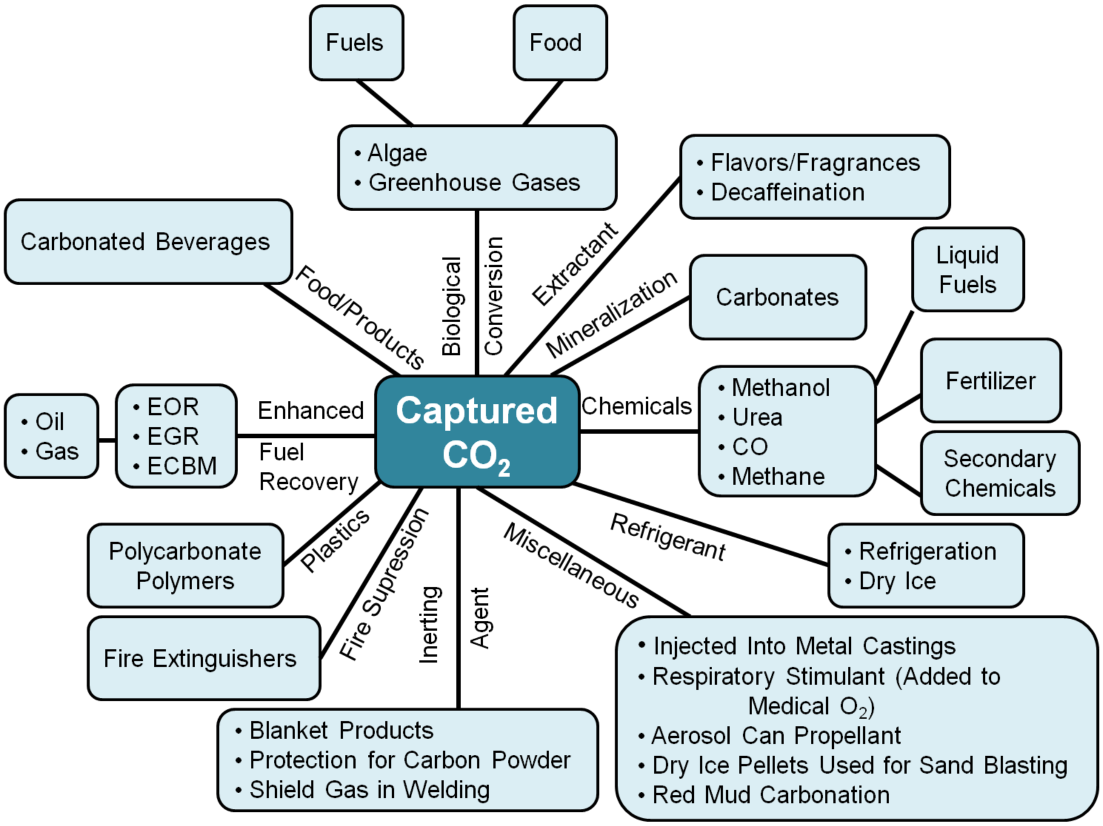

Figure 1.1. The illustration of use of CO_2 (Taken from the U.S. Department of Energy's National Energy Technology Laboratory. https://www.netl.doe.gov/).

CO_2 is a molecule which is thermodynamically stable, and its activation requires high energy input to overcome the energy barrier for the dissociation of C=O bond. However, CO_2 can be selectively activated by H_2 through catalytic processes, under appropriate conditions of pressure and temperature. Figure 1.2 shows the transformation of CO_2 to chemicals and fuels via different catalytic processes. Many studies in CO_2 reduction using H_2 are centered on the development of highly active, selective and stable catalysts for the production of CO, methanol and hydrocarbons [12]. Production of CO on a solid catalyst via the reverse water gas shift (RWGS) reaction is one of the key steps in the CO_2 hydrogenation to valuable chemicals and fuels. Currently, the RWGS reaction to CO, the syngas production from dry reforming of CH_4, and, the direct hydrogenation of CO_2 to methanol and hydrocarbons, are considered green technologies for CO_2 transformation to synthetic fuels [13].

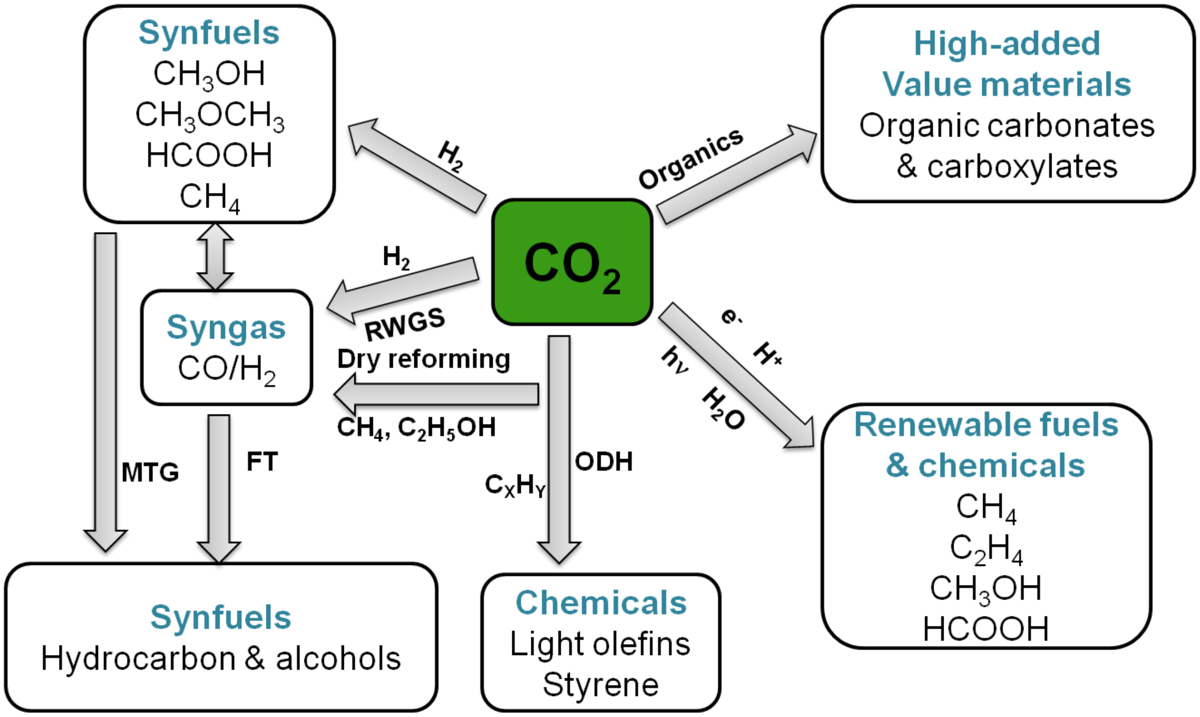

Figure 1.2. Catalytic routes for CO_2 activation in heterogeneous phase leading to fuels and chemicals (Redrawn from reference [8]).

1.2. Reverse water gas shift reaction (RWGS)

The RWGS reaction (Eq. 1.1) is considered a promising and cheap way for CO production from CO_2.

$$CO_2+H_2 \leftrightarrow CO+H_2O, \;\; \Delta H^0_{298K}=41.2 \text{ kJ/mol} \qquad (1.1)$$

Figure 1.3 shows the values of thermodynamic CO_2 conversion in the range 180-600 °C at 0.1 MPa and using $H_2/CO_2=1$ and $H_2/CO_2=3$ molar ratios. Thermodynamic evaluations at atmospheric pressure show that the equilibrium conversion increases significantly with the use of an excess of H_2, and with the reaction temperature.

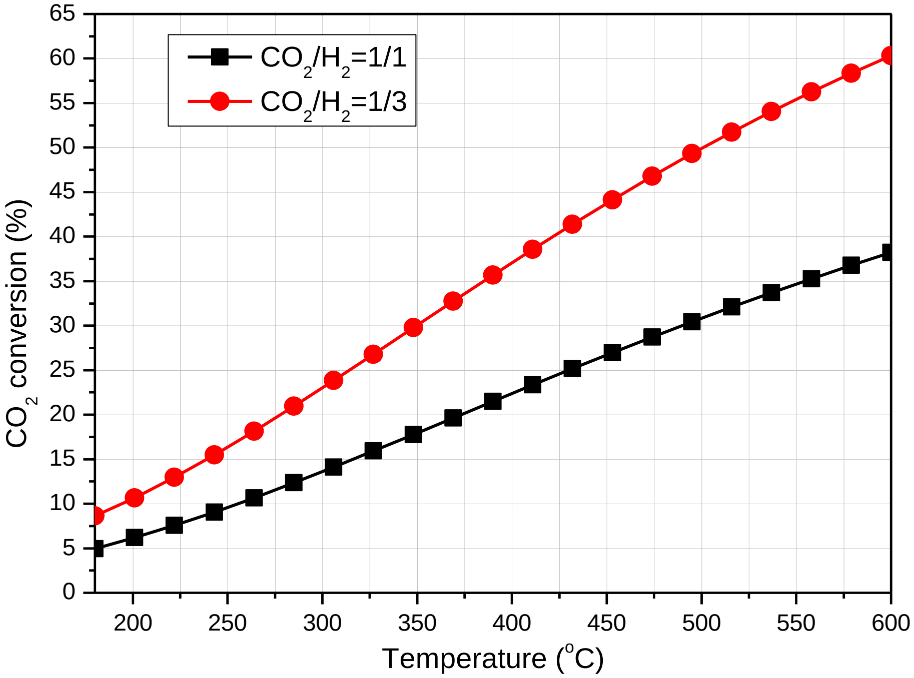

Figure 1.3. CO_2 equilibrium conversion in RWGS reaction at 0.1 MPa and CO_2/H_2=1/1, 1/3 (molar ratio).

The removal of water vapour from the reactor can also be used to drive the equilibrium towards CO production. After the RWGS and H_2O separation, the $CO/CO_2/H_2$ out-stream mixture can be subsequently used as syngas input for other large-scale and well-known chemical processes, such as the methanol synthesis or Fischer-Tropsch (Figure 1.2) [8].

However, under RWGS conditions, CH_4 can be produced from CO_2 and CO hydrogenation.

$$CO+3H_2 \leftrightarrow CH_4+H_2O, \quad \Delta H^0_{298K}=-206.5 \text{ kJ/mol} \qquad (1.2)$$

$$CO_2+4H_2 \leftrightarrow CH_4+2H_2O, \quad \Delta H^0_{298K}=-165.0 \text{ kJ/mol} \qquad (1.3)$$

Continuous efforts are applied to develop active and selective catalysts to overcome the slow kinetics of RWGS and to maximize the CO yield.

1.3. Catalysts for the RWGS reaction

Although supported metal catalysts (Cu, Ni and noble metals) have been the most studied for the RWGS, recently, the use of metal oxides and transition metal carbides (TMCs) has also attracted increasing attention [12-16].

1.3.1. Supported metal catalysts

Cu-based catalysts are currently used in the methanol synthesis [17] and water-gas shift (WGS) processes [18] due to their high activity and low cost. Taking into account the principle of microscopic reversibility, catalysts which are performant for WGS could be also applied for RWGS under appropriate reaction conditions.

The addition of promoters to Cu-based catalysts could improve their stability and inhibit the sintering of the Cu active phase during the catalytic reaction. In this context, the addition of iron and potassium to Cu/SiO_2 has been demonstrated to have a positive effect in the RWGS reaction at relatively high temperature [19-21]. The presence of iron increased the S_{BET} and Cu surface area as well as inhibited the sintering of active Cu at high reaction temperature, consequently, Cu-Fe/SiO_2 showed a higher activity and stability than its Cu/SiO_2 counterpart [19,21]. After 120 h of catalytic test at 600 °C, the CO_2 conversion decreased from 15% to 12% in the case of Cu-Fe/SiO_2 and from 8.5% to 0.3% for Cu/SiO_2. The promotion effect of potassium in Cu-K_2O/SiO_2 catalysts has been related with the formation of new active sites in the K_2O-Cu interface, which can form and decompose the formate intermediate increasing the CO_2 conversion [20]. Very recently, Pastor-Pérez et al. [22] reported that Cu-based catalysts, containing both iron and caesium (Fe-Cu-Cs/Al_2O_3), showed excellent CO_2 conversion, with selectivity to CO above 99%, in the temperature range of 400-750 °C. Catalysts based on mesoporous CeCu oxides have also shown high catalytic activity in RWGS reaction by the synergistic effect of surface oxygen vacancies and active Cu^0 [23].

It is well-known that ZnO and Al_2O_3 play an important role in Cu-based catalysts used for methanol synthesis [17] and WGS [24]. The study of Cu-ZnO/Al_2O_3 catalysts in RWGS reaction at atmospheric pressure and 240 °C indicated that the presence of Al_2O_3 decreased the crystallite size of CuO and ZnO particles and, led to high Cu surface area. Both Cu-ZnO and Cu-ZnO/Al_2O_3 showed a good linear relationship between the catalytic activity and the Cu surface area; the higher the Cu surface area**,** the higher the CO_2 conversion [25]. In addition, a promotion effect of Ga_2O_3 in terms of catalytic activity has been reported over Cu-Zn/SiO_2 catalysts in CO_2 conversion to methanol [26,27]. The presence of small Ga_2O_3 particles can facilitate the formation of an intermediate state of copper (Cu^+). The addition of Ga_2O_3 enhanced not only the catalytic activity but also the stability of catalysts.

The effect of different supports (Al_2O_3, CeO_2, SiO_2, TiO_2, and ZrO_2) on Cu-based catalysts for the RWGS reaction has been recently studied (reaction conditions: H_2:CO_2=0.67-1.5 molar ratio, T=280-360 °C, P=3-7 bar) [28]. Among the studied catalysts, Al_2O_3-supported showed the highest catalytic activity, and its activity decreased with increasing H_2/CO_2 molar ratio, this was related with the formation of different copper species [28].

On the other hand, the use of the atomic layer epitaxy (ALE) technique in the preparation of Cu/SiO_2 catalysts has been applied to produce catalysts with small Cu particles (about 2.9 nm) which showed high activity and stability in RWGS [29].

Besides Cu-, Ni-based catalysts have been proposed to be appropriate for the RWGS reaction. However, Ni-based catalysts favour CO_2 methanation [16]. Ni-based catalysts supported on CeO_2 have been extensively studied over the past decades. The preparation method [30] and the Ni loading [31-33] were demonstrated to influence the Ni particle size in the catalysts and therefore the catalytic behaviour of Ni-CeO_2 in RWGS reaction. Catalysts with a low Ni content (less than about 3% wt Ni) showed a small NiO particle size (less than 5 nm) and were selective to the CO production. Conversely, the presence of large Ni particles (≈30 nm) was found in catalysts with a higher Ni loading, these catalysts favoured the CH_4 formation [31-33]. Thus, the control of the Ni particle size is very important for the design of active and selective nickel catalysts for the RWGS reaction [34]. Oxygen vacancies and highly dispersed Ni were proposed to be the active sites for RWGS over Ni-based catalysts [31,35]. A $Ce_{0.75}Zr_{0.25}O_2$-supported Ni catalyst was reported to show high activity and stability in the RWGS reaction at 700 °C due to the generation of active sites by the incorporation of Ni into the $Ce_{0.75}Zr_{0.25}O_2$ lattice [36].

Additionally, the presence of Fe in 1.5wt%Ni/CeO_2, which showed high catalytic activity and a significant CO_2 methanation, enhanced the selectivity towards CO, but without a significant change in the catalytic activity [33]. Other bimetallic catalysts such as $Cu_{50}Ni_{50}$/C [37], $Cu_{50}Ni_{50}$/SDC (SDC, samarium-doped ceria) [38] and Fe-Mo/Al_2O_3 [39] have been found to have high CO selectivity and thermal stability in the RWGS reaction.

Although supported noble metals such as Pt, Pd and Au are also highly active and selective in the RWGS reaction, their high cost is an important drawback for large-scale utilization [12,40-48]. Kim et al. reported that the catalytic behaviour of Pt/anatase catalysts depended on the properties of anatase support [43]. It was suggested that Pt-O_v-Ti^{3+} generated at the Pt-TiO_2 interface was the active site for the CO_2 conversion to CO [43,44]. In this context, the calcination temperature of catalysts [45] and the reducibility of the supports [43,46] have been reported to influence the catalytic behaviour of catalysts in the RWGS reaction. A positive effect of potassium in the CO_2 conversion to CO over Pt-based catalysts has been suggested by Liang et al. on Pt/mullite catalysts [47]. The generated KO_x-Pt interface has been proposed to be the active site for the RWGS reaction through formate decomposition. In Pd/ZnO catalysts, Lebarbier et al. found that the catalytic activity in RWGS depended on the particle size of PdZn alloy formed [48]. Small PdZn alloy particles facilitated the CO_2 conversion and increased the CO formation rate.

Several metal oxide-based catalysts have been proposed as an alternative to metal-based catalysts for carrying out the RWGS at high temperature, this is the case of oxide systems based on ZnO [49-51]. ZnO/Al_2O_3 has been found to be highly active and stable for the RWGS reaction at high temperature range (400-700 °C); the formation of $ZnAl_2O_4$ was proposed to be the responsible for the high catalytic stability shown at 600 °C [50,51].

In_2O_3 and Ga_2O_3 are also active for the RWGS reaction at 200-650 °C. Sun et al. [52] prepared In_2O_3 and Ga_2O_3 using a thermal decomposition method and found that In_2O_3 showed a better catalytic behaviour than Ga_2O_3. The presence of CeO_2 improved the catalytic behaviour of Ga_2O_3 and In_2O_3, favouring the CO_2

adsorption and activation. In addition, the generation of oxygen vacancies could enhance the dissociative H_2 adsorption [53,54].

Moreover, other kind of oxide-based catalysts, like $BaZr_{0.8}Y_{0.16}Zn_{0.04}O_3$ and $La_{0.75}Sr_{0.25}FeO_3$ [55,56] have also been considered and studied in the RWGS reaction at high temperature.

1.3.2. Transition metal carbides (TMCs)

TMCs have attracted wide attention in catalysis due to their similar properties to precious metals. TMCs are considered potential materials useful for the CO_2 activation [57].

The activation of CO_2 and H_2 over TMCs has been theoretically studied by several research groups [58-62]. Most of these studies dealt with catalytic properties of specific surfaces. Using DFT calculations, the H_2 splitting and, the CO_2 activation and dissociation have been studied on TMC(001) (TMC=VC, MoC, TiC, ZrC and Mo_2C) surfaces [61]. All of the TMC(001) surfaces studied were able to adsorb and activate CO_2. Among them, Mo-terminated $Mo_2C(001)$ ($Mo_2C(001)$-Mo) was proposed to be the highest active for H_2 and CO_2 dissociation [61]. Moreover, the carbon/metal ratio (C/M) has been reported to be an important descriptor for the CO_2 conversion; TMCs with $C/M<1$ are more active than TMCs with $C/M>1$, and this has been related with the easiness of breaking of the C=O bonds [58,59].

Among the different TMCs-based catalysts, those based on molybdenum have been the most theoretically studied to date in the CO_2 activation. Experimental studies of CO_2 reduction with H_2 over molybdenum carbides have been mainly carried out using single crystal surfaces and/or at pressure higher than atmosphere. MoC and Mo_2C are known in different polymorphic phases.

The most common structures are hexagonal close-packed (hcp) for Mo_2C and face-centered cubic (fcc) for MoC [63].

Systematic theoretical studies on the CO_2 activation over different molybdenum carbide phases have been reported [57,60,64,65]. Using DFT calculations, a different adsorption and activation of CO_2 on cubic-MoC(001) and orthorhombic-Mo_2C(001) surfaces were found. Over the Mo_2C(001)-Mo polar surface, when CO_2 is adsorbed may suffer a spontaneous rupture of a C-O bond, leading to the formation of CO. On the MoC(001) nonpolar surface, CO_2 can be activated leading to the formation of C-C bonds [60]. Moreover, Mo_2C(001)-Mo and polycrystalline MoC were experimentally studied in the hydrogenation of CO_2 in the range 227-327 °C at a total pressure of 0.49 MPa. CO, CH_4 and CH_3OH were the main products obtained over Mo_2C(001)-Mo surface, while only CO and CH_3OH were produced on polycrystalline MoC [60].

DFT studies from Shi et al. [66] proposed that on both, Mo_2C(001) and Mo_2C(101) surfaces, the CO_2 dissociation ($CO_{2,ads} \rightarrow CO_{ads}+O_{ads}$), which can result in high CO selectivity, is more favorable than the CO_2 hydrogenation ($CO_{2,ads}+H_{ads} \rightarrow HCOO_{ads}$ or $COOH_{ads}$). Meanwhile, oxygen binding energy (OBE) is considered as an important parameter for CO_2 reduction over TMCs catalysts. DFT calculations showed that the removal of adsorbed O in the form of H_2O from the Mo_2C(0001) is feasible in the presence of an excess of H_2 [67].

CO production from CO_2 over different metal carbides (TiC, ZrC, NbC, TaC, WC and Mo_2C) has been experimentally studied recently [67-69]. The results showed that Mo_2C possesses much higher catalytic activity for CO_2 reduction to CO than other TMCs (Reaction conditions: T=300 °C, $CO_2/H_2=1/2$ and atmospheric pressure) [67]. The direct participation of Mo_2C in the reaction through a facile oxygen transfer over the catalyst is proposed [67,68]; the generated oxygen atom from CO_2 dissociation is incorporated into Mo_2C to produce CO and oxycarbide; this oxycarbide can be subsequently reduced by H_2 [68]. Among the TMCs catalysts, the Mo_2C could be the most interesting catalyst for the RWGS reaction, due to its dual functionality for H_2 dissociation and C=O bond scission and its low cost [12,68].

The RWGS reaction has been recently studied over nanostructured molybdenum carbides. Specifically, an excellent catalytic behaviour in CO_2 conversion to CO over MoC_{1-x} and Mo_2C nanowires has been reported at 600 °C [69]. However, the transformation of MoC_{1-x} into Mo_2C is proposed to occur during the catalytic test.

Supported molybdenum carbide on different metal oxides has been used as catalysts in different processes [70-72]. However, the use of supported molybdenum carbide as catalysts for RWGS has been limited. Brung et al. [70] have studied Mo_2C supported on Al_2O_3-, ZrO_2-, SiO_2- and TiO_2- in the dry reforming of methane to synthesis gas ($CO_2+CH_4 \rightarrow 2CO+2H_2$). The stability of the catalyst followed the order: $Mo_2C/Al_2O_3 > Mo_2C/ZrO_2 > Mo_2C/SiO_2 > Mo_2C/TiO_2$; the results suggested that the oxidation of the carbide to MoO_2 is responsible for the observed deactivation. Recently, Porosoff et al. [73] studied the CO_2 conversion to CO on potassium promoted $Mo_2C/\gamma\text{-}Al_2O_3$. DFT studies showed that the presence of K reduces the CO_2 dissociation barrier and enhances the CO selectivity. Meanwhile, experimental results showed that the addition of K also improves the catalyst stability along time [73].

On the other hand, metal carbides have been also studied as supports of different metals used as catalysts in CO_2 hydrogenation reaction [58,59,61,62]. Combined experimental and theoretical studies demonstrated a high catalytic activity to CO through the RWGS reaction over M/TiC(001) samples (M=Au, Cu or Ni) [59].

Different metals supported on Mo_2C have been studied in the CO_2 reduction by H_2 [63,68,74]. However, different results were found depending on the reaction conditions used, the metal loading and the preparation method of catalysts. Xu et al. [63] prepared M/Mo_2C (M=Cu, Ni or Co) catalysts by carburization of $Cu_3(MoO_4)_2(OH)_2$, $NiMoO_4$ and $CoMoO_4{\bullet}nH_2O$ using CH_4/H_2. Even though the metal content was not reported, according to precursors used the calculated metal weight percentage is about 49%, 36% and 37% for Cu, Ni and Co, respectively [63]. The CO_2 hydrogenation tests, at 2 MPa and temperature range of 200-300 °C using the reaction mixture of $Ar/CO_2/H_2$=10%/15%/75% (molar ratio) showed that the CO_2 conversion followed the order: $Cu/Mo_2C < Mo_2C < Ni/Mo_2C < Co/Mo_2C$. Meanwhile, the distribution of products (CO, methanol, methane and hydrocarbons) depended on M. The selectivity towards CO followed the order: $Co/Mo_2C < Ni/Mo_2C < Mo_2C < Cu/Mo_2C$. Ni/Mo_2C and Co/Mo_2C catalysts were selective to CH_4 and hydrocarbons under the experimental conditions used [63].

On the other hand, Porosoff et al. prepared a Co-Mo_2C catalyst (7.5 wt%) using an impregnation method and tested in the RWGS reaction at atmospheric pressure in a CO_2/H_2=1/2 mixture flow [68]. In this case, the addition of Co (7.5 wt%) to Mo_2C enhanced the CO_2 conversion (from 8.7% to 9.5%) as well as the CO:CH_4 ratio (from 15 to 51) at 300 °C.

Moreover, a series of Cu/Mo_2C catalysts with different Cu content (1-10%) were prepared by a co-precipitation method and then a carburization step using CH_4/H_2. The synthesized Cu/Mo_2C catalysts were tested in the RWGS reaction using CO_2/H_2=1/2 at atmospheric pressure. The results showed the improvement of CO_2 conversion by the presence of Cu compare to bare Mo_2C; the 1wt%Cu/Mo_2C catalyst showed higher catalytic activity than the other samples [74]. Meanwhile, the interaction between Cu and Mo_2C is proposed to enhance the dispersion of Cu preventing the aggregation of Cu particles. The CO selectivity was above 96% over the entire temperature range of 300-600 °C for all the studied Cu/Mo_2C catalysts; the main by-product was CH_4 [74]. Regarding the method used for the preparation of molybdenum carbides, the most common is by reaction at high temperature of molybdenum oxides with a mixture of H_2 and hydrocarbons (mainly CH_4) [72-74].

1.4. Mechanism of the RWGS reaction

Understanding the reaction mechanism is helpful to design specific catalysts**.** In some cases, the reaction mechanism could change as a function of the catalyst and the reaction conditions used. The reaction mechanism of the RWGS has been studied theoretically and experimentally. Two main reaction mechanisms have been proposed: the surface redox and the formate intermediate mechanism; these two reaction mechanisms are still being disputed [75-77].

The surface redox mechanism is the most accepted over Cu-based catalysts. An oxidation-reduction cycle is proposed to occur on the surface of copper with the following reaction steps [75,78, 79]:

$$CO_{2,g} \leftrightarrow CO_{2,ads} \qquad (1.4)$$

$$CO_{2,ads} \leftrightarrow CO_{ads} + O_{ads} \qquad (1.5)$$

$$CO_{ads} \leftrightarrow CO_{g} \qquad (1.6)$$

$$H_{2,g} \leftrightarrow 2H_{ads} \qquad (1.7)$$

$$H_{ads} + O_{ads} \leftrightarrow OH_{ads} \qquad (1.8)$$

$$H_{ads} + OH_{ads} \leftrightarrow H_2O_{ads} \qquad (1.9)$$

$$H_2O_{ads} \leftrightarrow H_2O_{g} \qquad (1.10)$$

Figure 1.4 shows the scheme of the redox mechanism over a Cu-based catalyst. CO_2 oxidizes Cu^0 and generates CO and Cu_2O, while the presence of H_2 has been proposed to reduce the formed Cu_2O to metallic Cu, which is the active phase; in this process, H_2O is formed and the RWGS is completed [79].

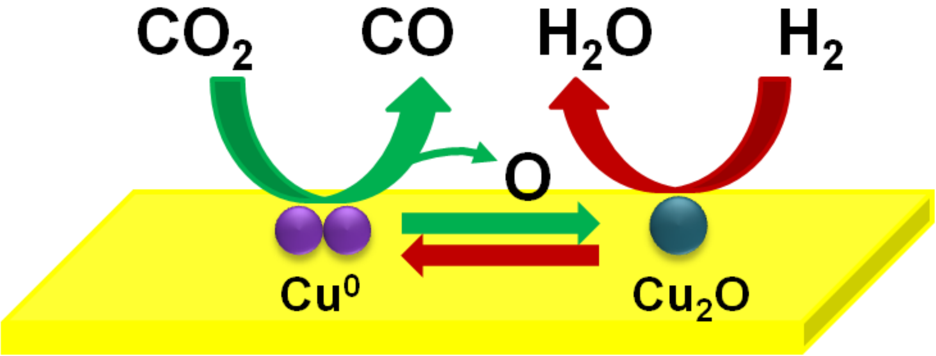

Figure 1.4. The occurrence of the redox mechanism on the Cu surface.

Fujita et al. [75] have proposed the redox mechanism for the RWGS reaction over Cu/ZnO catalysts prepared by a co-precipitation method. CO, CH_3OH and H_2O were found when CO_2-H_2 was contacted with the catalyst at 165 °C and atmospheric pressure. However, only CO was formed when the catalyst was treated with a CO_2-He mixture. Moreover, if H_2 was introduced after the CO_2 treatment, the amount of H_2O formed was similar to that of CO previously formed. Meanwhile, the formation of Cu(I) from CO_2 dissociation was confirmed by X-ray photoelectron spectroscopy (XPS) and CO adsorption followed by Fourier-transform infrared spectroscopy (FT-IR).

Wang et al. [80] studied the redox mechanism over Cu(111), Cu(100), and Cu(110) surfaces by DFT calculations. The results suggested that the RWGS is a structure-sensitive reaction on Cu. The activation energies for CO_2 dissociation follow the order: Cu(111)>Cu(100)>Cu(110). The calculations indicated that CO_2 dissociation is the rate-determining step.

As stated above, the decomposition of formate mechanism is also widely accepted for the RWGS over different catalysts [20,76,81,82]. In this case, the adsorption of CO_2, the formation of formate species, and the decomposition of formate take place. Following, the reaction steps proposed for the formate intermediate mechanism [29,83]:

$$H_{2,g} \leftrightarrow 2H_{ads} \tag{1.11}$$

$$CO_{2,g} \leftrightarrow CO_{2,ads} \tag{1.12}$$

$$CO_{2,ads} + H_{ads} \leftrightarrow HCOO_{ads} \tag{1.13}$$

$$HCOO_{ads} \leftrightarrow CO_{ads} + OH_{ads} \tag{1.14}$$

$$CO_{ads} \leftrightarrow CO_g \tag{1.15}$$

$$H_{ads} + OH_{ads} \leftrightarrow H_2O_{ads} \tag{1.16}$$

$$H_2O_{ads} \leftrightarrow H_2O_g \tag{1.17}$$

The formation of the adsorbed formate species is considered the critical step. An effective catalyst should be dual functional, with high activity for both, hydrogenation and C=O bond scission. Ishito et al. [40] reported a high CO selectivity over γ-Al_2O_3-supported Au catalysts; this was attributed to the formation of formate species on Au metal and the subsequent decomposition to CO on γ-Al_2O_3.

Although the redox mechanism is widely accepted for Cu-based catalysts, the formation of formate intermediate species over Cu-based catalysts has been also proposed [29,76]. For ZrO_2-promoted Cu/SiO_2 and Cu/ZrO_2 catalysts, hydrogen carbonate species formed from adsorbed CO_2 can react with H_2 and produce formate species [84].

Dietz et al. studied the RWGS reaction on Pt (111), Rh(111), Ni(111), Cu(111), Ag(111) and Pd(111) surfaces using DFT analysis [77]. Cu(111), Ni(111) and Rh(111) surfaces showed a lower CO_2 dissociation barrier than Pt(111), Pd(111) and Ag(111). Consequently, the former surfaces favoured the CO_2 dissociation to CO and O; it was suggested that CO_2 dissociation is more favoured when a stronger interaction metal-O exist. On the other hand, over Pt(111), Pd(111) and Ag(111) a COOH-mediated mechanism is proposed to take place.

Although using diffuse reflectance infrared Fourier transform spectroscopy (DRIFTS), the formate decomposition mechanism has been proposed for the RWGS over MoC_{1-x} and Mo_2C nanowires [69], other studies have proposed that the RWGS takes place over Mo_2C-based catalysts through the redox mechanism [63,67,68].

The CO_2 adsorption onto Mo_2C has been theoretically and experimentally studied. When CO_2 chemisorbs, it spontaneously decomposes on the catalyst surface resulting in the CO and O formation (Eq. 1.5) [12,85].

Then, the adsorbed CO can desorb and the dissociated oxygen atom is incorporated into Mo_2C, leading the formation of oxygen-modified carbide or molybdenum oxy-carbide (Mo_2C-O) [67,85]. The last step is the reaction of Mo_2C-O with H_2; Mo_2C-O species can form Mo_2C and H_2O when an excess of H_2 is present.

Figure 1.5 shows the CO_2 adsorption and dissociation profile on Mo_2C(001)-Mo determined by DFT calculations [60]. It indicates that CO and O moieties are present at the Mo_2C(001)-Mo surface [60].

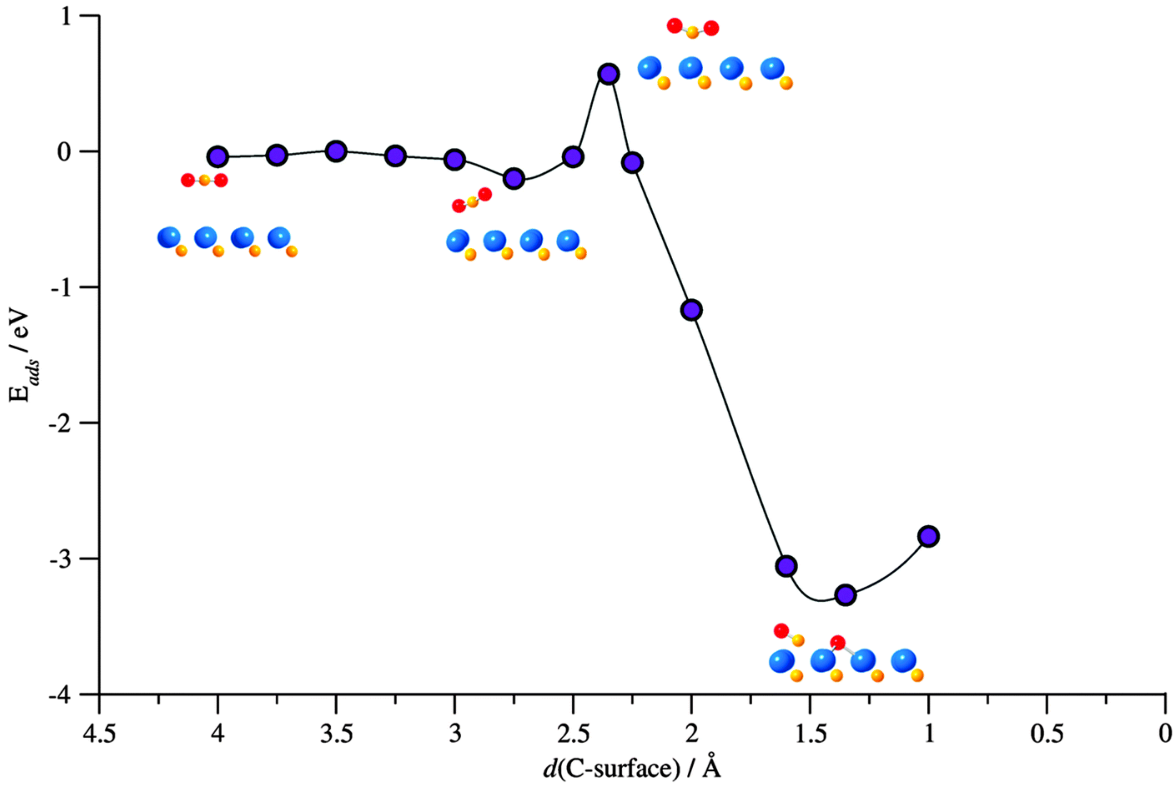

Figure 1.5. CO_2 adsorption profile on $Mo_2C(001)$-Mo. Sketches of energy minima and some intermediate steps are shown. Blue and orange balls denote Mo and C atoms, respectively. (Reproduced from Reference [60] with permission from the PCCP Owner Societies).

1.5. Methanol steam reforming reaction (MSR)

Hydrogen is a promising energy carrier for electricity generation via fuel cell systems [86-89]. The chemical storage and transportation of H_2 into a liquid fuel is of current interest because it could facilitate the H_2 use in mobile applications. In-situ H_2 production can be achieved by the reforming of alcohols and hydrocarbons.

Methanol, the simplest alcohol with a high H/C ratio (H/C=4, molar ratio) and no C-C bonds would be considered as a convenient chemical storage molecule for H_2 [90]. Although methanol is nowadays produced from fossil fuels, it can be also produced from biomass [91], H_2 stored in methanol can be in-situ released through the catalytic MSR process at moderate reaction conditions, as shown in Eq. 1.18.

$$CH_3OH+H_2O \leftrightarrow CO_2+3H_2, \qquad \Delta H^0=49.7 \text{ kJ/mol} \qquad (1.18)$$

During the MSR reaction, the methanol decomposition (Eq. 1.19) and then, the WGS reaction (Eq. 1.20) could take place [88,92]:

$$CH_3OH \leftrightarrow CO+2H_2, \qquad \Delta H^0=90.2 \text{ kJ/mol} \qquad (1.19)$$

$$CO+H_2O \leftrightarrow CO_2+H_2, \qquad \Delta H^0=-41.2 \text{ kJ/mol} \qquad (1.20)$$

Effective and clean H_2 production through MSR process requires the use of highly active, selective and stable catalysts. Moreover, the use of stoichiometric H_2O/CH_3OH (S/C=1) ratio, to avoid the use of a large excess of water, from a practical point of view, is highly desirable for a clean H_2 production via the MSR process.

Cu-based catalysts have been widely studied in MSR reaction [88,89,91]. The catalytic behaviour of Cu-based catalysts depends on their preparation method and the presence of promoters [88]. However, Cu-based catalysts show low thermal stability and sintering at temperatures above 300 °C [91,93,94]. To improve the performance of the catalysts and to inhibit the selectivity to CO by-product, different promoters, such as Al_2O_3, ZrO_2, and CeO_2 have been used. The addition of Al_2O_3 to Cu/ZnO catalysts has been reported to increase the Cu dispersion [95] and stabilize the crystal size of Cu, preventing the Cu particles from aggregation during reduction and reaction [96,97]. However, the presence of a large amount of Al_2O_3 decreases the catalytic activity in MSR reaction and favours the formation of formaldehyde as a by-product [98].

Matter et al. [99] studied the MSR reaction using $H_2O/CH_3OH=1.25$ over Zr-containing CuO-ZnO catalysts. Different calcination temperatures between 350-500 °C were investigated; catalyst calcined at 350 °C showed the presence of amorphous ZrO_2, high surface area, and the highest activity in MSR reaction. They suggested that prereduction is not necessary to activate the zirconia-containing CuO-ZnO system for MSR reaction [99]. For ZrO_2-supported Cu-ZnO-ZrO_2 catalyst, the ZrO_2 support can suppress the sintering of Cu particles during the reaction, and enhance the catalytic activity and the durability. It was suggested that the increase of Cu crystallite size lead to an increase in the CO production [100]. Moreover, the presence of ZrO_2 has been shown to improve the catalytic behaviour of Cu-ZnO-Al_2O_3 catalysts in MSR and to decrease the CO by-product formation [101]. Jones et al. [92] also investigated the CuO-ZnO-ZrO_2-Al_2O_3 system for MSR reaction; the results indicated the presence of a relatively high population of oxygen vacancies over the catalyst with ZrO_2 nanoparticles as support. The strong interactions of Cu-Zr and partially oxidized Cu surface species contribute to the catalytic activity [92]. Furthermore, the promotion effect of Ga_2O_3 has been recently demonstrated over Cu/ZnO catalyst in the MSR process [102].

In the present work, several Cu-based catalysts used in the RWGS were also studied in the MSR [103].

1.6. Objectives and structure of the thesis

1.6.1. Objectives of the thesis

Taking into account the background exposed before, the main objective of this work is to study the CO_2 conversion to CO via RWGS under mild conditions over multicomponent $CuZnOGa_2O_3M_xO_y$ (M=Al, Zr) and new Mo_xC-based catalysts.

In this work, the following specific purposes are proposed:

- Preparation and characterization of new Al_2O_3- and ZrO_2-containing multicomponent $CuZnOGa_2O_3$-based catalysts and their study in RWGS reaction. Evaluation of the catalytic behaviour of $CuZnOGa_2O_3$-based catalysts in MSR reaction under stoichiometric H_2O/CH_3OH ratio.

- Preparation of bulk and supported Mo_xC-based catalysts using sol-gel methods without additional reducing thermal treatment with H_2 and /or CH_4. Study of their catalytic behaviour in the RWGS reaction in the 275-400 °C range. Analysis of the well-defined polycrystalline hexagonal Mo_2C in the light of its characteristics and catalytic performance.

1.6.2. Structure of the thesis

The current dissertation has been divided into 5 chapters. This first chapter briefly summarizes the background, which motivated this study.

In Chapter 2, the characterization techniques, as well as the reaction systems used for the RWGS and MSR are presented.

Chapter 3 covers the study of $CuZnOGa_2O_3M_xO_y$ (M=Al, Zr) catalysts. The preparation, characterization as well as their catalytic behaviour in RWGS under 3 MPa and atmospheric pressure are presented. This chapter also reports the catalytic behaviour of multicomponent $CuZnOGa_2O_3$-based catalysts in MSR reaction.

Chapter 4 is devoted to the study of Mo_xC-based catalysts. The preparation and characterization of bulk Mo_xC, supported Mo_xC and MMo_xC (M=Cu, Co) catalysts are reported. The catalytic behaviour of Mo_xC-based catalysts in RWGS reaction is presented.

Chapter 5 summarizes the most relevant conclusions of this work.

1.7. References

[1] https://www.co2.earth/global-co2-emissions. (Accessed on 22 February 2018).

[2] http://www.iea.org/. CO_2 Emissions from Fuel Combustion: Overview (2017 edition). (Accessed on 19 December 2017).

[3] https://www.co2.earth/. (Accessed on 20 January 2018).

[4] https://climate.nasa.gov/evidence/. (Accessed on 25 March 2018).

[5] MacDowell N, Florin N, Buchard A, Hallett J, Galindo A, Jackson G, Adjiman CS, Williams CK, Shah N, Fennell P. An overview of CO_2 capture technologies. Energy Environ. Sci. 2010; 3:1645-1669.

[6] Wall T, Stanger R, Liu Y. Gas cleaning challenges for coal-fired oxy-fuel technology with carbon capture and storage. Fuel. 2013;108:85-90.

[7] Aspelund A, Jordal K. Gas conditioning-the interface between CO_2 capture and transport. Intl. J. Greenhouse Gas Control. 2007;1: 343-354.

[8] Homs N, Toyir J, Ramírez de La Piscina P. Chapter 1-Catalytic processes for activation of CO_2. In: Suib SL, (Ed.) New and future developments in catalysis: Activation of carbon Dioxide. Elsevier; 2013.

[9] Centi G, Perathoner S. Opportunities and prospects in the chemical recycling of carbon dioxide to fuels. Catal. Today. 2009;148:191-205.

[10] Hasan F, Webley PA. Utilization of CO_2 for fuels and chemicals. In: Montal. P, Dalai. AK (Ed.) Sustainable utilization of natural resources. CRC Press, 2017.

[11] Huang C-H, Tan C-S. A review: CO_2 utilization. Aerosol Air Qual. Res. 2014;14:480-499.

[12] Porosoff MD, Yan B, Chen JG. Catalytic reduction of CO_2 by H_2 for synthesis of CO, methanol and hydrocarbons: challenges and opportunities. Energy Environ. Sci. 2016;9:62-73.

[13] Daza YA, Kuhn JN. CO_2 conversion by reverse water gas shift catalysis: comparison of catalysts, mechanisms and their consequences for CO_2 conversion to liquid fuels. RSC Advances. 2016;6:49675-49691.

[14] Ma J, Sun N, Zhang X, Zhao N, Xiao F, Wei W, Sun Y. A short review of catalysis for CO_2 conversion. Catal. Today. 2009;148:221-231.

[15] Wang W, Wang S, Ma X, Gong J. Recent advances in catalytic hydrogenation of carbon dioxide. Chem. Soc. Rev. 2011;40:3703-3727.

[16] Su X, Yang X, Zhao B, Huang Y. Designing of highly selective and high-temperature endurable RWGS heterogeneous catalysts: recent advances and the future directions. J. Energy. Chem. 2017;26:854-867.

[17] Jadhav SG, Vaidya PD, Bhanage BM, Joshi JB. Catalytic carbon dioxide hydrogenation to methanol: A review of recent studies. Chem. Eng. Res. Des. 2014;92:2557-2567.

[18] Wainwright M, Trimm D. Methanol synthesis and water-gas shift reactions on Raney copper catalysts. Catal. Today. 1995;23:29-42.

[19] Chen C-S, Cheng W-H, Lin S-S. Enhanced activity and stability of a Cu/SiO_2 catalyst for the reverse water gas shift reaction by an iron promoter. Chem. Commun. 2001:1770-1771.

[20] Chen C-S, Cheng W-H, Lin S-S. Study of reverse water gas shift reaction by TPD, TPR and CO_2 hydrogenation over potassium-promoted Cu/SiO_2 catalyst. Appl. Catal. A:Gen. 2003;238:55-67.

[21] Chen C-S, Cheng W-H, Lin S-S. Study of iron-promoted Cu/SiO_2 catalyst on high temperature reverse water gas shift reaction. Appl. Catal. A:Gen. 2004;257:97-106.

[22] Pastor-Pérez L, Baibars F, Le Sache E, Arellano-Garcia H, Gu S, Reina T. CO_2 valorisation via reverse water-gas shift reaction using advanced Cs doped Fe-Cu/Al_2O_3 catalysts. J. CO_2 Util. 2017;21:423-428.

[23] Zhou G, Dai B, Xie H, Zhang G, Xiong K, Zheng X. CeCu composite catalyst for CO synthesis by reverse water-gas shift reaction: Effect of Ce/Cu mole ratio. J. CO_2 Util. 2017;21:292-301.

[24] LeValley TL, Richard AR, Fan M. The progress in water gas shift and steam reforming hydrogen production technologies-a review. Int. J. Hydrogen Energy. 2014;39:16983-17000.

[25] Stone FS, Waller D. Cu-ZnO and Cu-ZnO/Al_2O_3 catalysts for the reverse water-gas shift reaction. The effect of the Cu/Zn ratio on precursor characteristics and on the activity of the derived catalysts. Top. Catal. 2003;22:305-318.

[26] Toyir J, Ramírez de La Piscina P, Fierro JLG, Homs N. Catalytic performance for CO_2 conversion to methanol of gallium-promoted copper-based catalysts: influence of metallic precursors. Appl. Catal. B: Environ. 2001;34:255-266.

[27] Toyir J, Ramírez de La Piscina P, Fierro JLG, Homs N. Highly effective conversion of CO_2 to methanol over supported and promoted copper-based catalysts: influence of support and promoter. Appl. Catal. B: Environ. 2001;29:207-215.

[28] Jurković DL, Pohar A, Dasireddy VD, Likozar B. Effect of copper-based catalyst support on reverse water-gas shift reaction (RWGS) activity for CO_2 reduction. Chem. Eng. Technol. 2017;40:973-980.

[29] Chen CS, Wu JH, Lai TW. Carbon dioxide hydrogenation on Cu nanoparticles. J. Phys. Chem. C. 2010;114:15021-15028.

[30] Wang L, Liu H, Liu Y, Chen Y, Yang S. Influence of preparation method on performance of Ni-CeO_2 catalysts for reverse water-gas shift reaction. J. Rare. Earth. 2013;31:559-564.

[31] Wang L, Zhang S, Liu Y. Reverse water gas shift reaction over Co-precipitated Ni-CeO_2 catalysts. J. Rare. Earth. 2008;26:66-70.

[32] Lu B, Kawamoto K. Preparation of mesoporous CeO_2 and monodispersed NiO particles in CeO_2, and enhanced selectivity of NiO/CeO_2 for reverse water gas shift reaction. Mater. Res. Bull. 2014;53:70-78.

[33] Winter LR, Gomez E, Yan B, Yao S, Chen JG. Tuning Ni-catalyzed CO_2 hydrogenation selectivity via Ni-ceria support interactions and Ni-Fe bimetallic formation. Appl. Catal. B: Environ. 2018;224:442-450.

[34] Gonçalves RV, Vono LL, Wojcieszak R, Dias CS, Wender H, Teixeira-Neto Rossi LM. Selective hydrogenation of CO_2 into CO on a highly dispersed nickel catalyst obtained by magnetron sputtering deposition: A step towards liquid fuels. Appl. Catal. B: Environ. 2017;209:240-246.

[35] Rodrigues MT, Zonetti PC, Alves OC, Sousa-Aguiar EF, Borges LE, Appel LG. RWGS reaction employing Ni/Mg(Al, Ni)O-The role of the O vacancies. Appl. Catal. A: Gen. 2017;543:98-103.

[36] Zonetti PC, Letichevsky S, Gaspar AB, Sousa-Aguiar EF, Appel LG. The $Ni_xCe_{0.75}Zr_{0.25-x}O_2$ solid solution and the RWGS. Appl. Catal. A: Gen. 2014;475:48-54.

[37] Lortie M, Isaifan R, Liu Y, Mommers S. Synthesis of CuNi/C and CuNi/γ-Al_2O_3 catalysts for the reverse water gas shift reaction. Int. J. Chem. Eng. 2015 (2015).

[38] Lortie M, Isaifan RJ. Use of CuNi/YSZ and CuNi/SDC catalysts for the reverse water gas shift reaction. Journal of Catalysts. 2015 (2015).

[39] Kharaji AG, Shariati A, Takassi MA. A novel γ-Alumina supported Fe-Mo bimetallic catalyst for reverse water gas shift reaction. Chin. J. Chem. Eng. 2013;21:1007-1014.

[40] Ishito N, Hara K, Nakajima K, Fukuoka A. Selective synthesis of carbon monoxide via formates in reverse water-gas shift reaction over alumina-supported gold catalyst. J. Energ. Chem. 2016;25:306-310.

[41] Wang L, Khazaneh MT, Widmann D, Behm R. TAP reactor studies of the oxidizing capability of CO_2 on a Au/CeO_2 catalyst-A first step toward identifying a redox mechanism in the reverse water-gas shift reaction. J. Catal. 2013;302:20-30.

[42] Upadhye AA, Ro I, Zeng X, Kim HJ, Tejedor I, Anderson MA, Dumesic JA, Huber GW. Plasmon-enhanced reverse water gas shift reaction over oxide supported Au catalysts. Catal. Sci. Technol. 2015;5:2590-2601.

[43] Kim SS, Lee HH, Hong SC. The effect of the morphological characteristics of TiO_2 supports on the reverse water-gas shift reaction over Pt/TiO_2 catalysts. Appl. Catal. B: Environ. 2012;119:100-108.

[44] Chen X, Su X, Duan H, Liang B, Huang Y, Zhang T. Catalytic performance of the Pt/TiO_2 catalysts in reverse water gas shift reaction: Controlled product selectivity and a mechanism study. Catal. Today. 2017;281:312-318.

[45] Kim SS, Park KH, Hong SC. A study of the selectivity of the reverse water-gas-shift reaction over Pt/TiO_2 catalysts. Fuel Process. Technol. 2013;108:47-54.

[46] Kim SS, Lee HH, Hong SC. A study on the effect of support's reducibility on the reverse water-gas shift reaction over Pt catalysts. Appl. Catal. A: Gen. 2012;423:100-107.

[47] Liang B, Duan H, Su X, Chen X, Huang Y, Chen X, Delgado JJ, Zhang T. Promoting role of potassium in the reverse water gas shift reaction on Pt/mullite catalyst. Catal. Today. 2017;281:319-326.

[48] Lebarbier V, Dagle R, Datye A, Wang Y. The effect of PdZn particle size on reverse-water-gas-shift reaction. Appl. Catal. A: Gen. 2010;379:3-6.

[49] Park S-W, Joo O-S, Jung K-D, Kim H, Han S-H. ZnO/Cr_2O_3 catalyst for reverse-water-gas-shift reaction of CAMERE process. Korean J. Chem. Eng. 2000;17:719-722.

[50] Joo O-S, Jung K-D. Stability of $ZnAl_2O_4$ catalyst for reverse-water-gas-shift reaction (RWGSR). Bull. Korean Chem. Soc. 2003;24:86-90.

[51] Park S-W, Joo O-S, Jung K-D, Kim H, Han S-H. Development of ZnO/Al_2O_3 catalyst for reverse-water-gas-shift reaction of CAMERE (carbon dioxide hydrogenation to form methanol via a reverse-water-gas-shift reaction) process. Appl. Catal. A: Gen. 2001;211:81-90.

[52] Sun Q, Ye J, Liu Cj, Ge Q. In_2O_3 as a promising catalyst for CO_2 utilization: A case study with reverse water gas shift over In_2O_3. Greenhouse Gases Sci. Technol. 2014;4:140-144.

[53] Wang W, Zhang Y, Wang Z, Yan J-m, Ge Q, Liu C-j. Reverse water gas shift over In_2O_3-CeO_2 catalysts. Catal. Today. 2016;259:402-408.

[54] Zhao B, Pan Y-x, Liu C-j. The promotion effect of CeO_2 on CO_2 adsorption and hydrogenation over Ga_2O_3. Catal. Today. 2012;194:60-64.

[55] Kim DH, Park JL, Park EJ, Kim YD, Uhm S. Dopant effect of barium zirconate-based perovskite-type catalysts for the intermediate-temperature reverse water gas shift reaction. ACS Catal. 2014;4:3117-3122.

[56] Daza YA, Maiti D, Kent RA, Bhethanabotla VR, Kuhn JN. Isothermal reverse water gas shift chemical looping on $La_{0.75}Sr_{0.25}Co_{(1-Y)}Fe_YO_3$ perovskite-type oxides. Catal. Today. 2015;258:691-698.

[57] Kunkel C, Viñes F, Illas F. Transition metal carbides as novel materials for CO_2 capture, storage, and activation. Energy Environ. Sci. 2016;9:141-144.

[58] Vidal AB, Feria L, Evans J, Takahashi Y, Liu P, Nakamura K, Illas F, Rodriguez JA. CO_2 activation and methanol synthesis on novel Au/TiC and Cu/TiC catalysts. J. Phys. Chem. Lett. 2012;3:2275-2280.

[59] Rodriguez JA, Evans J, Feria L, Vidal AB, Liu P, Nakamura K, Illas F. CO_2 hydrogenation on Au/TiC, Cu/TiC, and Ni/TiC catalysts: Production of CO, methanol, and methane. J. Catal. 2013;307:162-169.

[60] Posada-Pérez S, Viñes F, Ramirez PJ, Vidal AB, Rodriguez JA, Illas F. The bending machine: CO_2 activation and hydrogenation on δ-MoC (001) and β-Mo_2C (001) surfaces. Phys. Chem. Chem. Phys. 2014;16:14912-14921.

[61] Posada-Pérez S, Vines F, Rodriguez JA, Illas F. Fundamentals of methanol synthesis on metal carbide based catalysts: Activation of CO_2 and H_2. Top. Catal. 2015;58:159-173.

[62] Rodriguez JA, Liu P, Stacchiola DJ, Senanayake SD, White MG, Chen JG. Hydrogenation of CO_2 to methanol: Importance of metal-oxide and metal-carbide interfaces in the activation of CO_2. ACS Catal. 2015;5:6696-6706.

[63] Xu W, Ramírez PJ, Stacchiola D, Brito JL, Rodriguez JA. The carburization of transition metal molybdates (M_xMoO_4, M= Cu, Ni or Co) and the generation of highly active metal/carbide catalysts for CO_2 hydrogenation. Catal. Lett. 2015;145:1365-1373.

[64] Posada-Pérez S, Ramírez PJ, Gutiérrez RA, Stacchiola DJ, Viñes F, Liu P, Illas F, Rodriguez JA. The conversion of CO_2 to methanol on orthorhombic β-Mo_2C and Cu/β-Mo_2C catalysts: mechanism for admetal induced change in the selectivity and activity. Catal. Sci. Technol. 2016.

[65] Tominaga H, Nagai M. Density functional study of carbon dioxide hydrogenation on molybdenum carbide and metal. Appl. Catal. A: Gen. 2005;282:5-13.

[66] Shi Y, Yang Y, Li Y-W, Jiao H. Activation mechanisms of H_2, O_2, H_2O, CO_2, CO, CH_4 and C_2H_x on metallic $Mo_2C(001)$ as well as Mo/C terminated $Mo_2C(101)$ from density functional theory computations. Appl. Catal. A: Gen. 2016;524:223-236.

[67] Porosoff MD, Kattel S, Li W, Liu P, Chen JG. Identifying trends and descriptors for selective CO_2 conversion to CO over transition metal carbides. Chem. Commun. 2015;51:6988-6991.

[68] Porosoff MD, Yang X, Boscoboinik JA, Chen JG. Molybdenum carbide as alternative catalysts to precious metals for highly selective reduction of CO_2 to CO. Angew. Chem. 2014;126:6823-6827.

[69] Gao J, Wu Y, Jia C, Zhong Z, Gao F, Yang Y, Liu B. Controllable synthesis of α-MoC_{1-x} and β-Mo_2C nanowires for highly selective CO_2 reduction to CO. Catal. Commun. 2016;84:147-150.

[70] Brungs AJ, York AP, Claridge JB, Márquez-Alvarez C, Green ML. Dry reforming of methane to synthesis gas over supported molybdenum carbide catalysts. Catal. Lett. 2000;70:117-122.

[71] Vo D-VN, Adesina AA. Fischer-Tropsch synthesis over alumina-supported molybdenum carbide catalyst. Appl. Catal. A: Gen. 2011;399:221-232.

[72] Wu Q, Christensen JM, Chiarello GL, Duchstein LD, Wagner JB, Temel B, Grunwaldt J-D, Jensen AD. Supported molybdenum carbide for higher alcohol synthesis from syngas. Catal. Today. 2013;215:162-168.

[73] Porosoff MD, Baldwin JW, Peng X, Mpourmpakis G, Willauer HD. Potassium-promoted molybdenum carbide as a highly active and selective catalyst for CO_2 conversion to CO. ChemSusChem. 2017;10:2408-2415.

[74] Zhang X, Zhu X, Lin L, Yao S, Zhang M, Liu X, Wang X, Li Y, Shi C, Ma D. Highly dispersed copper over β-Mo_2C as efficient and stable catalysts for RWGS reaction. ACS Catal. 2017;7:912-918.

[75] Fujita S-I, Usui M, Takezawa N. Mechanism of the reverse water gas shift reaction over Cu/ZnO catalyst. J. Catal. 1992;134:220-225.

[76] Chen C-S, Cheng W-H, Lin S-S. Mechanism of CO formation in reverse water-gas shift reaction over Cu/Al_2O_3 catalyst. Catal. Lett. 2000;68:45-48.

[77] Dietz L, Piccinin S, Maestri M. Mechanistic Insights into CO_2 activation via reverse water-gas shift on metal surfaces. J. Phys. Chem. C. 2015;119:4959-4966.

[78] Ernst K-H, Campbell CT, Moretti G. Kinetics of the reverse water-gas shift reaction over Cu (110). J. Catal. 1992;134:66-74.

[79] Ginés M, Marchi A, Apesteguia C. Kinetic study of the reverse water-gas shift reaction over $CuO/ZnO/Al_2O_3$ catalysts. Appl. Catal. A: Gen. 1997;154:155-171.

[80] Wang G-C, Nakamura J. Structure sensitivity for forward and reverse water-gas shift reactions on copper surfaces: a DFT study. J. Phys. Chem. Lett. 2010;1:3053-3057.

[81] Chen C-S, Cheng W-H. Study on the Mechanism of CO formation in reverse water gas shift reaction over Cu/SiO_2 catalyst by pulse reaction, TPD and TPR. Catal. Lett. 2002;83:121-126.

[82] Yoshihara J, Campbell CT. Methanol synthesis and reverse water-gas shift kinetics over Cu (110) model catalysts: Structural sensitivity. J. Catal. 1996;161:776-782.

[83] Choi S, Sang B-I, Hong J, Yoon KJ, Son J-W, Lee J-H, Kim B-K, Kim H. Catalytic behavior of metal catalysts in high-temperature RWGS reaction: In-situ FT-IR experiments and first-principles calculations. Scientific reports. 2017;7.

[84] Fisher IA, Woo HC, Bell AT. Effects of zirconia promotion on the activity of Cu/SiO_2 for methanol synthesis from CO/H_2 and CO_2/H_2. Catal. lett. 1997;44:11-17.

[85] Solymosi F, Oszkó A, Bánsági T, Tolmacsov P. Adsorption and reaction of CO_2 on Mo_2C catalyst. J. Phys. Chem. B. 2002;106:9613-9618.

[86] Pojanavaraphan C, Luengnaruemitchai A, Gulari E. Catalytic activity of Au-Cu/CeO_2-ZrO_2 catalysts in steam reforming of methanol. Appl. Catal. A: Gen. 2013;456:135-143.

[87] Lin S, Xie D, Guo H. Pathways of methanol steam reforming on PdZn and comparison with Cu. J. Phys. Chem. C. 2011;115:20583-20589.

[88] Sá S, Silva H, Brandão L, Sousa JM, Mendes A. Catalysts for methanol steam reforming-A review. Appl. Catal. B: Environ. 2010;99:43-57.

[89] Xu X, Shuai K, Xu B. Review on copper and palladium based catalysts for methanol steam reforming to produce hydrogen. Catalysts. 2017;7:183.

[90] Lindström B, Pettersson LJ, Govind Menon P. Activity and characterization of Cu/Zn, Cu/Cr and Cu/Zr on γ-alumina for methanol reforming for fuel cell vehicles. Appl. Catal. A: Gen. 2002;234:111-125.

[91] Palo DR, Dagle RA, Holladay JD. Methanol steam reforming for hydrogen production. Chem. Rev. 2007;107:3992-4021.

[92] Jones SD, Neal LM, Everett ML, Hoflund GB, Hagelin-Weaver HE. Characterization of ZrO_2-promoted Cu/ZnO/nano-Al_2O_3 methanol steam reforming catalysts. Appl. Surf. Sci. 2010;256:7345-7353.

[93] Matsumura Y. Development of durable copper catalyst for hydrogen production by high temperature methanol steam reforming. Int. J. Hydrogen Energy. 2013;38:13950-13960.

[94] Twigg MV, Spencer MS. Deactivation of copper metal catalysts for methanol decomposition, methanol steam reforming and methanol synthesis. Top. Catal. 2003;22:191-203.

[95] Agrell J, Birgersson H, Boutonnet M, Melián-Cabrera I, Navarro R, Fierro JG. Production of hydrogen from methanol over Cu/ZnO catalysts promoted by ZrO_2 and Al_2O_3. J. Catal. 2003;219:389-403.

[96] Wu G-S, Mao D-S, Lu G-Z, Cao Y, Fan K-N. The role of the promoters in Cu based catalysts for methanol steam reforming. Catal. Lett. 2009;130:177-184.

[97] Park JE, Yim S-D, Kim CS, Park ED. Steam reforming of methanol over $Cu/ZnO/ZrO_2/Al_2O_3$ catalyst. Int. J. Hydrogen Energy. 2014;39:11517-11527.

[98] Jones SD, Neal LM, Hagelin-Weaver HE. Steam reforming of methanol using Cu-ZnO catalysts supported on nanoparticle alumina. Appl. Catal. B: Environ. 2008;84:631-642.

[99] Matter PH, Braden DJ, Ozkan US. Steam reforming of methanol to H_2 over nonreduced Zr-containing CuO/ZnO catalysts. J. Catal. 2004;223:340-351.

[100] Matsumura Y. Stabilization of $Cu/ZnO/ZrO_2$ catalyst for methanol steam reforming to hydrogen by coprecipitation on zirconia support. J. Power Sources. 2013;238:109-116.

[101] Jeong H, Kim KI, Kim TH, Ko CH, Park HC, Song IK. Hydrogen production by steam reforming of methanol in a micro-channel reactor coated with Cu/ZnO/ZrO_2/Al_2O_3 catalyst. J. Power Sources. 2006;159:1296-1299.

[102] Toyir J, Ramírez de La Piscina P, Homs N. Ga-promoted copper-based catalysts highly selective for methanol steam reforming to hydrogen; relation with the hydrogenation of CO_2 to methanol. Int. J. Hydrogen Energy. 2015;40:11261-11266.

[103] Liu X, Toyir J, Ramírez de La Piscina P, Homs N. Hydrogen production from methanol steam reforming over Al_2O_3-and ZrO_2-modified $CuOZnOGa_2O_3$ catalysts. Int. J. Hydrogen Energy. 2017;42:13704-13711.

Chapter 2

Experimental section

In this chapter**,** the characterization techniques applied in this work for the determination of physicochemical properties of catalysts are briefly described; The reaction systems of the RWGS and MSR are also presented. The preparation procedures of the catalysts, as well as the specific reaction conditions for RWGS and MSR, will be described in chapters 3 and 4.

2.1. Characterization techniques

The calcined, H_2-reduced and post-reaction catalysts were characterized by the following techniques:

- Inductively-coupled plasma atomic emission spectrometry (ICP-AES)
- N_2 adsorption-desorption isotherms (BET)
- Powder X-Ray diffraction (XRD)
- Raman spectroscopy
- H_2-Temperature programmed reduction (H_2-TPR)
- N_2O chemisorption
- X-ray photoelectron spectroscopy (XPS)
- Temperature programmed desorption of CO_2 (CO_2-TPD), H_2 (H_2-TPD) and CO (CO-TPD)
- Chemisorption of CO_2 and CO studied by in-situ diffuse reflectance infrared Fourier transform spectroscopy (CO_2-DRIFTS, CO-DRIFTS)
- Thermogravimetry-differential scanning calorimetry (TG-DSC)
- Scanning electron microscopy (SEM)

2.1.1. Inductively-coupled plasma atomic emission spectrometry

ICP-AES is a quantitative analytical technique based on emission spectroscopy. In principle, the excited atoms and ions generated under the plasma conditions emit electromagnetic radiation characteristic of a particular element. The concentration of the desired elements is determined by the intensity of the light emitted at the characteristic wavelengths [1]. For the analysis of the chemical compositions of the catalysts, the solid samples were properly digested and consequently the corresponding solutions were prepared and analyzed.

For Al_2O_3-containing samples, about 50 mg of samples were digested with 2 mL H_2SO_4, 3 mL HNO_3 and 3 mL H_3PO_4 at 210 °C in a microwave oven.

For ZrO_2-containing samples, 50 mg of samples were digested with 0.5 g NH_4Cl, 4 mL HCl and 3 mL H_2SO_4 at 210 °C in a microwave oven.

For TiO_2- and SiO_2-containing samples, 50 mg of samples were digested with 4 mL HNO_3, 3 mL H_2SO_4 and 1 mL HF at 210 °C in a microwave oven.

The solutions which contained the digested samples were diluted with HPLC grade water up to 50 mL and then analyzed by ICP-AES; standarized solutions were used for quantification.

In this work, ICP-AES measurements were carried out using a Perkin Elmer Optima 3200RL apparatus in the Scientific and Technological Centers of the University of Barcelona (CCiTUB).

2.1.2. N_2 adsorption-desorption isotherms

Physisorption, using N_2, is a widely applied method to determine the total specific surface area of porous materials. The equation of Brunauer-Emmett-Teller (BET) method is described as [2]:

$$\frac{p}{v(p^0-p)} = \frac{1}{v_m c} + \frac{(c-1)}{v_m c} \times \frac{p}{p^0} \qquad (2.1)$$

Where "p/p^0" is the relative pressure, "p" is the equilibrium pressure of adsorbed gas, "p^0" is the saturation vapour pressure at the adsorption temperature, "v" is the volume of the adsorbed gas at relative pressure p/p^0, "v_m"

is the volume of the gas adsorbed when a monolayer is formed, and “c” is a constant (exponentially related to the energy of monolayer adsorption).

The specific BET surface area (S_{BET}) is given by the Eq. 2.2 [3]:

$$S_{BET}=\sigma_m \cdot n_m \cdot N_A/m \qquad n_m=\frac{V_m \cdot \rho}{M_m} \qquad (2.2)$$

Where “σ_m” (molecular cross-sectional area) is the area effectively occupied by one molecule of the adsorbate, “n_m” is the number of moles of the gas adsorbed in monolayer, “N_A” is the Avogadro constant, “ρ” is the density of adsorbed gas (N_2), “M_m” is the molecular mass of the adsorbate and “m” is the mass of adsorbent.

Porosity characteristics were obtained using the information provided by desorption isotherms, using the method of Barret, Joyner and Halenda [4].

N_2 adsorption-desorption isotherms were recorded at -196 °C using a Micromeritics Tristar II equipment in the Catalonia Institute for Energy Research (IREC). Prior to the measurements, the samples were degassed at 250 °C for 5 h under N_2 flow. The S_{BET} of catalysts was calculated by multi-point BET analysis from N_2 adsorption isotherms.

2.1.3. Powder X-Ray diffraction

Powder X-ray diffraction (XRD) is a characterization technique used to identify the crystalline phases present in a solid and to estimate the corresponding crystallite size.

The crystallite size was estimated using the Debye-Scherrer equation [5,6].

$$d=\frac{K\lambda}{b\cos\theta} \qquad (2.3)$$

Where, “d” is the crystallite size, “K” is a constant, “λ” is the X-ray wavelength, “θ” is the incident Bragg diffraction angle expressed in radians, “b” is the corrected full width at half maximum (FWHM) of the chosen peak of the desired phase. The “b” value is calculated according to the following equation [7]:

$$b=\sqrt{(B^2-\beta^2)} \qquad (2.4)$$

Where “B” is the observed FWHM of the chosen peak of the corresponding phase, and “β” is the instrumental broadening obtained from α-Al_2O_3 standard.

In this work, the XRD measurements were performed in CCiTUB using a PANalytical X’Pert PRO MPD Alpha1 powder diffractometer equipped with a Cu $K\alpha_1$ radiation in *Bragg-Brentano* $\theta/2\theta$ geometry of 240 mm of radius. The XRD profiles were recorded at $2\theta = 4$-$100°$ with a step size of 0.017° and measuring time of 50 s per step. For Co-containing Mo_xC samples, a counting time of 150 s per step was used.

2.1.4. Raman spectroscopy

Raman spectroscopy is an effective characterization technique which can be applied for the identification of oxides, and for the characterization of carbonaceous deposits [6,8,9]. In this work, Raman spectroscopy analyses were carried out over the fresh and spent catalysts.

Raman spectra were performed in CCiTUB using a Jobin-Yvon LabRam HR 800 coupled with an optical Olympus BXFM microscope, a 532 nm laser and a CCD detector. Raman spectra were collected in the range of 100-1800 cm^{-1} and with a laser power limited to 1.5 mW to minimize the laser-heating effects. In general, for a given sample, Raman spectra were collected at least in two different zones.

2.1.5. H_2-Temperature programmed reduction

H_2-Temperature programmed reduction (H_2-TPR) experiments were carried out to study the behaviour of catalysts under H_2 atmosphere with the temperature. The reduction temperature and the amount of H_2 consumption can be obtained from the H_2-TPR profiles. In general, the reduction temperature of a particular metal oxide depends on its particle size and on the interaction between the oxide and the support or other components in the catalyst. In our work, H_2-TPR was applied to study the reducibility of Cu^{2+} in multicomponent catalysts and the potential surface MoO_x or molybdenum oxycarbide species on the Mo_xC-based catalysts.

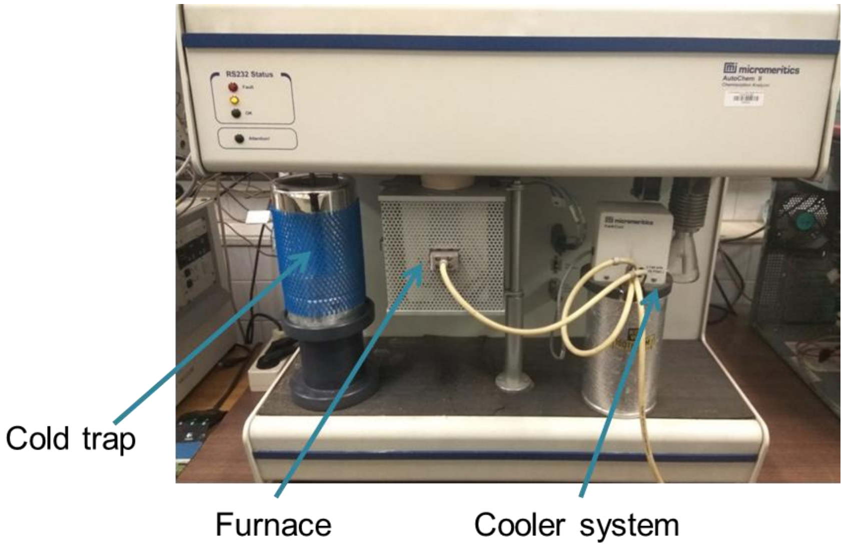

Figure 2.1. Micromeritics Autochem II 2920.

H_2-TPR experiments were performed using an Autochem HP 2950 chemisorption analyzer or a Micromeritics AutoChem II 2920 (Figure 2.1) in IREC and at the Catalytic Materials (MATCAT) laboratory in the Inorganic Chemistry section of University of Barcelona (MATCAT-UB). Approximately, 50 mg of calcined samples were placed in a U-shape reactor and fixed with quartz wool. Prior to the reduction measurement, the sample was pre-treated at 90 °C for 15 min under flowing He. After this treatment, the reactor was cooled to room temperature under He flow, and then the sample was exposed to a flow of H_2/Ar (12% vol/vol). Finally, the temperature was linearly increased up to 800 °C at a rate of 10 °C/min under continuous H_2/Ar flow. A thermal conductivity detector (TCD) was employed to determine the H_2 consumption.

2.1.6. N_2O chemisorption

N_2O chemisorption has been extensively applied to determine the dispersion of Cu (D_{Cu}) and exposed Cu surface area (S_{Cu}) in Cu-containing catalysts [9]. In these determinations, the CuO initially present in the calcined catalyst was firstly reduced to metallic Cu by H_2 thermal treatment (Eq. 2.5). After, the catalyst was exposed to a diluted N_2O flow, and it was considered that only the surface copper atoms were oxidized to Cu_2O by N_2O (Eq. 2.6). Lastly, a H_2-TPR experiment was performed and Cu_2O was reduced (Eq. 2.7) [10].

$$CuO+H_2\rightarrow Cu+H_2O \qquad (2.5)$$

$$2Cu_{Surface}+N_2O\rightarrow Cu_2O_{Surface}+N_2 \qquad (2.6)$$

$$Cu_2O_{Surface}+H_2\rightarrow 2Cu_{Surface}+H_2O \qquad (2.7)$$

The amount of H_2 consumed after the N_2O adsorption (Eq. 2.6 and 2.7) was used to estimate D_{Cu} and S_{Cu}.

During the realization of this PhD thesis, it was reported that the presence of ZnO influences the values of D_{Cu} and S_{Cu} calculated using the method exposed above. During the reduction of CuO (Eq. 2.5), ZnO_x in the Cu/ZnO interface can be formed. Then, during N_2O chemisorption, the N_2O can react with surface Cu and with interfacial Cu-ZnO_x species [11].

$$V_{oxygen}(\text{Cu-ZnO interface})+N_2O\rightarrow \text{Cu-ZnO}+N_2 \qquad (2.8)$$

After this step, the H_2 consumption will quantify not only the surface copper but also the interfacial Cu-ZnO_x oxygen defects (V_{oxygen}).

In this work, $CuZnOGa_2O_3$-based catalysts were compared as a function of the amount of H_2 consumption after N_2O chemisorption. This allows the estimation of the total amount of surface Cu and oxygen defects.

N_2O chemisorption was carried out using a Micromeritics AutoChem II 2920 chemisorption analyzer in MATCAT-UB laboratory. Prior to the N_2O adsorption, the calcined catalysts were pre-treated at 90 °C for 15 min under flowing He. Later, the catalysts were in-situ reduced in a H_2/Ar (12% vol/vol) flow at 275 °C for 1 h. The samples were then cooled to 50 °C and maintained for 15 min under He flow.

Afterwards, the samples were contacted with N_2O/He (6% vol/vol) flow at 50 °C for 0.5 h. The surface Cu^0 (Eq. 2.5) generated from the $CuZnOGa_2O_3$-based catalysts during the above reduction step and oxygen defects at the Cu-ZnO interface will react with N_2O to form Cu_2O (Eq. 2.6) and ZnO (Eq. 2.8). After the N_2O adsorption, the temperature was decreased to room temperature under He flow, and then the samples were purged with He for 15 min at this temperature. Finally, the H_2/Ar was introduced to the reactor to determine the H_2 consumption from room temperature up to 800 °C at 10 °C/min.

2.1.7. X-ray photoelectron spectroscopy

X-ray photoelectron spectroscopy (XPS) is a surface sensitive analysis technique which can quantitatively analyze the surface composition of catalysts, including the chemical state and the atomic concentration of different elements present on the surface. In principle, a monochromatic beam of X-rays radiation hits the sample causing the emission of electrons. The kinetic energies of the emitted electrons are measured by means of an energy analyzer. The binding energy (BE) of the electron emitted can be obtained from the following equation [12]:

$$E_b = h\nu - E_k - \emptyset \qquad (2.9)$$

Where “E_b” is the BE of the electron, “E_k” is the kinetic energy of the emitted electrons, “ϕ”is the work function of the spectrometer and “$h\nu$” is the energy of the incident X-ray. The atomic concentration of the elements on the surface can be calculated by the Eq. 2.10 [13]:

$$C_x = \frac{I_x/S_x}{\sum I_i/S_i} \qquad (2.10)$$

Where “C_x” is the atomic concentration of the element “x”; “I” is the area of the peak of a particular element and “S” is the corresponding atomic sensitivity factor.

XPS measurements were performed using a Perkin Elmer PHI-5500 Multitechnique System (Physical Electronics) with an Al Kα X-ray source ($h\nu$ = 1486.6 eV and 350 W) in CCiTUB. All of the measurements were carried out in an ultra-high vacuum chamber with a pressure in the $5\cdot10^{-9}$–$2\cdot10^{-8}$ torr range during data acquisition. The BE values were referred to the BE of C 1s of adventitious carbon at 284.8 eV. For Mo_xC-based catalysts, the C 1s peak position was determined using as reference the previously calibrated Au $4f_{7/2}$ peak at 84.0 eV.

2.1.8. Temperature programmed desorption of CO_2, H_2 and CO

Temperature programmed desorption (TPD) is a method widely applied to study the interaction of a gas with the surface of heterogeneous catalysts. In this work, $CuZnOGa_2O_3$-based catalysts were characterized using CO_2-TPD and H_2-TPD while Mo_xC-based catalysts were analyzed by CO-TPD. All the measurements were carried out using a Micromeritics AutoChem HP 2950 chemisorption analyzer in IREC.

CO_2-TPD

The sample was first treated under a He flow for 15 min at 90 °C and then with a H_2/Ar flow (12% vol/vol) for 2 h at 300 °C. Then, the temperature was cooled down to 35 °C under a He flow and was maintained for 1 h at this temperature. After, the sample was contacted with a CO_2/He (10% vol/vol) mixture for 1 h at 35 °C. The sample was then purged under flowing He for 2 h. Finally, the TPD profile was recorded from 35 to 500 °C at 5 °C/min under a He flow. During desorption, the TCD signal was registered.

CO-TPD

Prior to CO adsorption, the sample was treated with H_2/Ar (12% vol/vol) flow for 2 h at 300 °C, then temperature was cooled down to 35 °C under He and kept for 2 h. Afterwards, the CO/He (10% vol/vol) flow was dosed to the sample at 35 °C. Finally, the temperature was increased to 800 °C with a heating rate of 10 °C/min, under a He flow. During desorption, the TCD signal was registered.

H_2-TPD

H_2-TPD was carried out similarly to CO_2-TPD. In this case, after an initial treatment with He and H_2/Ar flows up to 300 °C**,** the temperature was subsequently decreased to 50 °C under H_2/Ar (12% vol/vol) mixture and kept for 0.5 h. Afterwards, an Ar flow was fed into the reactor for 1 h at 50 °C. Finally, the temperature was linearly increased up to 500 °C at 5 °C/min under Ar. The outlet gases were monitored by mass spectrometry using an OmniStar GSD320O2 equipment.

2.1.9. Chemisorption of CO_2 and CO studied by in-situ diffuse reflectance infrared Fourier transform spectroscopy

DRIFTS is a powerful technique to study the behaviour of catalysts in front of probe molecules. In this work, CO and CO_2 chemisorption was followed using in-situ DRIFTS equipment in IREC.

Measurements were carried out using a Bruker VERTEX 70 FTIR spectrometer equipped with a liquid nitrogen cooled MCT detector and a Harrick Scientific HVC-DRP-4 DRIFTS chamber with a thermocouple for temperature measurement and control. The outlet of the chamber was connected on-line with a ThermoStar GSD320T1 mass spectrometer. Figure 2.2 shows the Harrick Scientific HVC-DRP-4 reaction chamber.

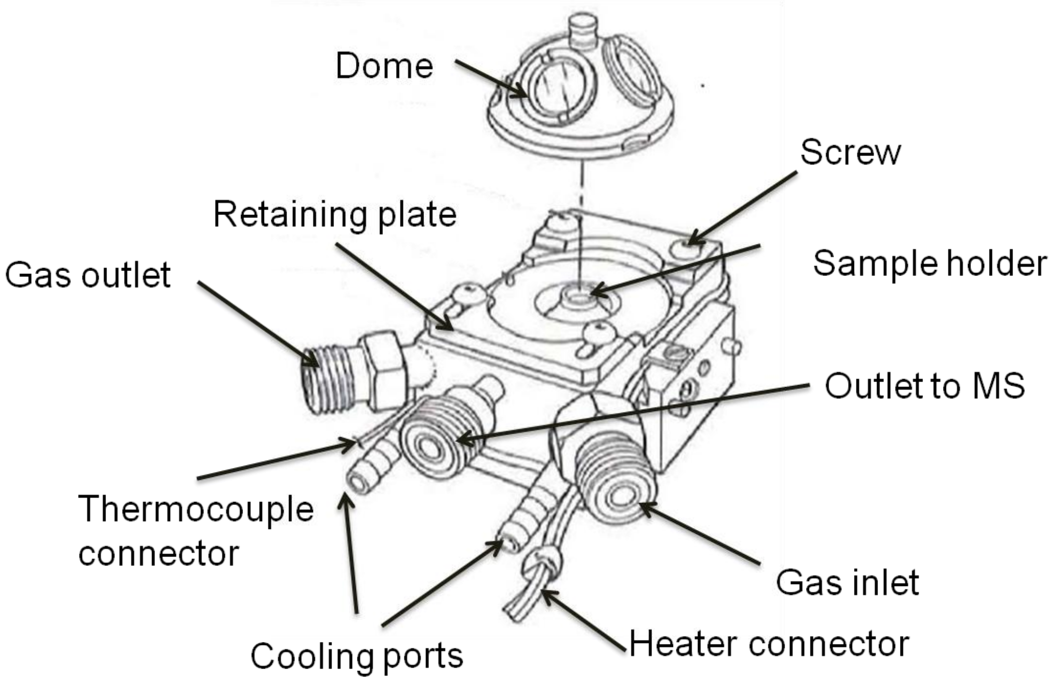

Figure 2.2. Harrick Scientific HVC-DRP-4 reaction chamber.

A small amount of catalyst (about 20 mg) was deposited in the sample holder of the reaction chamber. After purging the chamber with He flow, the desired mixture (CO/He or CO_2/He) was switched to the reaction chamber. The spectra were taken at a resolution of 4 cm^{-1} by collecting 256 scans in the range of 400-4000 cm^{-1}.

Specific details for CO_2-DRIFTS and CO-DRIFTS studies carried out with different catalysts will be described in the corresponding chapter.

2.1.10. Thermogravimetry-differential scanning calorimetry

In this work, thermogravimetry-differential scanning calorimetry (TG-DSC) was used to determine the enthalpy of CO_2 adsorption on Mo_xC-based catalysts at 35 °C. The system contains two cells for the measurement. One of the cells contains the sample while the other cell serves as reference. The two cells are maintained at the same temperature during the measurement. The adsorption of a gas on a solid sample results in a heat exchange. Then, a heat flow signal can be recorded. The value of the heat flow is obtained according to the Tian equation [12,14]:

$$\frac{dQ}{dT} = h\Delta T + c\frac{d\Delta T}{dt} \qquad (2.11)$$

Where “h” is the heat transfer coefficient and “c” is the heat capacity of the calorimeter.

The measurements were carried out using a Sensys evo TG-DSC instrument (Setaram) equipped with a 3D thermal flow sensor. The sample was firstly in-situ reduced in a H_2/Ar (12% vol/vol) flow at 300 °C for 3 h. Then, the sample was treated at 300 °C for 1 h and at 35 °C for 2 h under Ar flow. After that, a CO_2/He (10% vol/vol) mixture was introduced at 35 °C for 2 h. The exothermic peak corresponding to CO_2 adsorption was integrated to provide the total enthalpy of adsorption. The mean adsorption energy was calculated by considering the total amount of adsorbed CO_2 measured by the mass change of the sample which is determined by a coupled microbalance.

2.1.11. Scanning Electron Microscopy

Scanning Electron Microscopy (SEM) was used to study the morphology of catalysts. The combined energy dispersive X-ray (EDX) analysis allowed us to determine the distribution of a particular element in a specific area of the catalyst.

The morphology and the element distribution of the samples were determined using a ZEISS Auriga microscope equipped with an EDX detector in IREC.

2.2. Reaction systems for RWGS and MSR

The catalytic tests of the RWGS reaction were carried out using Microactivity-Reference units (PID Eng&Tech) at the MATCAT-UB laboratory and IREC. In all cases, a fixed-bed tubular reactor and different reactant mixture, $CO_2/H_2/N_2$=1/3/1 or 1/1/3 (molar ratio), under reaction pressure of 0.1-3 MPa were used. The outlet of the system was connected on-line through a thermostatic transfer line to a gas chromatograph.

Figure 2.3 shows the scheme of the Microactivity-Reference reaction system used. As shown in Figure 2.3, the reactant mixture of CO_2/H_2 was mixed with high purity N_2 before passing through the 6-port valves, and then the mixture was fed into the reactor downwards contacting with the catalyst. The mass flow of gas streams was measured and controlled by the means of mass flow controllers (MFC). Meanwhile, 316 stainless steel sintered filters were placed at both the inlet and outlet of the reactor to avoid the passing of possible fine catalyst particles.

Figure 2.4 shows an overview of the RWGS reaction system used for high pressure tests which includes the Microactivity-Reference unit (PID Eng&Tech), a gas chromatograph (GC) Varian 450GC-MS, and a control computer.

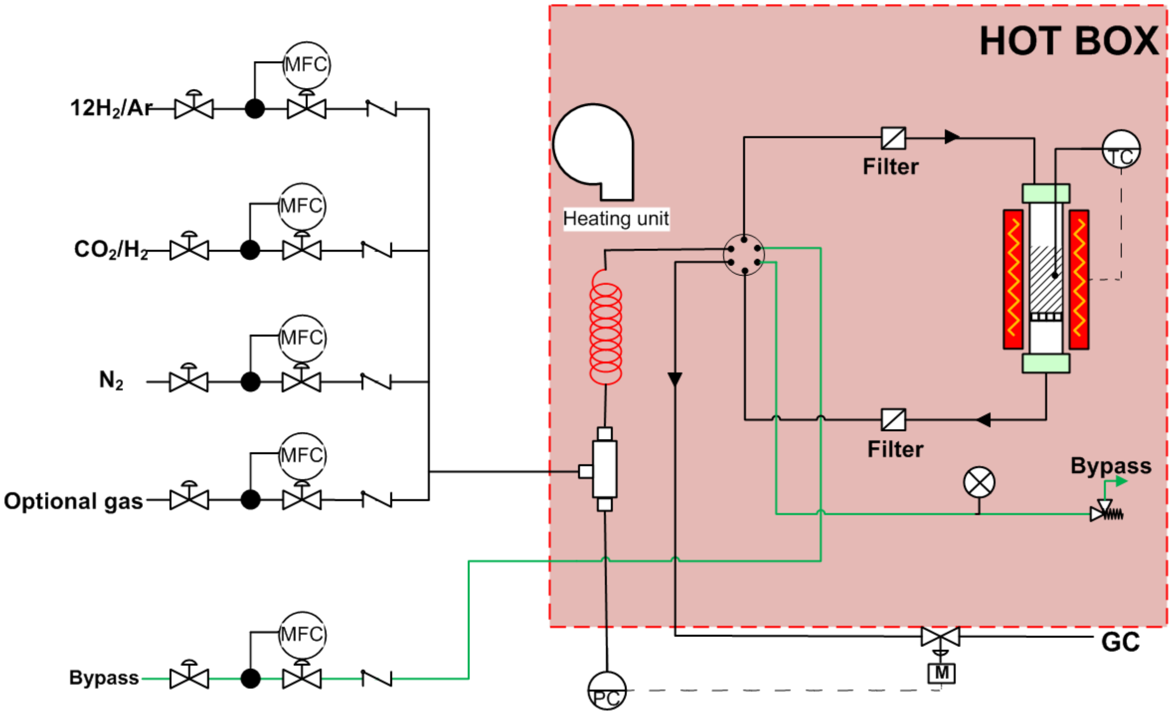

Figure 2.3. Scheme of the RWGS reaction system. MFC, Mass flow controller; PC, Pressure controller; TC, Temperature controller; M, Electric valve.

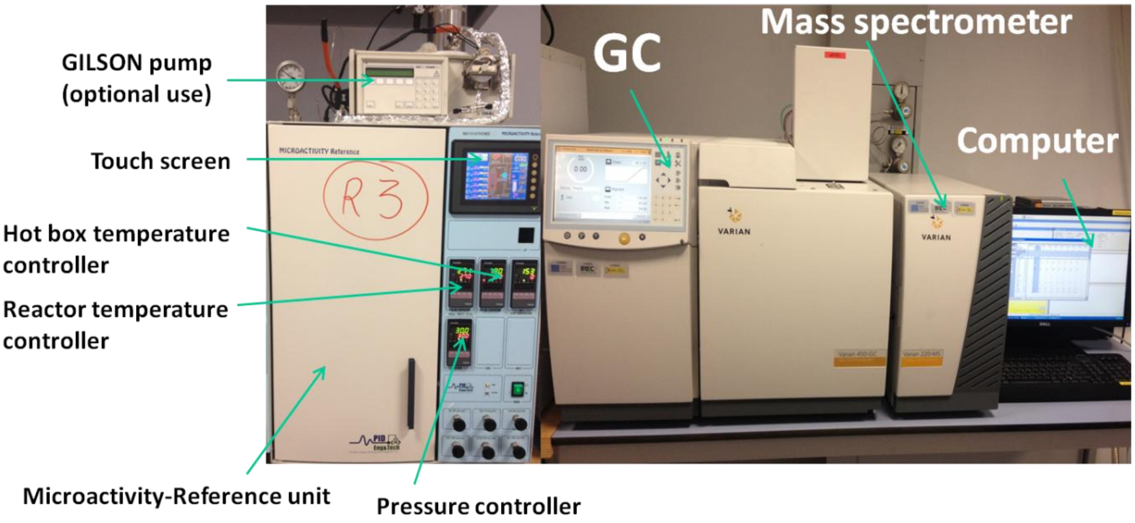

Figure 2.4. An overview of the reaction system for RWGS.

The inside view of the hot box is shown in Figure 2.5A. The temperature of the hot box was maintained at 180 °C during the RWGS reaction test. The catalyst was placed in a tubular fixed-bed reactor (316-L stainless steel, 305 mm long, 9 mm i.d.) equipped with a porous plate. The temperature of the reactor was controlled by a thermocouple which was in direct contact with the catalyst. The gas flows, reaction temperature and pressure, were remotely controlled by a Process@ program via Ethernet communication. Figure 2.5B shows the control panel that can display and modify the gas flow, reaction pressure and temperature online; while the session table was responsible for the reaction sequence.

The effluent of reaction was periodically analyzed on-line using a Varian 450-GC-MS (Figure 2.4) equipped with one TCD, two FID and a mass detector. The TCD channel has a Mol.Sieve 13X column (1.5 m) and uses Ar as carrier. The FID channels use He as carrier and have Hayesep Q (0.5 m) and CP-Sil 5 CB (25 m) columns. For proper quantification of CO and CO_2, they are first separated then converted into methane using an appropriate methanizer accessory incorporated into the chromatograph equipment. Then, CH_4 formed is determined in one FID channel. Identification of products can be completed when necessary by the MS detector. The analysis sequence was automatically controlled by the “SampleList” table which is an internal program of the workstation for Varian 450 GC.

Experiments performed at atmospheric pressure were carried out using a similar equipment but with a GC Varian 450 with only TCD and FID.

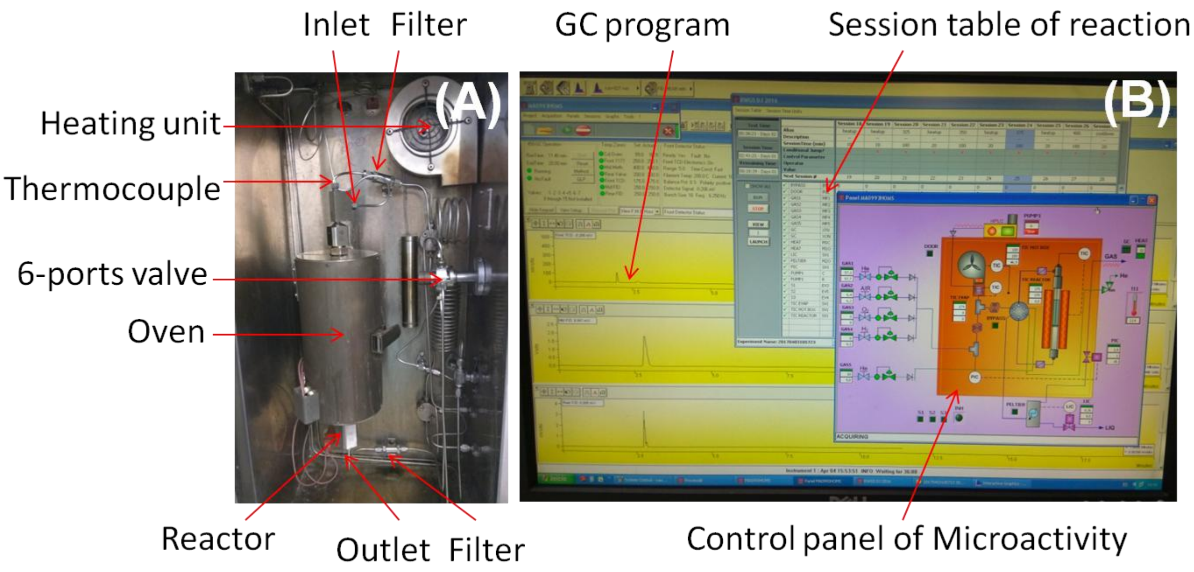

Figure 2.5. Inside view of hot box (A) and control programs of GC and Microactivity (B).

CO_2 conversion and product distribution were determined at each temperature by the average of at least 3 different analyses. The CO_2 conversion (X_{CO_2}) and selectivity (S_i) of each product excluding H_2O, are defined as follows:

$$X_{CO_2}(\%) = \left(1 - \frac{(C_{CO_2})_{outlet}}{(C_{CO_2})_{outlet} + n * \sum(Ci)_{outlet}}\right) \times 100 \tag{2.12}$$

$$S_i(\%) = \frac{(Ci\,)_{outlet}}{\sum(Ci)_{outlet}} \times 100 \tag{2.13}$$

Where $(C_i)_{outlet}$ is the molar concentration of the product "i" in the effluent, and "n" is the number of carbon atoms in the product.

Catalytic tests of the MSR reaction were also carried out using a Microactivity-Reference unit (PID Eng&Tech) at MATCAT-UB. In this case, the Microactivity-Reference unit was coupled with a GILSON liquid pump that allowed inject at atmospheric pressure the reactant mixture: $H_2O/CH_3OH=1/1$ (molar ratio). The outlet of the system was connected on-line through a thermostatic transfer line to a Varian 4900 micro-chromatograph. The scheme of the Microactivity-Reference reaction system is shown in Figure 2.6.

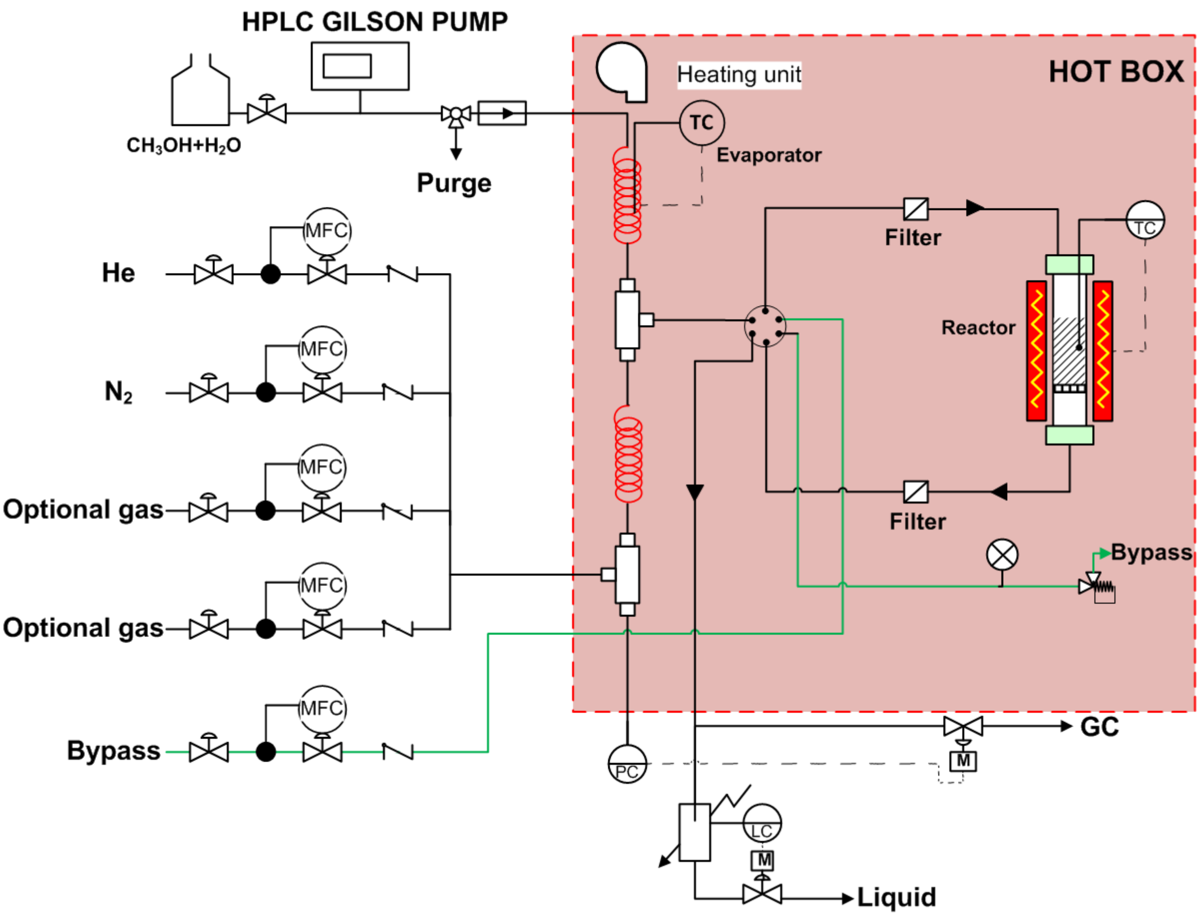

Figure 2.6. Scheme of the MSR reaction system. MFC, Mass flow controller; PC, Pressure controller; TC, Temperature controller; LC, Level controller; M, Electric valve.

Firstly, the CH_3OH/H_2O liquid mixture, controlled by the GILSON pump, was fed at constant flow, evaporated and pre-heated at 160 °C. Then, the CH_3OH/H_2O gas mixture was mixed with high purity N_2 and flowed to a 6-port valve which allows sending the mixture to the reactor, to the analysis system or to venting. A liquid-gas separator fitted with a high-resolution capacitive level sensor allowed the condensation of liquids at the outlet of the system. After condensation, the accumulated liquid (CH_3OH and H_2O) was removed automatically by a level control system. The collected liquid was periodically quantified and analyzed using the Varian 450 GC equipment mentioned above.

The gaseous reaction products were analyzed on-line using a Varian 4900 micro-GC equipped with three TCD and three channels. One using Ar carrier and M5A column (10 m), and the others using He carrier and 5CB (8 m), PPQ (10 m) columns.

MoreoverThe CH_3OH conversion (X_{CH_3OH}) and molar fraction of products (χ_i) are defined as following:

$$X_{CH_3OH}(\%) = \frac{(\text{Total flow})_{\text{outlet}} - \text{Flow } N_2}{(\text{Flow } CH_3OH)_{\text{inlet}} \times 4} \times 100 \quad (2.14)$$

$$\chi_i(\%) = \frac{(C_i)_{\text{outlet}}}{\sum (C_i)_{\text{outlet}}} \times 100 \quad (2.15)$$

Where $(C_i)_{\text{outlet}}$ is the molar concentration of the product “i” in the effluent.

2.3 References

[1] Mermet JM. Is it still possible, necessary and beneficial to perform research in ICP-atomic emission spectrometry? J Anal At Spectrom 2005;20:11-16.

[2] Brunauer S, Emmett PH, Teller E. Adsorption of gases in multimolecular layers. J. Am. Chem. Soc. 1938;60:309-319.

[3] Thommes M, Kaneko K, Neimark AV, Olivier JP, Rodriguez-Reinoso F, Rouquerol J, et al. Physisorption of gases, with special reference to the evaluation of surface area and pore size distribution (IUPAC Technical Report). Pure Appl. Chem. 2015;87:1051-1069.

[4] Barrett EP, Joyner LG, Halenda PP. The determination of pore volume and area distributions in porous substances. I. Computations from nitrogen isotherms. J. Am. Chem. Soc. 1951;73:373-380.

[5] Patterson A. The Scherrer formula for X-ray particle size determination. Phys. rev. 1939;56:978-982.

[6] Niemantsverdriet JW. Spectroscopy in catalysis: an introduction. John Wiley & Sons; 2007.

[7] Alexander L, Klug HP. Determination of crystallite size with the X-Ray spectrometer. J. Appl. Phys. 1950;21:137-142.

[8] Chan S, Wachs I, Murrell L, Wang L, Hall WK. In situ laser Raman spectroscopy of supported metal oxides. The J. Phys. Chem. 1984;88:5831-5835.

[9] Cai W, Ramírez de La Piscina P, Toyir J, Homs N. CO_2 hydrogenation to methanol over CuZnGa catalysts prepared using microwave-assisted methods. Catal. Today. 2015;242:193-199.

[10] Yuan Z, Wang L, Wang J, Xia S, Chen P, Hou Z, Zheng X. Hydrogenolysis of glycerol over homogenously dispersed copper on solid base catalysts. Appl. Catal. B: Environ. 2011;101:431-440.

[11] Fichtl MB, Schumann J, Kasatkin I, Jacobsen N, Behrens M, Schlögl R, Muhler M, Hinrichsen O. Counting of oxygen defects versus metal surface sites in methanol synthesis catalysts by different probe molecules. Angew. Chem. Int. Ed. 2014;53:7043-7047.

[12] Imelik B, Vedrine JC (Eds.). Catalyst characterization: physical techniques for solid materials. Plenum Press, New York, 1994.

[13] Moulder JF, Stickle W, Sobol PE, Bomben KD. Handbook of X-ray photoelectron spectroscopy. Perkin-Elmer Corporation Physical Electronics Division. 1992.

[14] Córdoba Sola A. Estudio de catalizadores basados en Pt/TiO_2 en la fotoproducción de H_2 y otros productos valorizados a partir de etanol. PhD thesis. 2015, University of Barcelona.

Chapter 3

Cu-ZnO-Ga_2O_3-based catalysts in RWGS reaction

In this chapter, the preparation and characterization of new Cu-ZnO-Ga_2O_3-based catalysts are presented. The catalytic behaviour of Cu-ZnO-Ga_2O_3-based catalysts in the RWGS and stoichiometric MSR is also shown. Moreover, the effect of Ru on the catalyst which showed the best performance in the CO_2 reduction to CO was studied under the RWGS conditions used.

Catalysts were characterized after calcination, reduction and catalytic test using different techniques, such as ICP-AES, N_2 adsorption-desorption isotherms, XRD, Raman spectroscopy, H_2-TPR, N_2O chemisorption, XPS, CO_2-TPD, H_2-TPD, TPO and CO-DRIFTS.

3.1. Preparation of catalysts

Figure 3.1 shows the general preparation procedure of $CuZnOGa_2O_3M_xO_y$ (M=Al, Zr) catalysts.

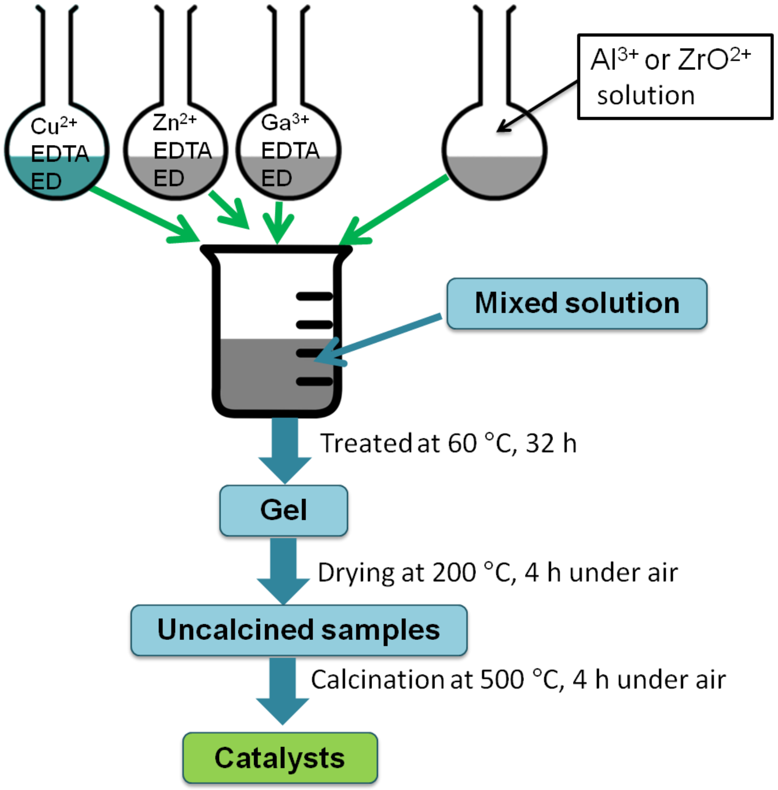

Figure 3.1. Preparation procedure of $CuZnOGa_2O_3M_xO_y$ (M=Al, Zr) catalysts.

The corresponding preparation details of Cu-ZnO-Ga_2O_3-Al_2O_3, Cu-ZnO-Ga_2O_3-ZrO_2, and Ru-containing samples are given below:

a) A series of multicomponent $CuZnOGa_2O_3M_xO_y$ (M=Al, Zr) catalysts with different compositions were prepared on the basis of the sol-gel method proposed by Mathew et al. for the preparation of pseudo-3D mesoporous γ-$Al_{2-X}M_xO_{3\pm y}$ (where M=Ti^{4+} through Ga^{3+}) materials [1].

   In all cases, separate 0.5 M aqueous solutions of $Cu(NO_3)_2{\cdot}3H_2O$, $Zn(NO_3)_2{\cdot}6H_2O$ and $Ga(NO_3)_3{\cdot}nH_2O$ containing ethylene diamine tetraacetic acid (EDTA, 0.5 M) and ethylene diamine (ED, 1 M) were prepared. Thereafter, appropriate amounts of the above mentioned solutions, which depended on the composition of the catalyst, were mixed in a beaker with an aqueous solution containing Al^{3+} ($Al(NO_3)_3{\cdot}9H_2O$, 0.5 M; EDTA, 0.5 M; ED, 1.5 M) or ZrO^{2+} ($ZrO(NO_3)_2{\cdot}xH_2O$, 0.5 M); the mixture was kept in a thermostatic bath at 60 °C for 32 h to obtain a gel. Finally, the gel was treated in an oven at 200 °C for 4 h before subsequent calcination in air at 500 °C. The catalysts were labelled as CuZnxGaM (M=Al, Zr), where x corresponds to the weight percentage of Ga_2O_3 in the catalyst. For comparison, a catalyst Cu-ZnO (CuZn) and two samples without Cu, ZnO-Ga_2O_3-Al_2O_3 (Zn2GaAl) and ZnO-Ga_2O_3-ZrO_2 (Zn2GaZr) were prepared.

b) Ru-containing samples based on CuZn3GaZr were prepared following a similar preparation method than that mentioned above. The appropriate amount of $Ru(NO)(NO_3)_3$ solution (Ru 1.5% w/v, Alfa Aesar**)** was added to the solution containing Cu^{2+}, Zn^{2+}, Ga^{3+} and ZrO^{2+} to form the gel. Afterwards, the gel was treated at 200 °C for 4 h and at 450 °C for 6 h in an oven under air. The samples were denoted as xRuCuZnGaZr, where x is the weight percentage of Ru (0.2-2.0 wt %) in the catalysts.

3.2. Characterization of catalysts

3.2.1. CuZnxGaM (M=Al, Zr) catalysts

Table 3.1 shows the chemical composition determined from ICP-AES and the S_{BET} values of the calcined CuZnxGaM (M=Al, Zr) catalysts prepared in this work.

Table 3.1. Chemical composition, S_{BET} values and, crystallite sizes of CuO and ZnO calculated from XRD of calcined CuZnxGaM (M=Al, Zr) catalysts.

Catalyst	Chemical analysis			S_{BET} (m^2/g)	Crystallite size	
	CuO (wt.%)	Ga_2O_3 (wt.%)	Al_2O_3 or ZrO_2(wt.%)		d_{CuO} (nm)	d_{ZnO} (nm)
CuZn	39.6	-	-	10.6	30.6	32.8
CuZn10Ga	39.5	9.9	-	26.4	25.2	21.9
CuZn1GaAl	35.5	1.4	24.0	44.7	21.1	25.0
CuZn3GaAl	35.4	2.8	18.0	39.3	20.5	23.7
CuZn6GaAl	27.4	5.7	36.2	46.2	21.7	(13.1)[a]
CuZn12GaAl	27.6	12.4	28.7	49.8	25.6	28.0
CuZn3GaZr	38.3	2.8	23.1	43.9	21.5	23.9
CuZn7GaZr	28.0	6.8	34.2	48.3	22.3	28.4
Zn2GaAl	-	2.3	36.1	89.6	-	(4.0)[a]
Zn2GaZr	-	2.4	37.6	39.8	-	16.1

[a] Crystallite size of $ZnAl_2O_4$ was determined using the XRD peaks at 2θ=59.2° and 2θ=36.7 ° for CuZn6GaAl and Zn2GaAl, respectively.

The bare CuZn catalyst showed the lowest S_{BET} (10.6 m^2/g), while the Zn2GaAl sample showed the highest S_{BET} (89.6 m^2/g). Moreover, CuZnxGaAl and CuZnxGaZr samples showed higher S_{BET} than that of CuZn10Ga sample. For the samples with similar Ga_2O_3 (3 wt% and 6-7 wt%) content, the S_{BET} of

CuZnxGaZr was slightly higher than that of the corresponding CuZnxGaAl sample.

XRD patterns of the calcined catalysts are presented in Figure 3.2. All CuO-containing catalysts showed the characteristic diffraction peaks that correspond to monoclinic CuO (JCPDS 01-080-1268).

Except for CuZn6GaAl and Zn2GaAl, well-defined diffraction peaks assigned to hexagonal ZnO (JCPDS 03-065-3411) were observed. The XRD peaks of Ga_2O_3 were not detected for any of the Ga_2O_3-containing samples. For Zn2GaAl, all of the observed diffraction peaks were ascribed to the presence of $ZnAl_2O_4$ (JCPDS 00-005-0669) spinel phase. Although the presence of crystalline $ZnAl_2O_4$ could be also proposed from CuZn1GaAl, CuZn6GaAl and CuZn12GaAl XRD patterns (Figure 3.2), the XRD patterns of $ZnAl_2O_4$ (JCPDS 00-005-0669) and $CuAl_2O_4$ (JCPDS 01-076-2295) are similar and this makes difficult to unambiguously assign the corresponding peaks in CuZn1GaAl, CuZn6GaAl and CuZn12GaAl patterns [2]. However, the formation of bulk $CuAl_2O_4$ species from CuO and Al_2O_3 has been reported to be not favoured at a temperature lower than 612 °C [3]. Meanwhile, the spinel $ZnAl_2O_4$ has been obtained in Cu-free systems prepared using sol-gel methods and calcined at 500 °C [4,5]. Taking into account this background, the presence of spinel $ZnAl_2O_4$ in the CuZnxGaAl catalysts, can be tentatively proposed. XRD patterns of CuZnxGaAl catalysts did not show characteristic peaks of Al_2O_3, this indicates that if there was some free Al_2O_3 in the solid, its crystallinity was low.

For CuZnxGaZr catalysts, the broad shoulders at $2\theta=28.7-31.1°$ and $2\theta=49.4-52.5°$ could be indicative of the presence of tetragonal ZrO_2 (JCPDS 01-080-0784) or cubic ZrO_2 (JCPDS 03-065-0461); tetragonal and cubic ZrO_2 are difficult to be clearly distinguished by XRD due to the proximity of their diffraction lines [6].

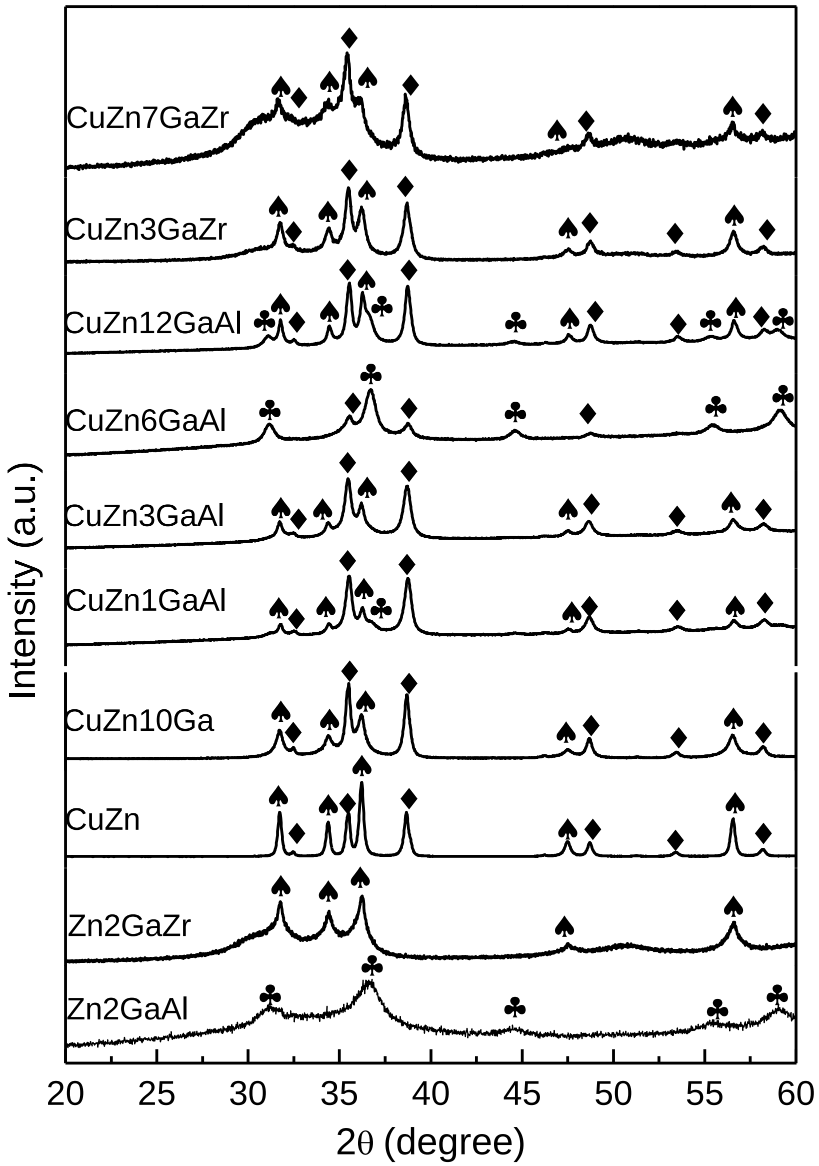

Figure 3.2. XRD patterns of calcined CuZnxGaM (M=Al, Zr) catalysts. (♠) ZnO; (♣) $ZnAl_2O_4$; (♦) CuO.

Table 3.1 also lists the crystallite sizes of CuO and ZnO for the calcined catalysts calculated using the Debye-Scherrer equation and CuO (111) and ZnO (110) XRD peaks at $2\theta=38.7°$ and 56.6°, respectively. The highest crystallite size of CuO (30.6 nm) and ZnO (32.8 nm) was obtained for the bare CuZn catalyst. The crystallite sizes of $ZnAl_2O_4$ were 13.1 nm and 4.0 nm in CuZn6GaAl and Zn2GaAl, respectively.

Figure 3.3 shows the Raman spectra of the calcined catalysts. Raman bands at about 282, 337 and 613 cm^{-1} have been assigned to CuO [7]. However, in our case, a slight shift of these Raman peaks was observed. This could be due to a possible interaction between CuO and other components in the catalyst or related to the particle size of CuO [8]. Peaks at about 434 and 568 cm^{-1} can be attributed to ZnO [9,10]. Furthermore, CuZn12GaAl (highest Ga_2O_3 content) showed a band at 185 cm^{-1} which can be ascribed to Ga_2O_3 [11]. Finally, the Raman spectrum of the CuZn7GaZr catalyst showed a characteristic band of tetragonal ZrO_2 at 141 cm^{-1} according with XRD results [12,13].

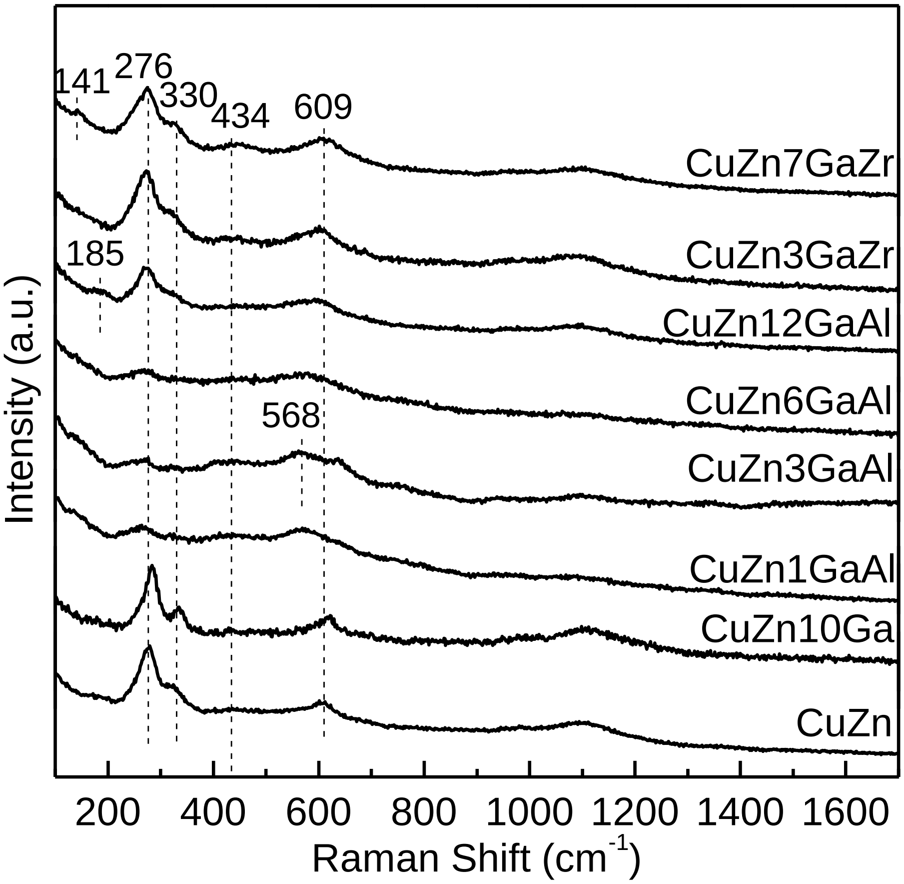

Figure 3.3. Raman spectra of calcined catalysts.

The H_2-TPR profiles of calcined samples are shown in Figure 3.4. Zn2GaAl and Zn2GaZr samples showed negligible H_2 consumption in the studied temperature range. The values of H_2 consumption for all CuO-containing samples appear in Table 3.2. Within the experimental error, a complete reduction of CuO can be proposed. However, the reduction of other reducible species in the catalysts cannot be ruled out.

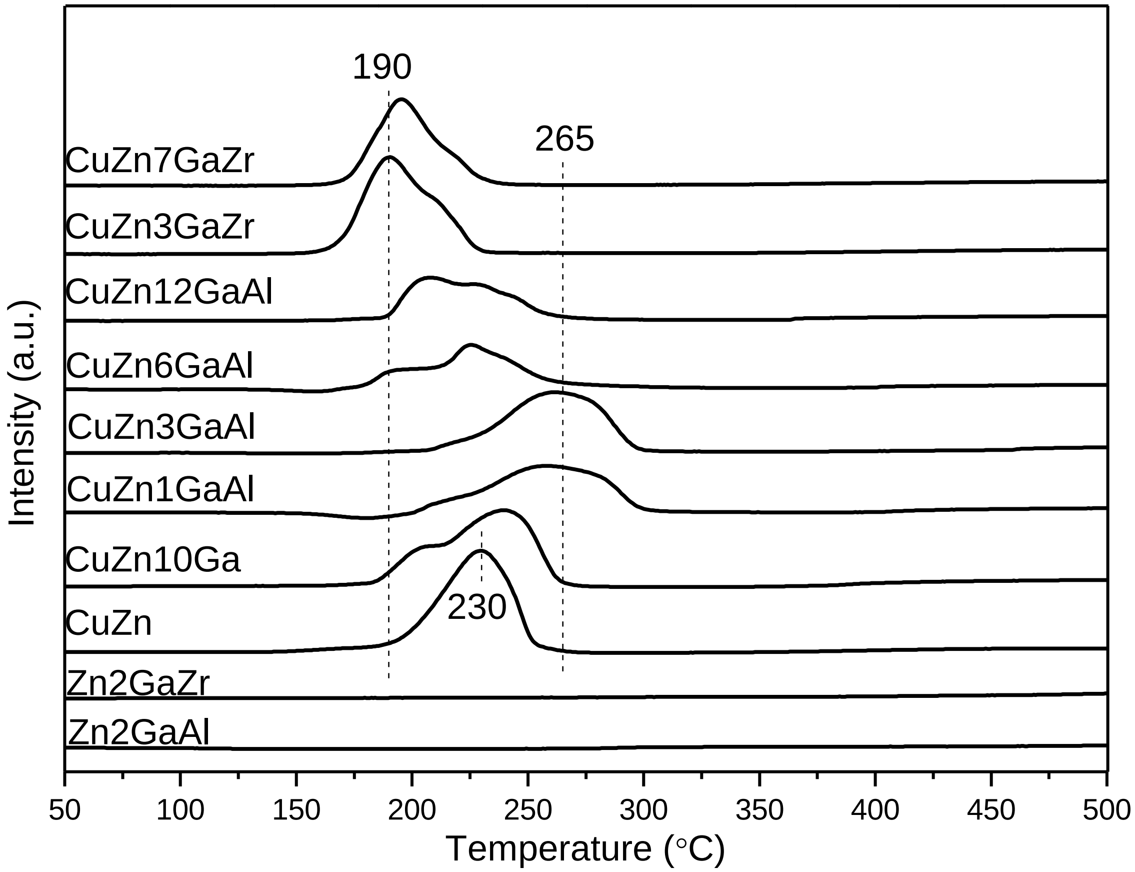

Figure 3.4. H_2-TPR profiles of calcined samples.

All CuO-containing catalysts showed H_2 consumption peaks at temperatures below 300 °C. The bare CuZn catalyst showed a slightly asymmetric single H_2 consumption peak centered at 230 °C [5,14]. Broader H_2 consumption peaks with different components were observed for the remaining samples. This can be related to the presence of CuO particles with different sizes or to the different interactions between the CuO particles and other oxide components in the catalysts [15,16].

The H_2 consumption peaks appearing at about 190-195 °C can be ascribed to highly dispersed CuO or small CuO particles which had a moderate interaction with other metal oxides [17,18]; the presence of oxygen vacancies at the CuO-oxide interface could facilitate the reduction of CuO species [5].

Table 3.2. Maximum of the CuO reduction peak (T_R^{Max}) and H_2 consumption determined for calcined catalysts from H_2-TPR; crystallite sizes of Cu^0 and ZnO in the reduced catalysts calculated from XRD patterns.

Catalyst	**H_2-TPR**		**d_{Cu} (nm)**	**d_{ZnO} (nm)**
	T_R^{Max} (^oC)	**H_2 consumption (mol H_2/mol Cu)**		
CuZn	230	0.98	46.8	35.3
CuZn10Ga	239	0.96	32.6	18.4
CuZn1GaAl	258	1.16	35.1	44.5
CuZn3GaAl	265	1.15	32.2	38.5
CuZn6GaAl	225	1.18	n.d.	(14.7)[a]
CuZn12GaAl	208	1.22	34.5	43.4
CuZn3GaZr	190	1.08	30.0	24.6
CuZn7GaZr	195	1.09	25.9	19.2

[a] $ZnAl_2O_4$ phase.
n.d.: not determined

CuZn1GaAl and CuZn3GaAl showed a higher reduction temperature than the other CuO-containing catalysts, this can be related to the presence of larger CuO particles and/or to a stronger interaction between CuO and the other species in the catalysts. Moreover, the broadness of the reduction peaks of CuZn1GaAl and CuZn3GaAl indicates the presence of more heterogeneous interactions of CuO with other components in these two catalysts [14]. The maximum of the reduction peak of CuO in CuZnxGaZr catalysts was at 190-195 °C, while all remaining catalysts showed reduction peaks located at higher temperatures than 190-195 °C, indicating the presence of a larger amount of smaller CuO particles in CuZnxGaZr than in the other catalysts. For CuZn6GaAl, the shoulder located at 190 °C suggests the presence of a small amount of small CuO particles.

Catalysts were also characterized using XRD after H_2 reduction at 275 °C, the corresponding XRD patterns appear in Figure 3.5.

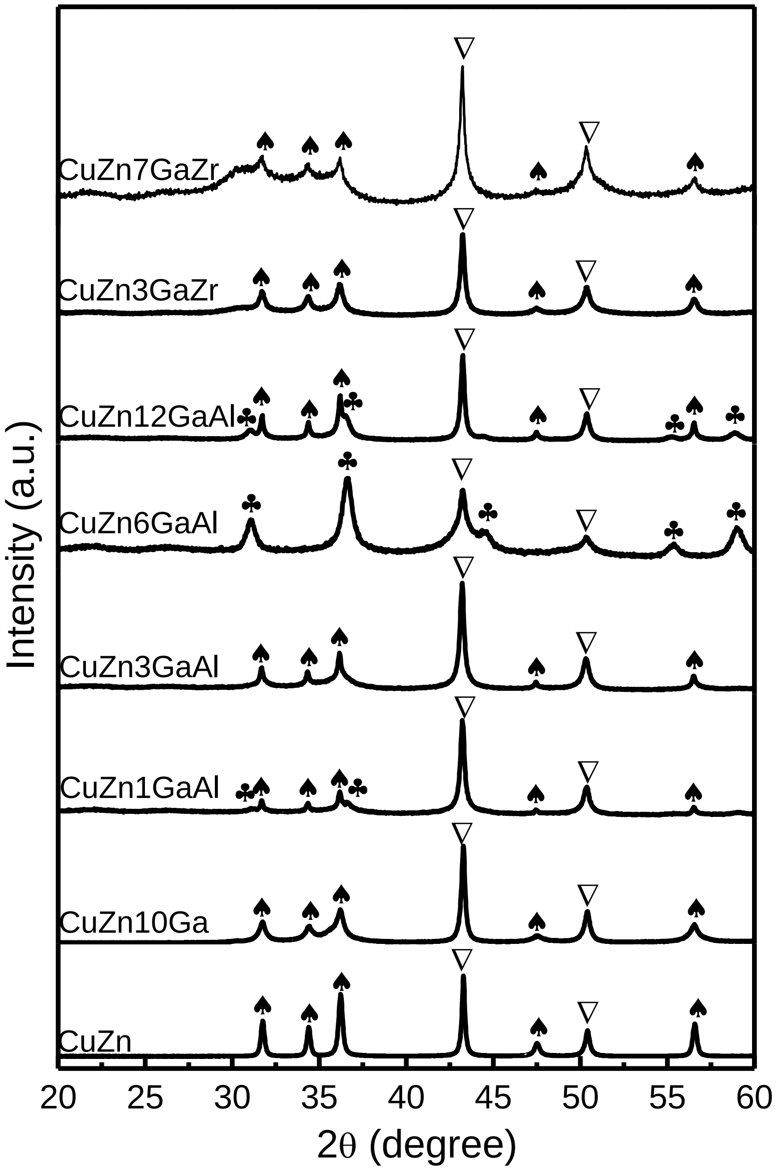

Figure 3.5. XRD patterns of H_2-reduced (T=275 °C) CuZnxGaM (M=Al, Zr) catalysts. (♠) ZnO; (♣) $ZnAl_2O_4$; (▽) Cu.

In all cases, characteristic peaks of cubic Cu^0 (JCPDS 00-004-0836) were observed and those of CuO were not, indicating the complete reduction of crystalline CuO under the conditions used. The diffraction peaks characteristic of ZnO and $ZnAl_2O_4$ observed for the calcined catalysts were also found for the corresponding H_2-reduced catalysts. For CuZnxGaZr samples, the broad peak centered at about 2θ=30.2° related with the most intense peak of tetragonal or cubic ZrO_2 was also found.

The crystallite sizes of Cu^0 and ZnO were calculated using the diffraction peaks at 2θ=43.3° (Cu^0 (111)) and at 2θ=56.6° (ZnO (110)); the results are listed in Table 3.2. For CuZn6GaAl, the crystallite size of Cu^0 cannot be estimated due to the proximity of Cu^0 (111) and $ZnAl_2O_4$ (400) peaks. The bare CuZn catalyst presented the largest crystallite size of Cu^0 (46.8 nm). In general, the crystallite size of Cu^0 in H_2-reduced catalysts is higher than that of CuO in the corresponding calcined catalysts. The crystallite size of ZnO was in the range of 18.4-44.5 nm. After H_2 reduction, CuZnxGaZr catalysts showed smaller ZnO crystallite size than H_2-reduced CuZnxGaAl catalysts, which in turn showed higher ZnO crystallite size than calcined CuZnxGaAl samples. For CuZn6GaAl, the crystallite size of $ZnAl_2O_4$ after H_2 reduction was 14.7 nm, only slightly higher than that after calcination (13.1 nm).

CuZn, CuZn3GaAl, CuZn6GaAl, CuZn3GaZr and CuZn7GaZr catalysts were used in the RWGS reaction. The samples were in-situ reduced with H_2 before each RWGS test. For this reason, we characterized more deeply these catalysts after H_2 reduction.

The S_{BET} values of H_2-reduced samples are shown in Table 3.3. After H_2 treatment, the lowest S_{BET} value (12.7 m^2/g) was found for the bare CuZn catalyst. For the catalysts which have similar Ga_2O_3 content, CuZnxGaZr showed higher

S_{BET} value than the corresponding CuZnxGaAl, similarly to the results of the calcined catalysts.

Table 3.3. S_{BET} of H_2-reduced catalysts and H_2 consumption after N_2O chemisorption.

Catalyst	**S_{BET} (m^2/g)**	**H_2 consumption ($\mu mol/g_{cat}$) after N_2O chemisorption**
CuZn	12.7	197
CuZn3GaAl	21.0	258
CuZn6GaAl	40.9	292
CuZn3GaZr	45.5	415
CuZn7GaZr	52.2	421

After H_2 reduction of the catalysts, N_2O chemisorption was carried out. As stated in the Experimental section, N_2O chemisorption is widely used for the quantification of Cu^0 on the surface of catalysts. However, it has been demonstrated that N_2O chemisorption quantifies not only the Cu^0 atoms but also the oxygen defects at the interface of Cu-ZnO_x in Cu/ZnO/Al_2O_3 and Cu/ZnO/MgO catalysts [19]. As mentioned in Chapter 2, catalysts were first reduced with H_2, during this treatment CuO is reduced to Cu (Eq. 2.5) but also the generation of oxygen defects at the Cu-support interface takes place. During N_2O chemisorption, surface Cu and oxygen vacancies react with N_2O to form Cu_2O and Cu-support interface (Eq. 2.6 and 2.8). After N_2O chemisorption, the formed Cu_2O and Cu-support interface were treated with H_2, and the amount of H_2 consumption was recorded; this amount can be related with the amount of surface Cu and oxygen vacancies on the catalysts.

The values of H_2 consumed after N_2O chemisorption are shown in Table 3.3. The values of H_2 consumption were in the range of 197-421 $\mu mol/g_{cat}$. The bare

CuZn catalyst showed the lowest H_2 consumption, indicating the presence of the fewest reducible species (Cu_2O and reducible species at the Cu-support interface) after N_2O chemisorption. Generally, ZrO_2-containing samples showed a higher value of H_2 consumption than Al_2O_3-containing samples. Moreover, a slight increase of the H_2 consumption was observed with the increasing of Ga_2O_3 content for both CuZnxGaZr and CuZnxGaAl samples. For the samples which contain a similar amount of Ga_2O_3, the corresponding CuZnxGaZr catalysts showed a higher H_2 consumption than the corresponding CuZnxGaAl catalysts. As shown in H_2-TPR profiles, CuZnxGaZr catalysts showed well-defined peaks at a lower reduction temperature than their CuZnxGaAl counterparts (Figure 3.4). These findings indicate that smaller Cu particles could be present in CuZnxGaZr; in these catalysts, ZrO_2 and Ga_2O_3 could favour the Cu dispersion and enable CuO species to be more easily reduced [20].

H_2-reduced catalysts were also characterized by XPS. Cu 2p, Zn $2p_{3/2}$, Al 2p, Zr 3d and Ga $2p_{3/2}$ core level spectra were recorded; the corresponding XPS profiles are shown in Figure 3.6. For all the samples, the BE values of Cu $2p_{3/2}$ were at 932.1-932.3 eV which are usually assigned to Cu^0 (932.0-932.5 eV) [21]. However, Cu^+ has been proposed to show similar BE values [22].

All the catalysts showed broad O 1s XPS peaks, indicating the presence of oxide and -OH species on the surface. For CuZnxGaZr, the O 1s peak was centered at 530.0-530.5 eV, meanwhile, for CuZn and CuZnxGaAl samples was at 531.0 eV. This finding indicates the main presence of O^{2-} on the surface of CuZnxGaZr and a higher contribution of -OH species on the CuZn and CuZnxGaAl catalysts [23]. BE values found for Zn $2p_{3/2}$ (1021.3-1021.9 eV), Al 2p at (74.1-74.2 eV) and Zr $3d_{5/2}$ (182.0 eV) indicated in all cases the presence of Zn^{2+}, Al^{3+} and Zr^{4+} species [21,22,24-26].

For all the Ga_2O_3-containing samples, Ga $2p_{3/2}$ BE values of 1117.5-1118.20 eV were found. Although according to the literature, these Ga $2p_{3/2}$ BE values can be attributed the presence of Ga_2O_3 [21], for pure β-Ga_2O_3, a value of 1119.4 eV has been reported [27].

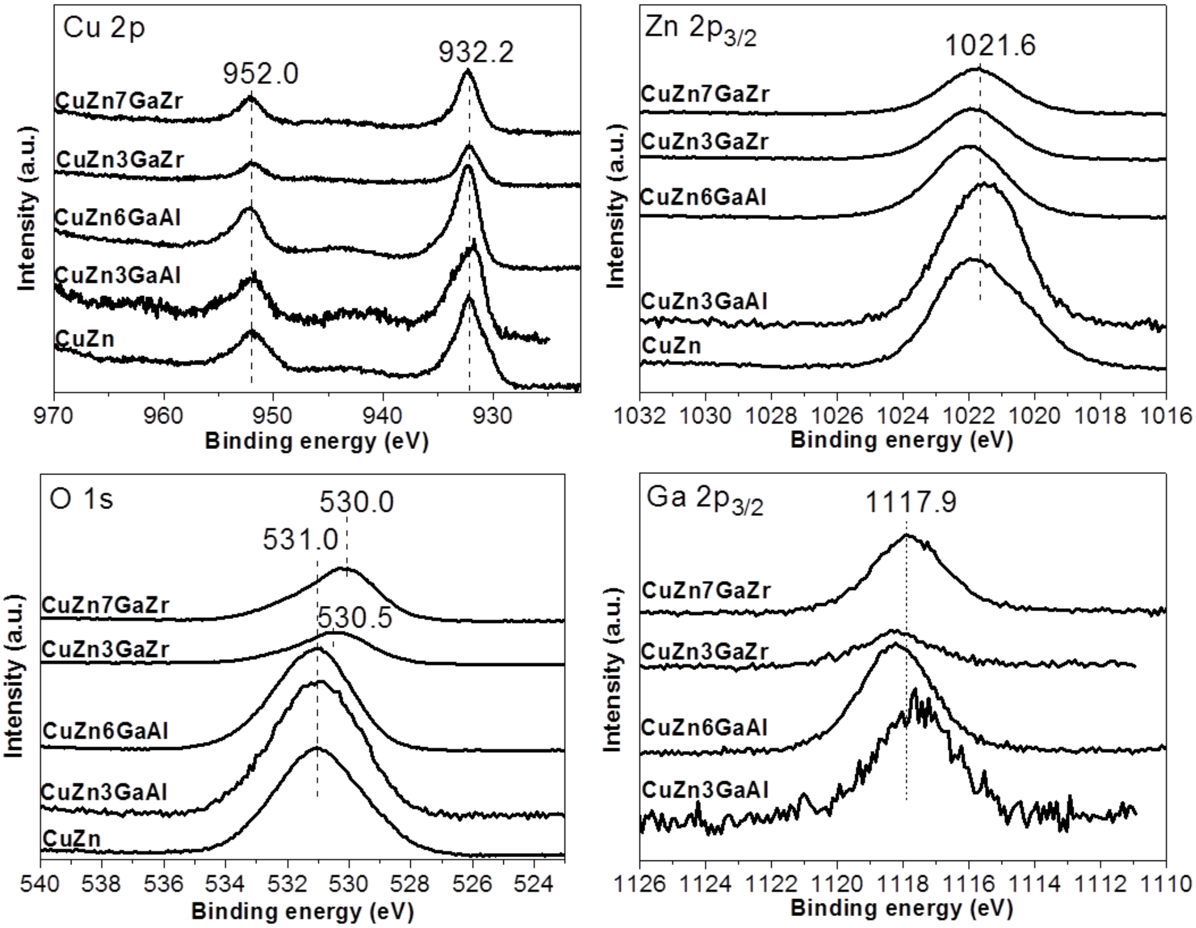

Figure 3.6. XPS profiles of H_2-reduced samples.

The surface atomic concentration of reduced catalysts determined by XPS is shown in Table 3.4. CuZnxGaAl showed lower surface Cu concentration than CuZn and CuZnxGaZr samples. In addition, the CuZnxGaZr catalysts possessed a higher concentration of surface Zn and Ga than CuZnxGaAl catalysts, indicating that the presence of ZrO_2 could favour the surface distribution of Cu, ZnO and Ga_2O_3. CuZnxGaAl catalysts showed mainly the presence of aluminium species on the surface.

Table 3.4. Surface atomic concentration (O excluded) of reduced catalysts determined by XPS.

Catalyst	mol/mol (%)			
	Cu	Zn	Ga	Al or Zr
CuZn	11.6	88.4	-	-
CuZn3GaAl	4.5	24.1	2.8	68.6
CuZn6GaAl	6.6	14.6	3.3	75.5
CuZn3GaZr	11.6	45.5	4.9	37.9
CuZn7GaZr	12.7	27.9	7.5	51.9

H_2-reduced samples were also characterized by CO_2-TPD, the profiles are shown in Figure 3.7A. The amount of basic sites present on catalysts is reflected in the peak area of CO_2 desorption profile [28]. CuZnxGaAl and CuZnxGaZr showed a broad CO_2 desorption peak in the temperature range of 50-500 °C; the corresponding peaks in the CO_2-TPD profile of the bare CuZn showed a lower intensity, that indicates the presence of a lower amount of surface basic sites on CuZn than on CuZnxGaM (M=Al, Zr).

Reduced catalysts were also characterized by H_2-TPD; H_2-TPD profiles of the reduced samples are shown in Figure 3.7B. The interaction of Cu catalysts with H_2 has been studied and used for the characterization of the exposed Cu sites [29]. It has been reported that H_2 desorption from surface adsorbed H atoms and subsurface atomic H on Cu takes place at about 27 and 287 °C, respectively [19.30]. For Cu-ZnO-based catalysts, H_2 desorption peaks at about 100-120 °C have been associated to the desorption of H atoms from highly defective ZnO at the Cu/ZnO interface [30], while the peaks in the range 350-500 °C have been ascribed to the desorption of H_2 on bulk Cu particles or on the ZnO surface [31,32]. Moreover, the dissociative chemisorption of H_2 on Ga_2O_3 has been observed at temperatures above 227 °C; heterolytic adsorption of H_2 at Ga-O-Ga sites produces OH and Ga-H, which can recombine and desorb as molecular H_2 at temperatures of 400 °C or higher [33].

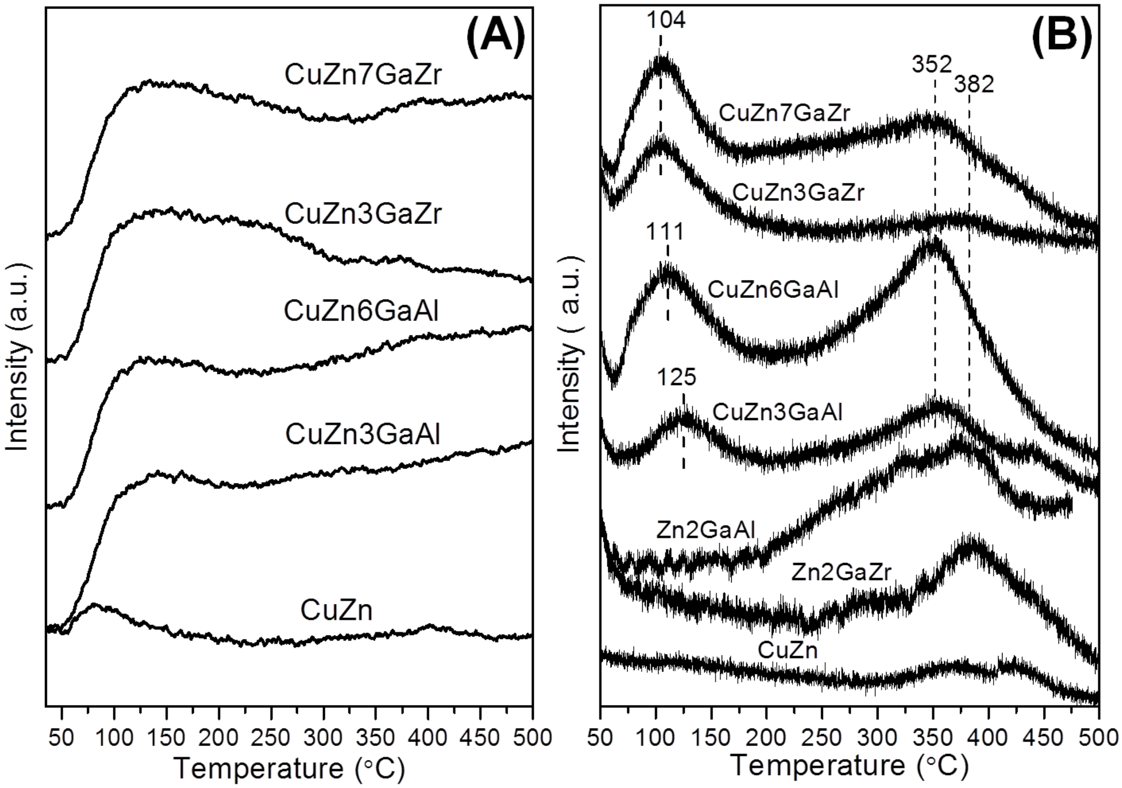

Figure 3.7. CO_2-TPD (A) and H_2-TPD (B) profiles of reduced catalysts as a function of desorption temperature.

In our case, two H_2 desorption peaks with maxima at about 104-125 °C and 352-382 °C were observed for CuZnxGaM (M=Al, Zr) samples. The Zn2GaZr and Zn2GaAl samples showed only one desorption peak at the high temperature range (352-382 °C). Peaks appearing at the low temperature range (104-125 °C) could be related to the presence of Cu^0, probably with atomic H on highly defective oxide (ZnO, Ga_2O_3 or ZrO_2) at the Cu-support interface [30]. Peaks at the high temperature range (352-382 °C) could be ascribed to the adsorption of H_2 on the support.

The intensity of the peaks corresponding to CuZn was lower than that of CuZnxGaZr and CuZnxGaAl, indicating a higher capacity for H_2 adsorption of multicomponent catalysts than the bare CuZn. Moreover, the peak intensity increased with the increase of Ga content for both CuZnxGaZr and CuZnxGaAl samples. This observation could be related with the capacity of Ga_2O_3 for H_2 adsorption [33] and the change of the Cu-support interface with the variation of Ga_2O_3 content.

3.2.2. xRuCuZnGaZr catalysts

As stated above, xRuCuZnGaZr catalysts based on CuZn3GaZr, with different Ru content (0.2-2 wt%) were prepared, characterized and studied in the RWGS reaction.

Table 3.5 shows the chemical composition and S_{BET} of xRuCuZnGaZr catalysts. The S_{BET} values were in the range of 31.3-41.4 m^2/g; all the samples showed a lower S_{BET} than the corresponding CuZn3GaZr.

Table 3.5. Chemical composition, S_{BET} and crystallite sizes of CuO and ZnO for calcined xRuCuZnGaZr catalysts.

Catalyst	**Chemical Analysis**				**S_{BET} (m^2/g)**	**Crystallite size (nm)**	
	Ru	**CuO**	**Ga_2O_3**	**ZrO_2**		**CuO**	**ZnO**
0.2RuCuZnGaZr	0.2	40.2	2.6	20.4	37.6	16.6	20.7
0.4RuCuZnGaZr	0.4	39.6	2.6	20.3	41.4	17.5	21.4
0.7RuCuZnGaZr	0.7	38.0	2.5	20.4	31.3	16.5	21.4
2.0RuCuZnGaZr	2.0	38.8	2.7	20.9	38.7	20.0	24.7
CuZn3GaZr	-	38.3	2.8	23.1	43.9	21.5	23.9

The XRD patterns of calcined xRuCuZnGaZr samples are shown in Figure 3.8. The characteristic diffraction peaks of CuO, ZnO and ZrO_2 observed for the calcined CuZn3GaZr, were also found for all the xRuCuZnGaZr catalysts. For 2.0RuCuZnGaZr, XRD peaks located at 2θ=28.1° and 54.3° were ascribed to (110) and (211) peaks of the tetragonal RuO_2 (JCPDS 01-071-2273). The crystallite sizes of CuO and ZnO calculated using the Scherrer equation are listed in Table 3.5. The 2.0RuCuZnGaZr catalyst showed the highest crystallite sizes of both CuO (20.0 nm) and ZnO (24.7 nm). The CuO crystallite sizes calculated for xRuCuZnGaZr were slightly lower than that of CuZn3GaZr (Table 3.5). On the other hand, the crystallite size of ZnO in 2.0RuCuZnGaZr was slightly higher than that of CuZn3GaZr, while those of the remaining xRuCuZnGaZr were slightly lower (Table 3.5).

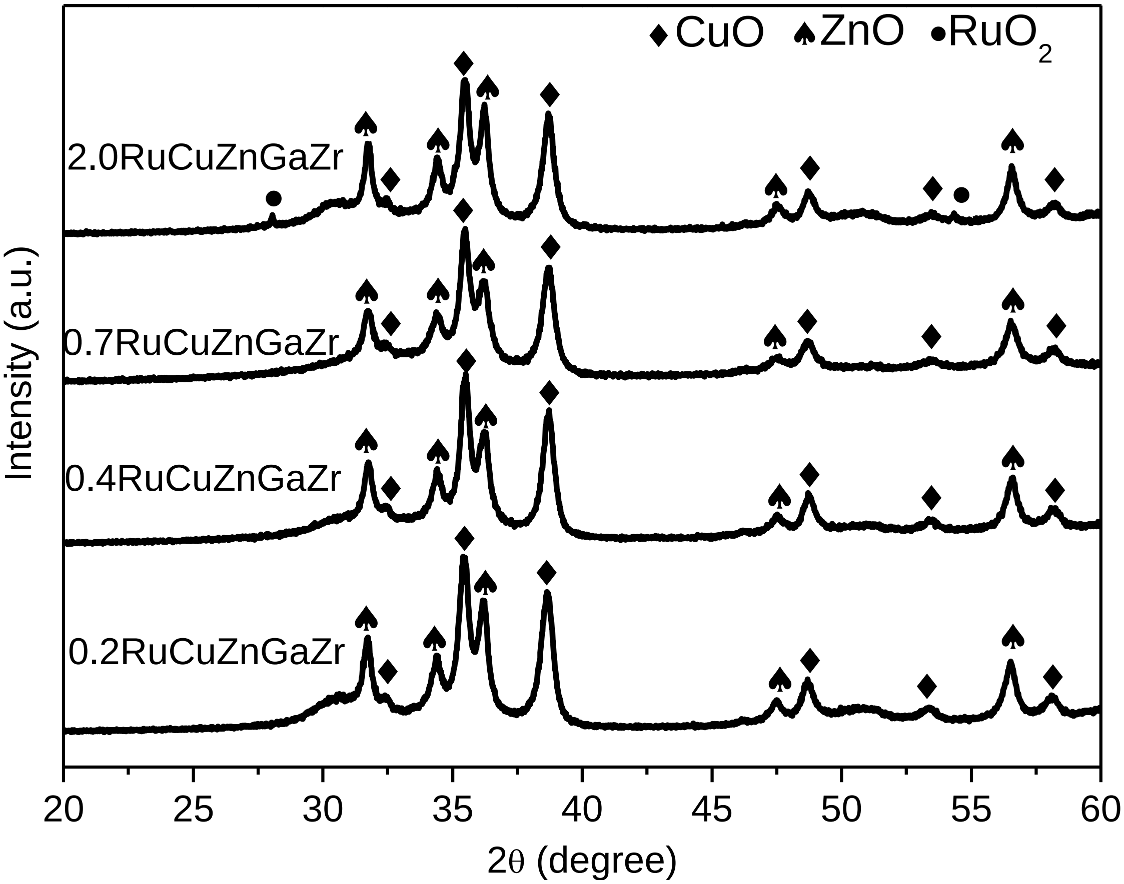

Figure 3.8. XRD patterns of calcined xRuCuZnGaZr samples.

The Raman spectra of calcined xRuCuZnGaZr catalysts are shown in Figure 3.9. In all cases, the Raman spectra of xRuCuZnGaZr were similar to that of the corresponding CuZn3GaZr. Raman bands assigned to CuO centered at 273, 328 and 601 cm^{-1} were observed for all the xRuCuZnGaZr catalysts. The band located at 434 cm^{-1} related with the presence of ZnO was also visible for xRuCuZnGaZr catalysts.

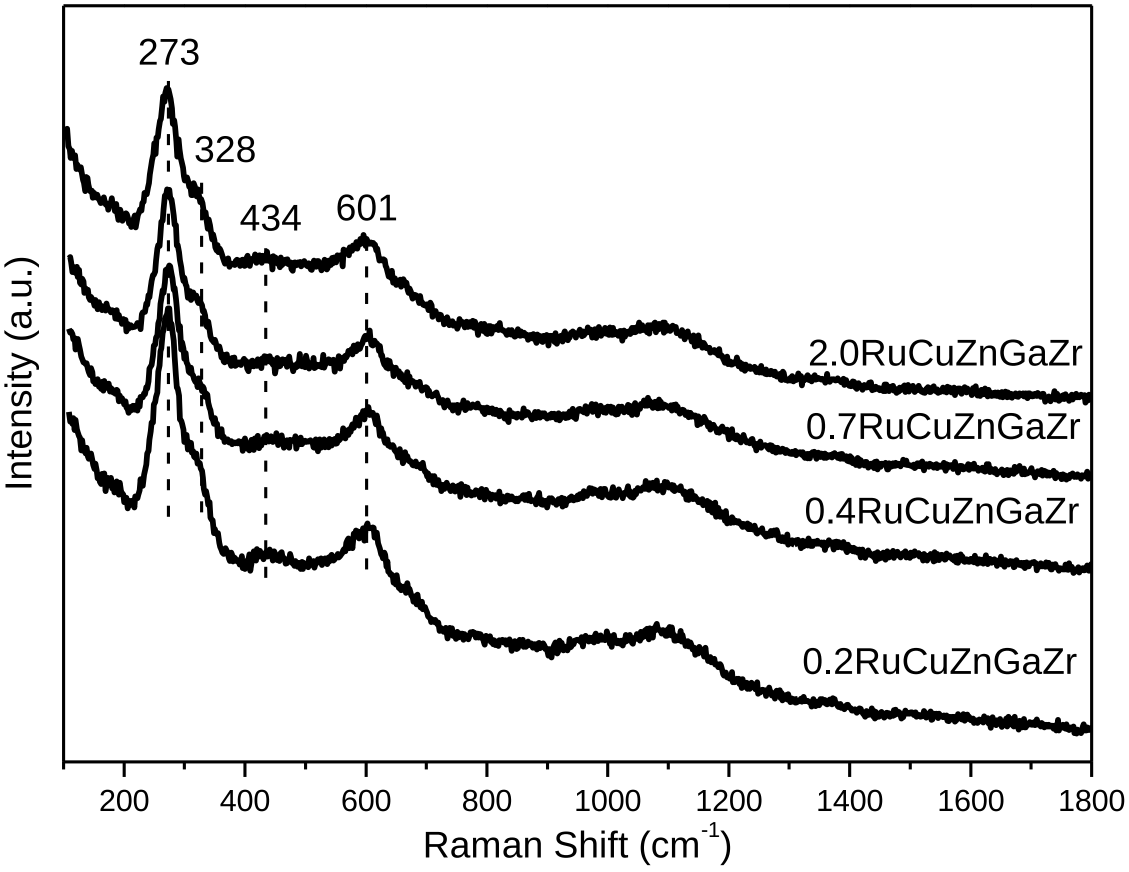

Figure 3.9. Raman spectra of calcined xRuCuZnGaZr samples.

Figure 3.10 shows the H_2-TPR profiles of calcined xRuCuZnGaZr catalysts. The H_2-TPR profile of CuZn3GaZr catalyst was also presented for comparison. In general, for xRuCuZnGaZr catalysts, the H_2 consumption peak shifted to lower temperatures when the Ru content in the catalysts increased. A similar shift of reduction temperatures was found by Chang et al. for CuO-ZnO-Al_2O_3 (30/60/10) with 0.5-2.0 Ru wt% catalysts [34]. This shift was attributed to the easiness of dissociative hydrogen adsorption on Ru and then the spillover of hydrogen which facilitates the reduction of CuO [34-36]. Taking into account the H_2 consumption necessary for RuO_2 and CuO reduction:

$$RuO_2+2H_2 \rightarrow Ru+2H_2O \qquad (3.1)$$

$$CuO+H_2 \rightarrow Cu+H_2O \qquad (3.2)$$

The theoretical H_2 consumption was calculated; the experimental H_2 consumption/theoretical H_2 consumption ratio values were 0.93, 0.97, 0.94 and 0.86 for 0.2RuCuZnGaZr, 0.4RuCuZnGaZr, 0.7RuCuZnGaZr and 2.0RuCuZnGaZr, respectively. Within the experimental error, a complete reduction of RuO_2 and CuO can be proposed.

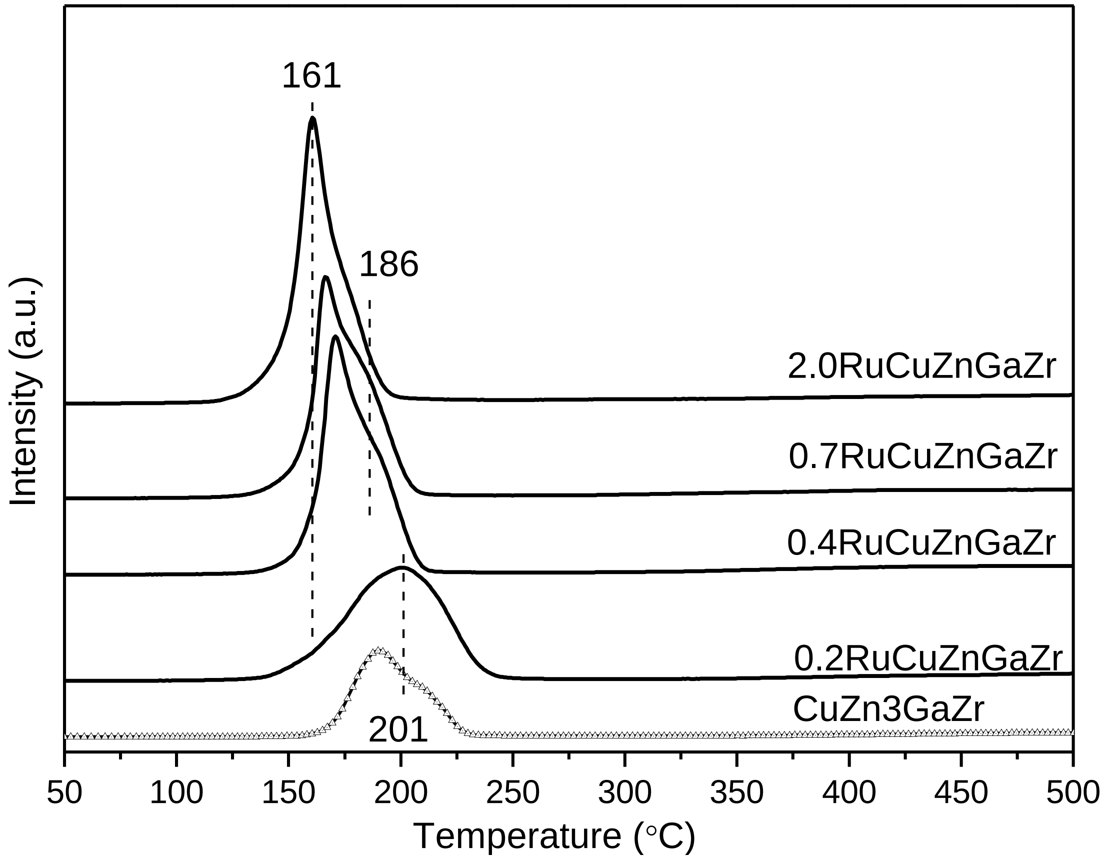

Figure 3.10. H_2-TPR profiles of calcined xRuCuZnGaZr samples.

The CO_2-TPD profiles of reduced xRuCuZnGaZr catalysts are shown in Figure 3.11. The corresponding profile of CuZn3GaZr sample is presented in dashed line for comparison purpose. Although slight differences in the profiles can be seen, in all cases, a broad desorption peak between 50-500 °C was obtained.

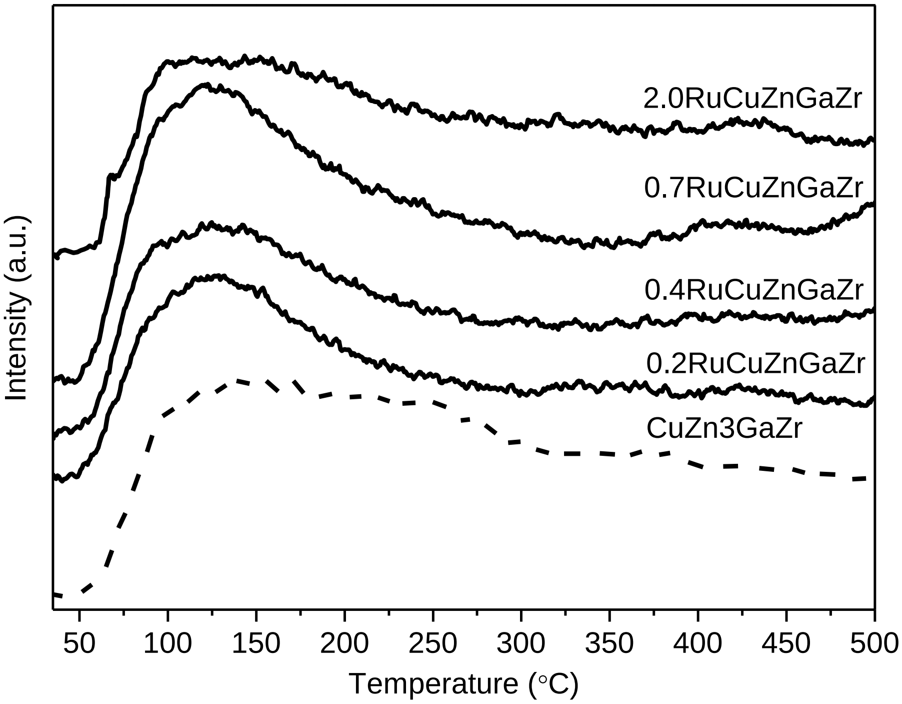

Figure 3.11. CO_2-TPD profiles of reduced xRuCuZnGaZr catalysts as a function of desorption temperature.

3.3. Catalytic behaviour in RWGS reaction

As mentioned above, we studied the RWGS reaction over CuZn, CuZn3GaAl, CuZn6GaAl, CuZn3GaZr, CuZn7GaZr and xRuCuZnGaZr catalysts; for comparative purposes, Zn2GaAl and Zn2GaZr were also studied in the RWGS. The catalytic tests were carried out at a pressure of 3 MPa, temperature of 250-270 °C, gas hourly space velocity (GHSV) of 3000 h^{-1} and using $CO_2/H_2/N_2$ (1/3/1, molar ratio) as reactant mixture. Prior to each run, the catalysts were in-situ reduced in a H_2/Ar (12% vol/vol) stream at 300 °C for 2 h at atmospheric pressure and then at 3 MPa for 1 h to achieve the total reduction of CuO species according to H_2-TPR profiles (Figure 3.4).

In general, about 150 mg of sieved samples (0.2-0.4 mm) were diluted with inactive SiC (Prolabo, 0.5 mm) up to 1 mL.

Moreover, the influence of the GHSV and the total pressure on the RWGS reaction was also investigated over CuZn3GaZr, which showed the highest catalytic activity and CO production.

3.3.1. RWGS reaction over CuZnxGaM (M=Al, Zr) catalysts

Effect of temperature on the RWGS reaction

After reduction at 300 °C and 3 MPa, the temperature was decreased to 240 °C and the samples were then exposed to the reactant mixture $CO_2/H_2/N_2$ (1/3/1, molar ratio). The sequence of reaction temperatures was 250 °C (15h)→260 °C (5h)→270 °C (5h)→250 °C (15h).

Figure 3.12 displays the CO_2 conversion of CuZn and CuZnxGaM (M=Al, Zr) catalysts as a function of reaction temperature. Zn2GaAl and Zn2GaZr showed quite low activity in the RWGS reaction, the corresponding values of CO_2 conversion are listed in Table 3.6.

As shown in Figure 3.12, CO_2 conversion increased with the increase of reaction temperature. As stated above, after the increase of reaction temperature from 250 to 270 °C, the temperature was decreased to 250 °C. Except for CuZn6GaAl, in all cases, the initial CO_2 conversion at 250 °C was higher than that obtained at 250 °C at the final stage of the catalytic test.

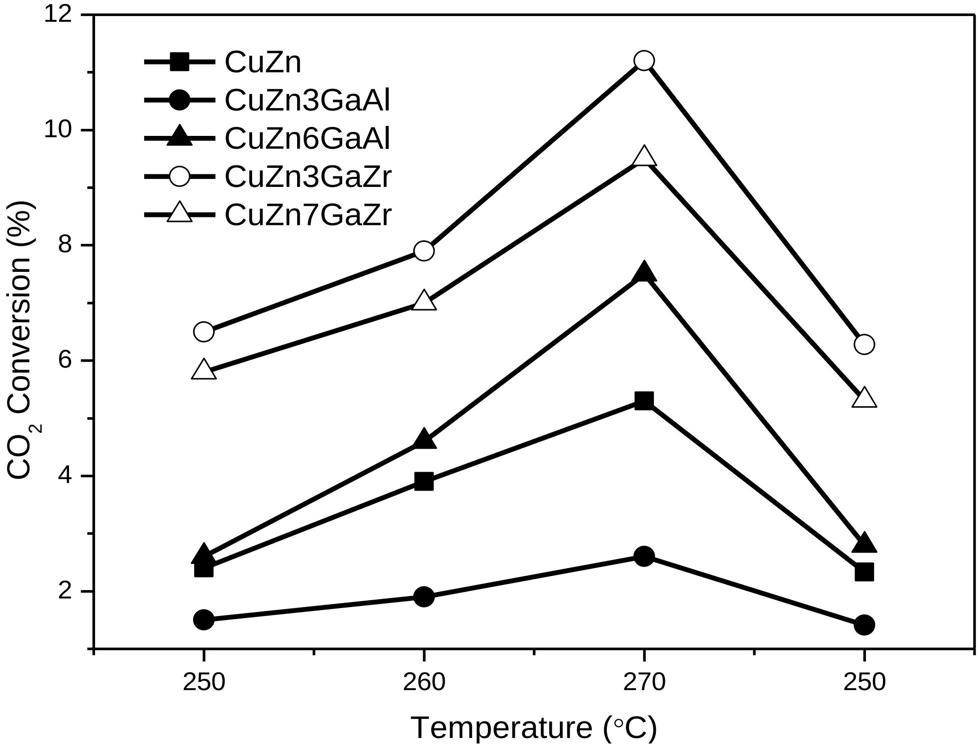

Figure 3.12. CO_2 conversion obtained over CuZnxGaM (M=Al, Zr) catalysts. Reaction conditions: T=250-270 °C, P=3 MPa, GHSV=3000 h^{-1}, $CO_2/H_2/N_2$=1/3/1.

CuZnxGaZr catalysts were more active than CuZn and CuZnxGaAl catalysts. For CuZn3GaZr, the CO_2 conversion could reach up to 11.2% at 270 °C and 3 MPa. As discussed above, the presence of a larger amount of surface Cu, Ga and Zn (Table 3.4) in CuZnxGaZr than those on CuZnxGaAl was determined by XPS. Moreover, N_2O chemisorption pointed out the presence of a larger amount of surface Cu^0 and oxygen defects at the Cu-support interface on CuZnxGaZr when compared with CuZn or CuZnxGaAl catalysts.

Table 3.6 shows the catalytic behaviour of all catalysts in the RWGS reaction. Although in all cases CO was the main product observed, CH_3OH and very small amounts of CH_4 were also produced. As expected, in general, the CO selectivity increased and the CH_3OH selectivity decreased with the increase of reaction temperature (Table 3.6). CuZnxGaZr showed a higher CO production than CuZn and CuZnxGaAl in the overall temperature range studied.

Table 3.6. Catalytic behaviour in the RWGS reaction of CuZnxGaM (M=Al, Zr) catalysts. Reaction conditions: T=250-270 °C, P=3 MPa, $CO_2/H_2/N_2$=1/3/1, GHSV=3000 h^{-1}.

Catalyst	T(°C)	CO_2 conversion (%)	CO yield mmol/Kg_{cat}•h	Selectivity (%)	
				CH_3OH	CH_4
CuZn	250	2.4	3354	14.0	<0.01
	260	3.9	5817	8.6	0.01
	270	5.3	8098	6.8	0.01
CuZn3GaAl	250	1.5	1634	33.9	1.1
	260	1.9	2141	28.3	1.3
	270	2.6	3319	21.9	1.4
CuZn6GaAl	250	2.6	3879	9.4	0.03
	260	4.6	7061	6.4	0.03
	270	7.5	11788	4.2	0.04
CuZn3GaZr	250	6.5	9226	12.7	0.2
	260	7.9	11635	10.1	0.1
	270	11.2	17047	6.9	0.1
CuZn7GaZr	250	5.8	8050	14.5	0.01
	260	7.0	10133	11.8	0.02
	270	9.5	14321	8.2	0.02
Zn2GaAl	250	0.1	137	18.9	1.9
	260	0.2	207	19.1	1.7
	270	0.2	317	18.7	1.4
Zn2GaZr	250	0.1	82	28.9	4.0
	260	0.1	118	28.0	3.8
	270	0.2	179	27.8	3.5

For CuZnxGaAl, the low catalytic activity could be related with the presence of a small amount of Cu on the surface (Table 3.4). Although CuZnxGaZr and CuZn presented a similar amount of surface Cu (Table 3.4); the CuZnxGaZr catalysts have much higher S_{BET} values and a larger amount of reducible oxide species at the Cu-support interface than CuZn. We propose that synergy involving the surface Cu and the oxygen vacancies at the Cu-support interface is responsible for the better performance in the RWGS reaction of CuZnxGaZr with respect to CuZn and CuZnxGaAl samples. On this matter, for binary Cu/ZnO catalysts, an important role of optimized Cu/ZnO interfaces in the activation and dissociation of CO_2, which is considered the rate-determining step of the RWGS reaction, has been recently proposed [37].

Figure 3.13 shows the XRD patterns of the post-reaction catalysts. After RWGS reaction, for all Cu-containing catalysts, characteristic peaks of Cu^0 are present. However, for CuZnxGaAl, low intensity peaks indicative of the CuO presence were also found. The absence of characteristic CuO peaks in the XRD patterns of CuZnxGaZr could be related to the lower reduction temperature of CuO in these catalysts compared to CuZnxGaAl catalysts (Figure 3.4).

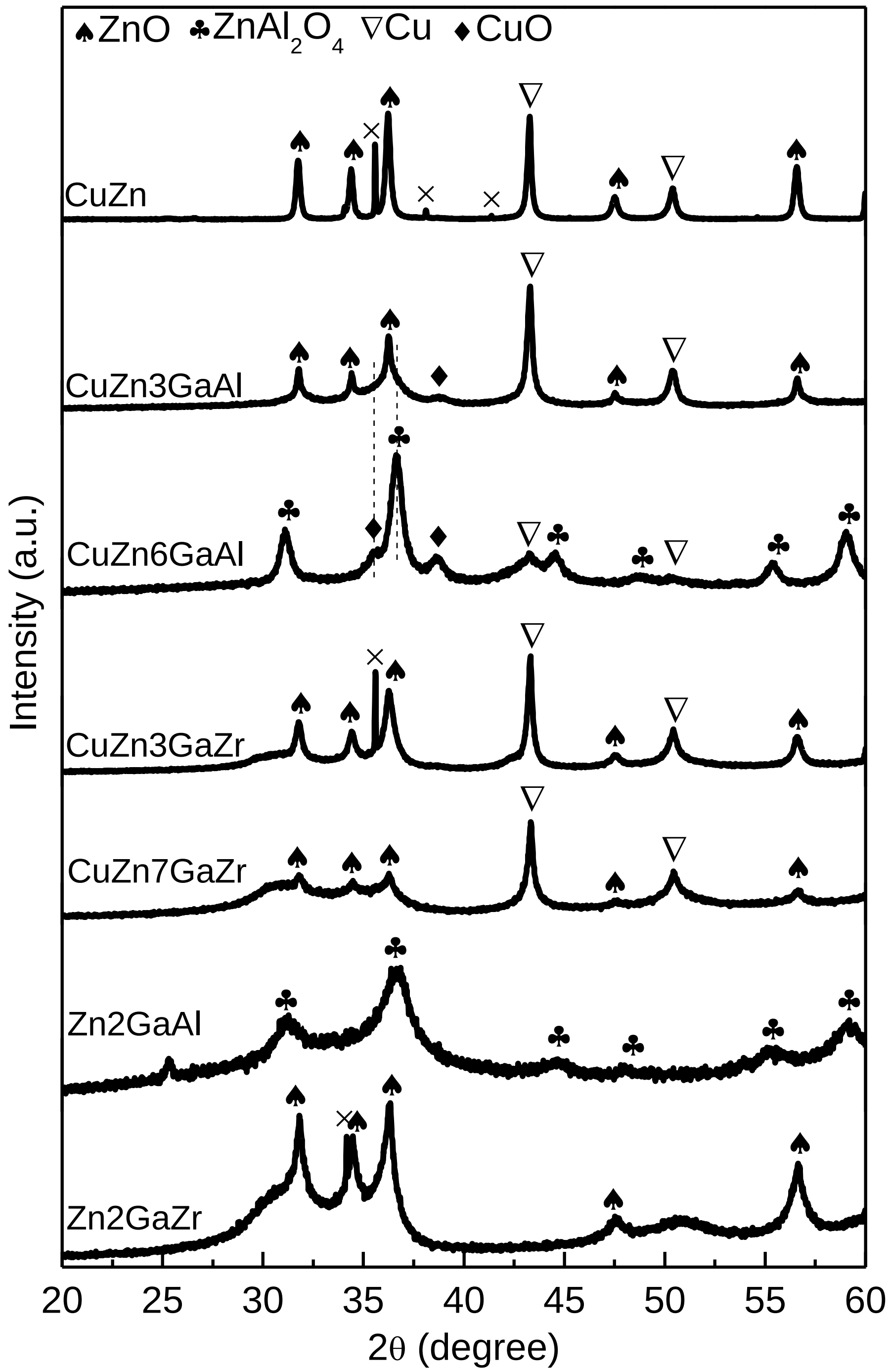

Figure 3.13. XRD patterns of post-reaction catalysts. "×" corresponds to SiC impurity used as a diluent in the catalytic tests. Reaction conditions: T=250-270 °C, P=3 MPa, $CO_2/H_2/N_2$=1/3/1, GHSV=3000 h^{-1}.

The estimated crystallite sizes of Cu^0 and ZnO are compiled in Table 3.7. There are no large differences in the crystallite sizes of Cu and ZnO between the post-reaction catalysts and those of the corresponding reduced catalysts (Table 3.2).

Table 3.7. Crystallite sizes of Cu^0 and ZnO in post-reaction catalysts determined by XRD. Reaction conditions: T=250-270 °C, P=3 MPa, $CO_2/H_2/N_2=1/3/1$, GHSV=3000 h^{-1}.

Catalyst	**d_{Cu} (nm)**	**d_{ZnO} (nm)**
CuZn	39.4	34.2
CuZn3GaAl	27.9	33.4
CuZn6GaAl	n.d.	(14.6)[a]
CuZn3GaZr	31.5	23.8
CuZn7GaZr	29.5	23.0

[a] $ZnAl_2O_4$ phase.
n.d. not determined

Effect of the GHSV on the RWGS reaction

As was previously pointed out, the highest CO_2 conversion (11.2%) and CO production (17047 mmol/Kg•h) were obtained over the CuZn3GaZr catalyst at 270 °C and 3 MPa. The CuZn3GaZr sample was used to study the effect of contact time on the RWGS reaction and to investigate the relationship between CO formation and methanol synthesis under the reaction conditions used.

A new experiment was carried out by varying the GHSV from 10000 h^{-1} up to 48000 h^{-1} at 270 °C under a total pressure of 3 MPa. The obtained CO_2 conversion and corresponding CO and methanol selectivities as a function of GHSV are shown in Figure 3.14.

Under the experimental conditions used, CO_2 reduction by H_2 mainly produced CO through the RWGS reaction. The values of CO_2 conversion highly changed with the change of the contact time; CO_2 conversion increased from 5.5 to 12.6% with the increase of contact time.

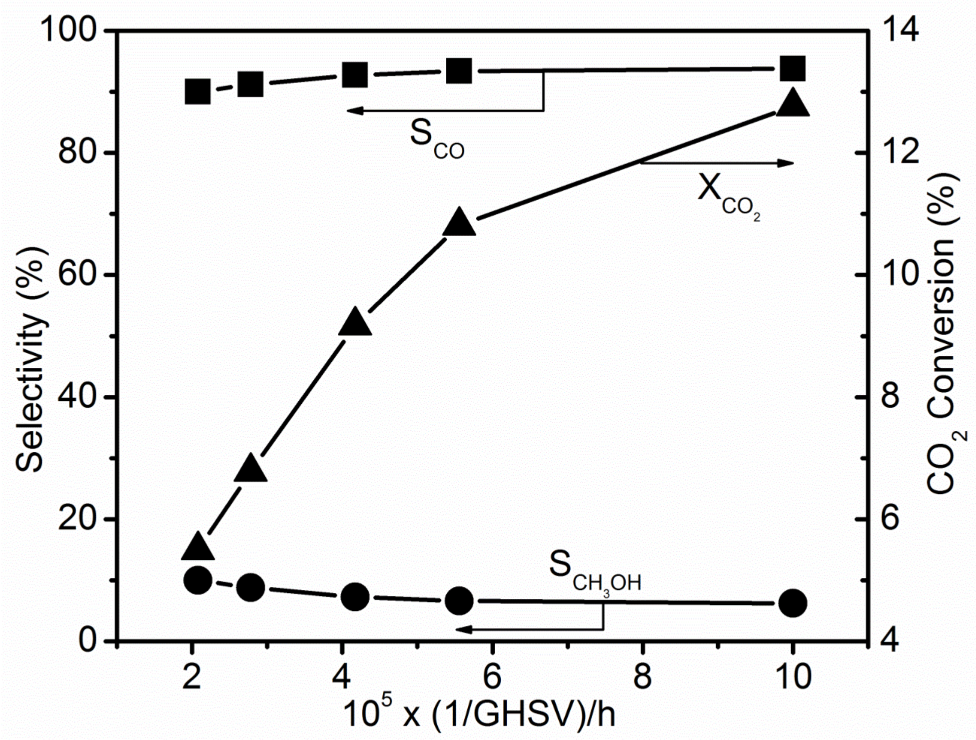

Figure 3.14. Effect of the GHSV on CO_2 conversion (X_{CO_2}), and CO (S_{CO}) and CH_3OH (S_{CH_3OH}) selectivity over the CuZn3GaZr catalyst. Reaction conditions: T=270 °C, P=3 MPa, GHSV=10000-48000 h^{-1}, $CO_2/H_2/N_2$=1/3/1.

However, only a slight change in CO and methanol selectivity was observed. These results suggest that CO and methanol are primary products formed through independent reaction pathways [5].

CO formation: $CO_2+H_2\leftrightarrow CO+H_2O$ (3.3)

Methanol synthesis: $CO_2+3H_2\leftrightarrow CH_3OH+H_2O$ (3.4)

However, we could not discard that a small fraction of CO formed could come from the decomposition of methanol.

$$CH_3OH \rightarrow CO+2H_2 \qquad (3.5)$$

Simultaneous formation of CO and CH_3OH has been previously observed on Cu-ZnO-ZrO_2 catalysts [38]. Competitive elementary steps have been also proposed for the parallel formation of CO and methanol in the CO_2 hydrogenation over Cu-ZnO-based catalysts [39,40]. Recently, H/D exchange experiments have been performed on Cu-based catalysts, results suggested that methanol synthesis and RWGS reaction take place via parallel pathways involving different intermediates and surface sites [41]; as stated in the Introduction section, RWGS reaction over Cu-based catalysts more likely proceeds through the surface redox mechanism [42, 43].

Effect of the reaction pressure on the RWGS reaction

Besides the influence of the contact time, the effect of total pressure on the RWGS reaction was also studied over the CuZn3GaZr catalyst. The experiment was performed at a constant GHSV of 3000 h^{-1}, a temperature of 270 °C and pressure of 3-0.1 MPa. Figure 3.15 shows CO_2 conversion and selectivities to CO and CH_3OH as a function of the total pressure used. As expected, the decrease of total pressure reduced CO_2 conversion from 10.7% (at 3 MPa) to 5.2% (at 0.1 MPa). Meanwhile, CH_3OH selectivity decreased significantly from 6.7% (3 MPa) to 0.4% (0.1 MPa) with the decreasing of pressure; this catalytic behaviour corresponds well with the equilibrium shift of the CH_3OH formation (Eq. 3.4) when the pressure decreases. Under these conditions, CH_4 selectivity was always below 0.2%.

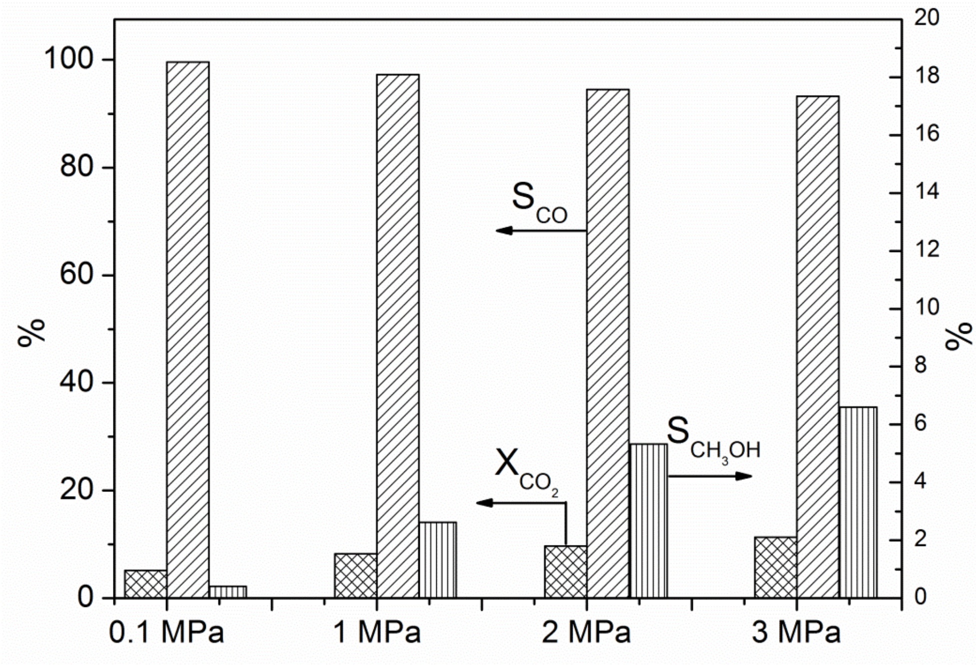

Figure 3.15. CO_2 conversion (▩), and CO (▨) and CH_3OH (▥) selectivity values as a function of reaction pressure (0.1-3 MPa) over the CuZn3GaZr catalyst. T=270 °C, GHSV=3000 h^{-1}, $CO_2/H_2/N_2$=1/3/1.

Finally, the catalytic behaviour of CuZn3GaZr in the RWGS was studied at atmospheric pressure in the range 275-325 °C under GHSV of 3000 h^{-1}. Before switching to the reactant mixture, the sample was in-situ reduced in a H_2/Ar (12% vol/vol) flow at 325 °C for 3 h under atmospheric pressure. Then the RWGS was studied following the sequence: 325 °C (3h)→300 °C (3h)→275 °C (3h). Table 3.8 shows the CO_2 conversion and selectivity values of products as a function of temperature. Both CO_2 conversion and CO yield increased significantly when the temperature increased from 275 to 325 °C. CO selectivity was 99.7-99.8% in the mentioned range of temperatures. At temperatures higher than 275 °C, negligible selectivity to methanol was obtained and only a small amount of CH_4 was found ($S_{CH_4} \leq 0.3\%$).

Table 3.8. Catalytic behaviour of CuZn3GaZr in the RWGS reaction. Reaction conditions: GHSV=3000 h^{-1}, $CO_2/H_2/N_2$=1/3/1, T=275-325 °C, P=0.1 MPa.

T(°C)	CO_2 conversion (%)	CO yield mmol/Kg_{cat}•h	Selectivity (%)		
			CO	CH_3OH	CH_4
325	16.8	27415	99.7	<0.01	0.3
300	9.6	15612	99.8	<0.02	0.2
275	4.6	7472	99.7	0.2	0.1

For CO production, the estimated apparent activation energy (Ea) from Arrhenius plot (Figure 3.16) was 70.9±3.7 kJ/mol. This value is similar to that previously reported for $CuZrO_2CeO_2$ catalysts with similar Cu content [44]. For Cu/ZnO-Al and Cu/ZnO-Ga catalysts with a lower Cu content (approx. 10 wt%) and prepared by impregnation, apparent Ea value of 112 kJ/mol in the 190-250 ºC range has been recently reported [45].

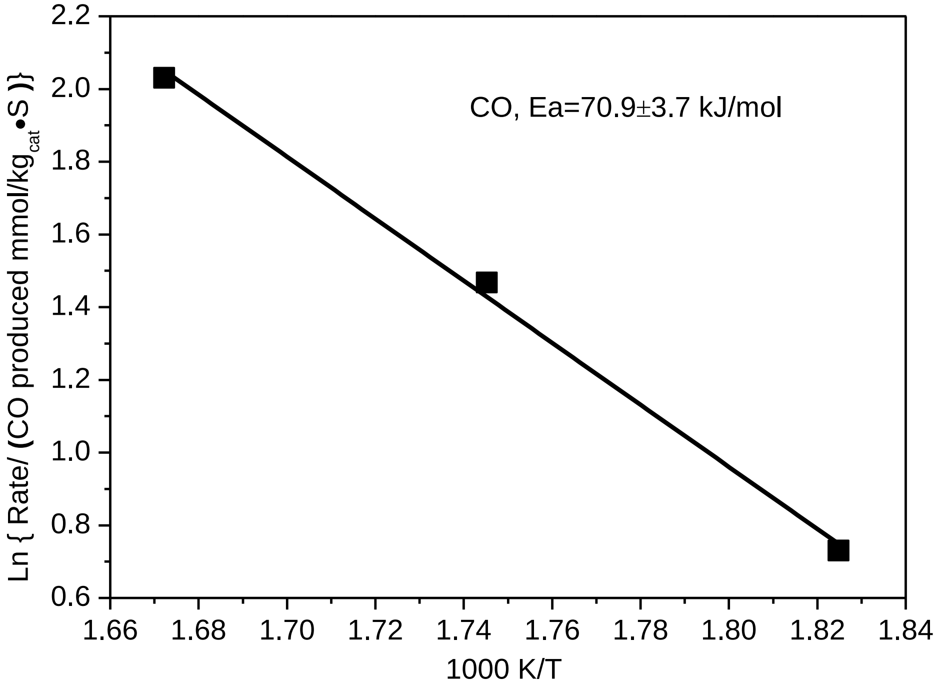

Figure 3.16. Arrhenius plot of CO production over CuZn3GaZr at 275-325 °C. Reaction conditions: GHSV=3000 h^{-1}, $CO_2/H_2/N_2$=1/3/1, P=0.1 MPa.

3.3.2 RWGS reaction over xRuCuZnGaZr catalysts

As mentioned above, xRuCuZnGaZr catalysts based on CuZn3GaZr and containing 0.2-2.0 Ru wt% were also tested in the CO_2 reduction by H_2 ($CO_2/H_2/N_2$=1/3/1) at 3 MPa and GHSV of 3000 h^{-1} in the range of 250-270 °C; the sequence of reaction temperature was 250 °C (3h)→260 °C (3h)→270 °C (3h)→250 °C (3h). Prior to reaction, the samples were in-situ reduced at 270 °C for 5 h. Lee et al. [46] have studied the CO_2 and CO hydrogenation over Ru-modified $Cu/ZnO/Al_2O_3$ catalysts (2 wt%) at 250 °C and 3 MPa; only CO and CH_3OH were found when a $H_2/CO_2=4$ (molar ratio) mixture was used; the CO_2 conversion showed only a slight increase from 7.0 to 7.4% with the presence of Ru on $Cu/ZnO/Al_2O_3$, but the methanol yield enhanced [46].

Under our conditions, xRuCuZnGaZr catalysts showed lower values of CO_2 conversion than CuZn3GaZr. Moreover, a slight decrease of CO_2 conversion was found when the temperature returned back to 250 °C after 12 h of reaction, compared with the initial CO_2 conversion at this temperature.

Table 3.9 compiles CO_2 conversion and selectivity values to CO, methanol and methane. The highest CH_3OH selectivity (35.0%) was found for 0.2RuCuZnGaZr catalyst at 250 °C under 1.8% CO_2 conversion; as expected, the selectivity to methanol decreased when the temperature increased. However, it is difficult to compare the selectivity values of xRuCuZnGaZr and CuZn3GaZr due to the difference in the CO_2 conversion.

CO and CH_3OH were the main products for 0.2RuCuZnGaZr, 0.4RuCuZnGaZr and 0.7RuCuZnGaZr catalysts, only very small amounts of CH_4 (<0.5%) were observed. Only over 2.0RuCuZnGaZr, a significant amount of CH_4 was obtained under the conditions used. The low CH_4 selectivity obtained over xRuCuZnGaZr ($x \leq 0.7$) catalysts can be related to the presence of highly dispersed Ru on the catalysts [47].

Table 3.9. Catalytic behaviour of xRuCuZnGaZr samples in RWGS reaction. Reaction conditions: GHSV=3000 h^{-1}, $CO_2/H_2/N_2$=1/3/1, P=3 MPa.

Catalyst	T(°C)	CO_2 conversion (%)	CO yield mmol/Kg_{cat}•h	Selectivity (%) CO	CH_3OH	CH_4
0.2RuCuZnGaZr	250	1.8	1890	64.7	35.0	0.3
	260	2.4	2809	71.7	27.9	0.4
	270	3.2	4103	77.4	22.1	0.5
0.4RuCuZnGaZr	250	3.7	4969	81.0	19.0	0.1
	260	5.0	7004	85.5	14.4	0.1
	270	6.7	9864	89.3	10.6	0.1
0.7RuCuZnGaZr	250	2.8	3408	74.5	25.4	0.1
	260	3.3	4208	78.2	21.7	0.1
	270	4.1	5504	82.2	17.7	0.1
2.0RuCuZnGaZr	250	1.5	1086	44.9	28.1	27.0
	260	1.6	1186	45.4	25.9	28.7
	270	2.1	1743	51.0	21.6	27.4
CuZn3GaZr	250	6.5	9226	87.1	12.7	0.2
	260	7.9	11635	89.7	10.1	0.1
	270	11.2	17047	93.0	6.9	0.1

3.4. Methanol steam reforming over CuOZnO-based catalysts

Calcined CuZn, CuZn10Ga, CuZn1GaAl, CuZn12GaAl, CuZn3GaZr and CuZn7GaZr catalysts were studied in the MSR reaction (Eq. 1.18) under atmospheric pressure and a GHSV of about 2200 h^{-1}. The sieved samples (0.2-0.4 mm, diameter) were diluted with inactive SiC to reach a catalytic bed of 1 mL; different amounts of calcined samples (75-300 mg) were used to keep the conversion of CH_3OH below the 100% under the conditions used. Firstly, the temperature was increased up to 275 °C at 2 °C/min under a He flow. The MSR reaction was tested under stoichiometric H_2O/CH_3OH=1 at 275 °C for 44 h and then, the temperature was decreased to 250 °C and the reaction kept under these conditions for 6 h.

All of catalysts showed similar distribution of products at both temperatures 275 °C and 250 °C; H_2 and CO_2 were the main products being in all cases the H_2/CO_2 molar ratio close to the expected stoichiometric value of 3. Small amounts of CO were detected as by-product; its molar fraction in the product was always lower than 0.6%.

The H_2 production rate obtained at 275 °C as a function of reaction time is shown in Figure 3.17; meanwhile, the initial and final CH_3OH conversion achieved under the experimental conditions used are listed in Table 3.10.

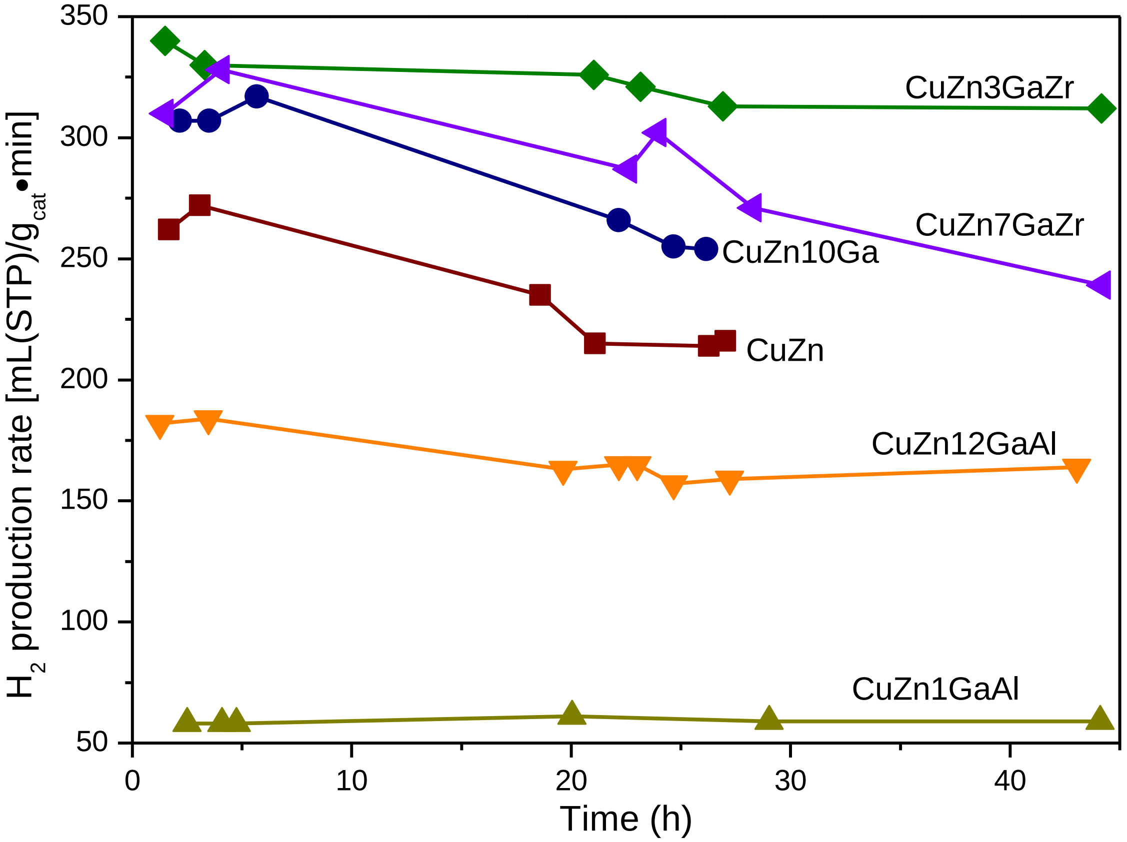

Figure 3.17. H_2 production rate as a function of reaction time during the MSR. Reaction conditions: T=275 °C, GHSV=2200 h^{-1}, $CH_3OH/H_2O/N_2$=1/1/1.3 molar ratio, P=0.1 MPa.

CuZn10Ga showed higher H_2 production rate than the bare CuZn catalyst, and lower than CuZnxGaZr samples. CuZnxGaAl samples resulted in a relatively low catalytic activity, but showed higher stability than CuZn and CuZn10Ga under the reaction conditions used. Under our reaction conditions, the CuZn3GaZr catalyst showed the highest H_2 production rate during the time on stream; the H_2 production rate at the final stage of reaction was about 312 $mL/g_{cat}\bullet min$. Moreover, CuZn3GaZr was more stable than CuZn7GaZr; for CuZn7GaZr catalyst, the conversion of CH_3OH decreased from 75 to 57% after approximately 44 h in MSR reaction at 275 °C, whereas only a deactivation of 8.5% was observed for CuZn3GaZr.

Table 3.10. Initial and final (44 h) CH_3OH conversion of CuZnxGaM (M=Al, Zr) catalysts. Reaction conditions: T=275 °C, GHSV=2200 h^{-1}, $CH_3OH/H_2O/N_2$=1/1/1.3 molar ratio, P=0.1 MPa, catalysts=75-300 mg.

Catalyst	**CH_3OH conversion (%)**	
	Initial	**Final (44 h)**
CuZn	63	52
CuZn10Ga	74	60
CuZn1GaAl	57	57
CuZn12GaAl	88	79
CuZn3GaZr	82	75
CuZn7GaZr	75	57

As stated above, after the study of MSR at 275 °C, the reaction temperature was decreased to 250 °C, the corresponding initial and final hydrogen production rate, as well as the CO concentration and CH_3OH conversion obtained over CuZnxGaM (M=Al, Zr) are shown in Table 3.11. The MSR reaction was maintained about 6 h at 250 °C.

Table 3.11. H_2 production rate, CO molar fraction in product and CH_3OH conversion during the MSR over CuZnxGaM (M=Al, Zr) catalysts at 250 °C. These measurements were done after 44 h at 275 °C under MSR. Reaction conditions: T=250 °C, GHSV=2200 h^{-1}, $CH_3OH/H_2O/N_2$=1/1/1.3 molar ratio, P=0.1 MPa, catalysts=75-300 mg.

Catalyst	**H_2 production rate mL(STP)/g_{cat}•min**		**χ_{CO} (%)**	**CH_3OH conversion (%)**
	Initial	**Final**		
CuZn1GaAl	31	30(6h)	0.5	29.2(6h)
CuZn12GaAl	90	89(6h)	0.3	43.1(6h)
CuZn3GaZr	173	177(6h)	0.3	42.9(6h)
CuZn7GaZr	139	125(5h)	0.4	30.3(5h)

CuZnxGaZr catalysts also showed a higher catalytic activity in MSR reaction at 250 °C when compared with CuZnxGaAl. In all cases, the value of CO molar concentration at 250 °C was lower than that obtained at 275 °C, indicating that CO formation could result from the RWGS reaction.

As discussed above, the catalysts prepared in this work are highly active for the RWGS reaction. The higher catalytic activity in the MSR of CuZnxGaZr when compared with CuZnxGaAl could be related with the higher reducibility of the CuZnxGaZr catalysts which can help to maintain the active site of Cu during the MSR reaction. Furthermore, the characterization by N_2O chemisorption and XPS indicated the presence of a high amount of surface Cu and interfacial oxygen vacancies on CuZnxGaZr.

Characterization of post-reaction catalysts

After the MSR catalytic tests, the samples were characterized by XRD, Raman spectroscopy, TPO and DRIFTS.

The XRD patterns of the catalysts after MSR reaction are shown in Figure 3.18. In all cases, the characteristic peaks of Cu^0 (111) and Cu^0 (200) at 2θ=43.3°

and 50.4°, respectively, can be observed. Meanwhile, except for CuZn10Ga catalyst, the most intense diffraction peak of CuO was still visible at $2\theta=38.8°$. For CuZnxGaAl catalysts, the peaks centered at $2\theta=31.2$, 36.8, 44.6, 55.7 and 59.3° were ascribed to the $ZnAl_2O_4$ crystalline phase, as has been already proposed for the calcined catalysts. Moreover, for the post-reaction CuZn1GaAl, the presence of a small peak located at $2\theta=42.3°$ fitted well with the (200) diffraction line of Cu_2O (JCPDS 01-078-2076).

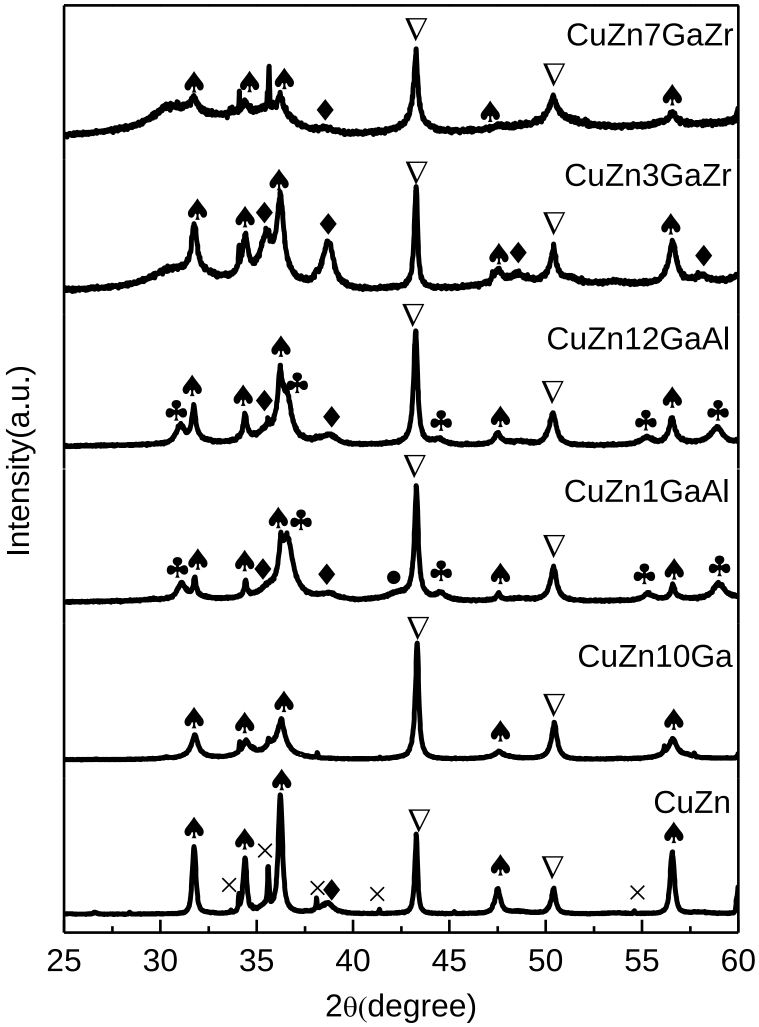

Figure 3.18. XRD patterns of catalysts after MSR reaction. (♠) ZnO; (♣) $ZnAl_2O_4$; (∇) Cu; (•) Cu_2O; (♦) CuO. Reaction conditions: T=250 °C, GHSV=2200 h^{-1}, $CH_3OH/H_2O/N_2=1/1/1.3$ molar ratio, P=0.1 MPa, catalysts=75-300 mg.

For all post-reaction catalysts, the crystallite size of Cu^0 was calculated using the Debye-Scherrer equation and the XRD peak at $2\theta=43.3°$. The values of Cu^0 crystallite size were 54 nm (CuZn), 42 nm (CuZn10Ga), 40 nm (CuZn1GaAl), 39 nm (CuZn12GaAl), 39 nm (CuZn3GaZr) and 40 nm (CuZn7GaZr), respectively. The bare CuZn catalyst resulted in a higher Cu^0 crystallite size than that of other catalysts containing Ga_2O_3 and Al_2O_3 or ZrO_2 components, which could play a textural promoter role. The crystallization of the Cu species could be restricted in these multicomponent systems due to interfacial contact [48].

Raman spectroscopy was performed to study the carbon deposits of the post-reaction catalysts. Carbon deposits generally present two specific Raman bands at about 1340 cm^{-1} (D band), which is characteristic for poorly structured carbonaceous deposits, and 1580 cm^{-1} (G band), which is assigned to well-structured carbon deposits [49]. Figure 3.19 shows the Raman spectra of post-reaction catalysts in the 1100-1700 cm^{-1} region, in which both D and G bands could be found.

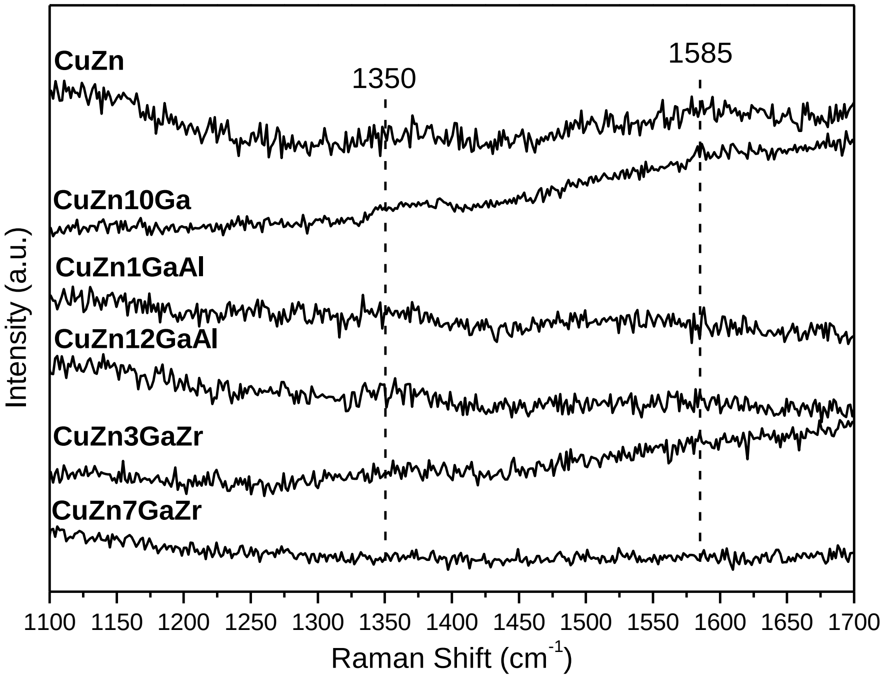

Figure 3.19. Raman spectra of catalysts after MSR reaction.

Raman spectra of post-reaction catalysts do not show significant bands related with the presence of carbonaceous deposits. Moreover, TPO analysis followed by TG-MS of post-reaction catalysts only show the evolution of reactant species and a very small amount of CO_2 at temperatures lower than 250 °C, this confirmed the formation of a negligible amount of carbon deposits during the MSR catalytic test.

Used catalysts were also studied by DRIFTS-MS. Post-reaction catalysts were in-situ treated in the DRIFTS chamber under He flow up to 250 °C, until no evolution of adsorbed products was detected. The temperature was then cooled down to 25 °C, and the spectra were registered. The corresponding DRIFT spectra in the 1750-1250 cm^{-1} region, in which the characteristic infrared absorptions of carboxylate and carbonate species are expected, are shown in Figure 3.20A.

In all cases, broad bands with different relative maxima in the 1600-1350 cm^{-1} region were obtained. Some differences can be observed in this region; for post-reaction CuZn7GaZr, CuZn and CuZn10Ga catalysts, a band at about 1595 cm^{-1} could be reasonably related to the ν_{as}(COO) of formate species over ZnO and/or Ga_2O_3, while the ν_s(COO) vibration mode could be present below 1400 cm^{-1} [50]. For post-reaction CuZn7GaZr, the band at 1595 cm^{-1} was more visible (Figure 3.20A), indicating the presence of more abundant formate species on ZnO and/or Ga_2O_3 components, and this may be related with the observed progressive deactivation of this catalyst. For Cu/ZnO and Cu-Ga/ZnO systems after MSR reaction, bands at 1605-1533 cm^{-1}, 1379-1351 cm^{-1} and 1385-1380 cm^{-1} have been assigned to the ν_{as}(COO), ν_s(COO) and δ(CH) of different surface formate species [50]. In our case, the presence of different formate species was confirmed by the ν(C-H) vibrations observed in 2975-2840 cm^{-1} region (Figure 3.20B). Moreover, as shown in Figure 3.20B, a very low intensity band at about 2727 cm^{-1} which could be attributed to the characteristic ν(C-H) of adsorbed formaldehyde [51,52], was also visible in the spectrum of CuZn10Ga catalyst. According to the above discussion, we propose the presence of different surface formate species on CuZnxGaM (M=Al, Zr) post-reaction systems. However, the specific assignation of the bands is not straightforward and the simultaneous presence of surface carbonates species cannot be ruled out; the ν_3 vibration mode of free CO_3^{2-} ion can give an infrared band at about 1440 cm^{-1}.

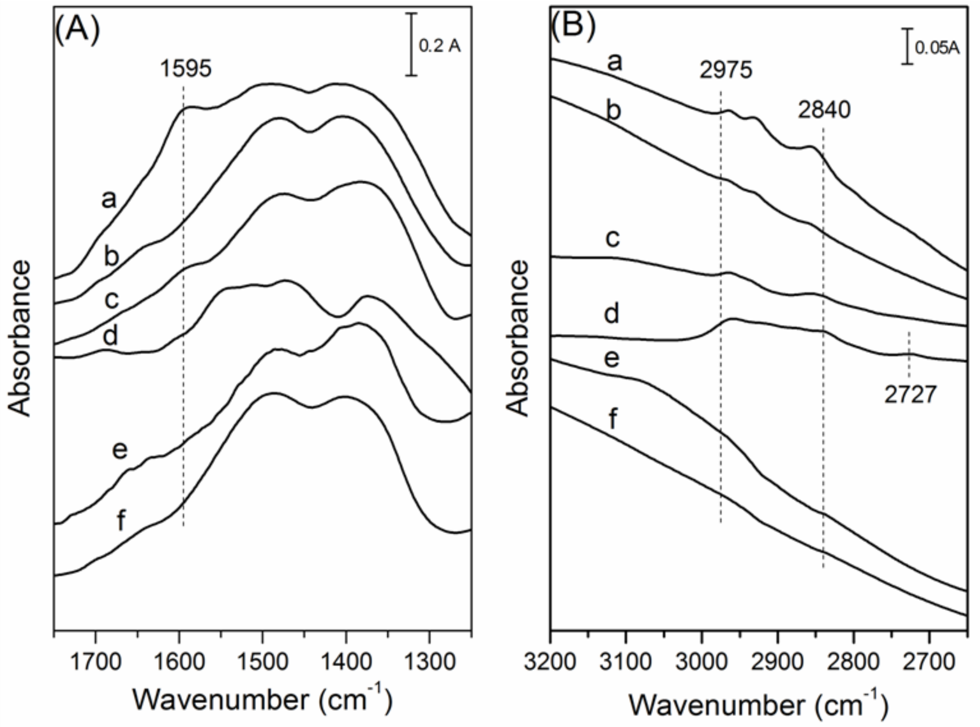

Figure 3.20. DRIFT spectra of post-reaction MSR catalysts, registered at 25 °C previous He treatment at 250 °C. (A) 1750-1250 cm^{-1} region; (B) 3200-2650 cm^{-1} region; (a) CuZn7GaZr; (b) CuZn3GaZr; (c) CuZn; (d) CuZn10Ga; (e) CuZn12GaAl; (f) CuZn1GaAl.

The post-reaction catalysts were further characterized by CO chemisorption followed by in-situ DRIFTS. Prior to CO adsorption, the post-reaction catalysts were also in-situ treated in the DRIFTS chamber under a He flow up to 250 °C, until no evolution of adsorbed products was detected. The temperature was then cooled down to 25 °C under He flow. After, the sample was exposed to a CO/He

(10% vol/vol) mixture at 25 °C for 20 min. Then, the flow was switched to He, and the final spectrum was registered at 25 °C. The spectra were obtained at a resolution of 4 cm^{-1} by collecting 256 scans. The corresponding spectra registered in the ν(CO) region for all the catalysts are shown in Figure 3.21.

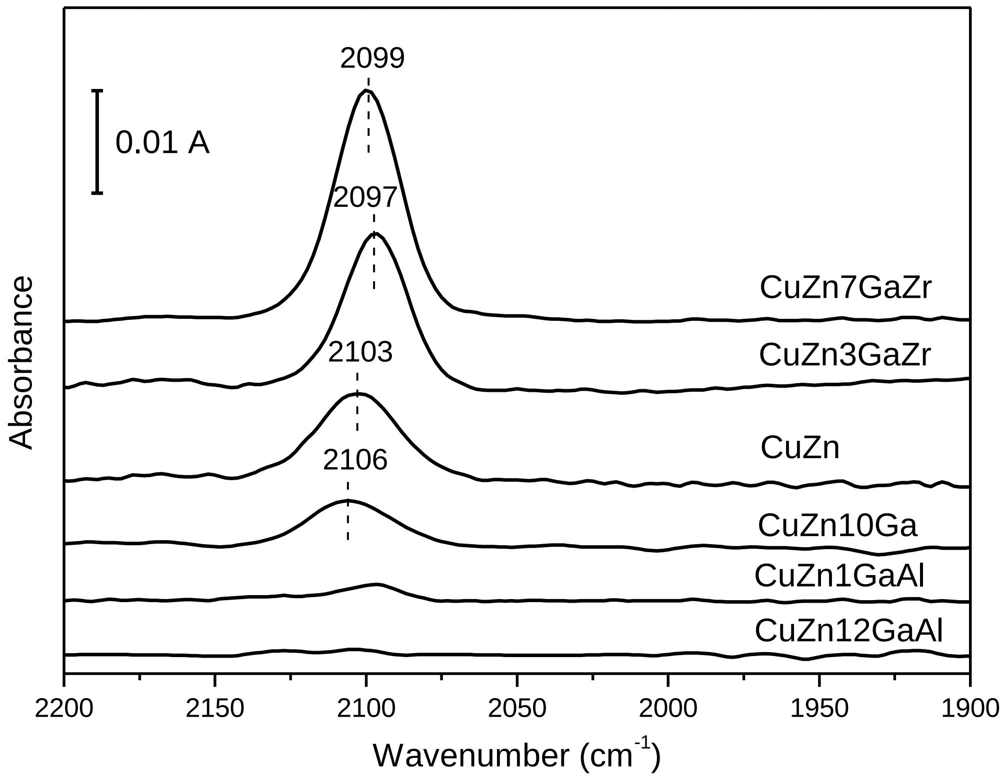

Figure 3.21. DRIFT spectra of post-reaction MSR catalysts after CO chemisorption at 25 °C.

Bands between 2150 and 2075 cm^{-1} could be related to the coordination of CO on Cu sites [53]. CuZn1GaAl and CuZn12GaAl which showed a lower activity, showed very low intensity ν(CO) bands, indicating the presence of a lower number of available Cu species on the surface of these two catalysts than on the remaining catalysts.

For CuZn and CuZn10Ga, the observed broad band can be related to the contribution of CO coordinated to different Cu sites with different oxidation states;

after MSR, Cu^{2+}, Cu^+ and Cu^0 species may co-exist on the surface of CuZn and CuZn10Ga; a ν(CO) band at 2106 cm^{-1} has been related to the presence of Cu^+ species [50,53]. For CuZn7GaZr and CuZn3GaZr, a more intense and clear band was observed at 2099-2097 cm^{-1}, this band was attributed to the CO coordination on metallic Cu sites [50,53], indicating the main presence of Cu^0 on the surface of the catalysts. As discussed above, CuO present in CuZnxGaZr catalysts can be easily reduced to metallic Cu at low temperature, which favouring the performance of these systems under the MSR used.

3.5 References

[1] Mathew T, Sivaranjani K, Gnanakumar ES, Yamada Y, Kobayashi T, Gopinath CS. γ-$Al_{2-x}M_xO_{3\pm y}$ (M=Ti^{4+} through Ga^{3+}): potential pseudo-3D mesoporous materials with tunable acidity and electronic structure. J. Mater. Chem. 2012;22:13484-13493.

[2] Barroso MN, Gomez MF, Gamboa JA, Arrúa LA, Abello MC. Preparation and characterization of CuZnAl catalysts by citrate gel process. J. Phys. Chem. Solids. 2006;67:1583-1589.

[3] Jacob K, Alcock C. Thermodynamics of $CuAlO_2$ and $CuAl_2O_4$ and phase equilibria in the system Cu_2O-CuO-Al_2O_3. J. Am. Ceram. Soc. 1975;58:192-195.

[4] Wei X, Chen D. Synthesis and characterization of nanosized zinc aluminate spinel by sol-gel technique. Mater. Lett. 2006;60:823-827.

[5] Liu X, Ramírez de La Piscina P, Toyir J, Homs N. CO_2 reduction over Cu-ZnGaMO (M=Al, Zr) catalysts prepared by a sol-gel method: Unique performance for the RWGS reaction. Catal. Today. 2017;296:181-186.

[6] Yermán L, Homs N, de la Piscina PR. Hydrogen production from oxidative steam-reforming of n-propanol over Ni/Y_2O_3-ZrO_2 catalysts. Int. J. Hydrogen Energy. 2012;37:7094-7100.

[7] Wang W, Zhou Q, Fei X, He Y, Zhang P, Zhang G, Peng L, Xie W. Synthesis of CuO nano-and micro-structures and their Raman spectroscopic studies. CrystEngComm. 2010;12:2232-2237.

[8] Xu J, Ji W, Shen Z, Li W, Tang S, Ye X, Jia D, Xin X. Raman spectra of CuO nanocrystals. J. Raman Spectrosc. 1999;30:413-415.

[9] Jin Y, Cui Q, Wen G, Wang Q, Hao J, Wang S, et al. XPS and Raman scattering studies of room temperature ferromagnetic ZnO: Cu. J. Phys. D: Appl. Phys. 2009;42:215007.

[10] Damen TC, Porto S, Tell B. Raman effect in zinc oxide. Phys. Rev. 1966;142:570-574.

[11] Gao Y, Bando Y, Sato T, Zhang Y, Gao X. Synthesis, Raman scattering and defects of β-Ga_2O_3 nanorods. Appl. Phys. Lett. 2002;81:2267-2269.

[12] Wang L-C, Liu Q, Chen M, Liu Y-M, Cao Y, He H-Y, Fan K-N. Structural evolution and catalytic properties of nanostructured Cu/ZrO_2 catalysts prepared by oxalate gel-coprecipitation technique. J. Phys. Chem. C. 2007;111:16549-16557.

[13] Xie S, Iglesia E, Bell AT. Water-assisted tetragonal-to-monoclinic phase transformation of ZrO_2 at low temperatures. Chem. Mater. 2000;12:2442-2447.

[14] Liu X, Toyir J, Ramírez de La Piscina P, Homs N. Hydrogen production from methanol steam reforming over Al_2O_3- and ZrO_2-modified CuOZnOGa_2O_3 catalysts. Int. J. Hydrogen Energy. 2017;42:13704-13711.

[15] Agrell J, Birgersson H, Boutonnet M, Melián-Cabrera I, Navarro R, Fierro JLG. Production of hydrogen from methanol over Cu/ZnO catalysts promoted by ZrO_2 and Al_2O_3. J. Catal. 2003;219:389-403.

[16] Jones SD, Hagelin-Weaver HE. Steam reforming of methanol over CeO_2-and ZrO_2-promoted Cu-ZnO catalysts supported on nanoparticle Al_2O_3. Appl. Catal. B: Environ. 2009;90:195-204.

[17] Jeong H, Kim KI, Kim TH, Ko CH, Park HC, Song IK. Hydrogen production by steam reforming of methanol in a micro-channel reactor coated with Cu/ZnO/ZrO_2/Al_2O_3 catalyst. J. Power Sources. 2006;159:1296-1299.

[18] Lindström B, Pettersson LJ, Govind Menon P. Activity and characterization of Cu/Zn, Cu/Cr and Cu/Zr on γ-alumina for methanol reforming for fuel cell vehicles. Appl. Catal. A: Gen. 2002;234:111-125.

[19] Fichtl MB, Schumann J, Kasatkin I, Jacobsen N, Behrens M, Schlögl R, Muhler M, Hinrichsen O. Counting of oxygen defects versus metal surface sites in methanol synthesis catalysts by different probe molecules. Angew. Chem. Int. Ed. 2014;53:7043-7047.

[20] Xiao J, Mao D, Guo X, Yu J. Effect of TiO_2, ZrO_2, and TiO_2-ZrO_2 on the performance of CuO-ZnO catalyst for CO_2 hydrogenation to methanol. Appl. Surf. Sci. 2015;338:146-153.

[21] Mathew T, Yamada Y, Ueda A, Shioyama H, Kobayashi T. Metal oxide catalysts for DME steam reforming: Ga_2O_3 and Ga_2O_3-Al_2O_3 catalysts with and without copper. Appl. Catal. A: Gen. 2005;286:11-22.

[22] Ladera R, Pérez-Alonso FJ, González-Carballo JM, Ojeda M, Rojas S, Fierro JLG. Catalytic valorization of CO_2 via methanol synthesis with Ga-promoted Cu-ZnO-ZrO_2 catalysts. Appl. Catal. B: Environ. 2013;142:241-248.

[23] Gogurla N, Sinha AK, Santra S, Manna S, Ray SK. Multifunctional Au-ZnO plasmonic nanostructures for enhanced UV photodetector and room temperature NO sensing devices. Scientific reports. 2014;4.

[24] Velu S, Suzuki K, Gopinath CS, Yoshida H, Hattori T. XPS, XANES and EXAFS investigations of CuO/ZnO/Al_2O_3/ZrO_2 mixed oxide catalysts. Phys. Chem. Chem. Phys. 2002;4:1990-1999.

[25] Grohmann I, Peplinski B, Unger W. New entries in the XPS fingerprint database for the characterization of precipitated Cu-Zn-Al oxide catalysts. Surf. Interface Anal. 1992;19:591-594.

[26] Okal J, Tylus W, Kępiński L. XPS study of oxidation of rhenium metal on γ-Al_2O_3 support. J. Catal. 2004;225:498-509.

[27] Chen H, Hu J, Li G-D, Gao Q, Wei C, Zou X. Porous Ga-In bimetallic oxide nanofibers with controllable structures for ultrasensitive and selective detection of formaldehyde. ACS Appl. Mater. Interfaces. 2017;9:4692-4700.

[28] Hattori H. Heterogeneous basic catalysis. Chem. Rev. 1995;95:537-558.

[29] Schittkowski J, Buesen D, Toelle K, Muhler M. The temperature-programmed desorption of H_2 from Cu/ZrO_2. Catal. Lett. 2016;146:1011-1017.

[30] Waugh K. The absorption and locking-in of hydrogen in copper. Solid State Ionics. 2004;168:327-342.

[31] Arena F, Italiano G, Barbera K, Bordiga S, Bonura G, Spadaro L, Frusteri F. Solid-state interactions, adsorption sites and functionality of Cu-ZnO/ZrO_2 catalysts in the CO_2 hydrogenation to CH_3OH. Appl. Catal. A: Gen. 2008;350:16-23.

[32] Gao P, Li F, Zhao N, Xiao F, Wei W, Zhong L, Sun Y. Influence of modifier (Mn, La, Ce, Zr and Y) on the performance of Cu/Zn/Al catalysts via hydrotalcite-like precursors for CO_2 hydrogenation to methanol. Appl. Catal. A: Gen. 2013;468:442-452.

[33] Collins SE, Baltanás MA, Bonivardi AL. Hydrogen chemisorption on gallium oxide polymorphs. Langmuir. 2005;21:962-970.

[34] Chang C-C, Hsu C-C, Chang C-T, Chen Y-P, Liaw B-J, Chen Y-Z. Effect of noble metal on oxidative steam reforming of methanol over CuO/ZnO/Al_2O_3 catalysts. Int. J. Hydrogen Energy. 2012;37:11176-11184.

[35] Mierczynski P. Comparative studies of bimetallic Ru-Cu, Rh-Cu, Ag-Cu, Ir-Cu catalysts supported on ZnO-Al_2O_3, ZrO_2-Al_2O_3 systems. Catal. Lett. 2016;146:1825-1837.

[36] Soares AV, Salazar JB, Falcone DD, Vasconcellos FA, Davis RJ, Passos FB. A study of glycerol hydrogenolysis over Ru-Cu/Al_2O_3 and Ru-Cu/ZrO_2 catalysts. J. Mol. Catal. A: Chem. 2016;415:27-36.

[37] Galván CÁ, Schumann J, Behrens M, Fierro JLG, Schlögl R, Frei E. Reverse water-gas shift reaction at the Cu/ZnO interface: Influence of the Cu/Zn ratio on structure-activity correlations. Appl. Catal. B: Environ. 2016;195:104-111.

[38] Bonura G, Cordaro M, Cannilla C, Arena F, Frusteri F. The changing nature of the active site of Cu-Zn-Zr catalysts for the CO_2 hydrogenation reaction to methanol. Appl. Catal. B: Environ. 2014;152:152-161.

[39] Sun Q, Zhang Y-L, Chen H-Y, Deng J-F, Wu D, Chen S-Y. A novel process for the preparation of Cu/ZnO and Cu/ZnO/Al_2O_3 ultrafine catalyst: structure, surface properties, and activity for methanol synthesis from CO_2+H_2. J. Catal. 1997;167:92-105.

[40] Saito M, Fujitani T, Takeuchi M, Watanabe T. Development of copper/zinc oxide-based multicomponent catalysts for methanol synthesis from carbon dioxide and hydrogen. Appl. Catal. A: Gen. 1996;138:311-318.

[41] Kunkes EL, Studt F, Abild-Pedersen F, Schlögl R, Behrens M. Hydrogenation of CO_2 to methanol and CO on Cu/ZnO/Al_2O_3: Is there a common intermediate or not? J. Catal. 2015;328:43-48.

[42] Fujita S-I, Usui M, Takezawa N. Mechanism of the reverse water gas shift reaction over Cu/ZnO catalyst. J. Catal. 1992;134:220-225.

[43] Su X, Yang X, Zhao B, Huang Y. Designing of highly selective and high-temperature endurable RWGS heterogeneous catalysts: recent advances and the future directions. J. Energy. Chem. 2017;26:854-867.

[44] Mastalir A, Frank B, Szizybalski A, Soerijanto H, Deshpande A, Niederberger M, et al. Steam reforming of methanol over Cu/ZrO_2/CeO_2 catalysts: a kinetic study. J. Catal. 2005;230:464-475.

[45] Schumann J, Eichelbaum M, Lunkenbein T, Thomas N, Alvarez Galvan MC, Schlögl R, Behrens M. Promoting strong metal support interaction: Doping ZnO for enhanced activity of Cu/ZnO:M (M=Al, Ga, Mg) catalysts. ACS Catal. 2015;5:3260-3270.

[46] Lee JS, Moon KI, Lee SH, Lee SY, Kim YG. Modified Cu/ZnO/Al_2O_3 catalysts for methanol synthesis from CO_2/H_2 and CO/H_2. Catal. Lett. 1995;34:93-99.

[47] Kwak JH, Kovarik L, Szanyi Jn. CO_2 reduction on supported Ru/Al_2O_3 catalysts: cluster size dependence of product selectivity. ACS Catal. 2013;3:2449-2455.

[48] Behrens M, Studt F, Kasatkin I, Kühl S, Hävecker M, Abild-Pedersen F, Zander S, Girgsdies F, Kurr P, Kniep B-L. The active site of methanol synthesis over Cu/ZnO/Al_2O_3 industrial catalysts. Science. 2012;336:893-897.

[49] Bednarczuk L. Ni-based catalysts for H_2 production from ethanol steam reforming: Effect of the support and use of CO_2 as regenerating agent and reactant. PhD thesis. 2017, University of Barcelona.

[50] Toyir J, Ramírez de La Piscina P, Homs N. Ga-promoted copper-based catalysts highly selective for methanol steam reforming to hydrogen; relation with the

hydrogenation of CO_2 to methanol. Int. J. Hydrogen Energy. 2015;40:11261-11266.

[51] Edwards JF, Schrader GL. Infrared spectroscopy of copper/zinc oxide catalysts for the water-gas shift reaction and methanol synthesis. J. Phys. Chem. 1984;88:5620-5624.

[52] Busca G, Lamotte J, Lavalley JC, Lorenzelli V. FT-IR study of the adsorption and transformation of formaldehyde on oxide surfaces. J. Am. Chem. Soc. 1987;109:5197-5202.

[53] Llorca J, Homs N, Rossell O, Seco M, Fierro JLG, Ramírez de La Piscina P. Highly dispersed cobalt in $CuCo/SiO_2$ cluster-derived catalyst. J. Mol. Catal. A: Chem. 1999;149:225-232.

Chapter 4

Mo_xC-based catalysts in RWGS reaction

In this chapter, the study of Mo_xC-based catalysts for CO_2 conversion to CO under RWGS reaction conditions at moderate reaction temperature and atmospheric pressure is presented.

The chapter contains three sections corresponding to the study of: *i)* Bulk Mo_xC catalysts; *ii)* γ-Al_2O_3-, TiO_2-, SBA-15- and SiO_2-supported Mo_xC-U catalysts; and *iii)* Cu- and Co-modified Mo_xC-U catalysts. The preparation of the different catalysts, as well as their characterization before and after the catalytic test is presented. The catalytic tests were carried out at atmospheric pressure using $CO_2/H_2/N_2=1/1/3$ and $CO_2/H_2/N_2=1/3/1$ (molar ratio) reactant mixtures in the temperature range of 275-400 °C.

4.1. Bulk Mo_xC catalysts

4.1.1 Preparation of bulk Mo_xC catalysts

As stated in the Introduction section, Mo_xC materials are usually prepared by reaction at high temperature of molybdenum oxides, generally MoO_3, with mixtures of H_2 and hydrocarbons (CH_4, C_2H_6) [1,2]. However, these preparation methods involve high cost and extreme operation conditions [3]. Thus, the development of a cheap and easy to handle preparation method of Mo_xC-based materials is of great interest. In this context, the use of a sol-gel process in the presence of a carbon source would be an alternative method for a suitable synthesis of Mo_xC-based catalysts [4-6].

In the present work, bulk Mo_xC catalysts were prepared using sol-gel methods employing different carbon sources. Figure 4.1 shows the general scheme of the preparation procedure. In all cases, the Mo precursor ($MoCl_5$ or $(NH_4)_6Mo_7O_{24}\cdot4H_2O$) was mixed with the carbon source in water or ethanol to form a viscous solution. This viscous solution was then treated at 60 °C in an oven under air to form a gel. After this, the sample was transferred into a quartz tube reactor and then treated under Ar flow at 2 °C/min up to 150 °C and maintained 3 h; subsequently, the temperature was increased at 3 °C/min up to 800 °C and kept 3 h. Finally, the reactor was cooled down to room temperature under Ar flow and the catalyst was exposed to the ambient air, without any passivation procedure.

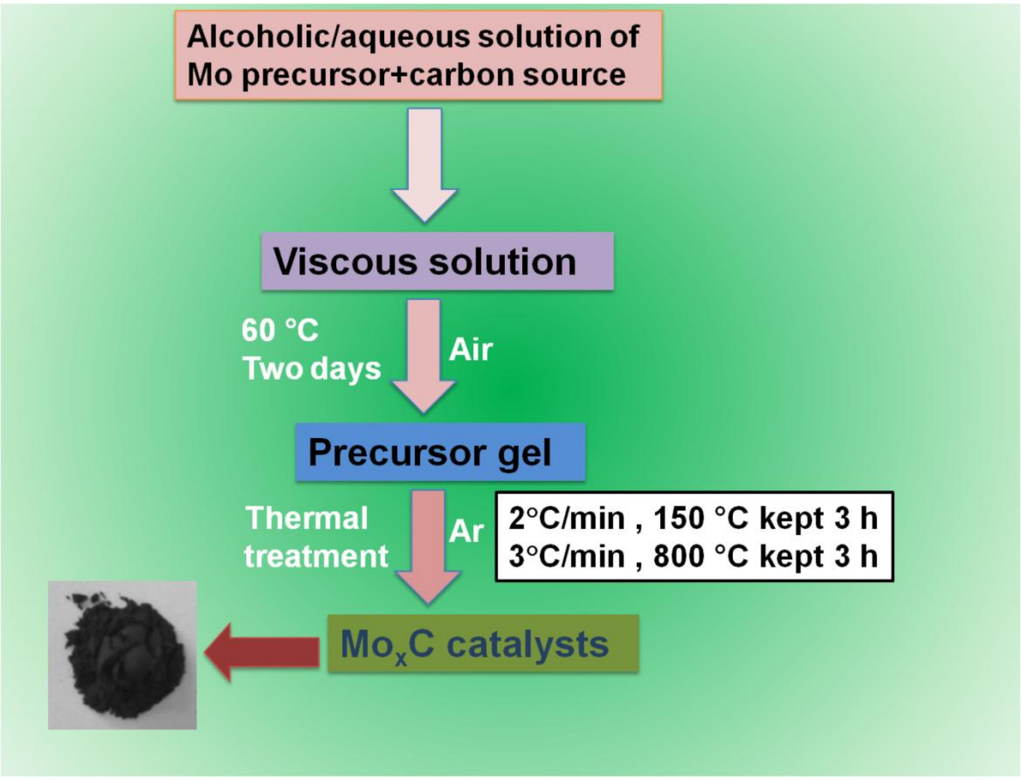

Figure 4.1. The scheme of Mo$_x$C preparation.

Three different sources of carbon were used: urea, a mixture of citric acid and urea in the presence of ethylene glycol, and, a mixture of EDTA and ED. The resulting catalysts were labelled as Mo$_x$C-U (urea), Mo$_x$C-CA (citric acid, urea and ethylene glycol) and Mo$_x$C-E (EDTA and ED).

The preparation of Mo$_x$C-U was carried out on the basis of the study of Giordano et al. [5]. Solid urea (urea/MoCl$_5$=7, molar ratio) was added with continuous stirring to an ethanol solution of $MoCl_5$ (1.3 M). Then, the sample was thermally treated as described in Figure 4.1.

The preparation method of Mo_xC-CA was based on that described by Zhao et al. [6]. The $(NH_4)_6Mo_7O_{24}{\cdot}4H_2O$ precursor was dissolved into an aqueous solution of citric acid with continuous stirring until a clear solution was obtained. Besides citric acid, we added solid urea to the solution to achieve a molar ratio of $(NH_4)_6Mo_7O_{24}{\cdot}4H_2O$/citric acid/urea of 1/7/7. Meanwhile, an appropriate amount of ethylene glycol (citric acid/ethylene glycol=1, molar ratio) was used for promoting the polymerization. Then, the sample was thermally treated as described before.

The preparation of Mo_xC-E was carried out following a new method proposed in this work. $(NH_4)_6Mo_7O_{24}{\cdot}4H_2O$ was used as molybdenum precursor; EDTA and ED were the carbon sources. Solid EDTA was first dissolved in an appropriate aqueous solution of ED. Then, the Mo precursor was added to the solution under continuous stirring to achieve the target concentration of Mo ([Mo]=0.25 M). The molar ratio of $(NH_4)_6Mo_7O_{24}{\cdot}4H_2O$/EDTA/ED was 1/3.5/7. Then, the viscous solution was thermally treated as described in Figure 4.1.

In Annex II, specific experimental details for the preparation of Mo_xC-U, Mo_xC-CA and Mo_xC-E samples are given.

4.1.2. Characterization of bulk Mo_xC catalysts

The BET surface area of Mo_xC-U, Mo_xC-CA and Mo_xC-E were 7.7, 14.5 and 8.9 m^2/g, respectively.

Figure 4.2 shows the XRD patterns of fresh Mo_xC catalysts prepared using the different methods**;** different crystalline phases of Mo_xC were identified. XRD peaks of Mo_xC-U can be clearly assigned to the only presence of hexagonal Mo_2C phase (JCPDS 00-035-0787). However, the XRD patterns of Mo_xC-CA and

Mo_xC-E showed broad peaks, which besides the presence of hexagonal Mo_2C (most intense peak at 2θ=39.3°), pointed to the presence of different phases: cubic Mo_2C (JCPDS 0-015-0457) and/or cubic MoC (JCPDS 03-065-0280). Using the Scherrer equation and the diffraction peak at 2θ=61.6°, the crystallite size of Mo_xC was calculated. The obtained values were 35.2, 12.2 and 4.6 nm for Mo_xC-U, Mo_xC-CA and Mo_xC-E, respectively.

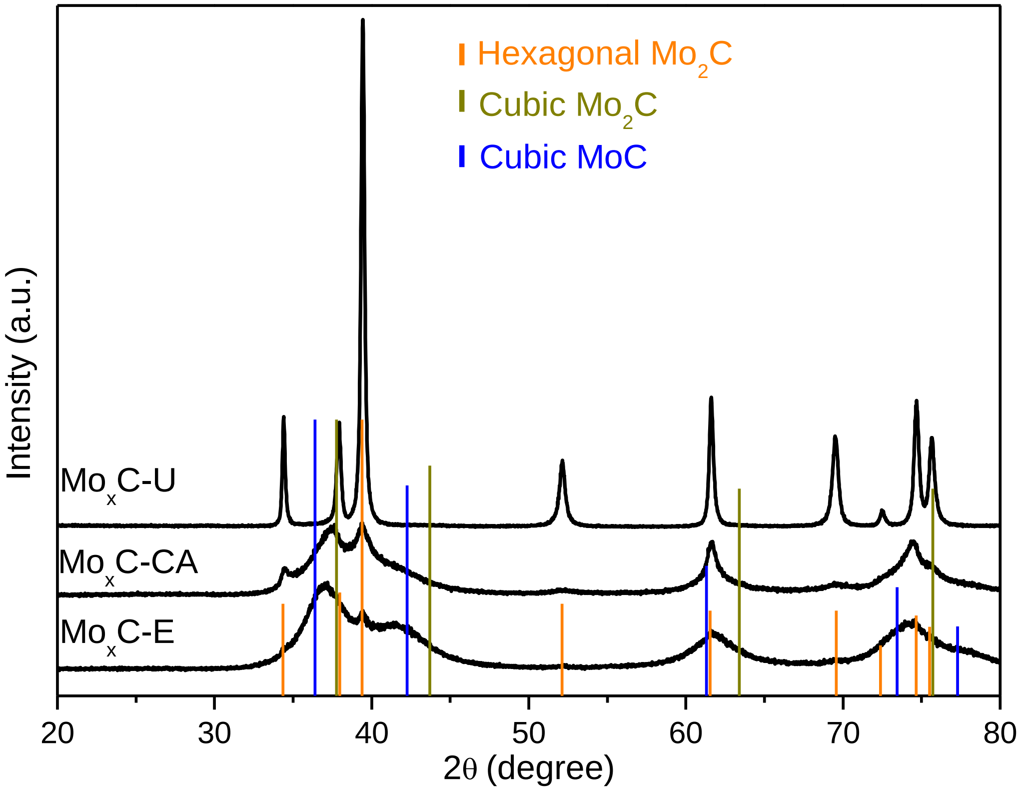

Figure 4.2. XRD patterns of Mo_xC samples prepared using different methods.

Raman spectra of different zones were recorded to investigate the possible presence of molybdenum oxides and/or residual carbon in the catalysts. It has been reported that the surface of freshly prepared carbides can be easily oxidized when carbides are exposed to air [7]. The surface oxidation of Mo_2C by O_2, CO_2 and H_2O has been studied by in-situ FT-IR spectroscopy; the formation of a thin layer of protective oxycarbide has been proposed when mild oxidants such as CO_2 or H_2O react with Mo_2C/Al_2O_3; however, this surface oxidation is more difficult to control when O_2 is used for passivation [7,8].

Representative Raman spectra of fresh Mo_xC samples are shown in Figure 4.3. The Raman spectra of Mo_xC-CA and Mo_xC-E, showed the presence of characteristic D (~1350 cm^{-1}) and G (~1595 cm^{-1}) bands, which correspond to the presence of poorly-structured carbonaceous deposits and well-structured carbon deposits, respectively. For Mo_xC-U, a negligible presence of free carbon can be proposed.

On the other hand, as can be seen in Figure 4.3, the Raman spectra are complex, exhibiting different bands in the 100-1000 cm^{-1} region. These bands can be related to the presence of different surface molybdenum oxide species such as MoO_3 and other intermediate oxides MoO_{3-x} [9-13]. The presence of different molybdenum oxide species could be a result of surface oxidation when the samples were exposed to air [7]. Raman bands at about 996, 823 and 667 cm^{-1} are characteristic of orthorhombic MoO_3 [9,11,12], and those at 850 and 775 cm^{-1} are related to the presence of monoclinic MoO_3 [12,14].

Raman spectra in Figure 4.3 indicate a heterogeneous distribution of surface molybdenum oxide species at least for Mo_xC-U and Mo_xC-E samples.

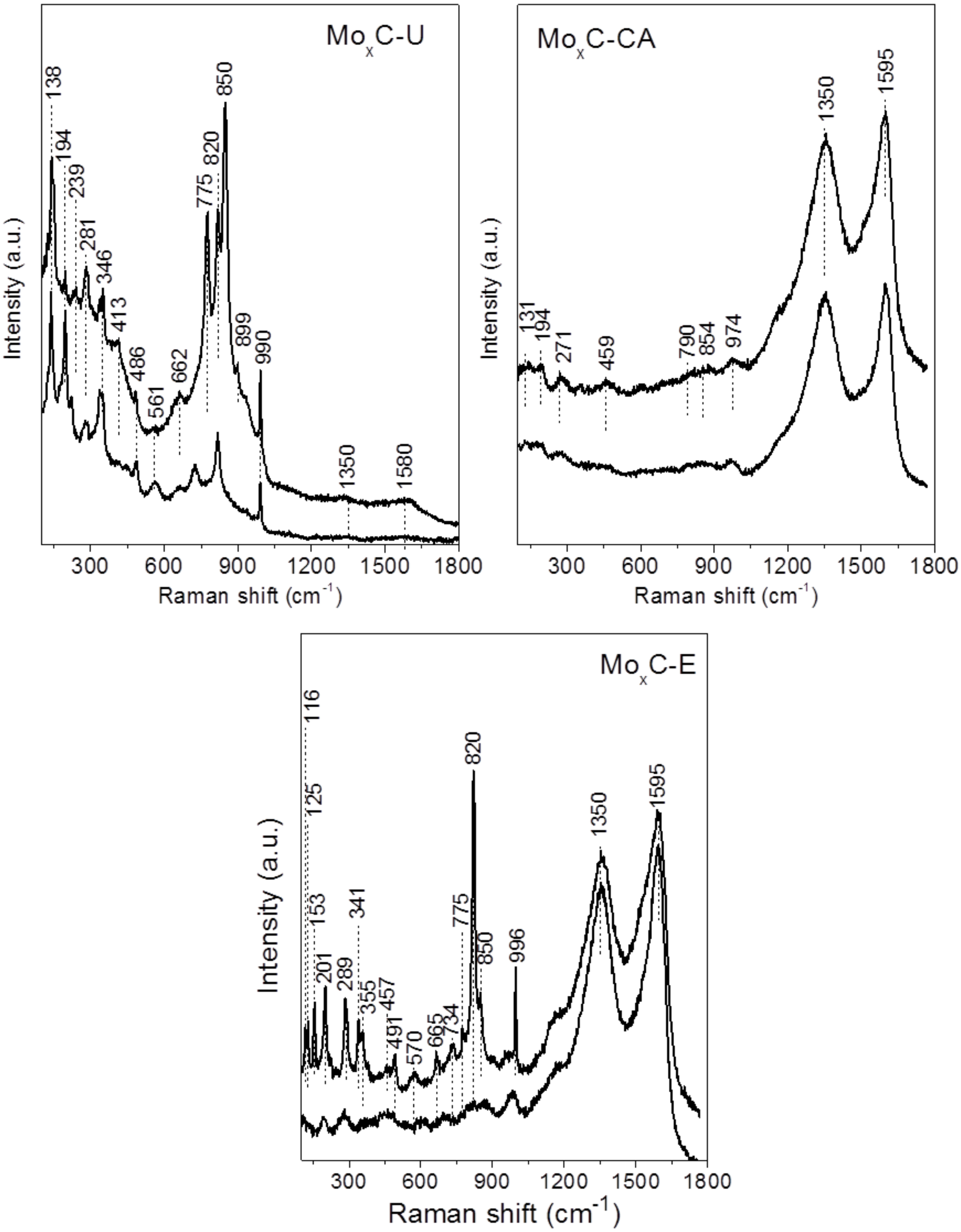

Figure 4.3. Raman spectra of fresh Mo_xC catalysts in two different representative zones.

The reducibility of the catalysts was studied by H_2-TPR; the corresponding profiles are shown in Figure 4.4. Three different H_2 consumption zones were observed: low temperature (below 325 °C), medium temperature (325-525 °C) and high temperature (above 625 °C).

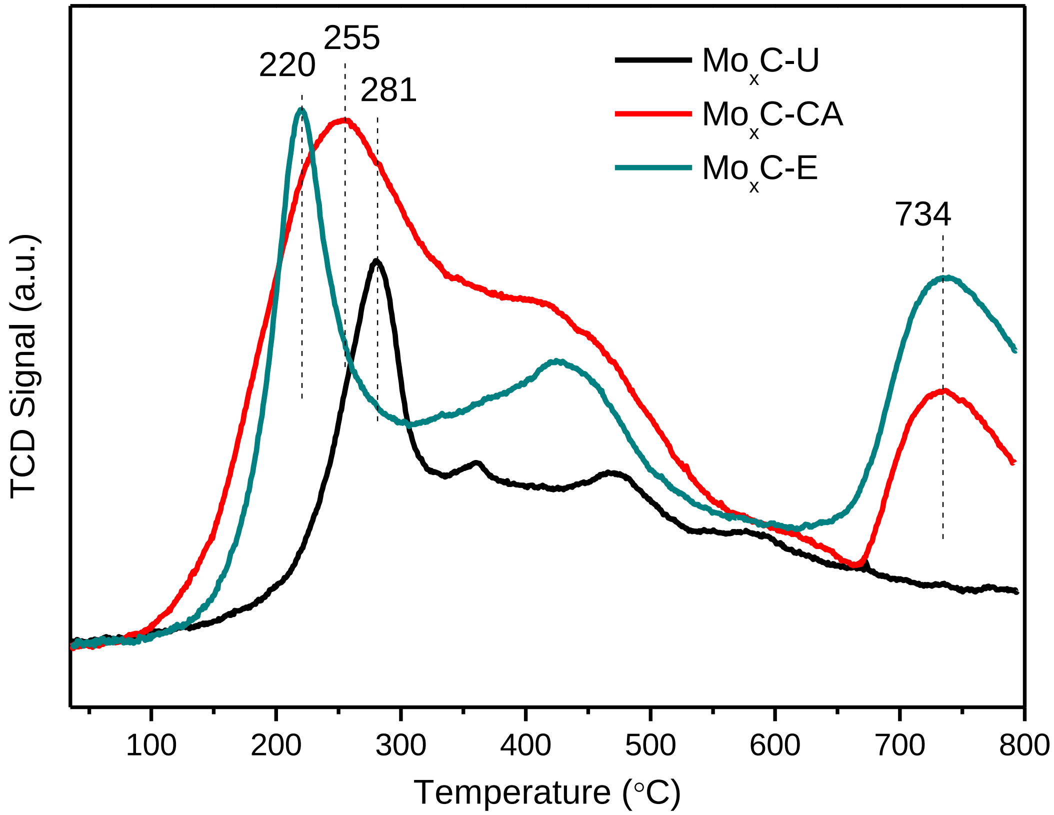

Figure 4.4. H_2-TPR profiles of fresh Mo_xC samples.

H_2 consumption at temperature below 325 °C has been related with the existence of molybdenum oxycarbide species [15]. Thus, H_2-TPR peaks at 220, 255 and 281 °C for Mo_xC-U, Mo_xC-CA and Mo_xC-E, respectively, could account for the reduction of molybdenum oxycarbide. The H_2 consumption observed in the 325-525 °C region for these three samples could be due to the reduction of surface MoO_3 species to MoO_2, which could take place through different intermediate species [16]. The reduction of MoO_2 to Mo is expected at temperature above 527 °C [16]. The observed H_2-TPR peak at 734 °C for Mo_xC-CA and Mo_xC-E could be due to the reduction of surface MoO_2. However, we cannot discard that at this temperature H_2 could react with residual carbon deposits in Mo_xC-CA and Mo_xC-E, then, the formation of CH_4 could mask the TCD signal.

Mo_xC catalysts were also characterized by XPS; the Mo 3d, C 1s and O 1s core levels were analyzed. The XPS results confirmed the absence of N and Cl species on the surface of the catalysts. Figure 4.5 shows the XPS profiles of Mo 3d core level of fresh Mo_xC catalysts.

It can be seen that Mo 3d spectra are complex. However, they can be properly analyzed by deconvoluting into four Mo $3d_{5/2}$-Mo $3d_{3/2}$ doublets. According to literature, the ratio of the intensity of Mo $3d_{5/2}$ peak to Mo $3d_{3/2}$ peak was fixed to be 1.5 and their splitting was set to 3.1 eV [17-19].

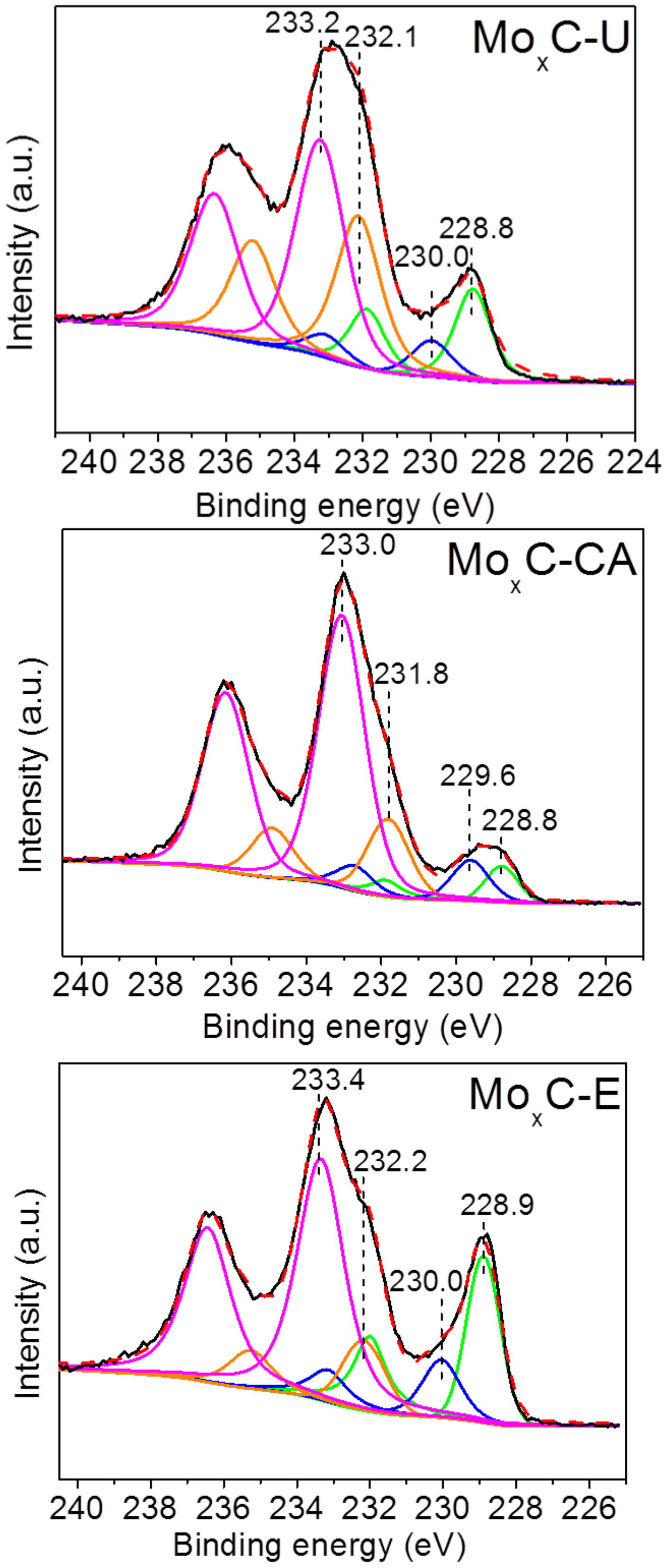

Figure 4.5. XPS profiles of Mo 3d core level of fresh Mo_xC catalysts.

The spectra can be analyzed taking into account the different chemical state of molybdenum species. Mo $3d_{5/2}$ components at 233.0-233.4 eV, 231.8-232.2 eV, and 229.6-230.0 eV were assigned to Mo^{6+}, Mo^{5+} and Mo^{4+} surface species, respectively [18,20], which may indicate the presence of surface MoO_3, MoO_2 and several oxide intermediate species. Although a peak at 228.9 eV has been ascribed to a molybdenum suboxide [21], the Mo $3d_{5/2}$ peak observed at 228.8-228.9 eV can be related to the presence of Mo_2C and/or oxycarbide species [20,22]; this peak is more intense for Mo_xC-E than those of Mo_xC-CA and Mo_xC-U. Raman spectra of Mo_xC-E (Figure 4.3) showed bands of very low intensity in the zone characteristic of molybdenum oxide species.

The corresponding BE values of Mo $3d_{5/2}$ for fresh catalysts are summarized in Table 4.1.

Table 4.1. BE values of Mo $3d_{5/2}$ for fresh Mo_xC catalysts.

Catalyst	BE (eV)			
	$Mo^{2<\delta+<3}$	Mo^{4+}	Mo^{5+}	Mo^{6+}
Mo_xC-U	228.8	230.0	232.1	233.2
Mo_xC-CA	228.8	229.6	231.8	233.0
Mo_xC-E	228.9	230.0	232.2	233.4

The high resolution C 1s spectra of fresh catalysts are shown in Figure 4.6. As stated in the Experimental section, the adventitious carbon peak at 284.8 eV was previously determined using Au as reference. In all cases, the C 1s spectra show an intense broad and asymmetric peak with maximum at 284.8 eV, that can be deconvoluted into four components at 283.5-283.8 eV, 284.8 eV, 285.7-286.2 eV and 288.7-289.2 eV. Components at about 283.5-283.8 eV are assigned to Mo-C in molybdenum carbide and/or oxycarbide species [20,22-25], whereas those at higher BE, 285.7-286.2 eV and 288.7-289.2 eV, are related to C-O and O=C-O, respectively [22-27].

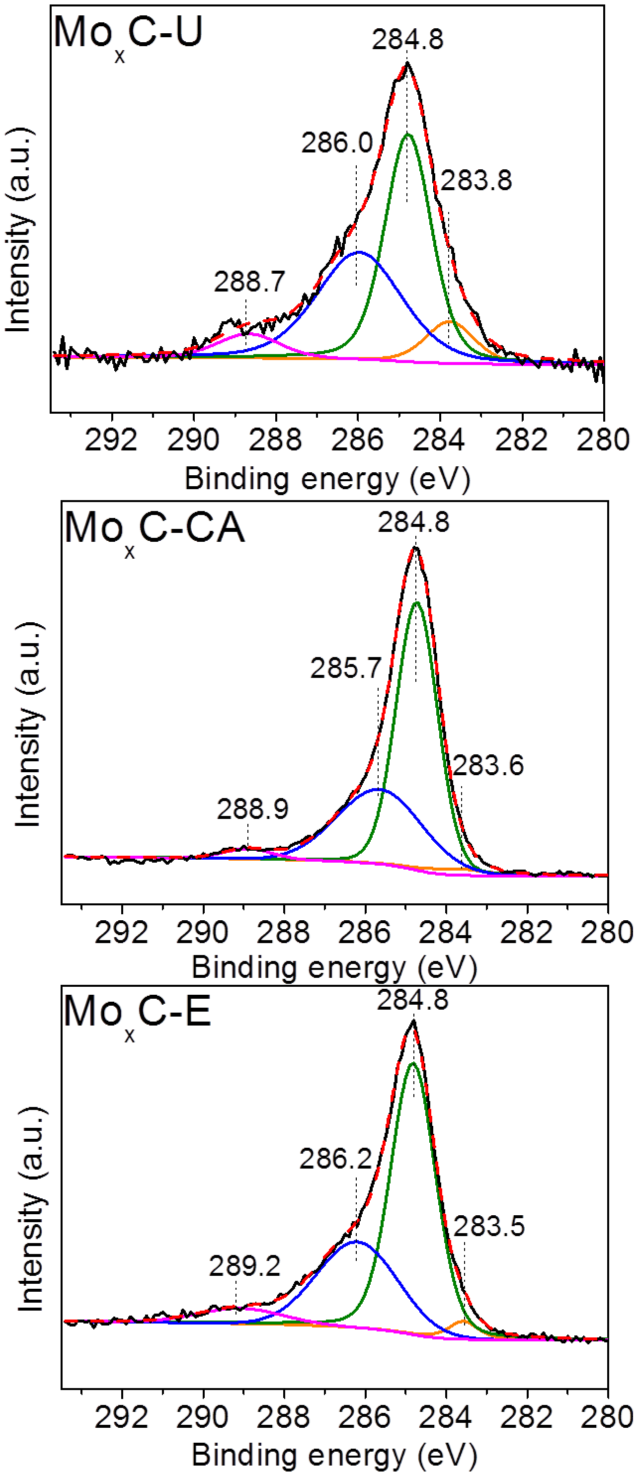

Figure 4.6. XPS profiles of C 1s of fresh Mo$_x$C catalysts.

The XPS profiles of O 1s are shown in Figure 4.7. In all cases, the spectra show a main broad and asymmetric peak centered at about 531.1 eV, which can be related to Mo-O bonds in molybdenum oxide and/or oxycarbide species on the surface [20,22,23,26]. The observed shoulder at high BE is associated to residual oxygen species bonded to carbon (C-O and C=O) [20,22,23,26].

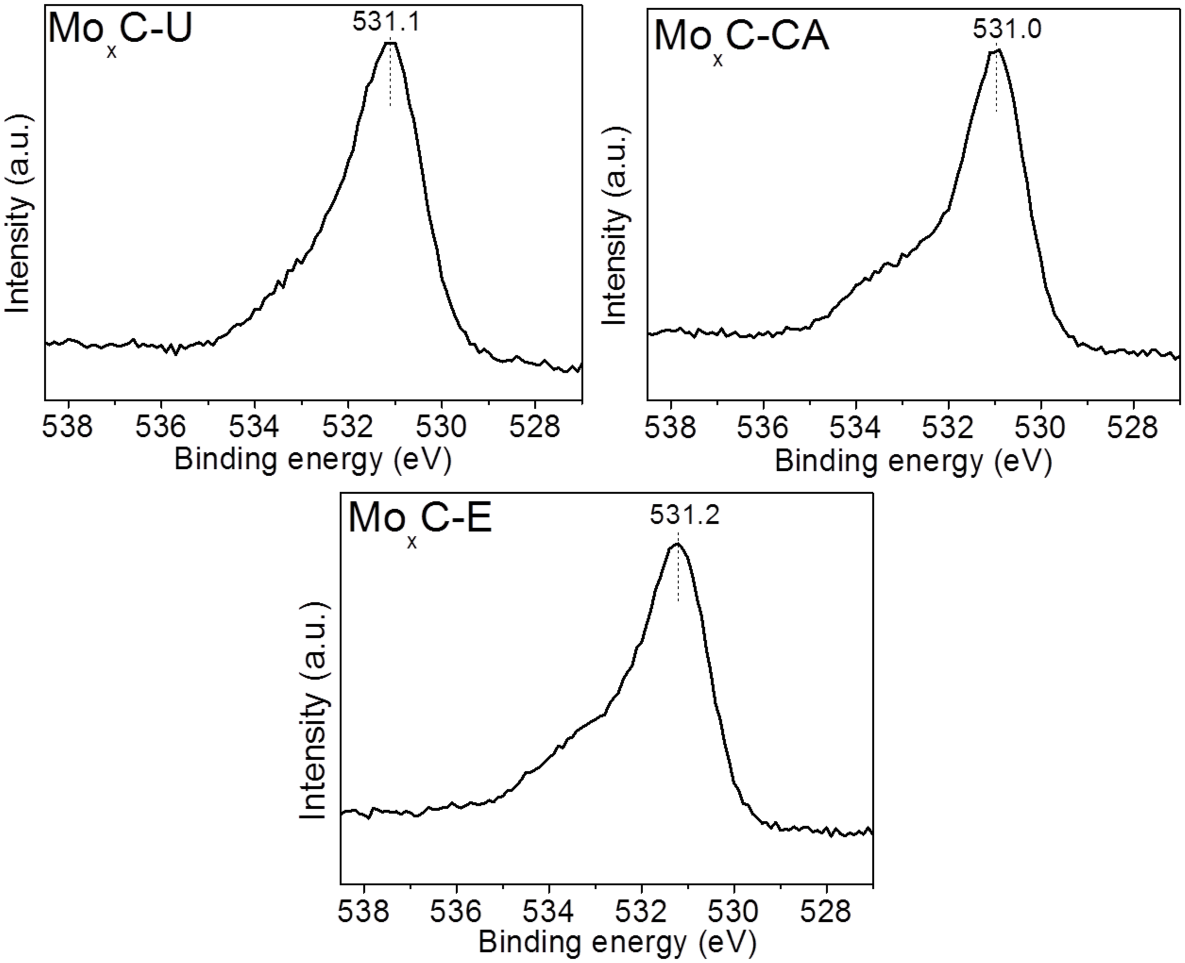

Figure 4.7. XPS profiles of O 1s of fresh Mo_xC catalysts.

The morphology of prepared Mo_xC samples was studied by SEM. The images of Mo_xC samples at low and high magnification are shown in Figure 4.8. For Mo_xC-U and Mo_xC-CA, similar morphology with rough and smooth surfaces was found. On the other hand, the Mo_xC-E sample showed the presence of uniform rods.

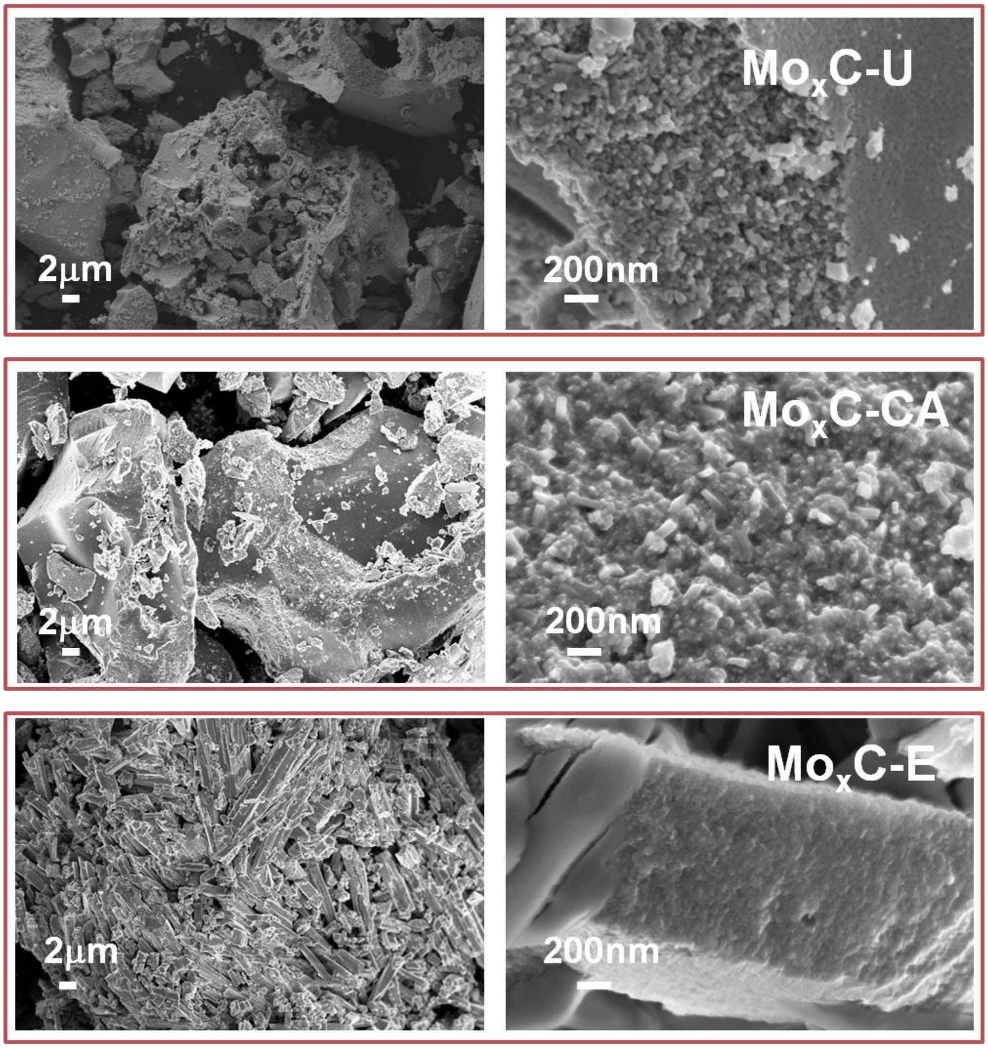

Figure 4.8. SEM images of fresh Mo_xC catalysts.

For Mo_xC-U sample, the EDX analysis was performed to measure the distribution of different elements; the corresponding mapping images are shown in Figure 4.9. The presence of Mo, C and O can be observed; the presence of oxygen was related to the existence of surface molybdenum oxide and/or oxycarbide species formed during the preparation and/or when the Mo_xC-U sample was exposed to air; these results accord with Raman, TPR and XPS results.

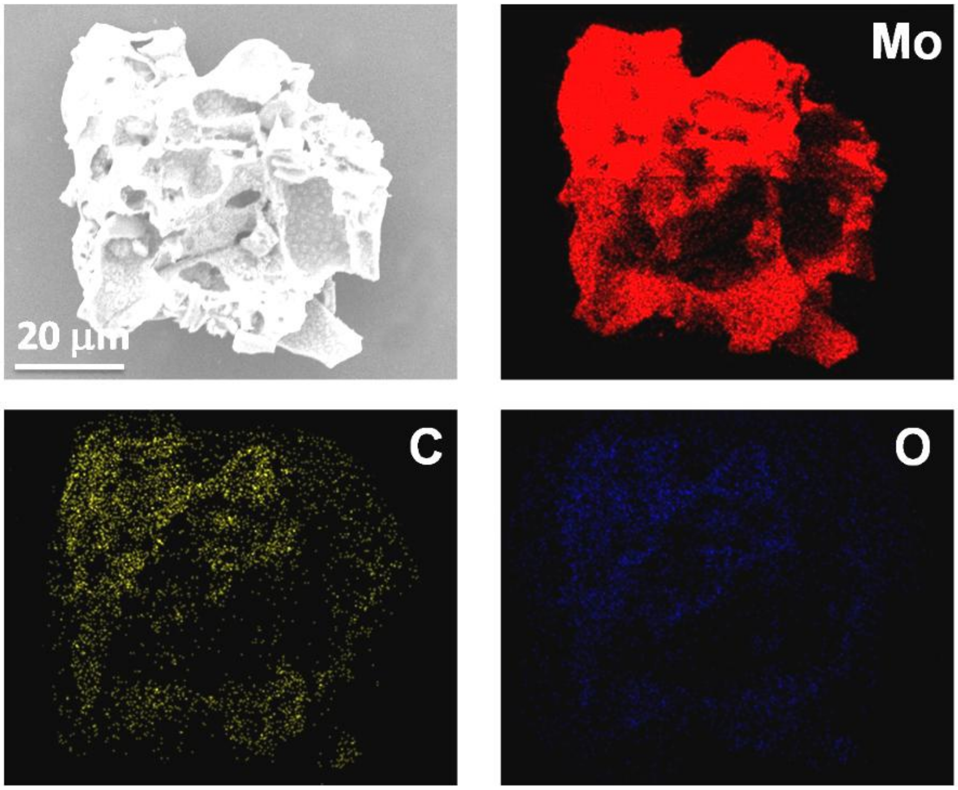

Figure 4.9. SEM images and element distribution determined by EDX of fresh Mo_xC-U.

Taking into account that the Mo_xC-U catalyst showed by XRD the only presence of hexagonal Mo_2C, this catalyst was more deeply characterized using different techniques. Moreover, the experimental results obtained with this catalyst have been successfully interpreted from periodic DFT calculations, employing a realistic consideration of the most stable Mo_2C surfaces in the frame of a collaboration with the group of Prof. F.Illas (University of Barcelona) [28].

Thus, Mo_xC-U was further characterized by in-situ DRIFTS using CO and CO_2 as probe molecules. The sample was first treated in-situ in the DRIFTS cell under a He flow up to 300 °C, and then cooled to 35 °C under He. Afterwards a CO/He (10% vol/vol) or CO_2/He (10% vol/vol) mixture was admitted at 35 °C and contacted with the sample for 20 min. Before recording the final spectra, the sample was exposed to He flow and cooled down to 25 °C. The corresponding final spectra were recorded at 25 °C in the range of 400-4000 cm^{-1} by collecting 256 scans at a spectral resolution of 4 cm^{-1}.

Figure 4.10 shows the CO-DRIFT spectrum of Mo_xC-U in the 2250-1250 cm^{-1} region. After CO adsorption, the spectrum shows several bands below 2000 cm^{-1}; the assignation of these bands was done on the basis of theoretical calculations [28]. The observed bands at 1919, 1827, 1772, 1747, 1647, and 1585 cm^{-1} were ascribed to the stretching modes of CO adsorbed on the (201)-Mo/C terminated surface of hexagonal Mo_2C; the two bands at 1772 and 1747 cm^{-1} were related to the symmetric and asymmetric coupling of adsorbed vicinal CO groups. Bands at 1507, 1458 and 1415 cm^{-1} were assigned to CO adsorbed on (001)-Mo and (001)-C terminated surfaces of hexagonal Mo_2C. The bands at 1993 and 1945 cm^{-1} were related to CO adsorbed on different sites of (001)-C and/or (101)-Mo/C surfaces of hexagonal Mo_2C. The band at 1699 cm^{-1} is of difficult assignation from the DFT calculations done; the presence of defects, CO adsorption on other less-stable surfaces or the change of CO vibrational frequency by neighboring oxygen adatoms could contribute to this band [28].

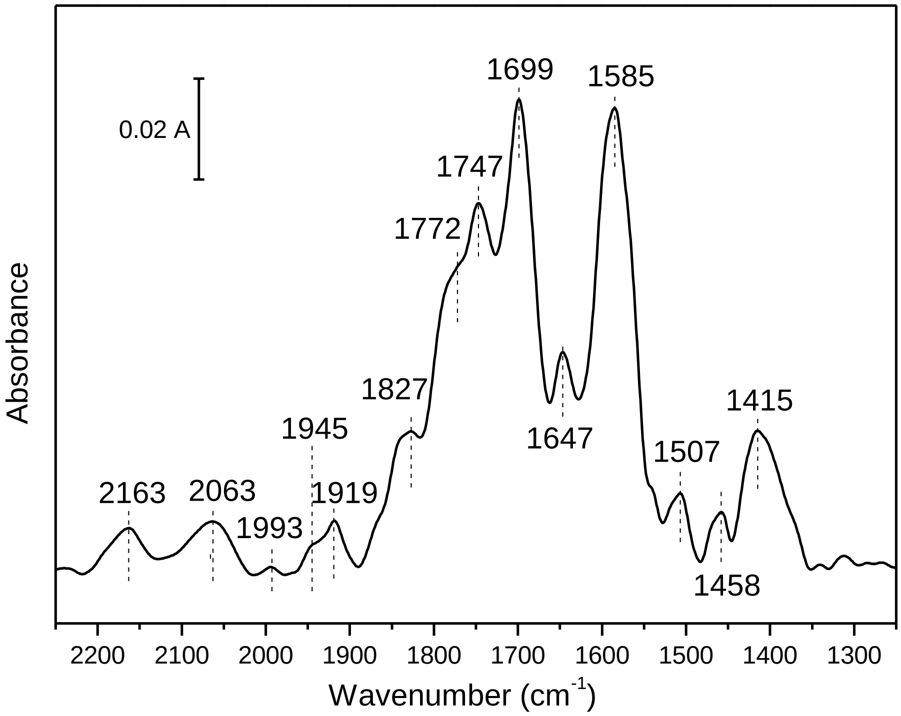

Figure 4.10. DRIFT spectrum after CO adsorption on Mo_xC-U at 35 °C.

Moreover, after CO adsorption on Mo_xC-U, two weak broad bands centered at 2163 and 2063 cm^{-1} were also observed. A band at 2183 cm^{-1} has been ascribed to the coordination of CO on Mo^{5+} sites [29]. However, a band at 2196 cm^{-1} has been related to ketene species for the Mo_2C/Al_2O_3 system [8]. Although DFT calculations indicated that the band at 2163 cm^{-1} could be related to C=C=O (ketene) species on (001)-C surface [28], the contribution to this band of CO coordinated to Mo^{5+} species can also be reasonably proposed [7,29]. The band at 2063 cm^{-1} was assigned to the coordination of CO on surface Mo^{n+} sites (n<4), likely molybdenum oxycarbide species. Previous work of CO adsorption onto Mo_2C/Al_2O_3 reported the observation of bands at 2054 and 2081 cm^{-1} that were attributed to CO adsorbed on Mo^{m+} and Mo^{k+} sites, where 0<m<2<k<3, respectively [7].

To analyze in depth the CO adsorption, the TPD of CO was carried out; the profile is shown in Figure 4.11. Prior to the CO adsorption, the Mo_xC-U sample was treated with He or H_2/Ar (12% vol/vol) flow at 300 °C; the obtained CO-TPD profiles were similar, and only that of the H_2-treated Mo_xC-U is shown. A total adsorption of 0.24 mmolCO/g was determined from TPD profile. A broad CO-TPD profile with several relative maxima was obtained (Figure 4.11). The broadness of the profile indicates the presence of different adsorption sites with different adsorption energies. The peaks at 142 and 190 °C could be related with CO desorption from the most stable (101)-Mo/C surface of hexagonal Mo_2C [28]. Moreover, CO adsorbed on (001)-C surface could also contribute to the TPD peaks at a temperature lower than 327 °C, while CO adsorbed on (201)Mo/C and (001)-Mo surfaces could be responsible for the CO desorption above 327 °C [28].

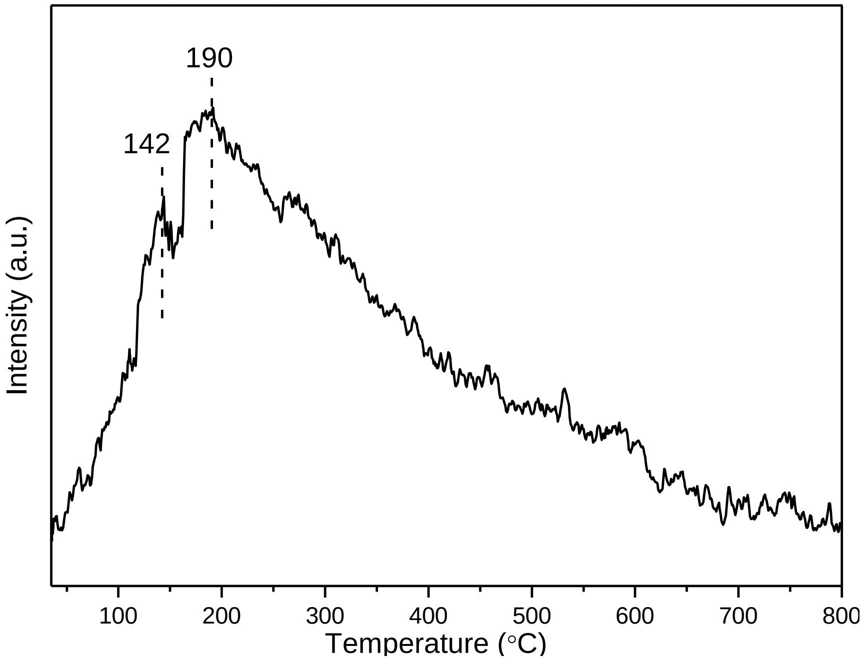

Figure 4.11. CO-TPD profile of adsorbed CO at 35 °C over reduced Mo_xC-U.

As stated above, the interaction of Mo_xC-U with CO_2 was also studied by in-situ DRIFTS. Figure 4.12 shows the corresponding spectrum, obtained after CO_2 adsorption, in the 2200-1000 cm^{-1} region. As shown in Figure 4.12A, after CO_2 adsorption, several IR bands above 2000 cm^{-1} were observed. As previously mentioned, two bands at 2063 and 2163 cm^{-1} were observed after CO adsorption

(Figure 4.10) and were ascribed to CO adsorbed onto different surface Mo^{n+} centres, and to C=C=O species on the (001)-C surface of hexagonal Mo_2C. This type of adsorbed species could also be responsible for the bands in the zone 2200-2000 cm^{-1} obtained after CO_2 adsorption. However, the bands above 2000 cm^{-1} obtained after CO_2 adsorption show a different position and relative intensity (Figure 4.12A) when compared to those observed after CO adsorption (Figure 4.10). This different vibrational frequency of CO could be due to the presence of O adatoms appearing after the CO_2 chemisorption. CO_2 dissociation to give CO+O over different surfaces of hexagonal Mo_2C, has been reported by DFT calculations [28].

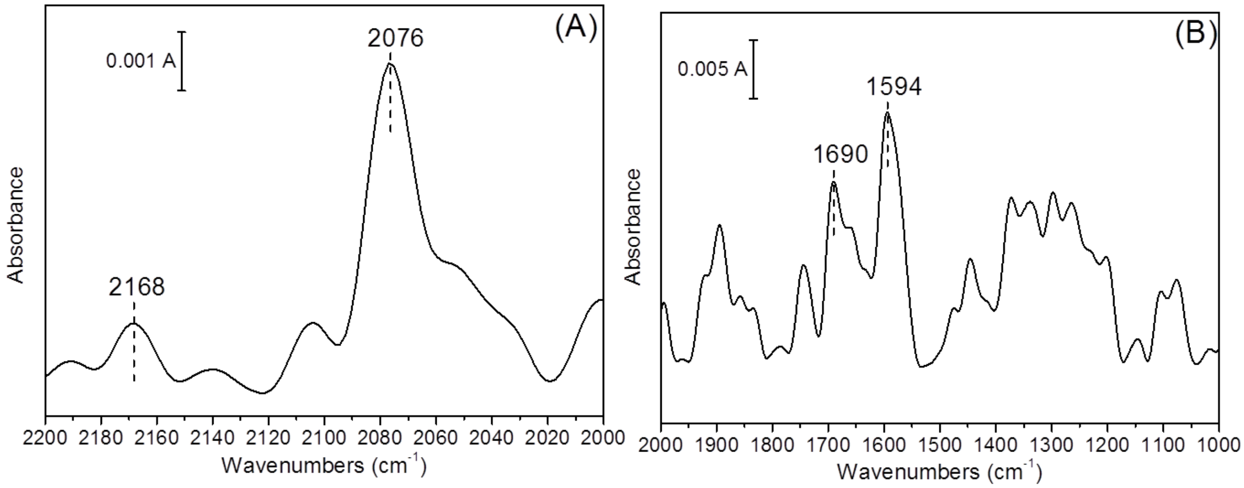

Figure 4.12. DRIFT spectra after CO_2 adsorption on Mo_xC-U at 35 °C: (A) 2200-2000 cm^{-1} zone; (B) 2000-1000 cm^{-1} zone.

The IR spectrum obtained in the 2000-1000 cm^{-1} zone after CO_2 adsorption is shown in Figure 4.12B. It was difficult to make a straightforward assignation of the bands, due to the complexity of the spectrum. According to the DFT calculations, CO_2 adsorbed on different hexagonal Mo_2C surfaces would raise $\nu_{as}(CO_2)$ and $\nu_s(CO_2)$ bands in the 1800-1200 cm^{-1} range and 1300-700 cm^{-1} range, respectively. Moreover, different $\nu(CO)$ bands generated from adsorbed

CO resulting from CO_2 scission can also contribute to different bands below 2000 cm^{-1}. Specifically, the main bands with maxima at 1690 and 1594 cm^{-1} could be contributed by adsorbed CO on hexagonal Mo_2C [28].

In order to improve the understanding of the reactivity of Mo_xC-U towards CO_2, fresh Mo_xC-U sample was treated with CO_2 at 400 °C, and then characterized by XRD, Raman and XPS. The experiment was carried out using a Sensys evo TG-DSC (Setaram) instrument coupled to a ThermoStar GSD320T1 mass spectrometer. Prior to the introduction of CO_2, fresh Mo_xC-U sample was treated at 150 °C under Ar flow for 2 h. Then, the temperature was increased up to 400 °C under CO_2/He (10%, vol/vol) flow, and maintained for 10 h. During the CO_2 treatment, CO was detected in the effluent by mass spectrometer.

Figure 4.13A shows the XRD pattern of Mo_xC-U after the CO_2 treatment. Besides the peaks corresponding to the presence of hexagonal Mo_2C, characteristic XRD peaks of monoclinic MoO_2 (JCPDS 00-032-0671) were observed. The presence of MoO_2 was also confirmed by Raman spectroscopy, as shown in Figure 4.13B. The Raman bands at 740, 589, 570, 495, 457, 358, 347, 227 and 202 cm^{-1} are characteristic of the presence of MoO_2 [9]. The formation of MoO_2 could result from the reaction of Mo_2C with atomic O which comes from the CO_2 dissociation on the surface of the catalyst.

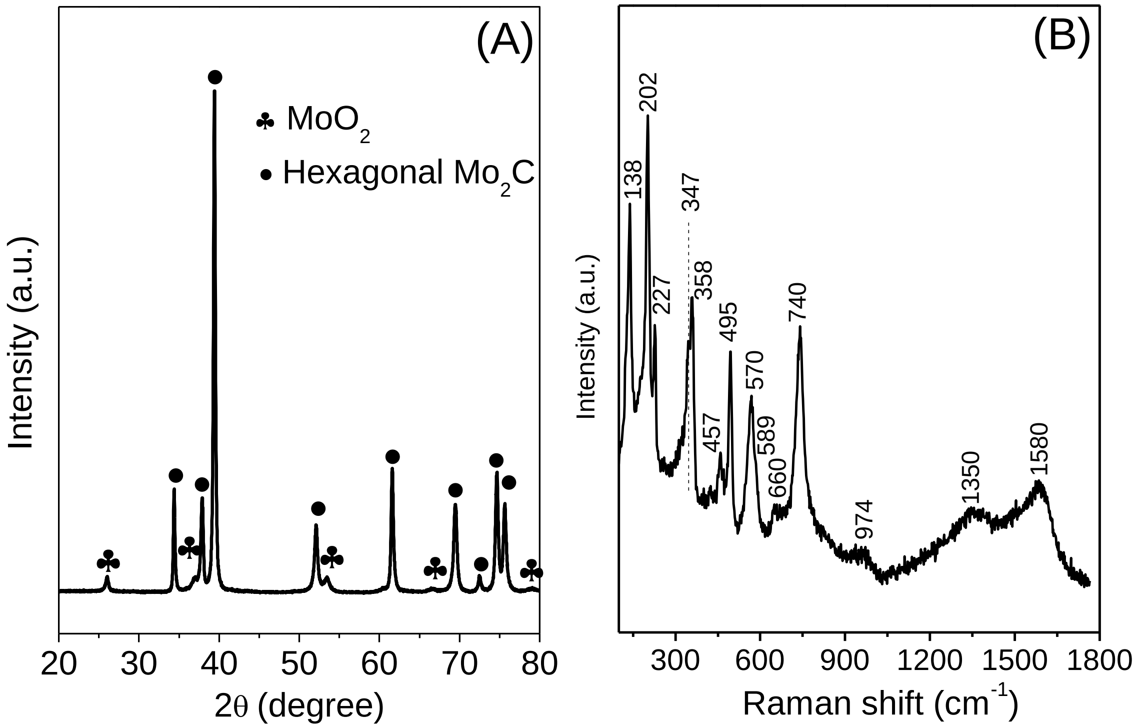

Figure 4.13. (A) XRD pattern of CO_2-treated (400 °C) Mo_xC-U; (B) Raman spectrum of CO_2-treated (400 °C) Mo_xC-U sample.

XPS analysis was carried out to study the surface change of the Mo_xC-U catalyst after the CO_2 treatment. The corresponding spectra of Mo 3d, C 1s and O 1s core levels are shown in Figure 4.14. For Mo 3d XPS profile, a slight difference was found compared to that of the fresh Mo_xC-U, indicating a transformation of molybdenum surface species on Mo_xC-U after CO_2 treatment. The Mo $3d_{5/2}$ component at 229.8 eV which is assigned to Mo^{4+} species was more visible and significant, pointing the presence of a larger amount of surface MoO_2 onto CO_2-treated Mo_xC-U than on the fresh sample; this finding is consistent with XRD and Raman results. For C 1s and O 1s, the obtained XPS profiles are similar to that of fresh Mo_xC-U discussed above.

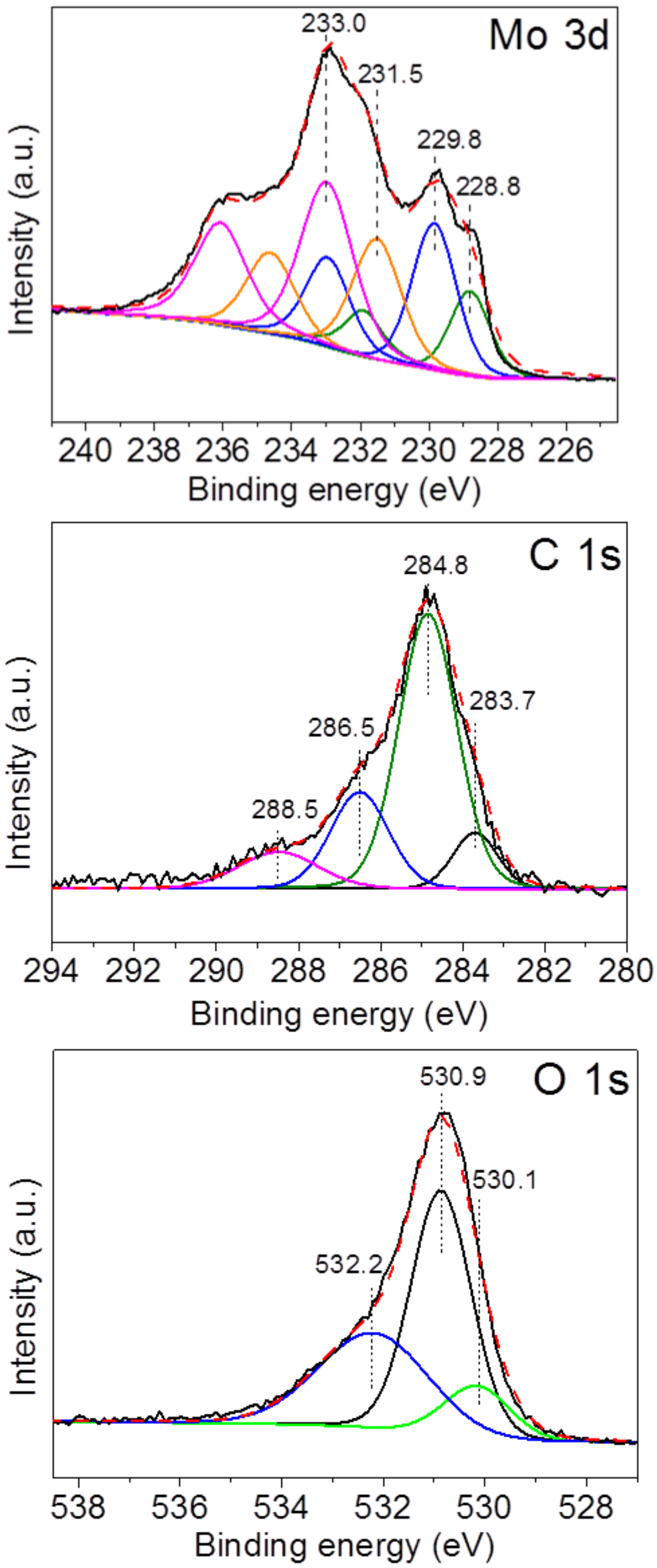

Figure 4.14. XPS profile of Mo 3d, C 1s and O 1s core levels of CO_2-treated (400 °C) Mo$_x$C-U catalyst.

After CO_2 treatment, Mo_xC-U was also characterized by H_2-TPR; the corresponding profile is shown in Figure 4.15A. Two H_2 consumption peaks at about 270 °C and 635 °C are observed. As previously discussed for fresh Mo_xC-U, the H_2 consumption at 270 °C is related to the reduction of molybdenum oxycarbide species. The new and intense peak at 635 °C, which was not present in the TPR profile of the fresh Mo_xC-U is ascribed to the reduction of MoO_2 [16].

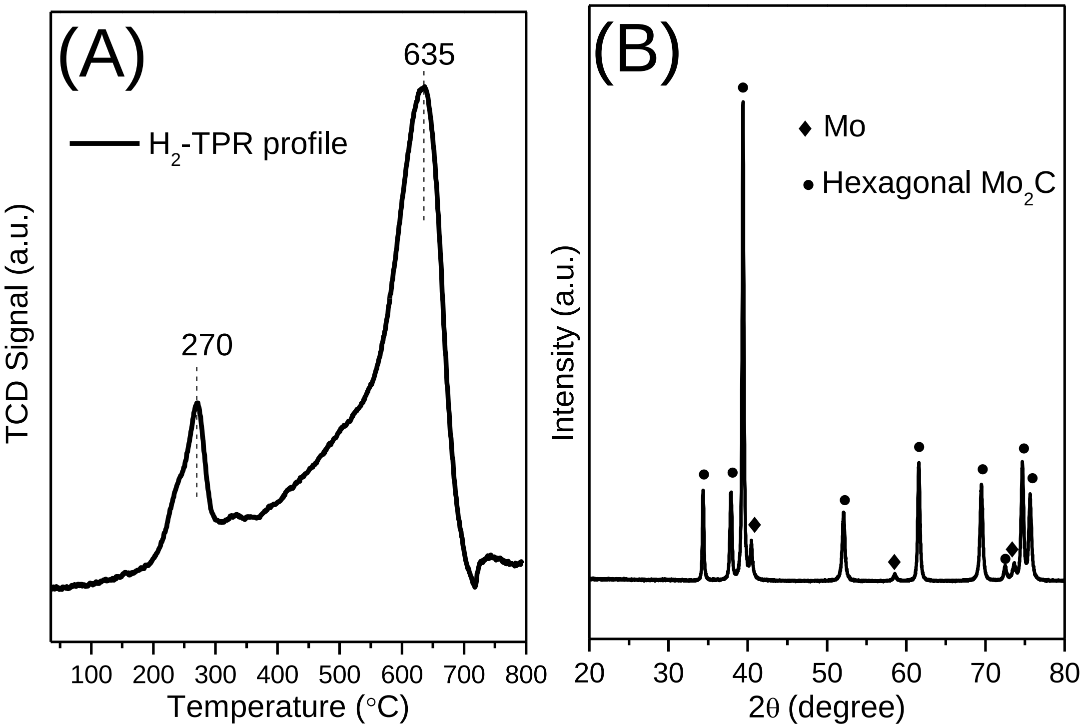

Figure 4.15. (A) H_2-TPR profile of CO_2-treated (400 °C) Mo_xC-U; (B) XRD pattern of Mo_xC-U after CO_2 treatment (400 °C) and H_2-TPR experiment.

To verify this, the sample resulting after the H_2-TPR experiment was analyzed by XRD. The corresponding XRD pattern did not show XRD peaks characteristics of MoO_2, but characteristic diffraction peaks of hexagonal Mo_2C and cubic Mo metal peaks at 2θ=40.5, 58.6 and 73.6 ° (JCPDS 00-004-0809) (Figure 4.15B) can be observed**.** This finding indicated that the crystalline MoO_2

was totally reduced to Mo at temperature above 500 °C during the H_2-TPR process.

For a better quantitative analysis of the adsorption of CO_2 on Mo_xC-U catalyst, CO_2 adsorption was studied by microcalorimetry. As mentioned in Chapter 2, the exothermic peak corresponding to CO_2 adsorption, as well as the total amount of adsorbed CO_2 were integrated to provide the mean adsorption energy. The mean CO_2 adsorption heat determined was -3.2 eV; this value is similar to the DFT calculated final states for CO+O on (201)-Mo/C (-3.62 eV) or (001)-Mo (-3.90 eV) surfaces of hexagonal Mo_2C [28]. This result indicates that the mentioned dissociative adsorption of CO_2 (CO+O) is a main contribution to the mean CO_2 adsorption heat on hexagonal Mo_2C. However, the obtained experimental heat is necessary to be regarded as an average of CO_2 adsorption in different situations, including CO_2 nondissociative adsorption and decomposition of CO_2 on other surfaces.

4.1.3. Bulk Mo_xC catalysts in RWGS reaction

The RWGS reaction tests over Mo_xC catalysts were carried out at atmospheric pressure using a GHSV of 3000 h^{-1} and a reactant mixture of $CO_2/H_2/N_2=1/3/1$ or $CO_2/H_2/N_2=1/1/3$. The catalyst was diluted with inactive SiC up to 1 mL. In general, 150 mg of fresh Mo_xC samples were employed in RWGS reaction without pre-treatment. Prior to entering the reactant mixture, the temperature was increased from room temperature up to 325 °C under a N_2 flow. The RWGS was studied at a moderate temperature range (275-400 °C); and in order to evaluate the catalytic stability of Mo_xC, the following reaction temperature sequence was used: 325 °C (3 h)→300 °C(3 h)→275 °C (10 h)→325 °C (3 h)→350 °C (3 h)→375 °C (3 h)→400 °C (3 h)→375 °C (5 h).

RWGS reaction using $CO_2/H_2/N_2$=1/3/1

All Mo_xC catalysts were active in the RWGS reaction under the experimental conditions used. Figure 4.16 shows the variation of CO_2 conversion (Figure 4.16A) and the selectivity to CO (Figure 4.16B) achieved over bulk Mo_xC catalysts as a function of the temperature. The corresponding values of CO_2 conversion and CO yield determined at different temperatures are listed in Table 4.2.

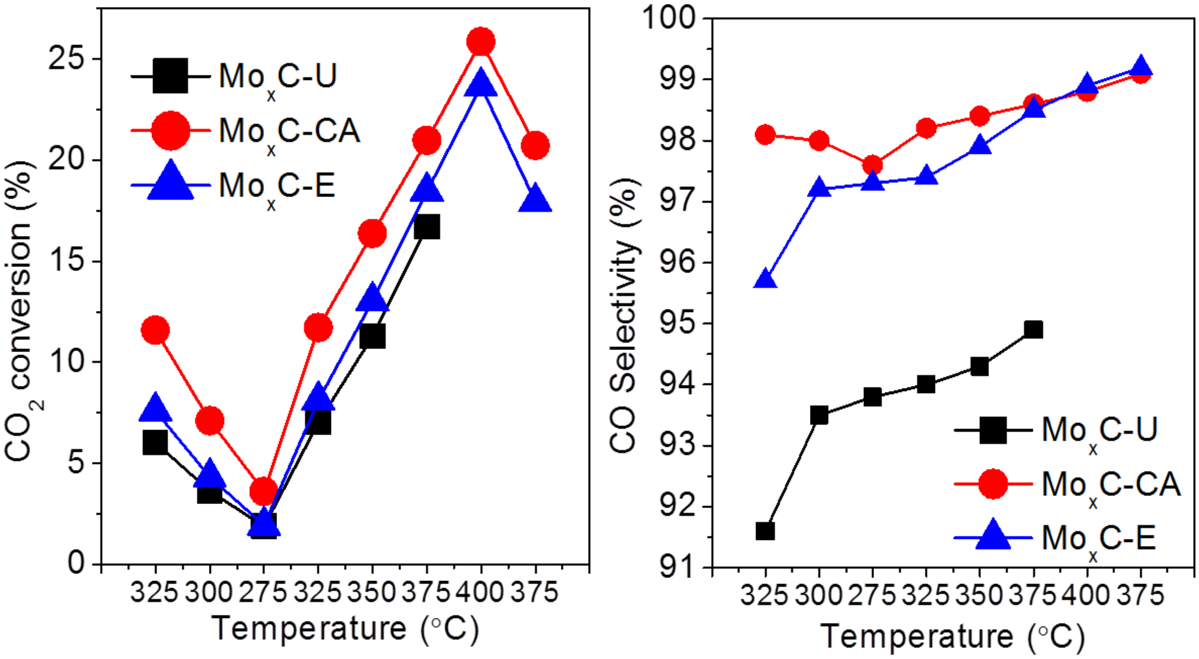

Figure 4.16. Catalytic behaviour of bulk Mo_xC in RWGS reaction: (A) CO_2 conversion; (B) CO selectivity. Reaction conditions: 150 mg catalyst, $CO_2/H_2/N_2$=1/3/1, GHSV=3000 h^{-1}, P=0.1 MPa, T=275-400 °C.

In all cases, CO_2 conversion increased with the increase of temperature. The CO_2 conversion followed the order: Mo_xC-CA>Mo_xC-E>Mo_xC-U. At 400 °C over Mo_xC-CA, which showed the highest S_{BET} (14.5 m^2/g), a CO_2 conversion of 25.9% was achieved; the corresponding equilibrium CO_2 conversion for RWGS at the experimental conditions used is about 37%. As can be seen in Figure 4.16A, Mo_xC-U which showed the lowest S_{BET} (7.7 m^2/g) and in which the only presence of hexagonal Mo_2C was found, showed a slightly lower activity than the other two catalysts.

Table 4.2. CO_2 conversion and CO yield values obtained over Mo_xC catalysts during the RWGS catalytic test. Reaction conditions: 150 mg catalyst, $CO_2/H_2/N_2$=1/3/1, GHSV=3000 h^{-1}, P=0.1 MPa, T=275-400 °C.

T(°C)	Time* (h)	CO_2 Conversion (%)			CO yield (mmol/Kg_{cat}•h)		
		Mo_xC-U	Mo_xC-CA	Mo_xC-E	Mo_xC-U	Mo_xC-CA	Mo_xC-E
325	3	6.0	11.6	7.6	8964	18600	11897
300	6.3	3.6	7.1	4.3	5517	11394	6868
275	17	1.9	3.6	1.9	2871	5747	3087
325	20.3	7.0	11.7	8.1	10769	18823	12953
350	23.7	11.3	16.4	13.1	17340	26360	20903
375	27	16.7	21.0	18.5	25864	33836	29772
400	30.3	-	25.9	23.7	-	41806	38268
375	35.7	-	20.7	17.9	-	33599	29092

* Total reaction time at the last stage of the corresponding temperature.

Under the reaction conditions used, the main product found was CO, only small amounts of CH_4 and negligible amounts of ethylene and propylene were detected as a function of the temperature. As shown in Figure 4.16B, all catalysts showed CO selectivity values higher than 90% in the studied temperature range. Mo_xC-U sample showed the lowest CO selectivity, while for Mo_xC-CA, CO selectivity reached up to 99% at 400 °C. Moreover, as shown in Table 4.2, Mo_xC-CA shows the highest CO yield under the conditions used.

With respect the stability of these systems under RWGS reaction conditions, we can analyze the catalytic behaviour obtained at 325 °C, initially and after 20.3 h of catalytic test. In all cases, a slight increase of the CO_2 conversion and CO selectivity were found (Figure 4.16). Accordingly, the CO yield at 325 °C after 20.3 h reaction was also higher than that initially found at this temperature

(325 °C, 3 h) (Table 4.2). This finding may indicate the rearrangement of the surface of catalyst during the reaction test under the experimental conditions used. Moreover, the CO_2 conversion obtained at 375 °C after 35.7 h of catalytic test, once the RWGS was studied at 400 °C, was only slightly lower than that found at 375 °C after 27 h of reaction.

The apparent Ea for CO production in the temperature range of 275-325 °C was calculated from the Arrhenius plots as shown in Figure 4.17. The obtained apparent Ea values were 72.0±2.3, 64.8±4.1, and 78.2±3.2 kJ/mol, for Mo_xC-U, Mo_xC-CA and Mo_xC-E, respectively. The Mo_xC-CA catalyst that showed the highest CO_2 conversion and CO selectivity also showed the lowest apparent Ea for CO production.

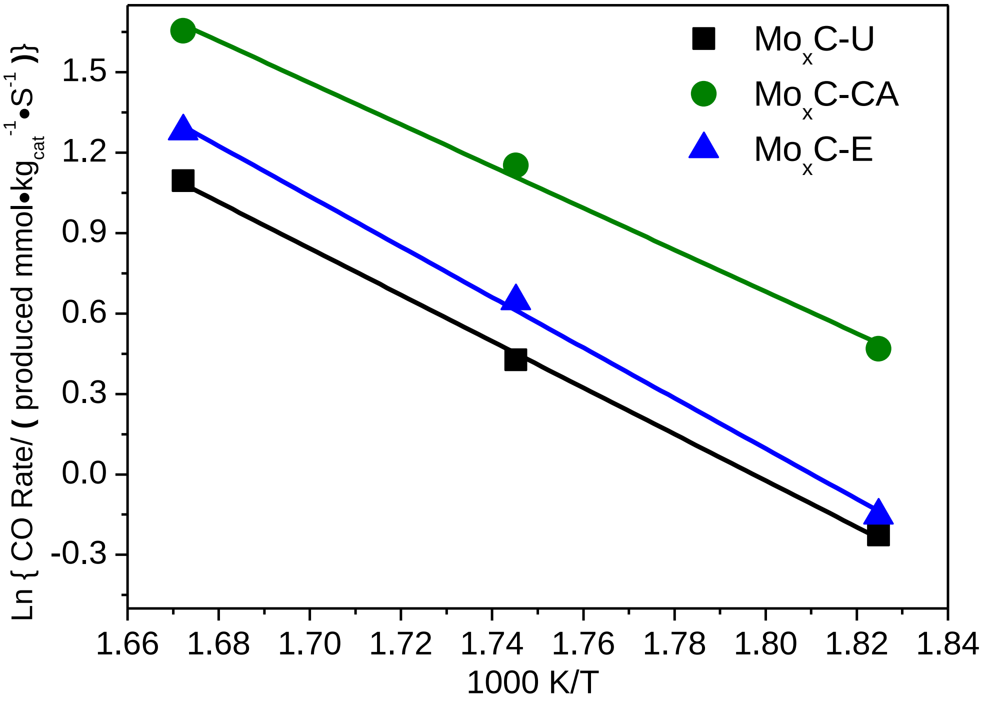

Figure 4.17. Arrhenius plots for CO production over Mo_xC catalysts. Reaction conditions: 150 mg catalyst, $CO_2/H_2/N_2$=1/3/1, GHSV=3000 h^{-1}, P=0.1 MPa, T=275-325 °C.

Post-reaction catalysts

Post-reaction catalysts were analyzed by XRD, Raman spectroscopy and S_{BET} measurements. Figure 4.18 shows the XRD patterns of post-reaction catalysts. Similar XRD patterns than those of the corresponding fresh catalysts (Figure 4.2) were obtained.

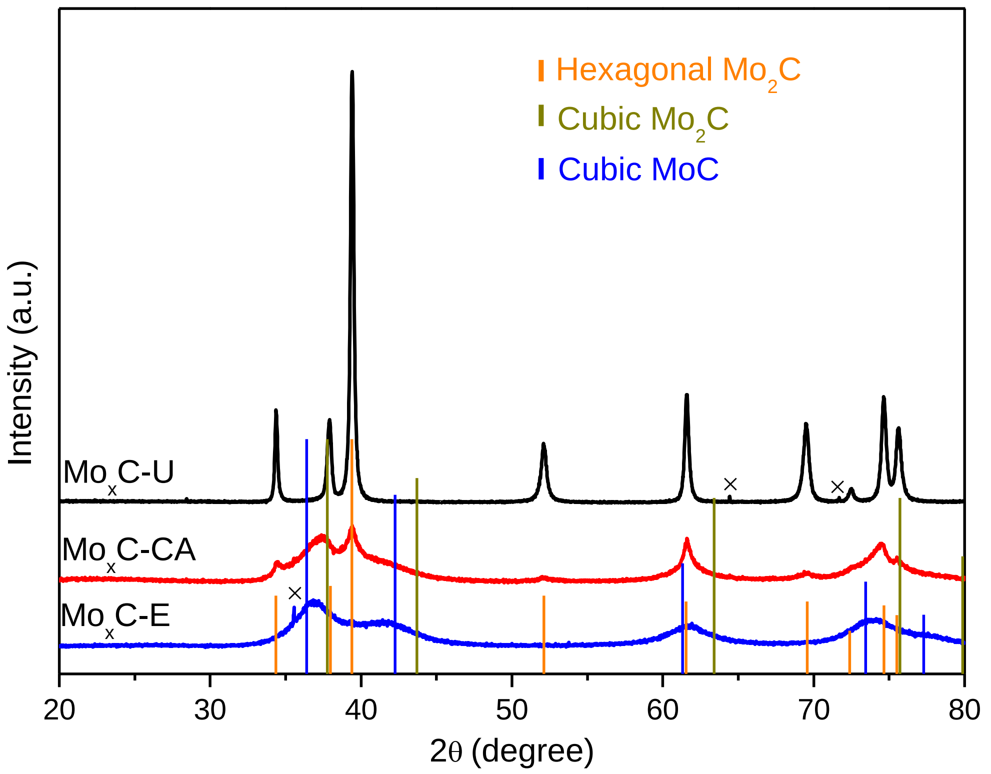

Figure 4.18. XRD patterns of the post-reaction Mo_xC catalysts. × signals correspond to impurities of SiC used as dilution agent in the catalytic test. Reaction conditions: 150 mg catalysts, $CO_2/H_2/N_2$=1/3/1, GHSV=3000 h^{-1}, P=0.1 MPa, T=275-400 °C.

The crystallite size of Mo_xC calculated using the diffraction peak at 2θ=61.6 ° was about 32.5, 14.8 and 3.2 nm for Mo_xC-U, Mo_xC-CA and Mo_xC-E, respectively. These values are quite similar to those determined for fresh catalysts (35.2 nm, Mo_xC-U; 12.2 nm, Mo_xC-CA; 4.6 nm, Mo_xC-E).

S_{BET} of post-reaction Mo_xC-U and Mo_xC-E catalysts was 5.3 and 11.5 m^2/g, respectively; these values are similar to those of fresh catalysts (7.7 m^2/g, Mo_xC-U; 8.9 m^2/g, Mo_xC-E). The S_{BET} of Mo_xC-CA was not determined.

Figure 4.19 shows the Raman spectra of post-reaction catalysts. Raman spectra below 1000 cm^{-1} of post-reaction Mo_xC-U and Mo_xC-E showed bands with lower intensity than that of fresh catalysts (Figure 4.3); this could be related to the decrease of the number of oxide species on the surface of Mo_xC produced during the RWGS.

Raman spectra of post-reaction and fresh Mo_xC-CA were very similar (Figure 4.19 and 4.3); as stated above, in this case only bands with a very low intensity were found in the range 100-1000 cm^{-1} in all the zones analyzed. For Mo_xC-CA and Mo_xC-E, the D and G bands were also found after reaction.

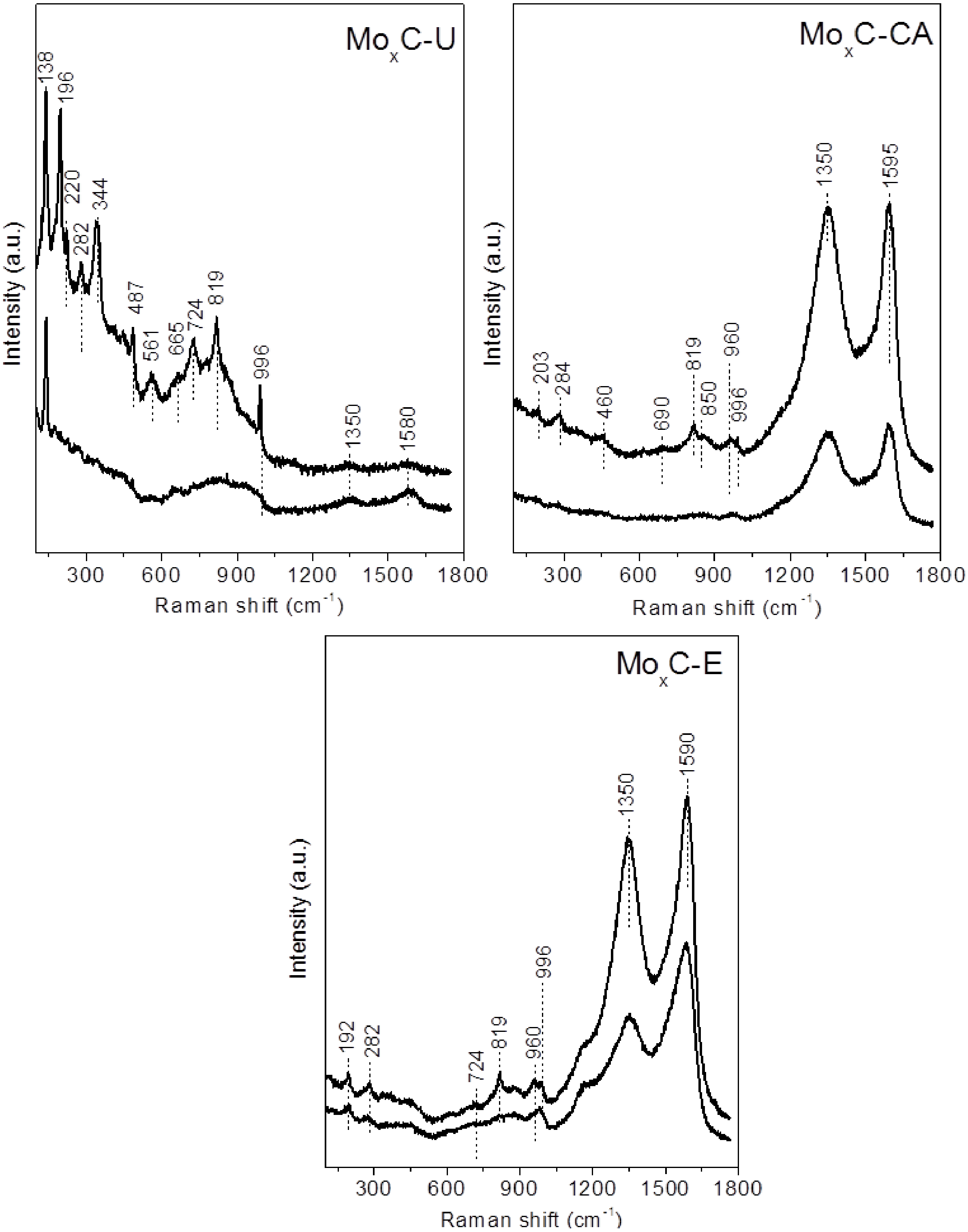

Figure 4.19. Raman spectra of post-reaction Mo_xC catalysts in two different representative zones. Reaction conditions: $CO_2/H_2/N_2=1/3/1$, GHSV=3000 h^{-1}, P=0.1 MPa, T=275-400 °C.

RWGS reaction using $CO_2/H_2/N_2$=1/1/3

As stated above, Mo_xC-U showed the only presence of the hexagonal Mo_2C phase and some of its characteristics experimentally determined, were possible to be rationalized in the light of theoretical studies carried out in the group of Prof. Illas (UB).

Mo_xC-U was chosen for a deeper study of the RWGS reaction; the RWGS reaction was also studied over Mo_xC-U using the stoichiometric CO_2/H_2=1/1 reactant mixture. Figure 4.20 shows the variation of CO_2 conversion and CO selectivity, with the reaction temperature, at atmospheric pressure under these conditions. As expected, CO_2 conversion and CO selectivity increased with the increase of temperature.

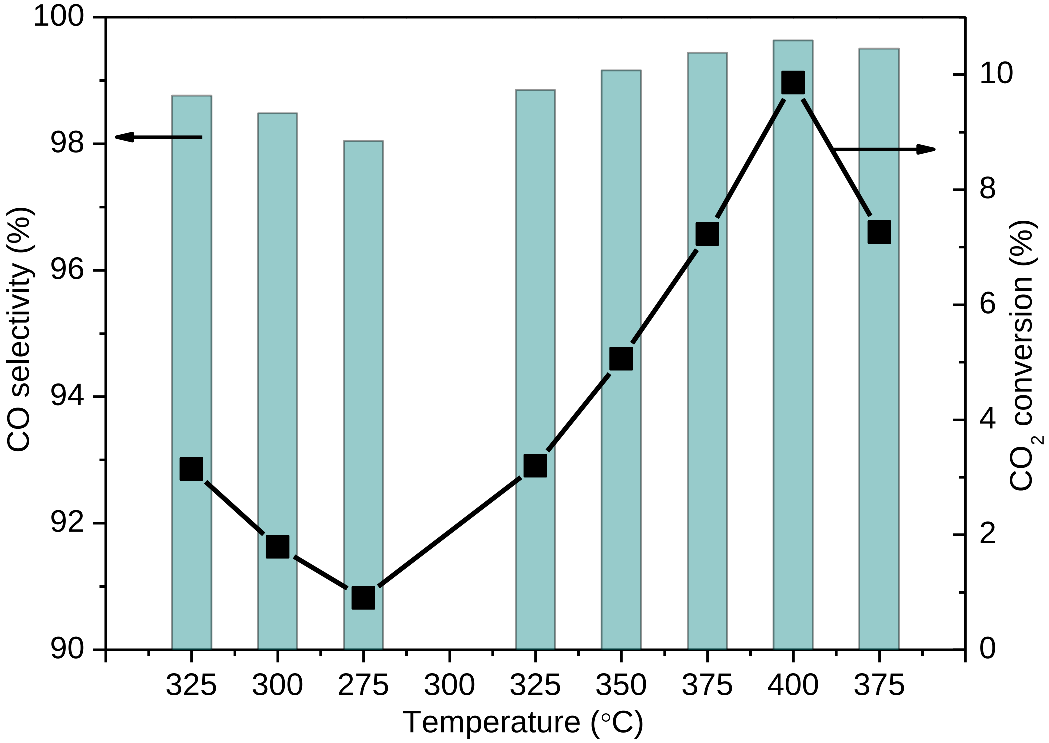

Figure 4.20. Catalytic behaviour of Mo_xC-U in RWGS reaction; CO_2 conversion and CO selectivity as a function of reaction temperature. Reaction conditions: 150 mg catalyst, $CO_2/H_2/N_2$=1/1/3, GHSV=3000 h^{-1}, P=0.1 MPa.

Values of CO_2 conversion were lower than those obtained when a $CO_2/H_2=1/3$ mixture (Figure 4.16) was used. However, higher values of CO selectivity were obtained; CO selectivity was always higher than 98% and approached to 100% at 400 °C. Besides CO, only very small amounts of CH_4 were detected. Moreover, similar values of CO_2 conversion and selectivity to CO were found at 375 ° after 27 h and 35.7 h on-stream.

Post-reaction Mo$_x$C-U was characterized by XRD, Raman spectroscopy, XPS and SEM. The corresponding XRD pattern and Raman spectrum are shown in Figure 4.21.

The XRD pattern registered for the used catalyst (Figure 4.21A) was similar to that of the fresh sample (Figure 4.2), indicating the only presence of hexagonal Mo_2C. After reaction, a crystallite size of 35.5 nm, also similar to that of fresh catalyst (35.2 nm), was calculated. As shown in Figure 4.21B, after the RWGS reaction, characteristic Raman bands of orthorhombic (998, 823, 668 cm^{-1}) and monoclinic (852 and 780 cm^{-1}) MoO_3 were found [9,12,14].

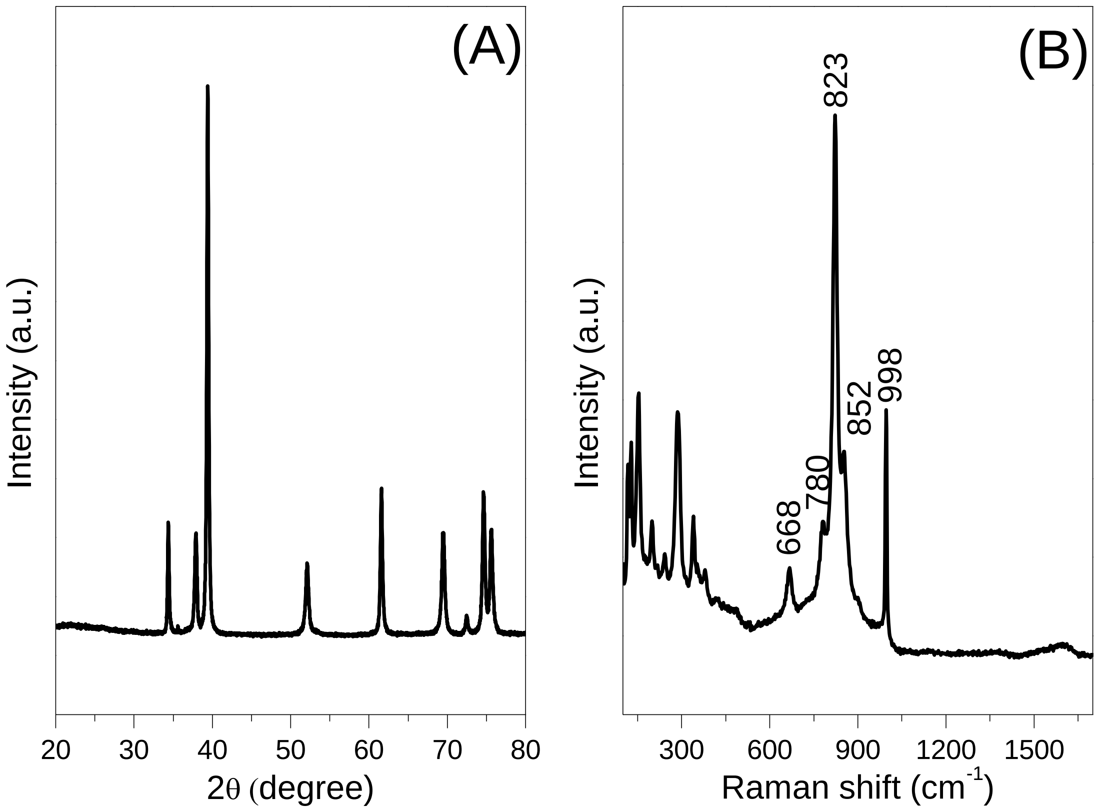

Figure 4.21. (A) XRD pattern and, (B) Raman spectrum of post-reaction Mo_xC-U sample. Reaction conditions: 150 mg catalyst, $CO_2/H_2/N_2$=1/1/3, GHSV=3000 h^{-1}, P=0.1 MPa, T=275-400 °C.

Figure 4.22 shows the XPS profiles of Mo 3d, C 1s and O 1s core levels of post-reaction Mo_xC-U catalyst. The spectrum of Mo 3d level of the catalyst after reaction has no significant differences with respect to that of fresh sample. The C 1s and O 1s profiles of Mo_xC-U after reaction showed some differences when they are compared to those of fresh Mo_xC-U. After the catalytic test using $CO_2/H_2/N_2$=1/1/3 mixture, a higher amount of C-O, C=O and carbide species on the surface is proposed to exist.

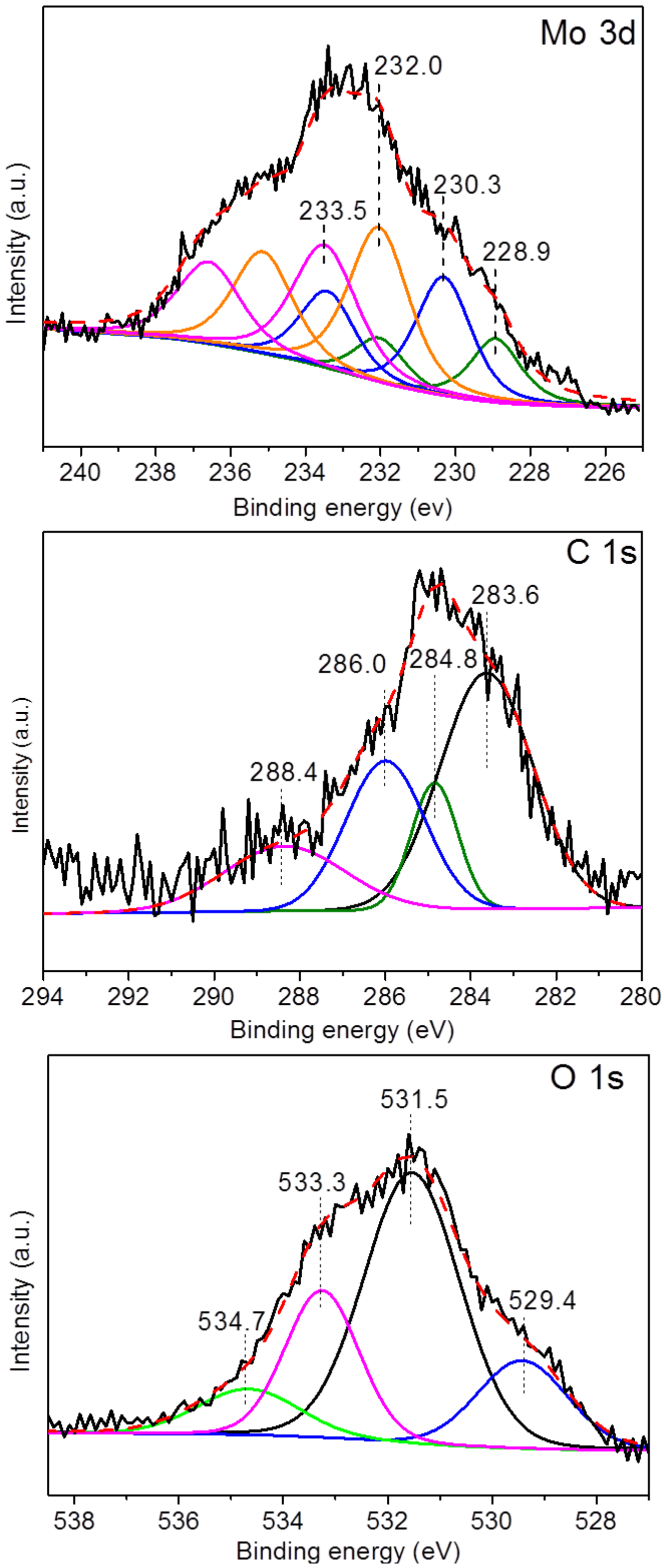

Figure 4.22. XPS profiles of Mo 3d, C 1s and O 1s of post-reaction Mo_xC-U catalyst. Reaction conditions: 150 mg catalyst, $CO_2/H_2/N_2=1/1/3$, GHSV=3000 h^{-1}, P=0.1 MPa, T=275-400 °C.

Figure 4.23 presents the SEM images and element distribution determined by EDX of post-reaction Mo_xC-U catalyst. No significant changes in the morphology of the catalyst were produced during the catalytic test; after reaction also a homogeneous distribution of Mo, C and O was found.

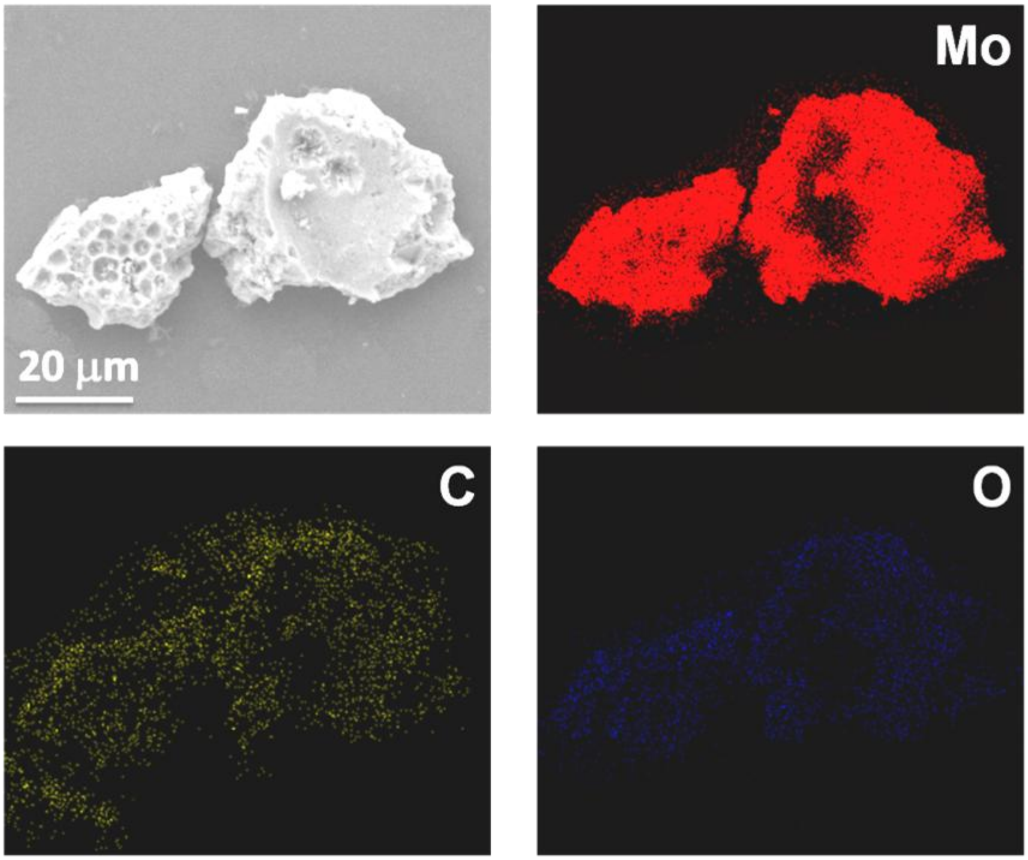

Figure 4.23. SEM images and element distribution determined by EDX of post-reaction Mo_xC-U. Reaction conditions: 150 mg catalyst, $CO_2/H_2/N_2$=1/1/3, GHSV=3000 h^{-1}, P=0.1 MPa, T=275-400 °C.

Taking into account that the CO_2 conversion achieved over the Mo_xC-U using the reactant mixture $CO_2/H_2/N_2$=1/1/3 (about 10% at 400 °C) was far from the corresponding equilibrium (ca. 22% at 400 °C), we performed a new catalytic test using 300 mg of Mo_xC-U instead 150 mg.

The new catalytic test was carried out at GHSV of 3000 h^{-1} with the following temperature sequence:

275 °C (3 h)→300 °C (3 h)→325 °C (3 h)→350 °C (3 h)→375 °C (3 h)→400 °C (3 h). Figure 4.24 shows the values of CO_2 conversion and CO selectivity obtained as a function of temperature. Higher values of CO_2 conversion were obtained if they are compared with those achieved when 150 mg of catalyst were used. The CO_2 conversion reached about 16% at 400 °C. As expected, CO was the main product and only very small amounts of CH_4 as by-product were detected. In all the temperature range, the CO selectivity was above 97.5%; again, the selectivity values slightly increased with the increase of temperature, reaching about 99.5% at 400 °C.

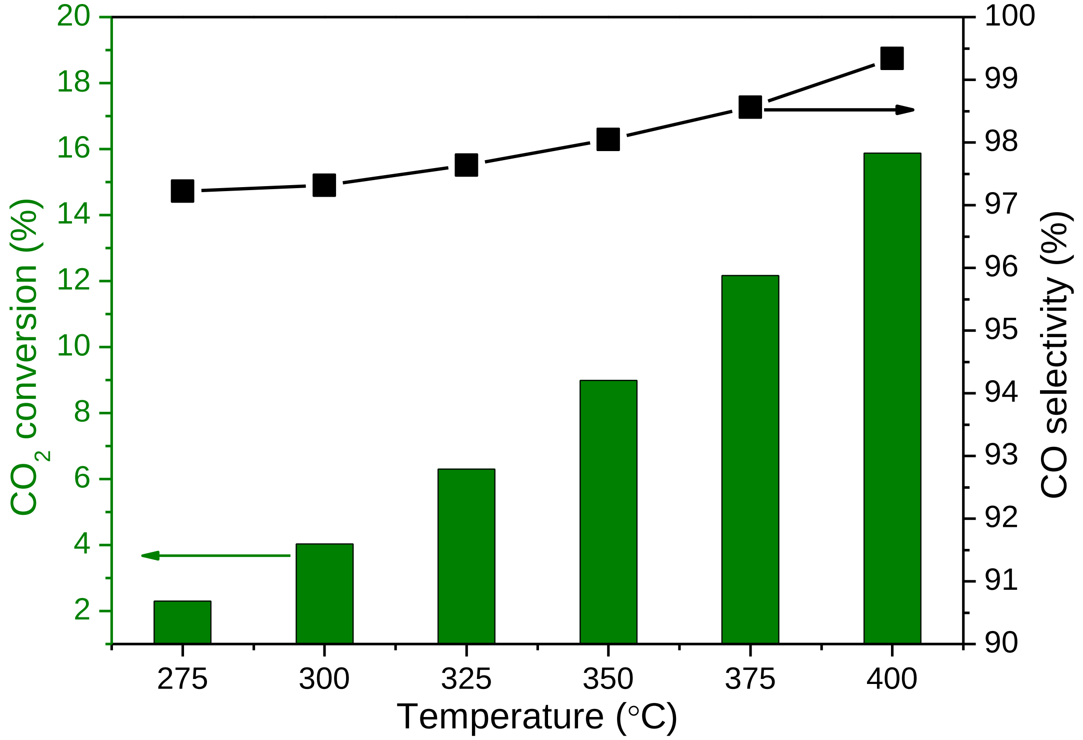

Figure 4.24. Catalytic behaviour of Mo_xC-U in the RWGS reaction. CO_2 conversion and CO selectivity as a function of reaction temperature. Reaction conditions: 300 mg catalyst, $CO_2/H_2/N_2$=1/1/3, GHSV=3000 h^{-1}, T=275-400 °C, P=0.1 MPa.

The apparent Ea values for CO production were calculated from the Arrhenius plots (Figure 4.25) in the temperature ranges of 275-325 °C and 350-

400 °C; apparent Ea values of 55.2±2.3 (275-325 °C) and 40.6±0.5 kJ/mol (350-400 °C) were obtained. The apparent Ea value of 55.2±2.3 kJ/mol, obtained in the 275-325 °C region, is close to the DFT calculated energy barriers for CO_2 dissociation over (101)-Mo/C surface (0.59 eV) of hexagonal Mo_2C [28].

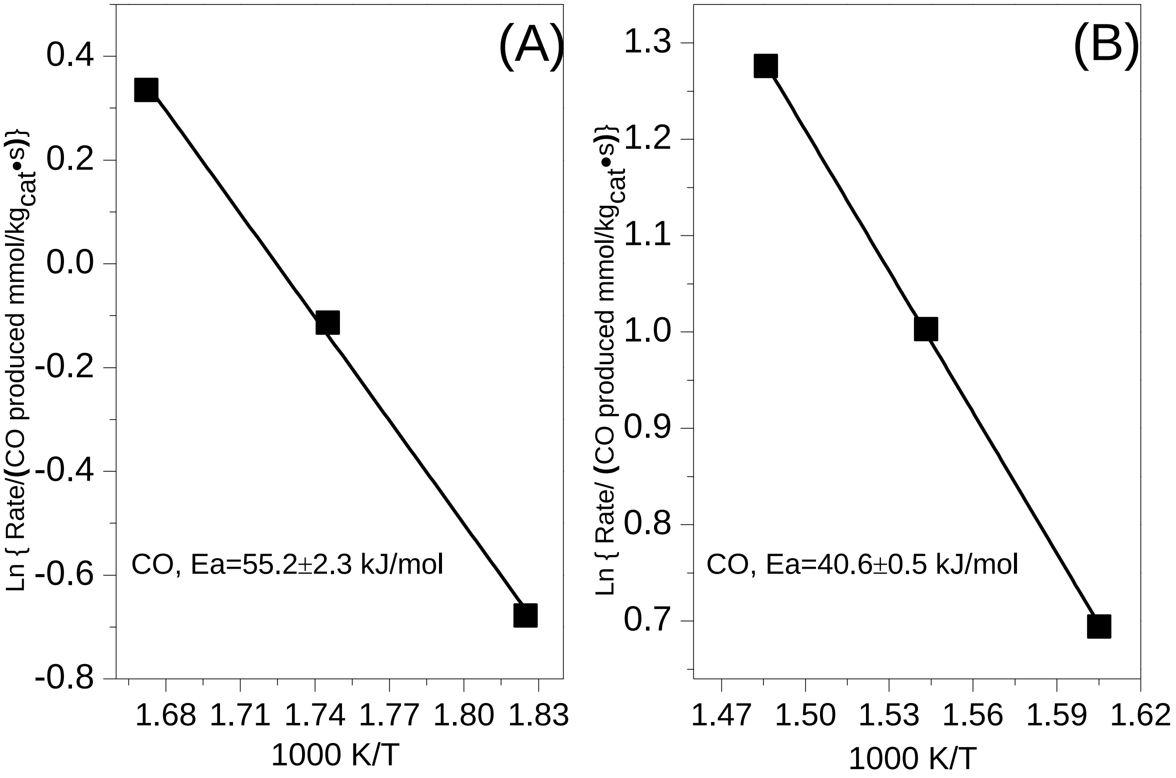

Figure 4.25. Arrhenius plots of CO production over Mo_xC-U sample at 275-325°C (A) and 350-400 °C (B). Reaction conditions: $CO_2/H_2/N_2$=1/1/3, GHSV=3000 h^{-1}, P=0.1 MPa.

After the catalytic test previously discussed (Figure 4.24), temperature was kept at 400 °C and the GHSV was increased up to 6000 h^{-1}. The variation of CO_2 conversion and CO selectivity is shown in Figure 4.26. The CO_2 conversion decreased from 16 to 13.5% when the contact time decreased. However, the selectivity toward CO approached 100% under the experimental conditions used.

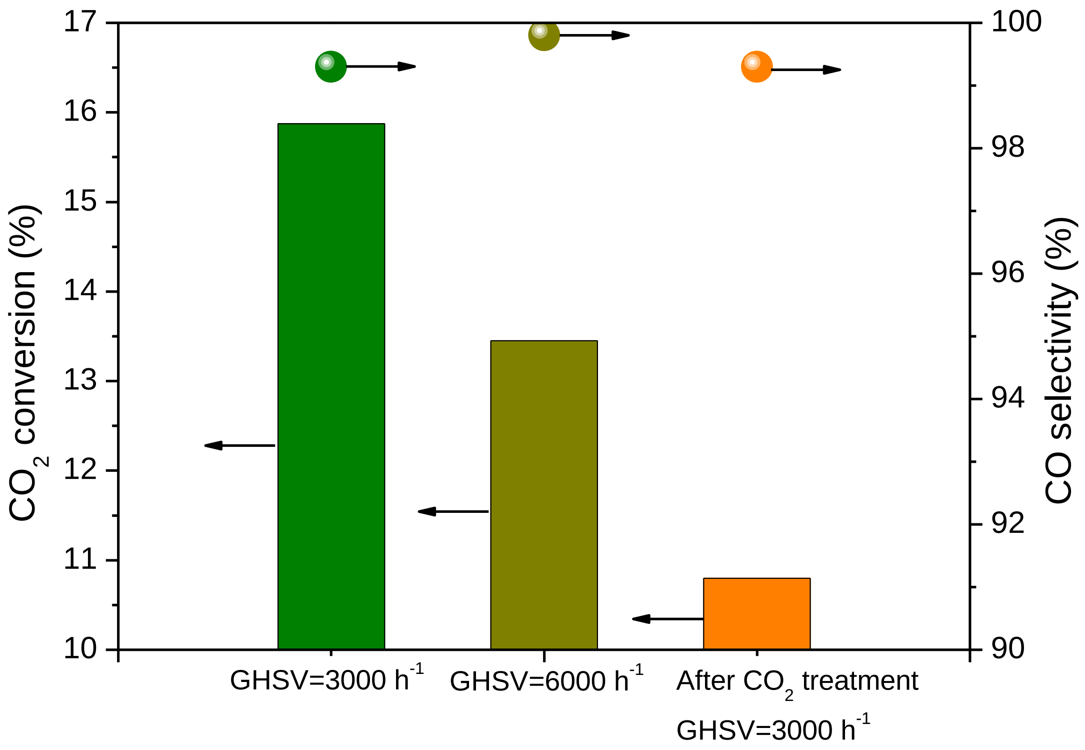

Figure 4.26. Catalytic behaviour of Mo_xC-U in the RWGS. Variation of CO_2 conversion and CO selectivity as a function of GHSV, and values obtained after treatment of Mo_xC-U with CO_2 at 400 °C (22 h). Reaction conditions: 300 mg catalyst, $CO_2/H_2/N_2$=1/1/3, T=400 °C, P=0.1 MPa.

As stated above, the CO formation over Mo_xC-U catalyst could be related to the easiness of CO_2 dissociation. Moreover, the characteristics of the catalyst changed after a treatment with CO_2 at 400 °C. For a more complete study of Mo_xC-U, a new separate RWGS experiment was carried out after a CO_2 treatment at 400 °C. In order to have a comparison with previous results, 300 mg of fresh Mo_xC-U sample were in-situ treated with CO_2/He flow at 400 °C for 22 h previously to the RWGS test. During the CO_2 treatment, CO was detected in the reactor effluent by GC; its concentration decreased with time. After this treatment, the catalyst was exposed to $CO_2/H_2/N_2$=1/1/3 reactant mixture under a GHSV of 3000 h^{-1}.

Figure 4.26 presents the CO_2 conversion and CO selectivity when RWGS was carried out over the CO_2-treated Mo_xC-U catalyst. The CO_2 conversion was very much lower than that reached over the fresh Mo_xC-U. Meanwhile, fresh and CO_2-treated Mo_xC-U showed similar values of CO selectivity. The lower activity of CO_2-treated Mo_xC-U when compared with fresh Mo_xC-U is related to the formation of MoO_2 during the CO_2 treatment, according with XRD, Raman and H_2-TPR results (Figures 4.13 and 4.15) discussed above. The oxidation of Mo_2C to MoO_2 led to the decrease of the number of surface active centres for RWGS. The deactivation reported during the dry reforming of CH_4 with CO_2 has been also related to the oxidation of Mo_2C to MoO_2 [30]. However, under the RWGS conditions used in the present work, a high stability was observed. H_2 in the reactant mixture could reduce oxycarbide species but could not reduce MoO_2.

4.2. Supported Mo_xC-U catalysts

4.2.1. Preparation of supported Mo_xC-U catalysts

Taking into account that the characterization of Mo_xC-U points out the only presence of hexagonal Mo_2C, the method used for the preparation of Mo_xC-U was applied for the preparation of γ-Al_2O_3-, TiO_2-, SBA-15- and SiO_2-supported Mo_xC-U. The following commercial oxides were used as supports:

- **γ-Al_2O_3:** purchased from Alfa Aesar; the pellets were powdered before using.
- **TiO_2:** purchased from TECNAN which contains rutile and anatase phases, named as TiO_2-AR.
- **TiO_2 (anatase):** supplied by Sigma-Aldrich, labelled as TiO_2-A.
- **SiO_2:** Aerosil 200 (Degussa).
- **SBA-15:** purchased from Glantreo.

Moreover, TiO_2-A was heated at 850 °C for 12 h under ambient air in an oven; Rutile TiO_2 obtained was also used as support, it was denoted as TiO_2-R.

Preparation of supported catalysts: A viscous solution, which contained $MoCl_5$, urea and ethanol similar to the one used in the preparation of Mo_xC-U, was contacted with the corresponding support with continuous stirring overnight. Supported samples with different content of Mo (1, 5 or 25 wt%) were prepared. After adding the support to the viscous solution, the samples were dried at 60 °C in an oven under air. Then, they were treated at 150 °C for 3 h and at 800 °C for 3 h under Ar flow in a quartz tubular reactor. Finally, the reactor was cooled down to room temperature under Ar flow, and then the catalyst was exposed to the ambient air without any passivation. Samples were labelled as yMo_xC/Support, where “y” is the weight percentage of Mo in the catalyst. More details of preparation are given in Annex II.

4.2.2. Characterization of supported Mo_xC-U catalysts

Table 4.2 shows the values of Mo content and, those of S_{BET} of fresh yMo_xC/Support catalysts. For comparison, the values of S_{BET} of the supports after a treatment up to 800 °C (3 h) under Ar are also given.

In general, the values of S_{BET} were lower than those of the corresponding supports, and, they diminished with the Mo content.

Table 4.2. Mo content determined from ICP-AES analysis and, S_{BET} of fresh catalysts and supports.

Catalyst	wt% Mo	BET (m^2/g)
$25Mo_xC/\gamma\text{-}Al_2O_3$	25.1	118.8
$25Mo_xC/SiO_2$	25.5	129.3
$25Mo_xC$/SBA-15	22.4	379.4
$25Mo_xC/TiO_2$-AR	27.5	38.7
$25Mo_xC/TiO_2$-A	26.1	26.7
$25Mo_xC/TiO_2$-R	24.6	<5
$5Mo_xC/\gamma\text{-}Al_2O_3$	4.5	190.7
$5Mo_xC/SiO_2$	5.4	176.1
$5Mo_xC$/SBA-15	5.7	443.8
$5Mo_xC/TiO_2$-AR	4.7	5.4
$1Mo_xC/TiO_2$-AR	1.1	7.9
$\gamma\text{-}Al_2O_3$	-	203.9
SiO_2	-	181.0
SBA-15	-	436.1
TiO_2-AR	-	12.8

The crystalline phases present in yMo_xC/Support catalysts were determined using XRD (Figures 4.27-4.30). Figure 4.27 shows the XRD patterns of $\gamma\text{-}Al_2O_3$-supported catalysts, the XRD profile of $\gamma\text{-}Al_2O_3$ is also presented for comparison purposes. For $25Mo_xC/\gamma\text{-}Al_2O_3$, the characteristic diffraction peaks of hexagonal Mo_2C and $\gamma\text{-}Al_2O_3$ can be observed. However, from the XRD pattern of $5Mo_xC/\gamma\text{-}Al_2O_3$, the presence of hexagonal Mo_2C cannot be deduced; this might be due to the presence of a small amount of Mo_2C or/and a low crystallinity of Mo_2C in the catalyst.

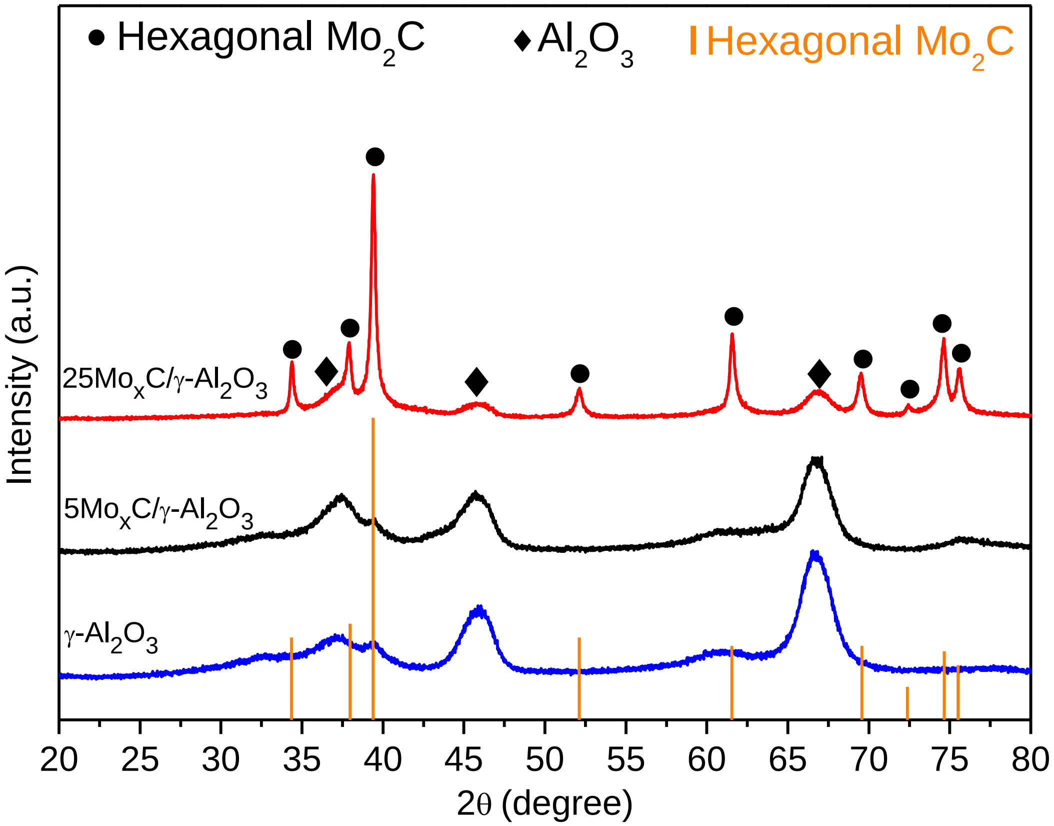

Figure 4.27. XRD patterns of fresh yMo_xC/γ-Al_2O_3 catalysts.

Figure 4.28 shows the XRD patterns of SiO_2-supported catalysts. For $25Mo_xC/SiO_2$, the main presence of hexagonal Mo_2C can be deduced. Moreover, the peaks with maximum at 2θ=36.9° and 2θ=42.1° might be related to the presence of cubic MoC. For $5Mo_xC/SiO_2$, XRD peaks assigned to the hexagonal Mo_2C and cubic Mo (JCPDS 00-004-0809) were clearly observed. Moreover, in $5Mo_xC/SiO_2$, the presence of tetragonal Mo_2N (JCPDS 01-075-1150) could not be ruled out; indeed, the presence of both hexagonal Mo_2C and tetragonal Mo_2N could contribute to the peak centered at 2θ=37.7°.

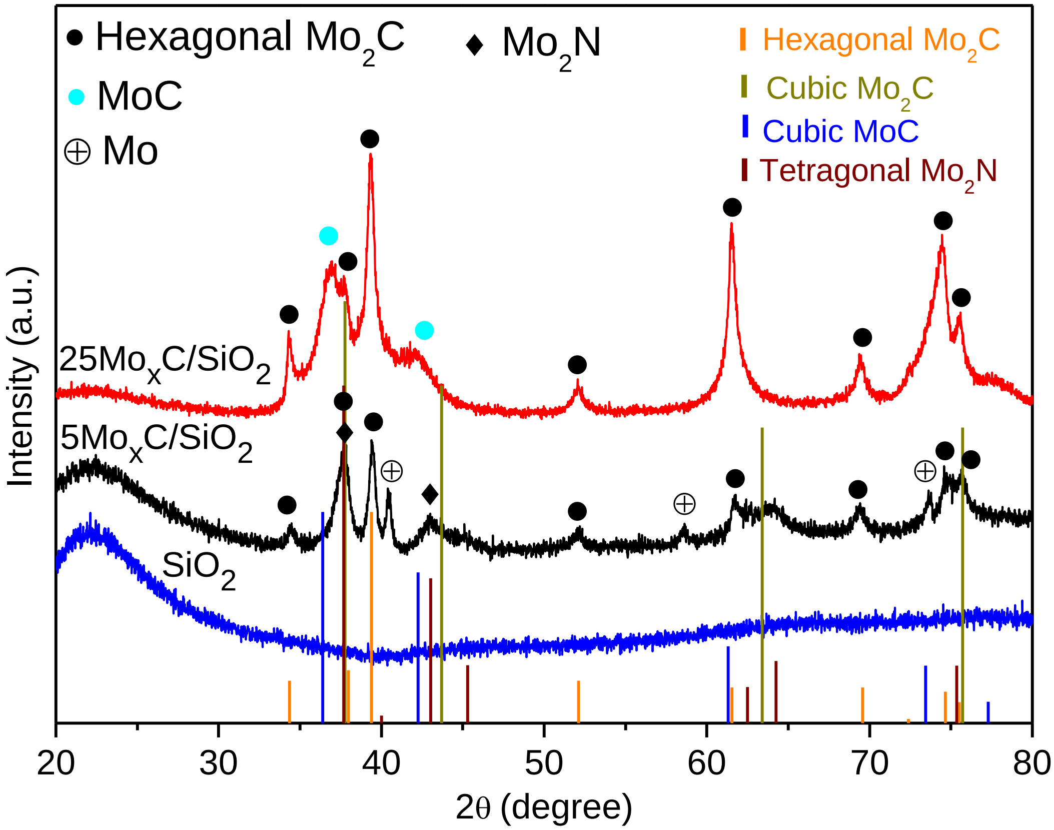

Figure 4.28. XRD patterns of fresh yMo_xC/SiO_2 catalysts.

Figure 4.29 shows the XRD patterns of 25Mo_xC/SBA-15, 5Mo_xC/SBA-15 and that of the corresponding SBA-15 support.

For 25Mo_xC/SBA-15, several broad peaks were observed, close to the zone in which peaks of cubic Mo_2C and MoC are expected; this fact makes difficult the straightforward assignation of these peaks (Figure 4.29). Moreover, two sharp peaks at 2θ=40.5° and 2θ=39.4° attributed to the most intense peak of Mo metal and hexagonal Mo_2C, respectively, were found.

From XRD pattern of 5Mo_xC/SBA-15, the presence of mainly cubic Mo_2C can be proposed; the low intensity peak at 2θ=40.5° could be indicative of the formation of a small amount of crystalline Mo.

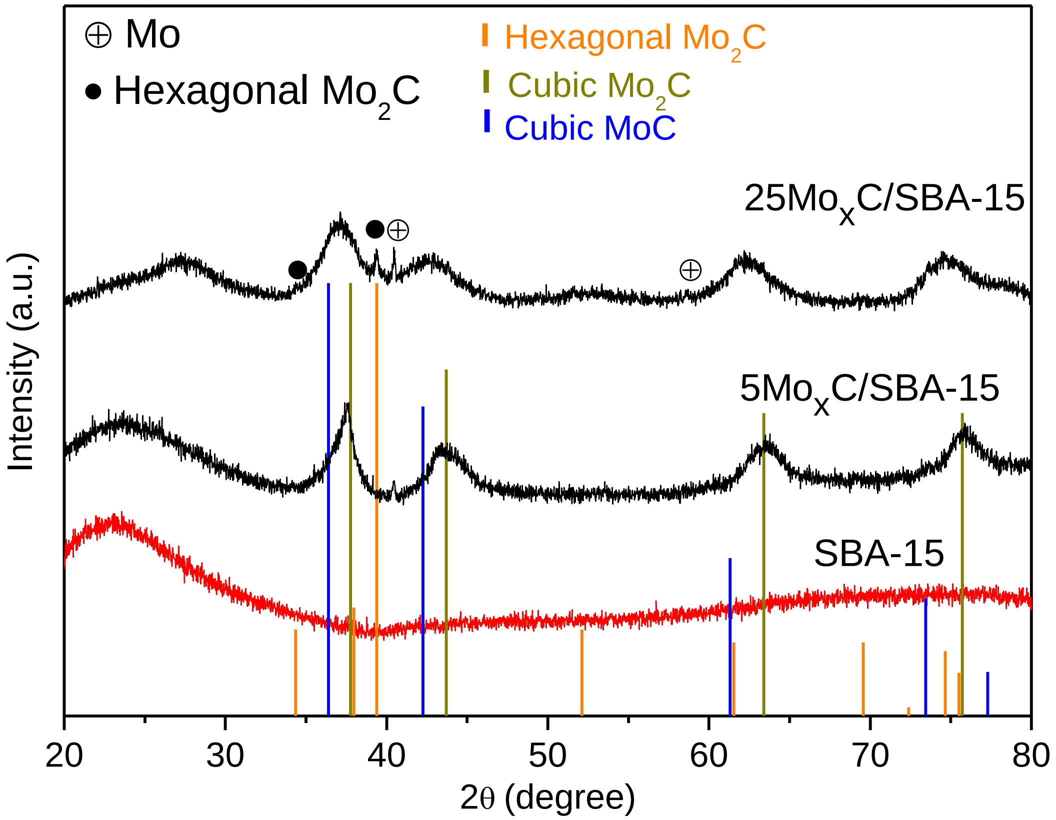

Figure 4.29. XRD patterns of fresh yMo_xC/SBA-15 catalysts.

Figure 4.30 shows the XRD pattern of yMo_xC/TiO_2 catalysts and that of TiO_2-AR support. In the XRD patterns of yMo_xC/TiO_2-AR, characteristic peaks of rutile and anatase can be found. For $1Mo_xC/TiO_2$-AR and $5Mo_xC/TiO_2$-AR, the intensity of the peaks related to rutile are higher than that of the characteristic peaks of anatase. The same situation was found for the support used in the preparation of catalysts. However, in the XRD pattern of $25Mo_xC/TiO_2$-AR, the intensity of the peaks of anatase is higher than that of rutile peaks. This indicates a transformation of the support during the preparation of the catalyst. The higher BET surface area of $25Mo_xC/TiO_2$-AR when compared to that of TiO_2-AR may be related with the mentioned change. From XRD pattern of $25Mo_xC/TiO_2$-AR, the presence of hexagonal Mo_2C with a poor crystallinity cannot be ruled out.

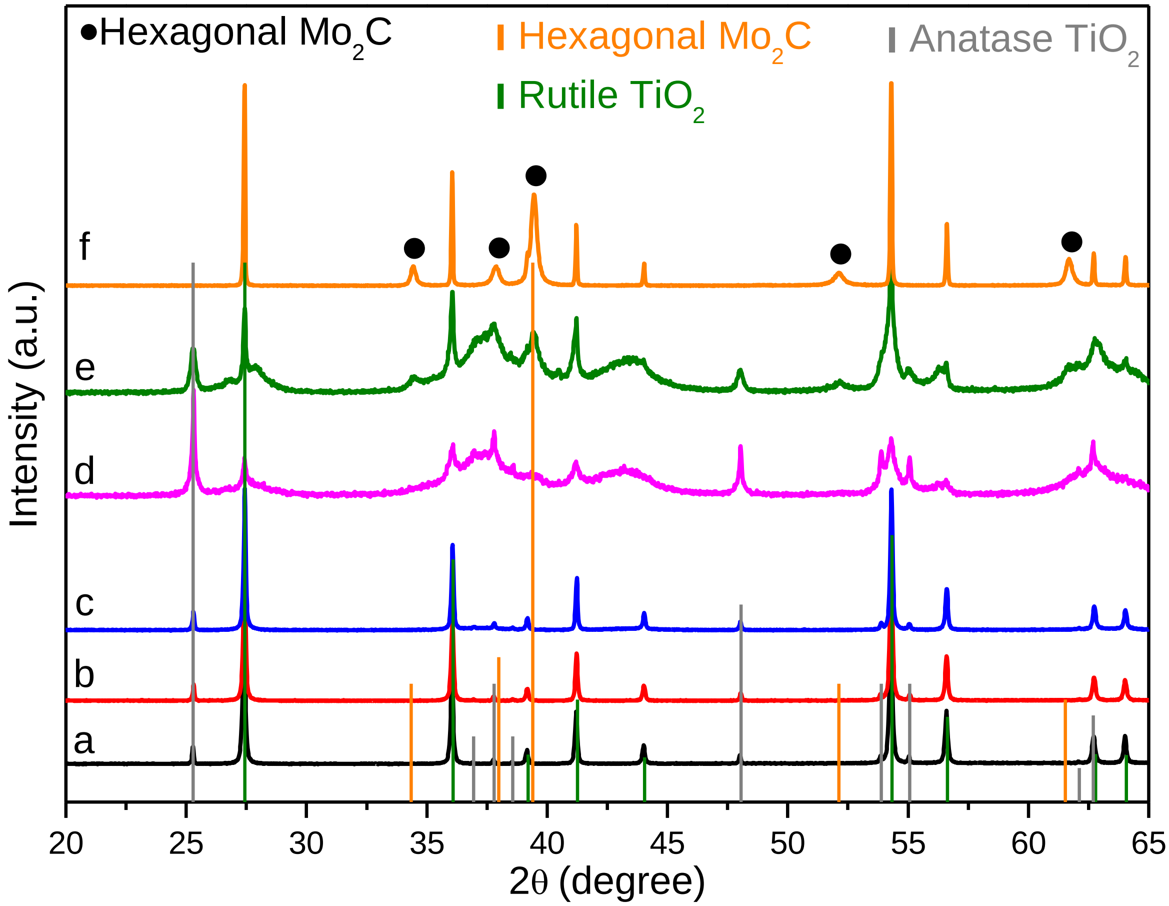

Figure 4.30. XRD patterns of fresh yMo_xC/TiO_2 catalysts. (a) TiO_2-AR; (b) $1Mo_xC/TiO_2$-AR; (c) $5Mo_xC/TiO_2$-AR; (d) $25Mo_xC/TiO_2$-AR; (e) $25Mo_xC/TiO_2$-A; (f) $25Mo_xC/TiO_2$-R.

XRD pattern of $25Mo_xC/TiO_2$-A points the presence of both anatase and rutile TiO_2, indicating a partial transformation of anatase to rutile during the preparation of the catalyst. For $25Mo_xC/TiO_2$-A, the presence of poorly crystalline hexagonal Mo_2C can be proposed. In the XRD pattern of $25Mo_xC/TiO_2$-R, definite peaks characteristic of the presence of rutile and hexagonal Mo_2C are only found. It is not possible the identification of Mo_xC phase in $1Mo_xC/TiO_2$-AR and $5Mo_xC/TiO_2$-AR catalysts.

Figure 4.31A shows the Raman spectra of fresh $25Mo_xC$/Support catalysts. As previously discussed for bulk Mo_xC-U, some of the Raman bands appearing below 1000 cm^{-1} can be related to the presence of different MoO_3 and/or MoO_{3-x}, which resulted from the surface oxidation when the samples were exposed to the air [7].

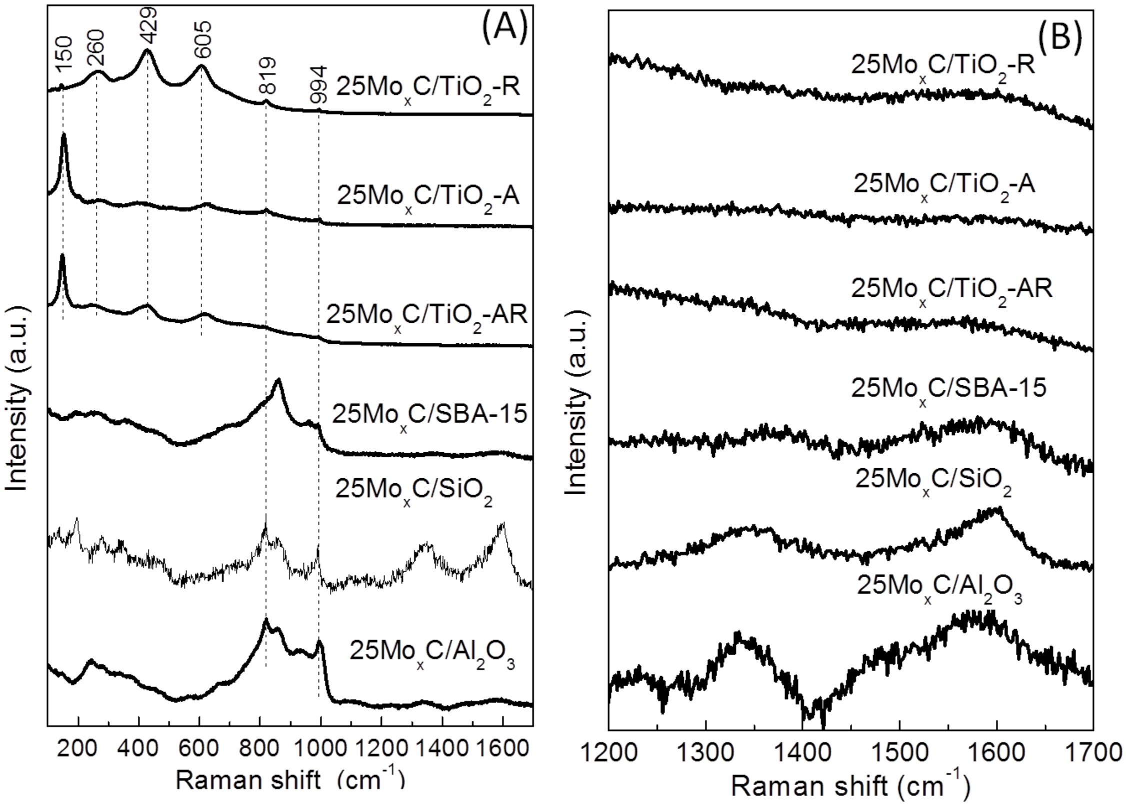

Figure 4.31. Raman spectra of the fresh $25Mo_xC$/Support catalysts. (A) 100-1700 region; (B) zoom in of 1200-1700 region.

Characteristic Raman bands of orthorhombic MoO_3 at 994 and 819 cm^{-1}, with different intensities were observed in all cases [10].

For all the TiO_2-supported catalysts, Raman bands due to the presence of rutile TiO_2 were found at 260, 429 and 605 cm^{-1} [31]. For $25Mo_xC/TiO_2$-A and $25Mo_xC/TiO_2$-AR catalysts, the band located at 150 cm^{-1} is assigned to anatase TiO_2 [31,32]. For $25Mo_xC/TiO_2$-R, besides the bands characteristics of rutile TiO_2, a very small band at 150 cm^{-1} could be related with the presence of anatase TiO_2; however, the presence of crystalline anatase TiO_2 could not be determined by XRD on $25Mo_xC/TiO_2$-R.

To verify the presence of carbonaceous deposits, the 1200-1700 cm^{-1} region, where characteristic bands (D and G) of carbonaceous species can be observed, was enlarged. The corresponding Raman spectra are shown in Figure 4.31B. Only for $25Mo_xC/\gamma\text{-}Al_2O_3$, $25Mo_xC/SiO_2$ and $25Mo_xC$/SBA-15 catalysts, D and G bands with very low intensity were observed.

The reducibility of $25Mo_xC$/Support catalysts was analyzed by H_2-TPR; the corresponding profiles are shown in Figure 4.32. In some cases, the H_2-TPR profiles of catalysts containing 5 wt% Mo are shown (dashed line) for a comparison purpose.

For all the samples with 25 wt% Mo loading, a broad H_2 consumption peak with maximum at a temperature below 500 °C was obtained. Except $5Mo_xC/SiO_2$, catalysts with 5 wt% Mo loading show H_2 consumption peaks at a similar position than those of the corresponding catalysts with 25 wt% Mo loading. H_2-TPR profiles of $25Mo_xC/SiO_2$, $25Mo_xC/TiO_2$-A and $25Mo_xC/TiO_2$-R showed peaks at relatively low temperature. As previously mentioned, the peaks observed below 325 °C can be ascribed to the reduction of molybdenum oxycarbide [15]. The reduction of MoO_3 starts at about 400 °C [33]. A shift in the reduction temperature of supported species could be related to their particle size and/or the strength of the interaction between them and the corresponding support.

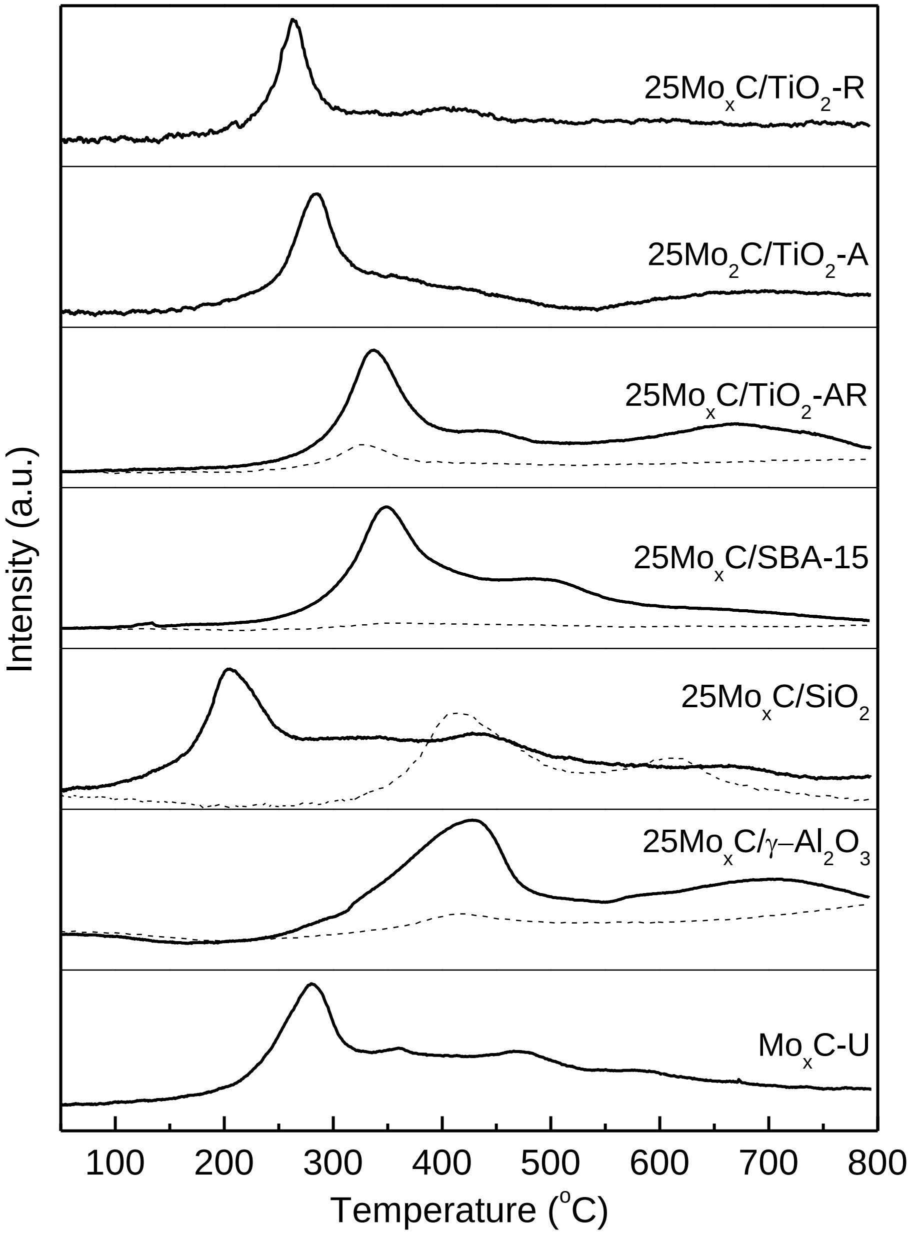

Figure 4.32. TPR profiles of the fresh yMo_xC/Support catalysts. Dashed lines correspond to the catalysts containing 5 wt% Mo.

4.2.3. RWGS reaction over supported Mo_xC-U catalysts

The RWGS reaction tests over yMo_xC/Support catalysts were performed at atmospheric pressure, at 275-400 °C, GHSV of 3000 h^{-1} and using $CO_2/H_2/N_2$=1/3/1 or 1/1/3 reactant mixtures. 150 mg of catalysts were diluted with SiC up to 1 mL. The following reaction temperature sequence was used:

325 °C (3 h)→300 °C (3 h)→275 °C (10 h)→325 °C (3 h)→350 °C (3 h)→375 °C (3 h)→400 °C (3 h)→375 °C (5 h).

RWGS reaction using $CO_2/H_2/N_2$=1/3/1

Figure 4.33 shows the CO_2 conversion and CO selectivity achieved over 25Mo_xC/Support catalysts as a function of reaction temperature. The corresponding values of CO_2 conversion and CO selectivity obtained over the Mo_xC-U sample are also shown for comparison.

As expected, in all cases, CO_2 conversion and CO selectivity increased with the increase of temperature. 25Mo_xC/SiO_2 presented the highest value of CO_2 conversion (about 28%) at 400 °C; the corresponding equilibrium CO_2 conversion for RWGS at the experimental conditions used is about 37%. 25Mo_xC/γ-Al_2O_3 and 25Mo_xC/SBA-15 catalysts showed similar CO_2 conversion than that of bulk Mo_xC-U sample. Meanwhile, TiO_2-supported catalysts showed lower values of CO_2 conversion than those of bulk Mo_xC-U in all the tested temperatures.

As regards the CO_2 conversion at 325 °C, in all cases, this was slightly higher after about 20.3 h on stream than the initial one; similarly, the CO_2 conversion at 375 °C was slightly higher after 35.7 h than that after 27 h on-stream. This points that a surface rearrangement takes place on these systems.

All 25Mo_xC/Support catalysts showed high CO selectivity values. Except for 25Mo_xC/γ-Al_2O_3, in all cases, the CO selectivity values were higher than those of Mo_xC-U (Figure 4.33B). CH_4 was the main by-product and only very small amounts of ethylene and traces of propylene were formed.

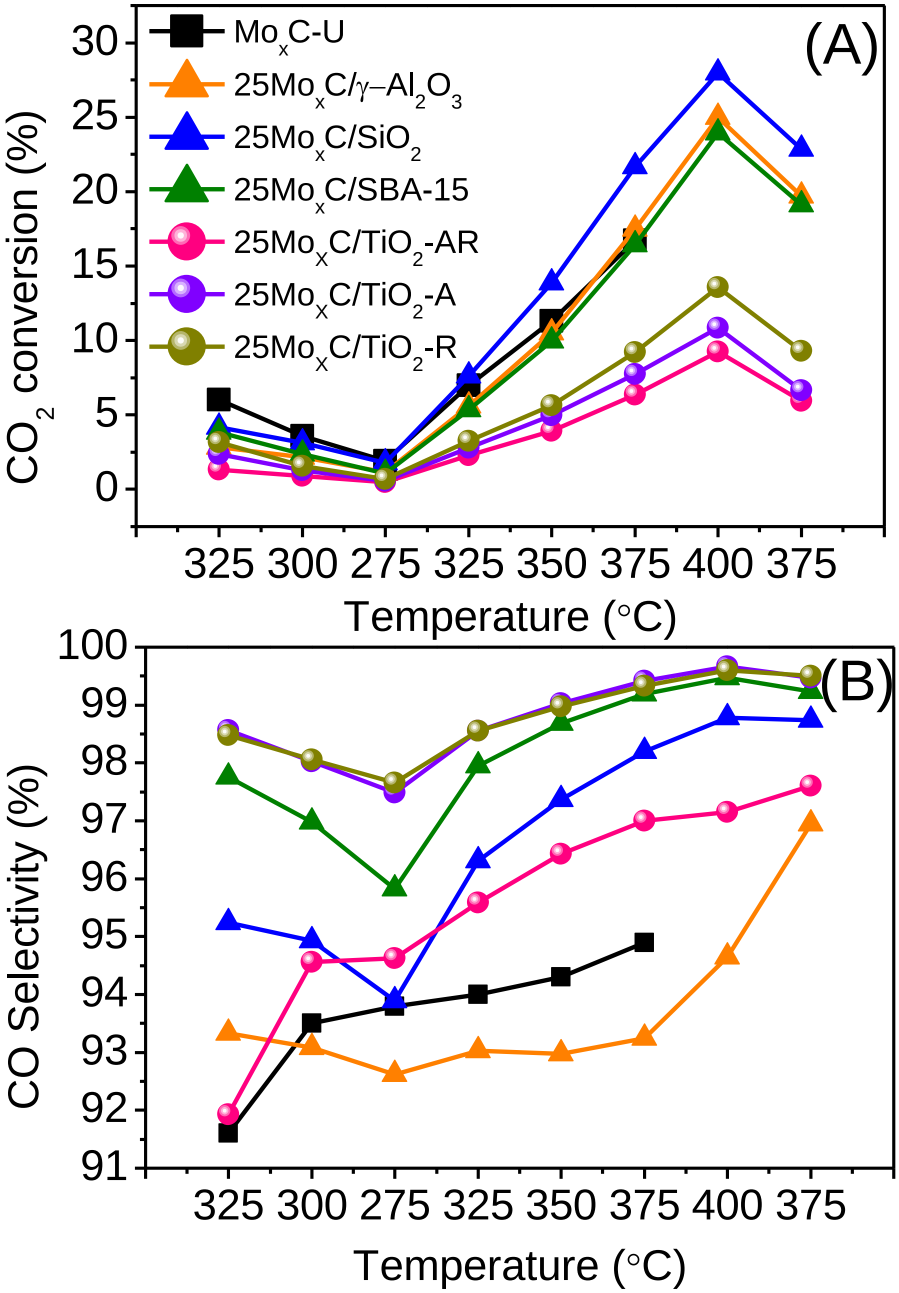

Figure 4.33. Catalytic behaviour of 25Mo$_x$C/Support in RWGS as a function of reaction temperatures: (A) CO$_2$ conversion; (B) CO selectivity. Reaction conditions: CO$_2$/H$_2$/N$_2$=1/3/1, GHSV=3000 h^{-1}, P=0.1 MPa.

Figure 4.34 shows the CO$_2$ conversion and CO selectivity of 5Mo$_x$C/Support catalysts as a function of reaction temperature. CO$_2$ conversion values obtained over 5Mo$_x$C/Support were lower than those achieved over 25Mo$_x$C/Support. In general, higher values of CO selectivity were achieved with 5Mo$_x$C/Support when compared with 25Mo$_x$C/Support catalysts. However, the difference in conversion values makes difficult a comparison of 5Mo$_x$C/Support and 25Mo$_x$C/Support in terms of selectivity. In all cases, CO was also the main product and CH_4 the main by-product formed.

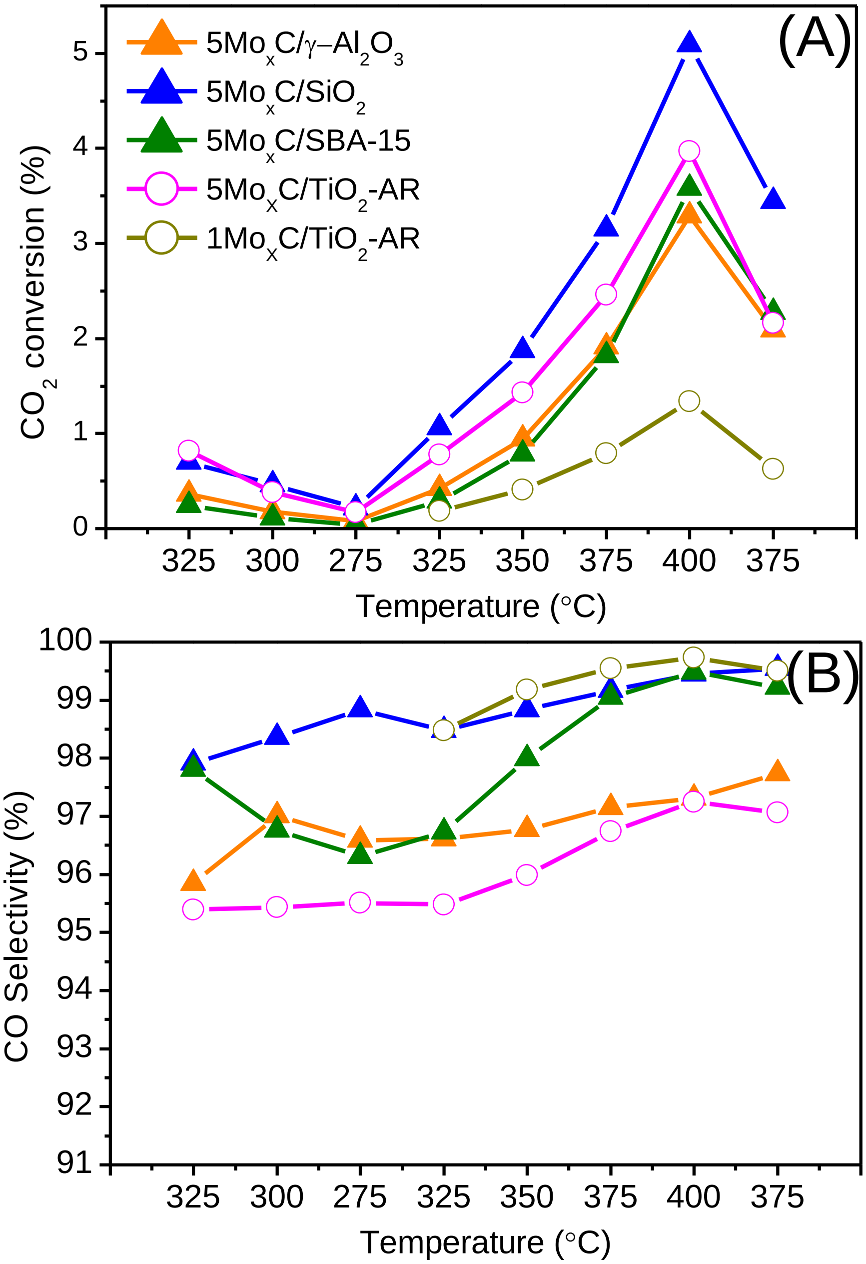

Figure 4.34. Catalytic behaviour of 5Mo$_x$C/Support in RWGS as a function of reaction temperatures: (A) CO_2 conversion; (B) CO selectivity. Reaction conditions: $CO_2/H_2/N_2$=1/3/1, GHSV=3000 h^{-1}, P=0.1 MPa.

In order to properly compare the catalytic behaviour of the catalysts, the values of CO production were normalized according to the amount of active phase present in the supported catalysts. Table 4.3 lists the values of mol CO/mol Mo•h for all supported catalysts; the variation of these values with the reaction temperature is similar to the trend of the corresponding CO_2 conversion values.

As shown in Table 4.3, in general, mol CO/mol Mo•h obtained over yMo_xC/Support catalysts are higher than that observed over the bulk Mo_xC-U catalysts. 25Mo_xC/SiO_2 showed the highest values of mol CO/mol Mo•h in the temperature range studied. Among the 25Mo_xC/Support catalysts, those prepared with TiO_2, which had a lower area than 25Mo_xC/γ-Al_2O_3, 25Mo_xC/SiO_2 and 25Mo_xC/SBA-15, showed lower normalized CO production. 25Mo_xC/TiO_2-R showed slightly higher values of mol CO/mol Mo•h than 25Mo_xC/TiO_2-A and 25Mo_xC/TiO_2-AR; as stated above, only in 25Mo_xC/TiO_2-R, the presence of crystalline hexagonal Mo_2C was clearly found.

For 5Mo_xC/γ-Al_2O_3, 5Mo_xC/SiO_2 and 5Mo_xC/SBA-15, the values of mol CO/mol Mo•h were lower than those obtained over the corresponding 25Mo_xC/Support catalysts. Conversely, 5Mo_xC/TiO_2-AR exhibited higher normalized CO production than 25Mo_xC/TiO_2-AR catalyst.

Table 4.3. CO production (mol CO/mol Mo•h) over the supported Mo_xC catalysts at different temperatures, Reaction conditions: $CO_2/H_2/N_2=1/3/1$, GHSV=3000 h^{-1}, P=0.1 MPa.

		CO production (mol CO/mol Mo•h)											
		Catalyst											
T(°C)	**Time [*] (h)**	**Mo_xC-U**	**25Mo_xC /γ-Al_2O_3**	**25Mo_xC /SiO_2**	**25Mo_xC /SBA-15**	**25Mo_xC /TiO_2-AR**	**25Mo_xC /TiO_2-A**	**25Mo_xC /TiO_2-R**	**5Mo_xC /γ-Al_2O_3**	**5Mo_xC /SiO_2**	**5Mo_xC /SBA-15**	**5Mo_xC /TiO_2-AR**	**1Mo_xC /TiO_2-AR**
325	3	0.9	1.7	2.5	2.6	0.7	1.4	2.0	1.2	2.0	0.7	-	2.6
300	6.3	0.6	1.2	1.8	1.6	0.5	0.8	1.0	0.6	1.3	0.3	-	1.2
275	17	0.3	0.7	1.0	0.7	0.3	0.3	0.4	0.3	0.6	0.1	-	0.5
325	20.3	1.1	3.3	4.5	3.7	1.3	1.6	2.0	1.4	3.0	0.8	2.6	2.5
350	23.7	1.8	6.1	8.3	6.9	2.2	3.0	3.6	3.2	5.4	2.1	5.8	4.6
375	27	2.6	10.2	13.1	11.4	3.5	4.6	5.8	6.5	9.1	5.0	11.3	7.9
400	30.3	-	14.8	17.0	16.7	5.1	6.5	8.6	11.2	14.7	9.8	19.0	12.9
375	35.7	-	11.9	13.9	13.3	3.3	4.0	5.9	7.1	10.0	6.2	8.9	7.0

[*] Total reaction time at the last stage of the corresponding temperature.

The calculated apparent Ea values of catalysts for CO production obtained in the temperature ranges of 275-325 °C and 350-400 °C are shown in Table 4.4; the corresponding Arrhenius plots are shown in Figure A.1 in Annex I. All the apparent Ea values obtained at 275-325 °C region for supported catalysts are higher than that of Mo_xC-U (72.0±2.3 kJ/mol). In general, the apparent Ea values at 350-400 °C were lower than those obtained at 275-325 °C. Moreover, apparent Ea values of $25Mo_xC$/Support (γ-Al_2O_3-, SiO_2-, TiO_2-AR- and SBA-15-) were lower than those of the corresponding $5Mo_xC$/Support catalysts.

Table 4.4. Apparent Ea values for CO production of different yMo_xC/Support catalysts and S_{BET} of post-reaction catalysts. Reaction conditions: $CO_2/H_2/N_2$=1/3/1, GHSV=3000 h^{-1}, P=0.1 MPa.

Catalyst	**Ea (kJ/mol)**		**Post-reaction S_{BET} (m^2/g)**
	275-325 °C	**350-400 °C**	
$25Mo_xC/\gamma$-Al_2O_3	85.3±13.2	61.7±4.2	92.9
$25Mo_xC/SiO_2$	80.6±12.5	50.0±6.7	115.4
$25Mo_xC$/SBA-15	88.0±3.7	61.7±3.6	203.1
$25Mo_xC/TiO_2$-AR	83.4±13.6	60.0±2.8	32.3
$25Mo_xC/TiO_2$-A	86.5±1.4	55.0±3.3	18.3
$25Mo_xC/TiO_2$-R	85.0±0.4	61.8±2.6	<5
$5Mo_xC/\gamma$-Al_2O_3	92.0±3.3	87.9±5.0	127.5
$5Mo_xC/SiO_2$	86.3±5.0	70.1±0.1	108.7
$5Mo_xC$/SBA-15	105.6±1.8	106.8±4.5	383.5
$5Mo_xC/TiO_2$-AR	83.8±0.8	72.3±1.1	5.1
$1Mo_xC/TiO_2$-AR	-	82.5±3.6	nd

Post-reaction catalysts were characterized by S_{BET} measurements, XRD and Raman spectroscopy. S_{BET} values of post-reaction catalysts are shown in Table 4.4. In all cases, a decrease of S_{BET} during the catalytic test took place.

The XRD patterns of post-reaction catalysts are shown in Figure 4.35 and 4.36. In general, the XRD patterns of post-reaction yMo_xC/Support catalysts were similar to those of fresh catalysts; indicating a high stability of the crystalline phases in the catalysts during the catalytic reaction.

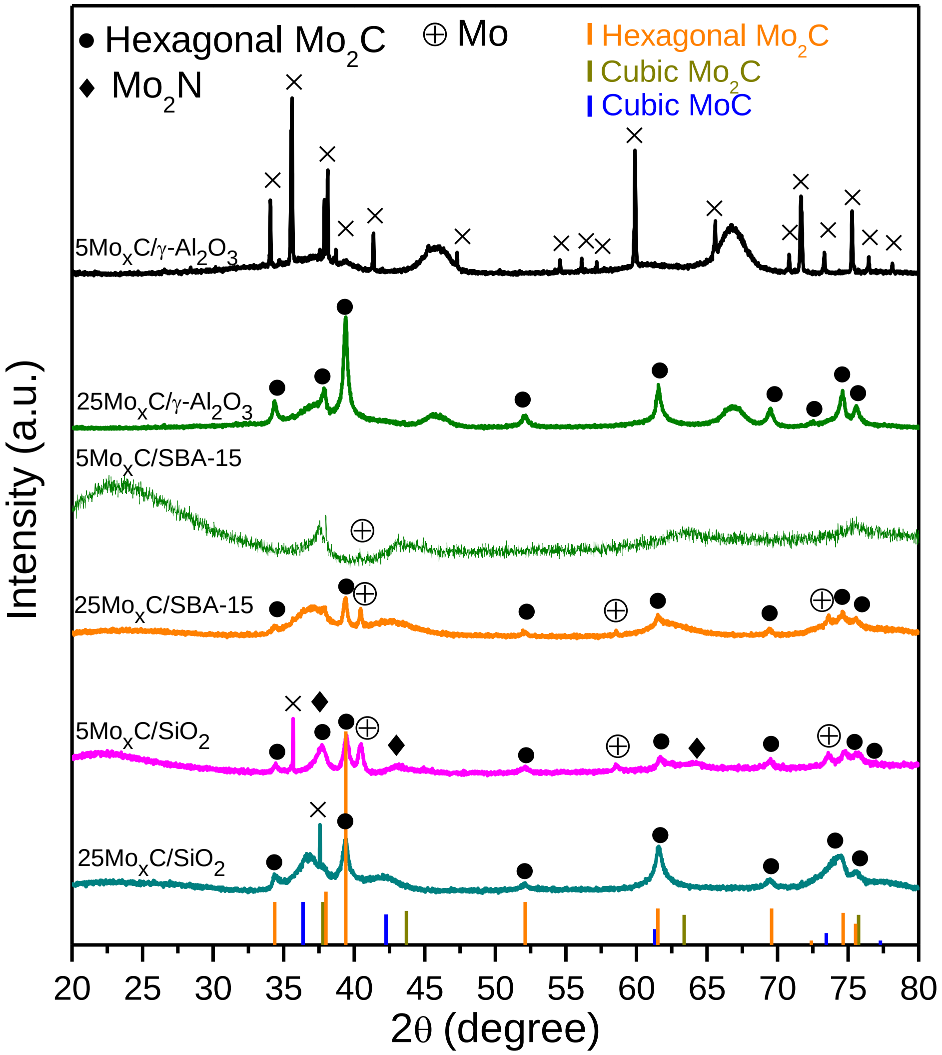

Figure 4.35. XRD patterns of post-reaction yMo_xC/Support catalysts. Reaction conditions: GHSV=3000 h^{-1}, P=0.1 MPa and $CO_2/H_2/N_2$=1/3/1. "×" corresponds to SiC, which was used as diluent in the catalytic bed.

For $25Mo_xC/\gamma\text{-}Al_2O_3$ and $25Mo_xC/SiO_2$ catalysts, it was possible to calculate the crystallite size of Mo_xC using the XRD peak at 2θ=61.6 ° for fresh and post-reaction samples. For both $25Mo_xC/\gamma\text{-}Al_2O_3$ and $25Mo_xC/SiO_2$, a slight decrease of crystallite size was determined to occur during the reaction; crystallite size decreased from 31.4 to 26.3 nm for $25Mo_xC/\gamma\text{-}Al_2O_3$, and from 21.2 to 16.3 nm for $25Mo_xC/SiO_2$.

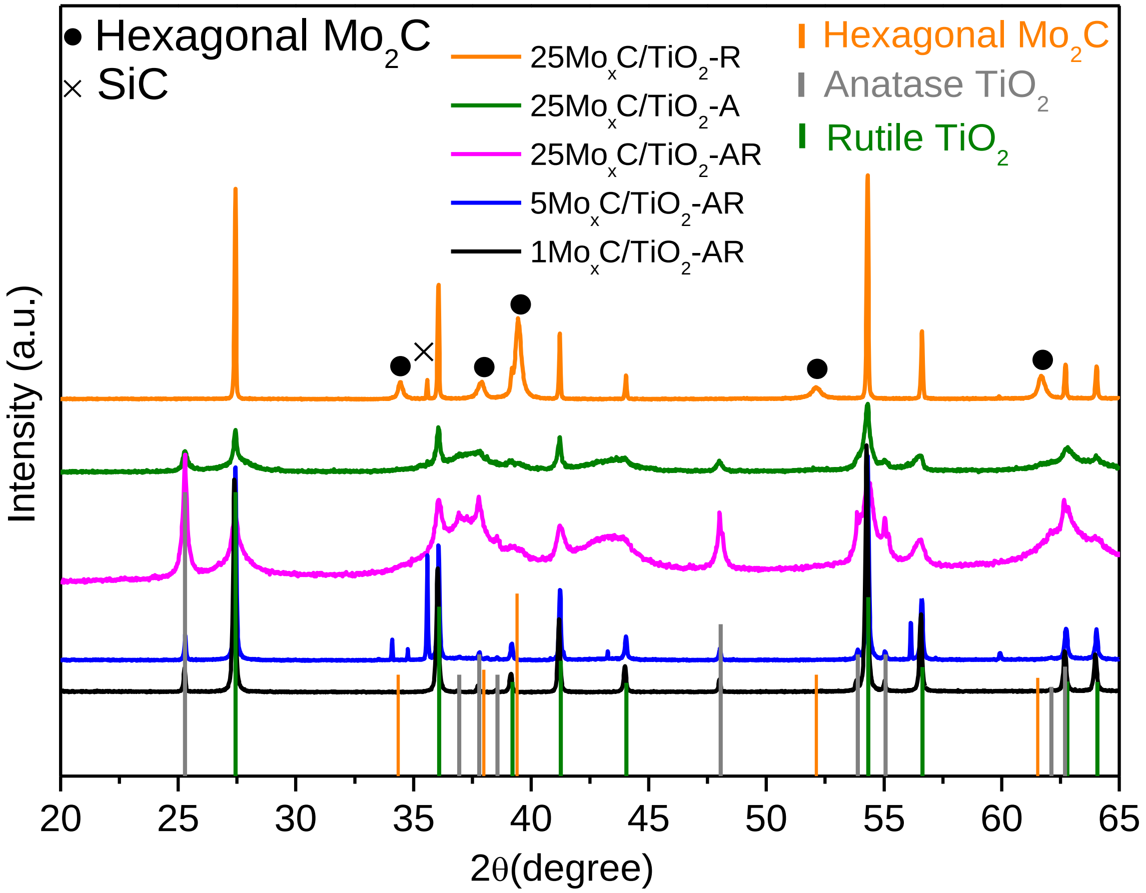

Figure 4.36. XRD patterns of TiO_2-supported Mo_xC post-reaction catalysts. Reaction conditions: GHSV=3000 h^{-1}, P=0.1 MPa and $CO_2/H_2/N_2$=1/3/1. × corresponds to SiC, which was used as diluent in the catalytic bed.

Raman spectra of post-reaction $25Mo_xC$/Support catalysts (Figure 4.37) were quite similar to those of fresh catalysts.

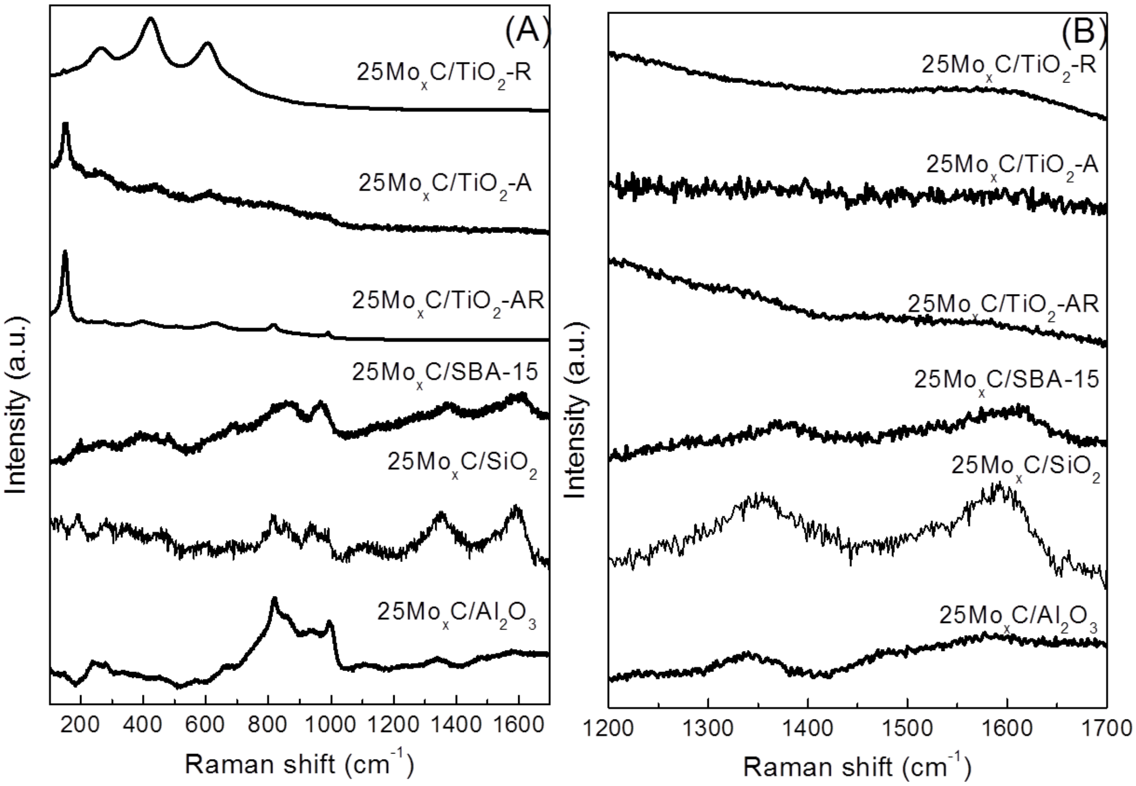

Figure 4.37. Raman spectra of post-reaction catalysts. Reaction conditions: GHSV=3000 h^{-1}, P=0.1 MPa and $CO_2/H_2/N_2$=1/3/1.

RWGS reaction using $CO_2/H_2/N_2$=1/1/3

Due to the high catalytic activity of the 25Mo$_x$C/Support catalysts, they were tested in the RWGS reaction using a stoichiometric ratio of reactant mixture $CO_2/H_2/N_2$=1/1/3; RWGS was studied at atmospheric pressure, in the temperature range of 275-400 °C at GHSV of 3000 h^{-1} using the sequence of change of temperature described above.

Figure 4.38 shows the variation of CO_2 conversion with the reaction temperature, and Figure 4.39 the CO selectivity values. As expected, when a mixture $CO_2/H_2/N_2$=1/1/3 was used, the CO_2 conversion was lower than when the reactant mixture was $CO_2/H_2/N_2$=1/3/1. Again, the CO_2 conversion increased with the increase of temperature. Using $CO_2/H_2/N_2$=1/1/3, the highest CO_2 conversion was also found over the 25Mo$_x$C/SiO$_2$ catalyst; however, the value of CO_2

conversion (13.5%) obtained at 400 °C over $25Mo_xC/SiO_2$ was far from the thermodynamic equilibrium (about 22%) at this temperature.

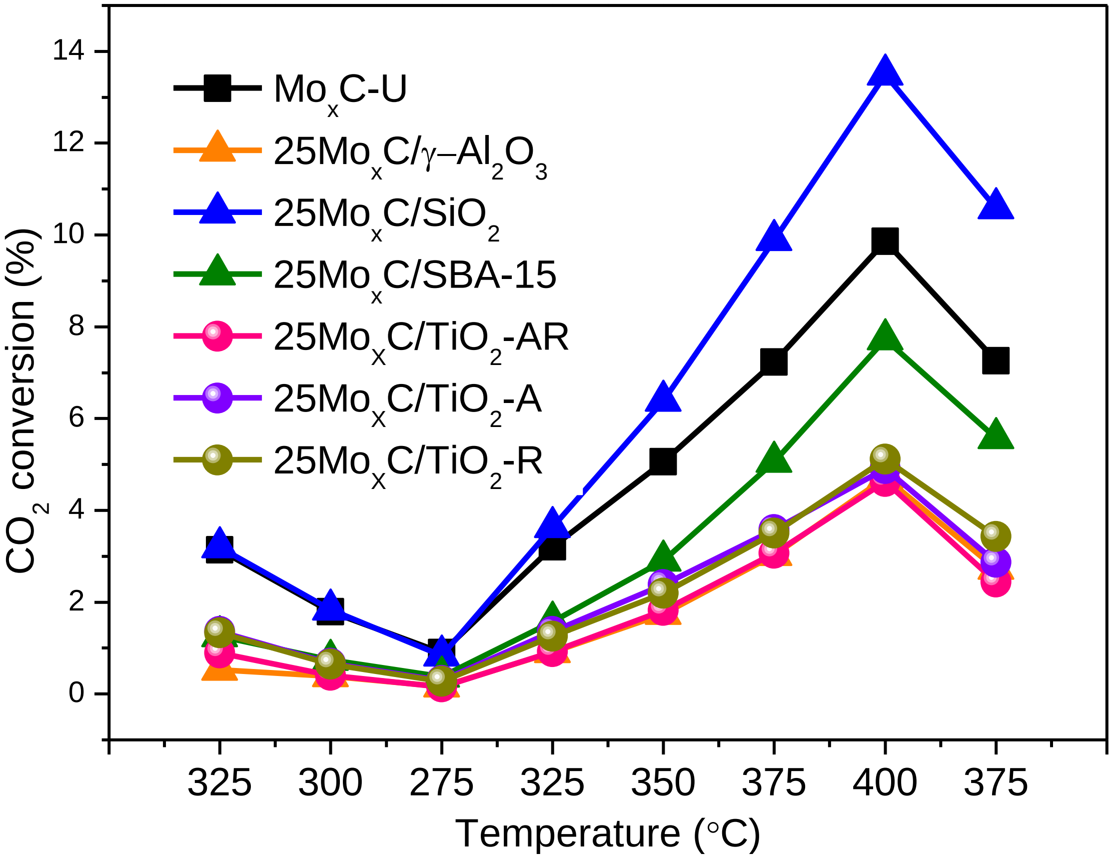

Figure 4.38. CO_2 conversion as a function of reaction temperature in RWGS reaction of $25Mo_xC$/Support catalysts. Reaction conditions: $CO_2/H_2/N_2$=1/1/3, GHSV=3000 h^{-1}, P=0.1 MPa.

In all cases, the main product was CO and only minor amounts of CH_4 were formed; in some cases, negligible amounts of ethylene were detected. The CO selectivity as a function of temperature is shown in Figure 4.39. Except for $25Mo_xC$/SBA-15, the CO selectivity was higher than 98% in all the temperature range; the values obtained over $25Mo_xC$/Support when $CO_2/H_2/N_2$=1/1/3 mixture was used were higher than those obtained with $CO_2/H_2/N_2$=1/3/1 reactant mixture.

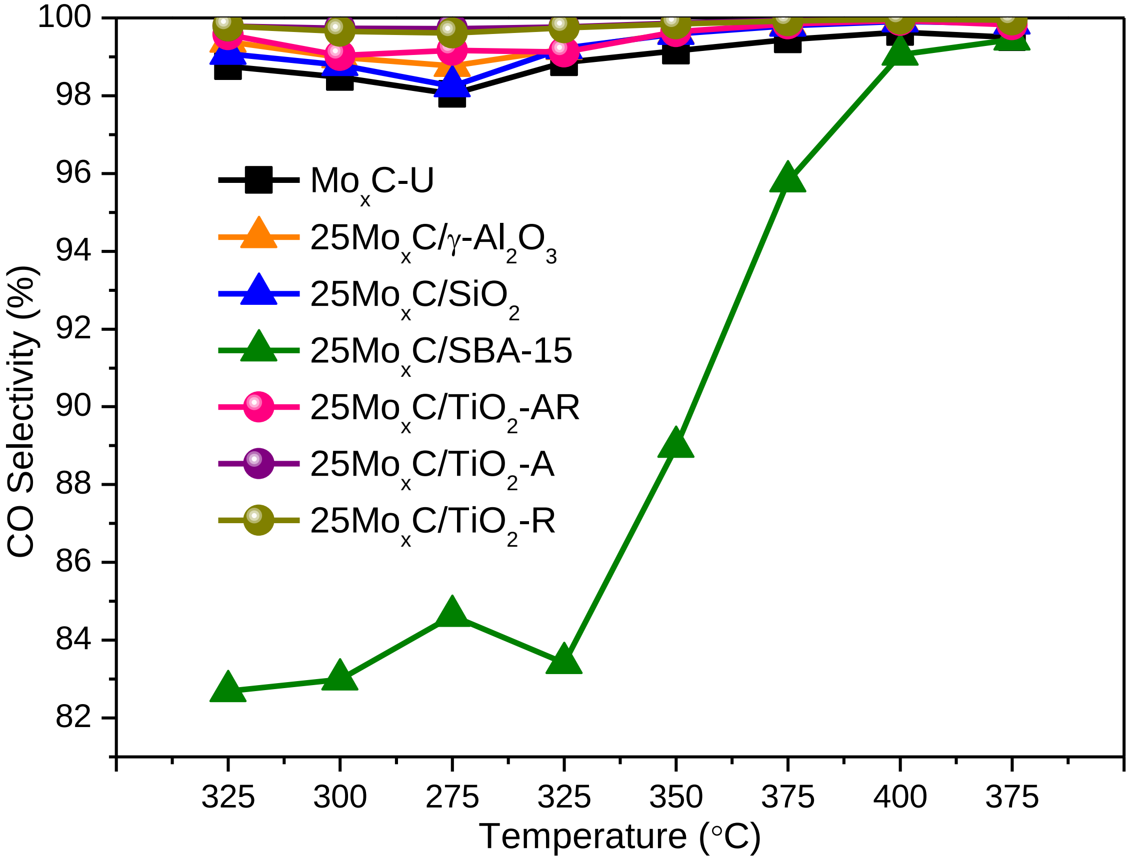

Figure 4.39. CO selectivity as a function of reaction temperature over 25Mo$_x$C/Support catalysts. Reaction conditions: $CO_2/H_2/N_2$=1/1/3, GHSV=3000 h^{-1}, P=0.1 MPa.

Values of CO production per mole of Mo (mol CO/mol Mo•h) are shown in Table 4.5; the values were much lower than the corresponding values obtained when a reactant mixture of $CO_2/H_2/N_2$=1/3/1 was used. In all cases, at temperature above 350 °C, the CO production over 25Mo$_x$C/Support catalysts was higher than that obtained over the bulk Mo$_x$C-U.

Table 4.5. CO production per mol Mo loading (mol CO/mol Mo•h) in the different supported catalysts at different temperatures. Reaction conditions: $CO_2/H_2/N_2$=1/1/3, GHSV=3000 h^{-1}, P=0.1 MPa.

T	Time* (h)	**CO production (mol CO /mol Mo•h)**						
		Catalyst						
		Mo_xC-U	**25Mo_xC/ γ-Al_2O_3**	**25Mo_xC/ SiO_2**	**25Mo_xC/ SBA-15**	**25Mo_xC/ TiO_2-AR**	**25Mo_xC/ TiO_2-A**	**25Mo_xC/ TiO_2-R**
325	3	0.5	0.3	2.0	0.7	0.5	0.8	0.8
300	6.3	0.1	0.2	1.1	0.4	0.2	0.4	0.4
275	17	0.3	0.1	0.5	0.2	0.1	0.2	0.2
325	20.3	0.5	0.6	2.2	0.9	0.5	0.8	0.8
350	23.7	0.8	1.1	3.9	1.9	1.0	1.4	1.4
375	27	1.2	1.9	6.1	3.5	1.7	2.1	2.2
400	30.3	1.6	2.9	8.3	5.5	2.6	3.0	3.3
375	35.7	1.2	1.7	6.5	4.0	1.4	1.7	2.2

* Total reaction time at the last stage of the corresponding temperature.

The apparent Ea values for CO production are listed in Table 4.6; the corresponding Arrhenius plots obtained at temperature range of 275-325°C and 350-400 °C are shown in Figure A.2 in Annex I. In all cases, the apparent Ea values obtained at both temperature ranges of 275-325°C and 350-400 °C are higher than those obtained for bulk Mo_xC-U, 55.2±2.3 kJ/mol (275-325°C) and 40.6±0.5 kJ/mol (350-400 °C).

The S_{BET} values of post-reaction catalysts are presented in Table 4.6. After the catalytic test with $CO_2/H_2/N_2$=1/1/3, the S_{BET} of 25Mo_xC/SBA-15 was significantly lower than that after the catalytic test using $CO_2/H_2/N_2$=1/3/1 reactant mixture (Table 4.4).

Table 4.6. Apparent Ea values for CO production of different $25Mo_xC$/Support and S_{BET} of post-reaction catalysts. Reaction conditions: $CO_2/H_2/N_2=1/1/3$, GHSV=3000 h^{-1}, P=0.1 MPa.

Catalyst	**Ea (kJ/mol)**		**Post-reaction S_{BET} (m^2/g)**
	275-325°C	**350-400 °C**	
$25Mo_xC/\gamma-Al_2O_3$	94.3±1.7	69.7±3.0	97.4
$25Mo_xC/SiO_2$	79.7±0.7	52.4±3.9	106.8
$25Mo_xC$/SBA-15	76.9±5.1	75.7±5.1	135.9
$25Mo_xC/ TiO_2$-AR	99.2±2.2	65.3±2.9	25.4
$25Mo_xC/ TiO_2$-A	84.7±1.8	50.6±2.6	15.6
$25Mo_xC/ TiO_2$-R	82.9±4.5	59.3±2.5	<5

The XRD patterns of post-reaction catalysts after the catalytic test using the $CO_2/H_2/N_2=1/1/3$ reactant mixture are shown in Figure 4.40.

The presence of crystalline MoO_2 can be inferred from the XRD patterns of post-reaction $25Mo_xC/SiO_2$, $25Mo_xC/TiO_2$-A and $25Mo_xC/TiO_2$-AR catalysts. Moreover, for post-reaction $25Mo_xC/SiO_2$, a significant change of XRD profile compared to the corresponding fresh catalyst was observed; the presence of hexagonal Mo_2C is inconclusive. Only a very small peak at $2\theta=39.4°$, which could be assigned to the most intense peak of hexagonal Mo_2C, was found. Several broad peaks at $2\theta=32-39°$, 40-46° and 57-65° are ascribed to cubic MoC. For $25Mo_xC$/SBA-15 catalyst, peaks characteristic of metallic Mo and hexagonal Mo_2C which were in the XRD pattern of the fresh catalyst were not present in the corresponding pattern of post-reaction catalysts.

As mentioned above, over hexagonal Mo_2C, the CO_2 dissociation to CO and O is proposed to occur during the RWGS reaction. Under these conditions, surface O can react with adsorbed H_2 and form water, this process will be less favoured when $CO_2/H_2/N_2$=1/1/3 is used instead $CO_2/H_2/N_2$=1/3/1 and, MoO_2 can be irreversibly formed.

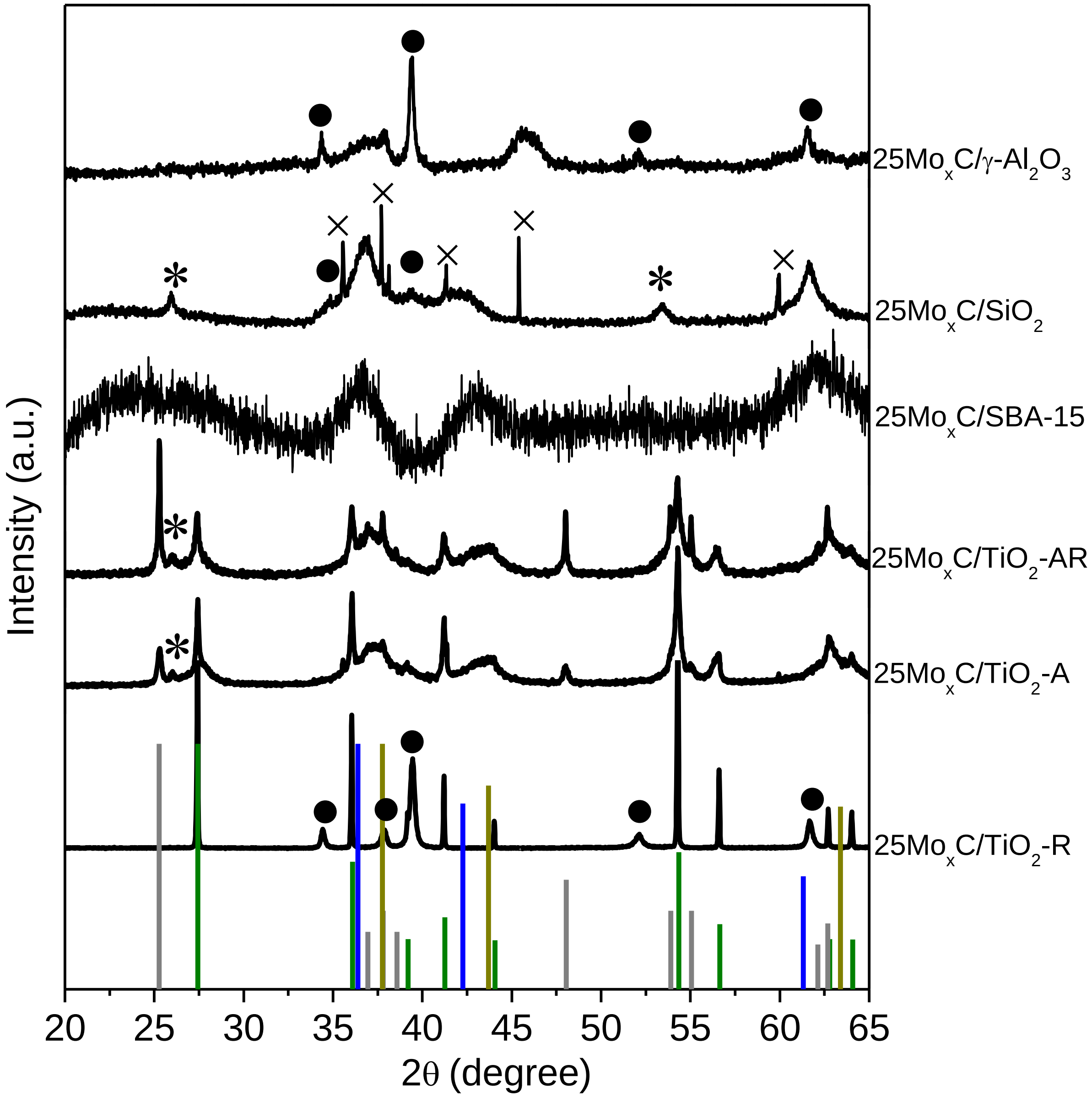

Figure 4.40. XRD patterns of post-reaction catalysts. Reaction conditions: GHSV=3000 h^{-1}, P= 0.1 MPa and $CO_2/H_2/N_2$=1/1/3. (×) Impurity of SiC; (•) Hexagonal Mo_2C; (∗) Hexagonal MoO_2; (|) Cubic MoC; (|) Cubic Mo_2C; (|) Rutile TiO_2; (|) Anatase TiO_2.

4.3. MMo_xC and and MMo_xC/γ-Al_2O_3 (M=Cu, Co) catalysts in RWGS reaction

In this section, the influence of the presence of Cu and Co on Mo_xC-U and 25Mo_xC/γ-Al_2O_3 systems is explored.

4.3.1. Preparation of MMo_xC and MMo_xC/γ-Al_2O_3 (M=Cu, Co) catalysts

The samples were prepared using similar preparation methods than those used for the preparation of Mo_xC-U and 25Mo_xC/γ-Al_2O_3. Figure 4.41 shows the general preparation procedure of Cu- and Co-containing catalysts.

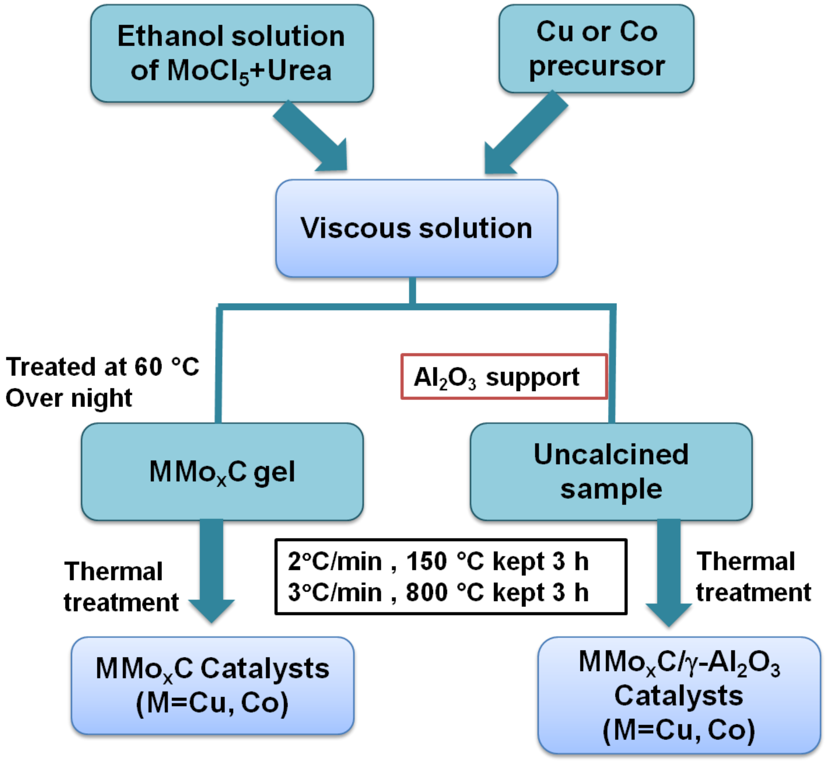

Figure 4.41. The scheme of preparation of MMo_xC and MMo_xC/γ-Al_2O_3 (M=Cu, Co) catalysts.

For the preparation of MMo_xC (M=Cu, Co) catalysts, an ethanol solution containing $MoCl_5$, urea, and the appropriate amount of $Cu(CH_3COO)_2$•H_2O or

$Co(CH_3COO)_2 \bullet 4H_2O$ was prepared with continuous stirring ($MoCl_5$/urea=7, molar ratio). Thereafter, the viscous solution was treated at 60 °C in an oven under air. MMo_xC (M=Cu, Co) catalysts were obtained after the usual thermal treatment, up to 800 °C under Ar flow in a quartz tube reactor. Finally, the reactor was cooled down to room temperature under Ar flow, and then the catalyst was exposed to ambient air without any passivation. In this work, catalysts containing 5 wt%Co ($5CoMo_xC$), 20 wt% Co ($20CoMo_xC$) and 20 wt%Cu ($20CuMo_xC$) were prepared.

On the other hand, $10CuMo_xC/\gamma\text{-}Al_2O_3$ (10 wt%, Cu) and $15CoMo_xC/\gamma\text{-}Al_2O_3$ (15 wt%, Co) catalysts were prepared using a similar procedure as described previously for the preparation of $25Mo_xC/\gamma\text{-}Al_2O_3$. An alcoholic solution containing the metal precursor ($Cu(CH_3COO)_2 \bullet H_2O$ or $Co(CH_3COO)_2 \bullet 4H_2O$), $MoCl_5$ and urea was first prepared. After, $\gamma\text{-}Al_2O_3$- was contacted with the above solution with continuous stirring overnight, then, the heat treatment was carried out.

Preparation details of MMo_xC and $MMo_xC/\gamma\text{-}Al_2O_3$ (M=Cu, Co) catalysts are given in Annex II.

4.3.2. Characterization of catalysts

Fresh MMo_xC and $MMo_xC/\gamma\text{-}Al_2O_3$ (M=Cu, Co) were characterized using S_{BET}, XRD, Raman spectroscopy and H_2-TPR.

Table 4.7 shows the metal content and S_{BET} of the fresh catalysts. The S_{BET} values of $10CuMo_xC/\gamma\text{-}Al_2O_3$ and $15CoMo_xC/\gamma\text{-}Al_2O_3$ were lower than that of $25Mo_xC/\gamma\text{-}Al_2O_3$.

Table 4.7. Metal content, S_{BET} values and crystallite sizes from XRD of fresh MMo_xC and $MMo_xC/\gamma\text{-}Al_2O_3$ (M=Cu, Co) catalysts.

Catalyst	Mo wt %	Cu or Co wt %	BET (m^2/g) fresh	Crystallite size (nm)	
				Mo_2C	Cu
$20CuMo_xC$	67.2	20.7	6.4	48.8	62.3
$5CoMo_xC$	86.8	5.3	<5	36.8	-
$20CoMo_xC$	70.0	21.5	<5	38.2	-
$10CuMo_xC/\gamma\text{-}Al_2O_3$	25.1	9.5	91.1	41.5	97.5
$15CoMo_xC/\gamma\text{-}Al_2O_3$	26.4	14.6	71.5	56.9	-

The XRD patterns of MMo_xC and $MMo_xC/\gamma\text{-}Al_2O_3$ (M=Cu, Co) catalysts are shown in Figure 4.42. For $20CuMo_xC$ and $10CuMo_xC/\gamma\text{-}Al_2O_3$ (Figure 4.42A) the characteristic diffraction peaks of hexagonal Mo_2C and cubic Cu^0 (JCPDS 00-004-0836) were found. Moreover, in the XRD pattern of $10CuMo_xC/\gamma\text{-}Al_2O_3$, two peaks of very low intensity at 2θ=35.6 and 48.7°, which can be related with (-111) and (-202) diffraction peaks of CuO (JCPDS 01-041-0254) can be observed.

The crystallite sizes of Mo_2C in $20CuMo_xC$ and $10CuMo_xC/\gamma\text{-}Al_2O_3$ (Table 4.7) are higher than those of Mo_2C in Mo_xC-U (35.2 nm) and $25Mo_xC/\gamma\text{-}Al_2O_3$ (31.4 nm), respectively. On the other hand, the presence of large Cu^0 crystallites was determined (Table 4.7).

As shown in Figure 4.42B, from the XRD patterns of $CoMo_xC$ and $CoMo_xC/\gamma\text{-}Al_2O_3$, the coexistence of different crystalline phases can be deduced. The presence of hexagonal Mo_2C and cubic $Co_6Mo_6C_2$ (JCPDS 01-080-0339) can be proposed. Moreover, for $5CoMo_xC$ $20CoMo_xC$, XRD diffraction peaks assigned to hexagonal MoC (JCPDS 00-045-1015) were clearly observed. In addition, the presence of metallic cubic Co (JCPDS 00-015-0806) can be deduced from XRD patterns of $20CoMo_xC$ and $15CoMo_xC/\gamma\text{-}Al_2O_3$ catalysts.

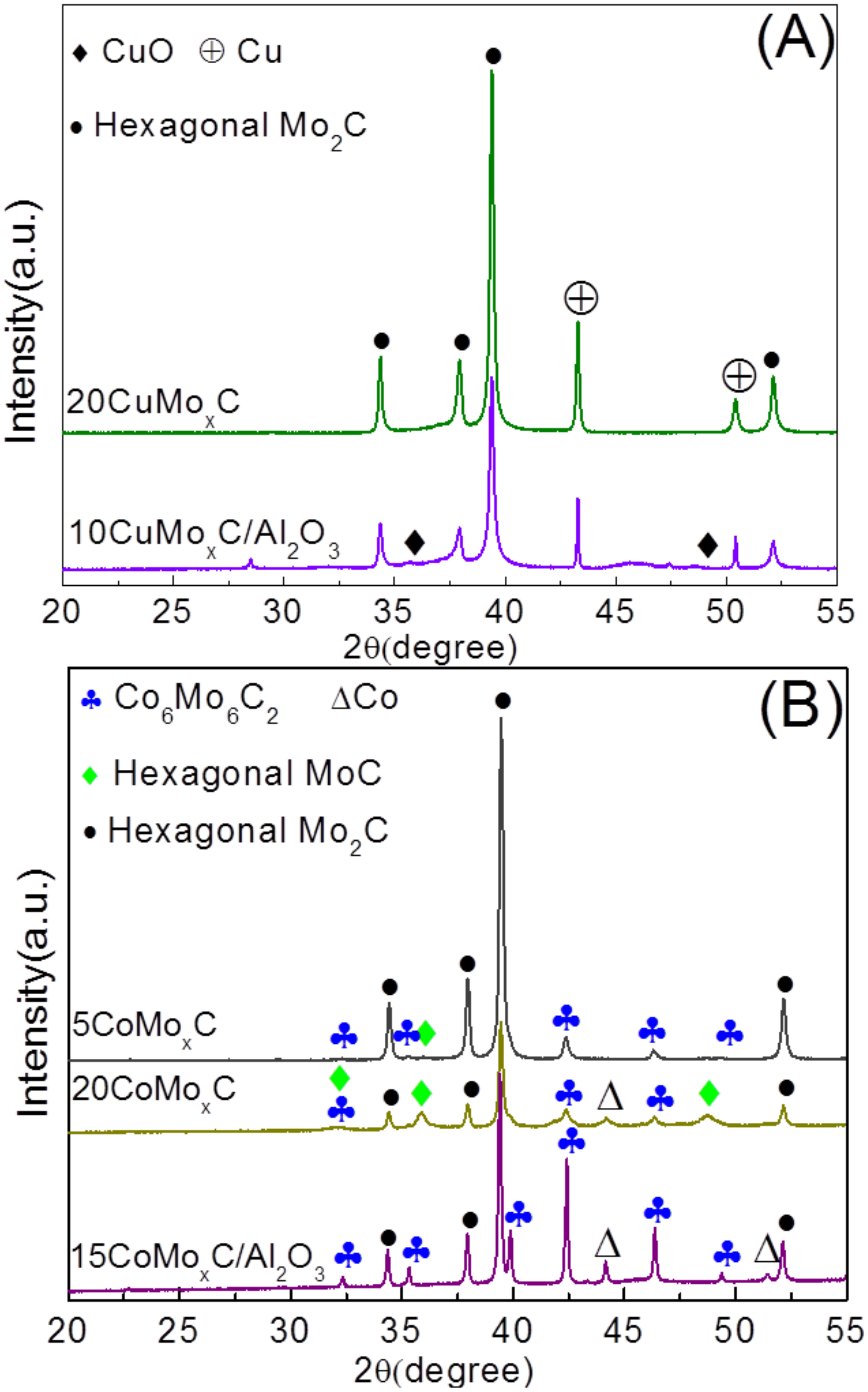

Figure 4.42. XRD patterns of fresh MMo$_x$C and MMo$_x$C/γ-Al$_2$O$_3$ (M=Cu, Co) catalysts.

Figure 4.43 shows the Raman spectra of fresh catalysts. Several Raman bands below 1000 cm^{-1} assigned to MoO$_3$ and/or MoO$_{3-x}$ species were observed, their profiles depended on the composition of the catalysts [9-13]. Raman bands at about 993, 821 and 657 cm^{-1} are characteristic of orthorhombic MoO_3 [9,11,12]. For 20CoMo$_x$C and 10CuMo$_x$C/γ-Al_2O_3, low intensity D and G Raman bands characteristic of carbon residues were visible.

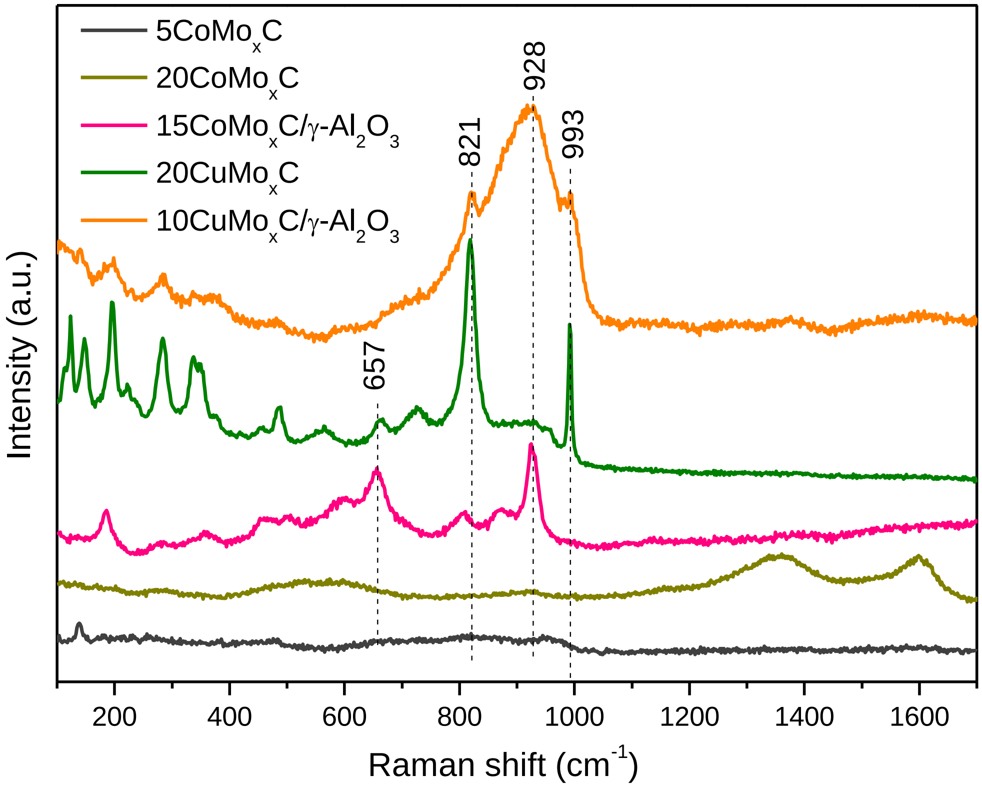

Figure 4.43. Raman spectra of fresh MMo$_x$C and MMo$_x$C/γ-Al_2O_3 (M=Cu, Co) catalysts.

Figure 4.44 shows the H_2-TPR profiles corresponding to 20CuMo$_x$C and MMo$_x$C/γ-Al_2O_3 (M=Cu, Co). For comparison purposes, profiles of Mo$_x$C-U and 25MMo$_x$C/γ-Al_2O_3 are also included. H_2 consumption for 20CuMo$_x$C was observed at a lower temperature than that of Mo$_x$C-U (Figure 4.44A); an easier reduction of oxycarbide species could account for this. A similar reason could explain the differences between H_2-TPR profiles of MMo$_x$C/γ-Al_2O_3 (M=Cu, Co) and 25MMo$_x$C/γ-Al_2O_3 (Figure 4.44B).

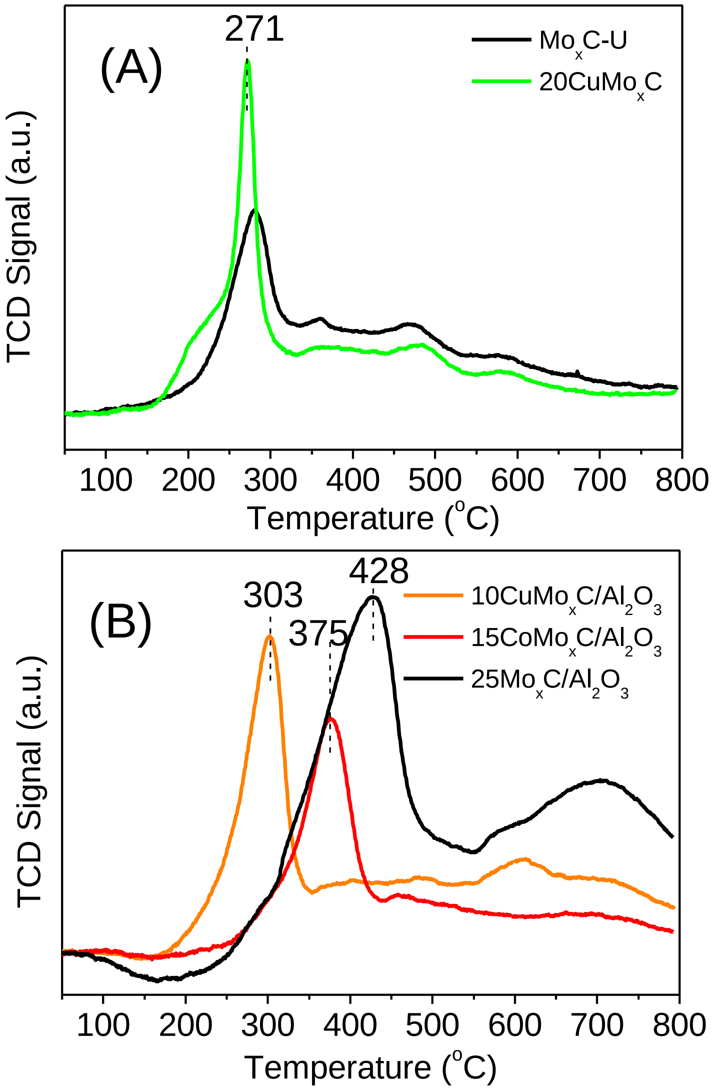

Figure 4.44. H_2-TPR of fresh MMo_xC and MMo_xC/γ-Al_2O_3 (M=Cu, Co) catalysts.

4.3.3. RWGS reaction over MMo_xC and MMo_xC/γ-Al_2O_3 (M=Cu, Co) catalysts

The RWGS reaction was carried out at atmospheric pressure in the 275-400 °C temperature region and at GHSV of 3000 h^{-1} using a reactant mixture of $CO_2/H_2/N_2$=1/3/1. Figure 4.45 shows the CO_2 conversion and CO selectivity of MMo_xC (M=Cu, Co) catalysts as a function of temperature; for comparison, the results of bulk Mo_xC-U are also included. The incorporation of Cu and Co to the bare Mo_xC-U did not show a positive effect in the catalytic activity. However, 20CuMo$_x$C which shows similar CO_2 conversion to Mo$_x$C-U was more selective to CO. As stated in the Introduction section, a positive effect of Cu in the catalytic activity of Mo_2C has been recently reported for catalysts containing 1 wt% Cu, having very high Cu dispersion [36].

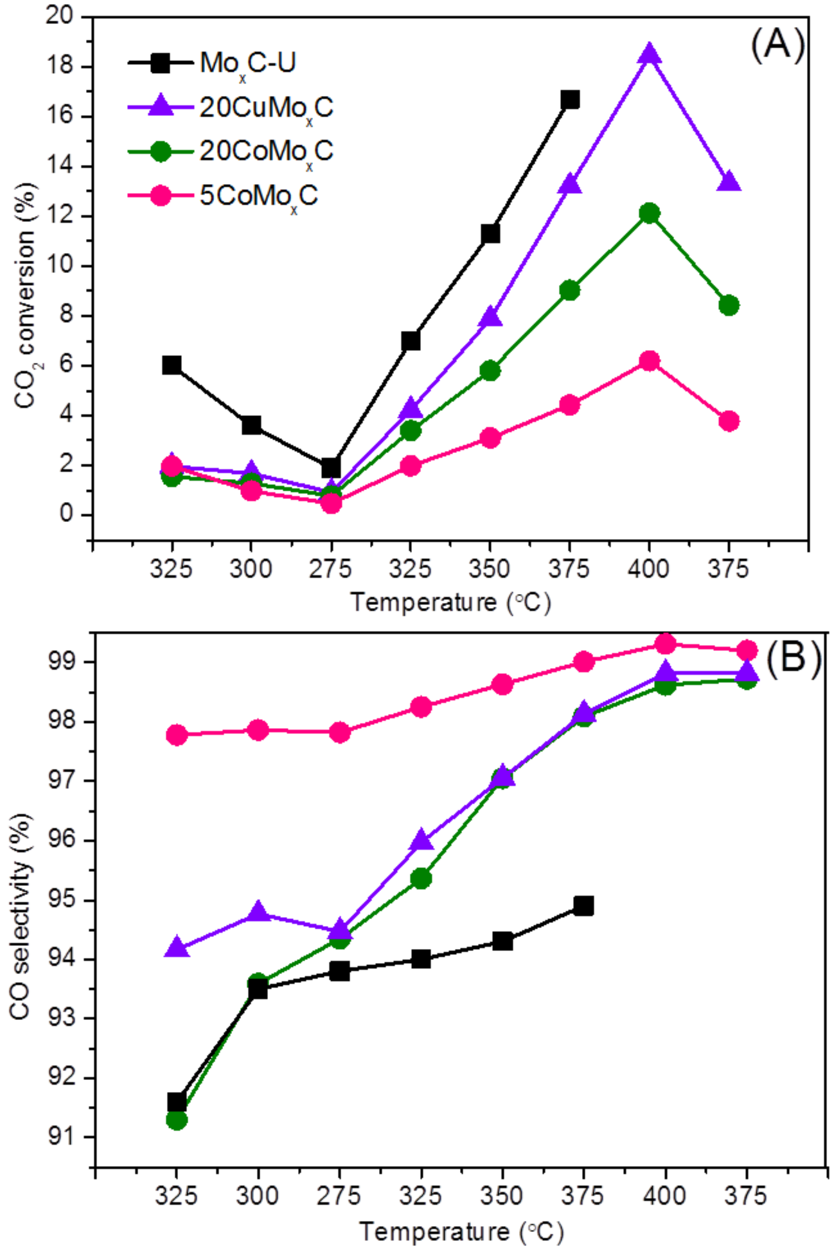

Figure 4.45. Catalytic behaviour of MMo$_x$C/γ-Al_2O_3 (M=Cu, Co) catalysts in RWGS as a function of reaction temperatures: (A) CO_2 conversion; (B) CO selectivity. Reaction conditions: $CO_2/H_2/N_2$=1/3/1, GHSV=3000 h^{-1}, P=0.1 MPa.

Figure 4.46 shows the CO_2 conversion and CO selectivity of $MMo_xC/\gamma\text{-}Al_2O_3$ (M=Cu, Co) catalysts as a function of temperature; for comparison, the corresponding profiles of $25Mo_xC/\gamma\text{-}Al_2O_3$ are also included.

$10CuMo_xC/\gamma\text{-}Al_2O_3$ and $15CoMo_xC/\gamma\text{-}Al_2O_3$ showed lower CO_2 conversion than $25Mo_xC/\gamma\text{-}Al_2O_3$ under the reaction conditions analyzed. On the other hand, the distribution of products for $10CuMo_xC/\gamma\text{-}Al_2O_3$ and $15CoMo_xC/\gamma\text{-}Al_2O_3$ was quite different. $10CuMo_xC/\gamma\text{-}Al_2O_3$ showed always a selectivity to CO higher than 95%, whereas the selectivity to CO over $15CoMo_xC/\gamma\text{-}Al_2O_3$ was always below 70%, being CH_4 the main by-product formed. This is probably related with the presence of Co^0 particles.

An optimization of the amount of Co introduced in Mo_xC-based catalysts could lead to a further improvement of the catalytic performance in RWGS of Mo_xC-based catalysts developed in this work.

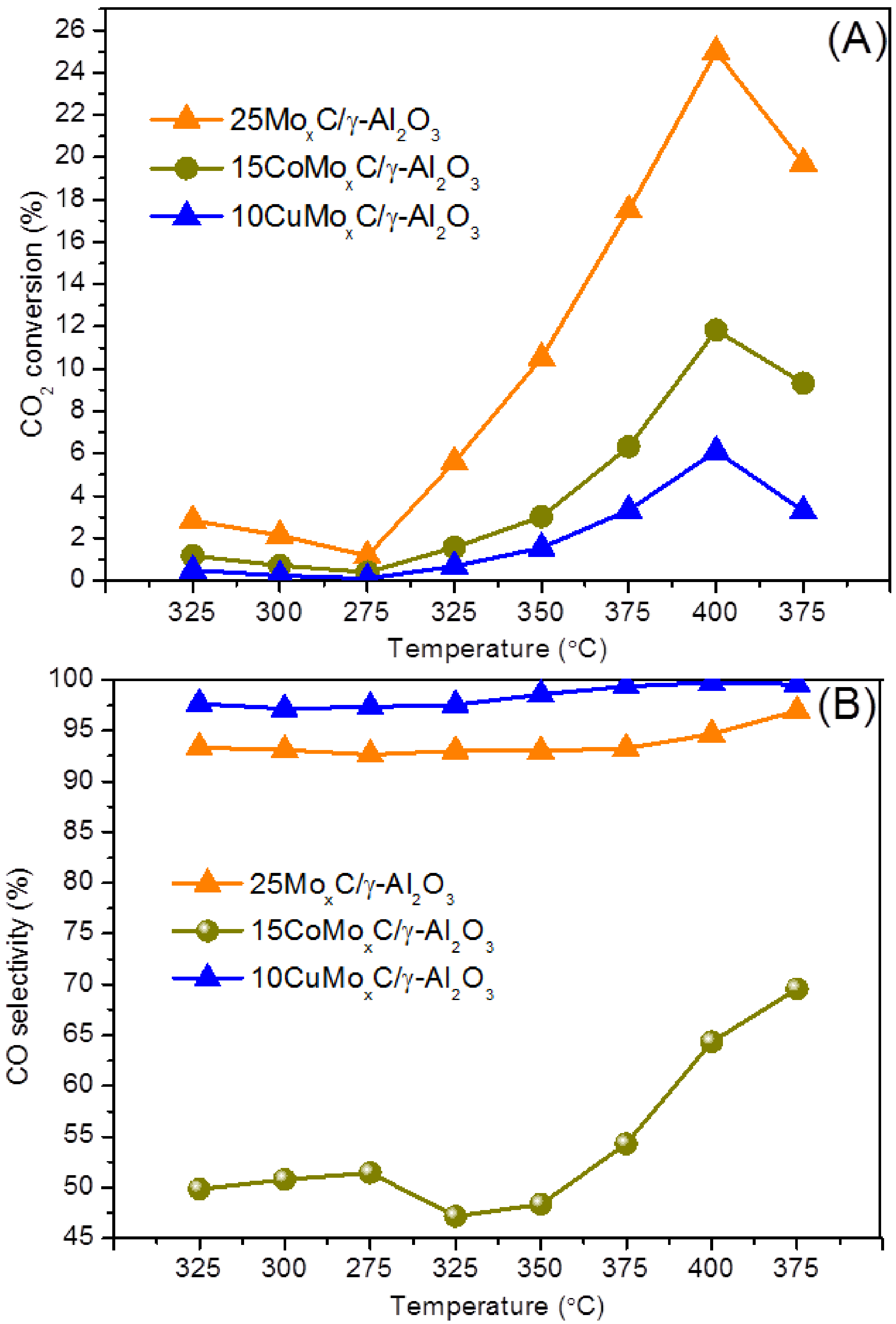

Figure 4.46. Catalytic behaviour of MMo$_x$C/γ-Al$_2$O$_3$ (M=Cu, Co) catalysts in RWGS as a function of reaction temperatures: (A) CO$_2$ conversion; (B) CO selectivity. Reaction conditions: CO$_2$/H$_2$/N$_2$=1/3/1, GHSV=3000 h^{-1}, P=0.1 MPa.

4.4. References

[1] Vitale G, Guzmán H, Frauwallner ML, Scott CE, Pereira-Almao P. Synthesis of nanocrystalline molybdenum carbide materials and their characterization. Catal. Today. 2015;250:123-133.

[2] Xu W, Ramirez PJ, Stacchiola D, Rodriguez JA. Synthesis of α-MoC_{1-x} and β-MoC_y Catalysts for CO_2 Hydrogenation by Thermal Carburization of Mo-oxide in Hydrocarbon and Hydrogen Mixtures. Catal. lett. 2014;144:1418-1424.

[3] Zhu Q, Chen Q, Yang X, Ke D. A new method for the synthesis of molybdenum carbide. Mater. Lett. 2007;61:5173-5174.

[4] Stux AM, Laberty-Robert C, Swider-Lyons KE. Pechini synthesis and characterization of molybdenum carbide and nickel molybdenum carbide. J. Solid State Chem. 2008;181:2741-2747.

[5] Giordano C, Erpen C, Yao W, Antonietti M. Synthesis of Mo and W carbide and nitride nanoparticles via a simple “urea glass” route. Nano Lett. 2008;8:4659-4663.

[6] Zhao L, Fang K, Jiang D, Li D, Sun Y. Sol-gel derived Ni-Mo bimetallic carbide catalysts and their performance for CO hydrogenation. Catal. Today. 2010;158:490-495.

[7] Wu W, Wu Z, Liang C, Ying P, Feng Z, Li C. An IR study on the surface passivation of Mo_2C/Al_2O_3 catalyst with O_2, H_2O and CO_2. Phys. Chem. Chem. Phys. 2004;6:5603-5608.

[8] Wu W, Wu Z, Liang C, Chen X, Ying P, Li C. In situ FT-IR spectroscopic studies of CO adsorption on fresh Mo_2C/Al_2O_3 catalyst. J. Phys. Chem. B. 2003;107:7088-7094.

[9] Dieterle M, Mestl G. Raman spectroscopy of molybdenum oxides Part II. Resonance Raman spectroscopic characterization of the molybdenum oxides Mo_4O_{11} and MoO_2. Phys. Chem. Chem. Phys. 2002;4:822-826.

[10] Dieterle M, Weinberg G, Mestl G. Raman spectroscopy of molybdenum oxides Part I. Structural characterization of oxygen defects in MoO_{3-x} by DR UV/VIS,

Raman spectroscopy and X-ray diffraction. Phys. Chem. Chem. Phys. 2002;4:812-821.

[11] Silveira JV, Batista JA, Saraiva GD, Mendes Filho J, Souza Filho AG, Hu S, Wang X. Temperature dependent behavior of single walled MoO_3 nanotubes: A Raman spectroscopy study. Vib. Spectrosc. 2010;54:179-183.

[12] Camacho-López M, Escobar-Alarcón L, Picquart M, Arroyo R, Córdoba G, Haro-Poniatowski E. Micro-Raman study of the m-MoO_2 to α-MoO_3 transformation induced by cw-laser irradiation. Opt. Mater. 2011;33:480-484.

[13] Frauwallner M-L, López-Linares F, Lara-Romero J, Scott CE, Ali V, Hernández E, Pereira-Almao P. Toluene hydrogenation at low temperature using a molybdenum carbide catalyst. Appl. Catal. A: Gen. 2011;394:62-70.

[14] Xiao T-c, Hanif A, York AP, Nishizaka Y, Green ML. Study on the mechanism of partial oxidation of methane to synthesis gas over molybdenum carbide catalyst. Phys. Chem. Chem. Phys. 2002;4:4549-4554.

[15] Wang G, Schaidle JA, Katz MB, Li Y, Pan X, Thompson LT. Alumina supported Pt-Mo_2C catalysts for the water–gas shift reaction. J. Catal. 2013;304:92-99.

[16] Arnoldy P, De Jonge J, Moulijn J. Temperature-programed reduction of molybdenum (VI) oxide and molybdenum (IV) oxide. J. Phys. Chem. 1985;89:4517-4526.

[17] Ji W, Shen R, Yang R, Yu G, Guo X, Peng L, Ding W. Partially nitrided molybdenum trioxide with promoted performance as an anode material for lithium-ion batteries. J. Mater. Chem. A. 2014;2:699-704.

[18] Oshikawa K, Nagai M, Omi S. Characterization of molybdenum carbides for methane reforming by TPR, XRD, and XPS. J. Phys. Chem. B. 2001;105:9124-9131.

[19] Ma Y, Guan G, Hao X, Zuo Z, Huang W, Phanthong P, Kusakabe K, Abudula A. Highly-efficient steam reforming of methanol over copper modified molybdenum carbide. RSC Advances. 2014;4:44175-44184.

[20] Porosoff MD, Yang X, Boscoboinik JA, Chen JG. Molybdenum carbide as alternative catalysts to precious metals for highly selective reduction of CO_2 to CO. Angew. Chem. 2014;126:6823-6827.

[21] Sullivan MM, Held JT, Bhan A. Structure and site evolution of molybdenum carbide catalysts upon exposure to oxygen. J. Catal. 2015;326:82-91.

[22] Gao Q, Zhao X, Xiao Y, Zhao D, Cao M. A mild route to mesoporous Mo_2C-C hybrid nanospheres for high performance lithium-ion batteries. Nanoscale. 2014;6:6151-6157.

[23] Zhu Y, Wang S, Zhong Y, Cai R, Li L, Shao Z. Facile synthesis of a MoO_2-Mo_2C-C composite and its application as favorable anode material for lithium-ion batteries. J. Power Sources. 2016;307:552-560.

[24] Ojha K, Saha S, Kolev H, Kumar B, Ganguli AK. Composites of graphene-Mo_2C rods: highly active and stable electrocatalyst for hydrogen evolution reaction. Electrochim. Acta. 2016;193:268-274.

[25] Li R, Wang S, Wang W, Cao M. Ultrafine Mo_2C nanoparticles encapsulated in N-doped carbon nanofibers with enhanced lithium storage performance. Phys. Chem. Chem. Phys. 2015;17:24803-24809.

[26] Bhaskar A, Deepa M, Narasinga Rao T. MoO_2/multiwalled carbon nanotubes (MWCNT) hybrid for use as a Li-ion battery anode. ACS applied materials & interfaces. 2013;5:2555-2566.

[27] Chen M, Liu J, Zhou W, Lin J, Shen Z. Nitrogen-doped graphene-supported transition-metals carbide electrocatalysts for oxygen reduction reaction. Scientific reports. 2015;5.

[28] Liu X, Kunkel CR, Ramirez de la Piscina P, Homs N, Viñes F, Illas F. Effective and highly selective CO generation from CO_2 using a polycrystalline α-Mo_2C catalyst. ACS Catal. 2017;7:4323-4335.

[29] Davydov A, Shepot'ko M. IR-spectroscopic investigation of the nature of surface centers and of the adsorption of methanol on an iron-molybdenum oxide catalyst. Theor. Exp. Chem. 1991;26:449-455.

[30] Brungs AJ, York AP, Claridge JB, Márquez-Alvarez C, Green ML. Dry reforming of methane to synthesis gas over supported molybdenum carbide catalysts. Catal. Lett. 2000;70:117-122.

[31] Suo Z-h, Kou Y, Niu J-z, Zhang W-z, Wang H-l. Characterization of TiO_2-, ZrO_2- and Al_2O_3-supported iron catalysts as used for CO_2 hydrogenation. Appl. Catal. A: Gen. 1997;148:301-313.

[32] Zhang W, He Y, Zhang M, Yin Z, Chen Q. Raman scattering study on anatase TiO_2 nanocrystals. J. Phys. D: Appl. Phys. 2000;33:912-916.

[33] Brito JL, Laine J, Pratt KC. Temperature-programmed reduction of Ni-Mo oxides. J. Mater. Sci. 1989;24:425-431.

[34] Lin Q, Liu XY, Jiang Y, Wang Y, Huang Y, Zhang T. Crystal phase effects on the structure and performance of ruthenium nanoparticles for CO_2 hydrogenation. Catal. Sci. Technol. 2014;4:2058-2063.

[35] Kim A, Sanchez C, Patriarche G, Ersen O, Moldovan S, Wisnet A, Sassoye C, Debecker D.P. Selective CO_2 methanation on Ru/TiO_2 catalysts: unravelling the decisive role of the TiO_2 support crystal structure. Catal. Sci. Technol. 2016;6:8117-8128.

[36] Zhang X, Zhu X, Lin L, Yao S, Zhang M, Liu X, et al. Highly dispersed copper over β-Mo_2C as efficient and stable catalysts for RWGS reaction. ACS Catal. 2017;7:912-918.

Chapter 5

Conclusions

New multicomponent CuZnxGaM (M=Al, Zr) catalysts were prepared using a surfactant-free sol-gel method. The crystallite size of CuO in calcined catalysts, and that of Cu^0 in H_2-reduced catalysts, was lower for CuZnxGaM (M=Al, Zr) catalysts than those determined in the reference CuZn. Both, calcined and H_2-reduced CuZnxGaZr catalysts, showed higher surface area than the CuZnxGaAl counterparts.

CuZnxGaZr catalysts showed an easier reducibility of CuO and a higher amount of Cu, Zn and Ga species on the surface than CuZnxGaAl counterparts. The presence of ZrO_2 could favour the surface dispersion of Cu, ZnO and Ga_2O_3; the surface of CuZnxGaAl was enriched with aluminium species. Moreover, the oxygen defects at Cu-Support interface were more abundant on CuZnxGaZr than on CuZnxGaAl catalysts.

In reduced catalysts, the reference CuZn showed a lower amount of surface basic sites than CuZnxGaM (M=Al, Zr). CuZnxGaM (M=Al, Zr) catalysts showed higher capacity of CO_2 and H_2 adsorption than the bare CuZn. The higher Ga content, the higher H_2 adsorption capacity.

Reduced catalysts were highly performant in the RWGS reaction at 250-270 °C, 3 MPa using a $CO_2/H_2/N_2=1/3/1$ reactant mixture. CuZnxGaZr were more active than CuZn and CuZnxGaAl catalysts. This is related with a synergetic effect of Cu and the oxygen vacancies at the Cu-Support interface. In all cases, CO_2 conversion and CO selectivity increased with the increase of temperature. CO was the main product, CH_3OH and very small amounts of CH_4 were also formed. Over the most performant CuZn3GaZr, CO and methanol are proposed to be primary products formed through independent reaction pathways. When the RWGS reaction was carried out at atmospheric pressure over the CuZn3GaZr, the CO selectivity approached 100% at 325 °C (CO_2 conversion=16.8%). The apparent Ea determined in the 275-325 °C range for CO production over CuZn3GaZr was 70.9±3.7 kJ/mol.

The presence of Ru (0.2-2.0 wt%) in CuZn3GaZr did not show a positive effect in the catalytic properties in the RWGS under the experimental conditions used.

Calcined $CuOZnOGa_2O_3$-based catalysts were efficient in the stoichiometric MSR reaction at atmospheric pressure and in the 250-275 °C range. The H_2/CO_2 ratio obtained was close to the stoichiometric (3); only very small amounts of CO were produced probably through the RWGS reaction. CuZnxGaZr samples showed higher H_2 production than the other samples, being CuZn3GaZr catalyst the most performant. Under MSR conditions, initial CuO was reduced to Cu^0. Surface formate species are proposed to be involved in the MSR reaction for the production of CO_2 and H_2.

New Mo_xC-based catalysts were prepared using sol-gel routes with different carbon precursors and without additional H_2 and/or CH_4 reducing thermal treatment.

Bulk polycrystalline Mo_xC-U, Mo_xC-CA and Mo_xC-E catalysts were highly efficient, stable and selective for the RWGS ($CO_2/H_2/N_2$=1/3/1) reaction in the 275-400 °C range and atmospheric pressure.

Mo_xC-CA having hcp-Mo_2C, fcc-Mo_2C and/or fcc-MoC and the highest S_{BET} (14.5 m^2/g) showed the best performance. A CO yield of 41.8 $mol/Kg_{cat}\bullet h$ was obtained at 400 °C with 98% selectivity to CO. The apparent Ea determined in the 275-325 °C range for CO production was 64.8±4.1 kJ/mol.

Mo_xC-U showed only the presence of polycrystalline hcp-Mo_2C. Its characteristics and catalytic properties were deeply analyzed and successfully interpreted in the light of theoretical studies carried out under a collaborative work.

The adsorption heat of CO_2 on Mo_xC-U was -3.2 eV. Over hcp-Mo_2C, CO_2 dissociates at 35 °C to CO+O surface species. Under RWGS conditions, the reaction proceeded by subsequent hydrogenation and CO and H_2O formation.

Over Mo_xC-U, using $CO_2/H_2/N_2=1/1/3$ reactant mixture, the CO selectivity at 400 °C, 0.1 MPa, was 99.5% (CO_2 conversion=16%). An apparent Ea of 55.2 ± 2.3 kJ/mol for CO production was determined for this catalyst in the 275-325 °C range.

Mo_xC phases were successfully supported over γ-Al_2O_3, SiO_2, SBA-15, TiO_2-AR, TiO_2-A and TiO_2-R using the urea-based sol-gel method and a thermal treatment under Ar at 800 °C. Different Mo_xC phases were obtained as a function of the support.

In general, for supported Mo_xC catalysts, a higher CO production (mol CO/mol Mo•h) when compared with that of Mo_xC-U was found. However, despite no significant deactivation was observed, different structural and morphologic changes were determined for post-reaction supported catalysts.

$25Mo_xC/SiO_2$ catalyst, which showed the presence of hcp-Mo_2C and fcc-MoC, was the most performant for CO production; it produced 17.0 mol CO/mol Mo•h at 400 °C, 0.1 MPa and $CO_2/H_2/N_2=1/3/1$. Using $CO_2/H_2/N_2=1/1/3$ reaction mixture, the CO yield was up to 5 times higher than that obtained over the bulk Mo_xC-U catalyst. MoO_2 was found in the post-reaction $25Mo_xC/SiO_2$ catalyst.

The introduction of Cu or Co (5-20 wt%) in Mo_xC-U and $25Mo_xC/\gamma$-Al_2O_3 systems had not a positive effect on the catalytic behaviour in RWGS; further studies, related to the preparation method and optimization of Cu and Co amount are necessary for new developments.

Annex I

Figures

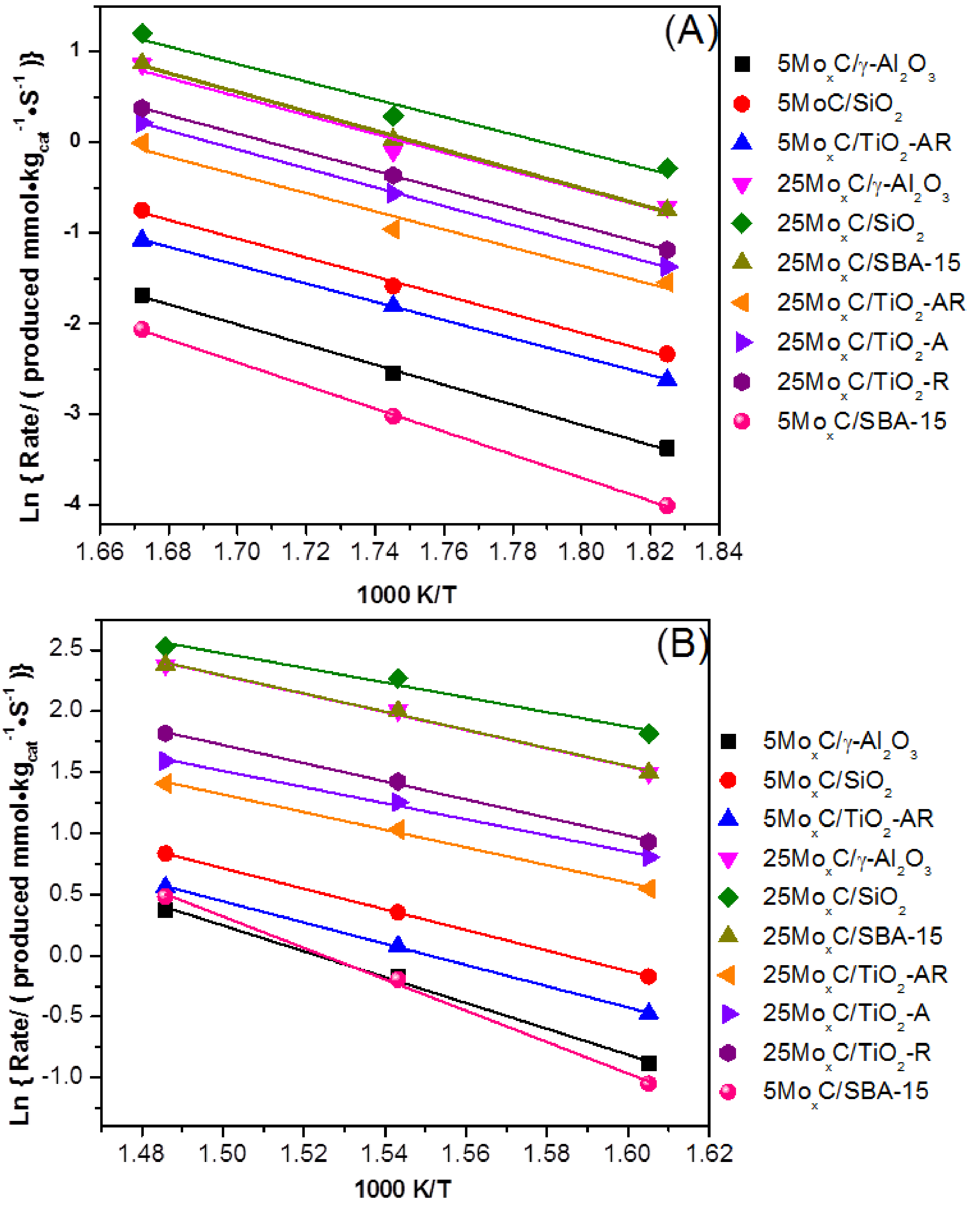

Figure A.1. Arrhenius plots obtained from CO production for supported Mo_xC samples. Reaction conditions: $CO_2/H_2/N_2$=1/3/1, GHSV=3000 h^{-1}, P=0.1 MPa. T=275-325°C (A), and T=350-400 °C (B).

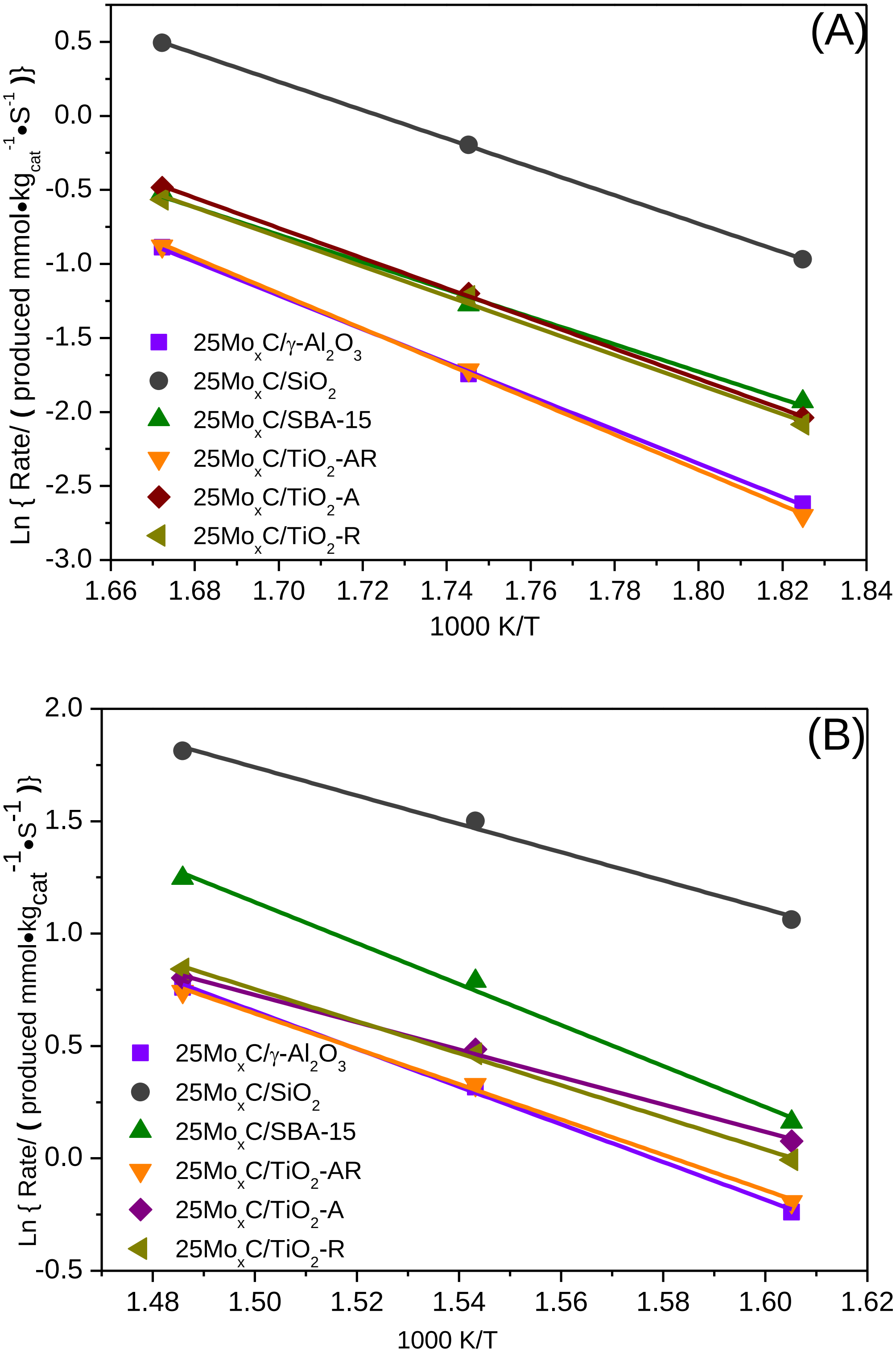

Figure A.2. Arrhenius plots obtained from CO production for supported Mo_xC samples. Reaction conditions: $CO_2/H_2/N_2$=1/1/3, GHSV=3000 h^{-1}, P=0.1 MPa. T=275-325°C (A), and T=350-400 °C (B).

Annex II

Preparation details of catalysts

a) Preparation details of bulk Mo_xC catalysts

To prepare 2 g of Mo_xC-U, approximately 15 mL of ethanol were added to 5.3 g of $MoCl_5$ to get a clear solution. Then, about 8.2 g of solid urea were dissolved in this alcoholic solution with continuous stirring until forming a viscous solution. This viscous solution was then treated at 60 °C in an oven under air to form a gel.

For the preparation of 2 g of Mo_xC-CA, an aqueous solution of citric acid (4.1 g citric acid, 14 mL H_2O) was first prepared. 8.5 g of $(NH_4)_6Mo_7O_{24}\cdot4H_2O$ precursor were then dissolved into this aqueous solution with continuous stirring. Next, 8.2 g of solid urea and 1.1 mL of ethylene glycol were added to the above solution with continuous stirring until a viscous solution was formed. Afterwards, this viscous solution was treated at 60 °C in an oven under air to form a gel.

For the preparation of 3 g of Mo_xC-E, 5.2 g of $(NH_4)_6Mo_7O_{24}\cdot4H_2O$ were dissolved in an aqueous solution, which contained 4.3 g of EDTA, 2.0 mL of ED and 116 mL H_2O, with continuous stirring until the formation of a viscous solution. After, this viscous solution was treated at 60 °C in an oven under air to form a gel.

In all cases, the formed gel was treated using the thermal treatment detailed in the Chapter 4 in a quartz tube reactor under Ar flow (20 mL/min) up to 800 °C.

b) Preparation details of supported Mo_xC-U catalysts

For the preparation of 2 g of γ-Al_2O_3-, TiO_2-, SBA-15- and SiO_2-supported catalysts with 25 wt% Mo loading; firstly, approximately 5 mL of ethanol was added to 1.61 g of $MoCl_5$ to get a clear solution. Then, about 2.5 g of solid urea were dissolved in this alcoholic solution with continuous stirring until forming a viscous solution. After, the corresponding support (1.4 g) was contacted with the above solution under continuous stirring overnight. Then, the sample was treated at 60 °C in an oven, followed by a thermal treatment under Ar flow (20 mL/min) in a quartz tube reactor similar to that applied in the preparation of bulk Mo_xC samples in two steps: at 150 °C (3 h) and at 800 °C (3 h).

c) Preparation details of MMo_xC and $MMo_xC/\gamma\text{-}Al_2O_3$ (M=Cu, Co) catalysts

To prepare 2 g of 20CuMo$_x$C, about 12 mL of ethanol were added to 4.3 g of $MoCl_5$ to form a clear solution, then 1.26 g $Cu(CH_3COO)_2{\bullet}H_2O$ and 6.9 g of urea were added to the above mentioned solution with continuous stirring. Once the viscous solution was formed, it was treated at 60 °C in an oven, followed by a thermal treatment under Ar flow as described above. 5CoMo$_x$C and 20CoMo$_x$C catalysts were prepared similarly using $Co(CH_3COO)_2{\bullet}4H_2O$.

Regarding $MMo_xC/\gamma\text{-}Al_2O_3$ (M=Cu, Co) samples: similarly to the preparation of $25Mo_xC/\gamma\text{-}Al_2O_3$ catalyst, appropriate amounts of $MoCl_5$ and, Cu or Co precursors were dissolved in 5 mL ethanol. After, the corresponding amount of the $\gamma\text{-}Al_2O_3$ support was contacted with the above mentioned solution with continuous stirring overnight. Then, the sample was treated at 60 °C in an oven, followed by the thermal treatment under Ar flow as described above.

Acknowledgements

Acknowledgements

These five years of PhD study have been a truly life-changing experience for me. I have met many lovely people in this charming city. I am grateful to all the people who gave me these five amazing and unforgettable years in Barcelona.

Firstly, I would like to give my sincere gratitude to my supervisors, **Dra. Pilar Ramírez de la Piscina Millán and Dr. Narcís Homs**. Thank you both for offering me this opportunity to join this wonderful Catalysis Materials (MATCAT) group in the University of Barcelona, and guiding my scientific research work. I am appreciative of in this five years with your guidance, encouragement, unreserved help, motivation and kindness, which really supported me through my whole PhD studies. Your broad-mindedness and professional qualities deeply impress me not only scientifically but also in the life experience, it will be a huge influence on my future career.

I am very thankful to Dr. Weijie Cai for giving me the first introduction to this scientific project when I first arrived at Barcelona.

I would like to express my deepest gratitude to all members of the MATCAT group. Alberto, Lukasz and Sonia, thanks for your kind help teaching me the different equipment in the laboratory. I am very happy to work with all of you. Moreover, I have really enjoyed our coffee and tea times which gave me many unforgotten and happy moments. I will never forget it. I have to mention my relaxed coffee moments with Lukasz in the weekend; neither will I forget when we drove to different towns in Catalunya, this is a really amazing experience for me in Spain. I wish to thank our technicians David, Marco and Dolores for their excellent work on different characterization measurements in IREC. Michael and Grace, thanks for your English correction for my PhD thesis. I also would like to express my thanks to Ariadna, Arturo, Albert, Blai, Callum, DJ, Grace, Jamil, Jura, Lewis, Mireia, Moaz, Neus, Yan and Zeno.

Lastly, I would like to thank all my Chinese friends Wenhua, Jiandong, Feng and Haibing. I also want to give my many thanks to this lovely couple, Tiantian-Zhishan, thank you very much for everything, you make me feel very at home in Barcelona.

I am also appreciative of the Chinese Scholarship Council (CSC) and IN2UB-APIF for providing me with the financial support for my PhD research.

Finally, I wish to express my gratitude to my parents and all the people in my family. Thank you for your love and unconditional support which is a powerful source for me to follow my dream. I also want to give a special thank to my husband and son, you give me the full understanding, support and inspiration. Thank you for your love!

To those who I have known over the past five years but not mentioned here, Thank you for everyone!